2014 SUMMER RESEARCH PROGRAM FOR HIGH SCHOOL JUNIORS

AT THE

UNIVERSITY OF ROCHESTER'S

LABORATORY FOR LASER ENERGETICS

STUDENT RESEARCH REPORTS

PROGRAM COORDINATOR

Dr. R. Stephen Craxton

September 2015   **Laboratory Report 383**

2014 SUMMER RESEARCH PROGRAM FOR HIGH SCHOOL JUNIORS

AT THE

UNIVERSITY OF ROCHESTER'S

LABORATORY FOR LASER ENERGETICS

STUDENT RESEARCH REPORTS

PROGRAM COORDINATOR

Dr. R. Stephen Craxton

LABORATORY FOR LASER ENERGETICS
University of Rochester
250 East River Road
Rochester, NY 14623-1299

During the summer of 2014, 16 students from Rochester-area high schools participated in the Laboratory for Laser Energetics' Summer High School Research Program. The goal of this program is to excite a group of high school students about careers in the areas of science and technology by exposing them to research in a state-of-the-art environment. Too often, students are exposed to "research" only through classroom laboratories, which have prescribed procedures and predictable results. In LLE's summer program, the students experience many of the trials, tribulations, and rewards of scientific research. By participating in research in a real

1

environment, the students often become more excited about careers in science and technology. In addition, LLE gains from the contributions of the many highly talented students who are attracted to the program.

The students spent most of their time working on their individual research projects with members of LLE's scientific staff. The projects were related to current research activities at LLE and covered a broad range of areas of interest including laser physics, computational modeling of implosion physics, radiation physics, experimental diagnostic development, cryogenic targets, theoretical and experimental chemistry, tritium capture, electronics, image display, and 3-D virtual modeling. The students, their high schools, their LLE supervisors, and their project titles are listed in the table. Their written reports are collected in this volume.

The students attended weekly seminars on technical topics associated with LLE's research. Topics this year included laser physics, fusion, holography, nonlinear optics, atomic force microscopy, electronic paper, and attosecond science. The students also received safety training, learned how to give scientific presentations, and were introduced to LLE's resources, especially the computational facilities.

The program culminated on 27 August with the "High School Student Summer Research Symposium," at which the students presented the results of their research to an audience including parents, teachers, and LLE staff. Each student spoke for approximately ten minutes and answered questions. At the symposium LLE presented its 18th annual William D. Ryan Inspirational Teacher Award. The recipient this year was Dr. Jeffrey Lawlis, Chair of the Science Department at Allendale Columbia High School. This award honors a teacher, nominated by alumni of the LLE program, who has inspired outstanding students in the areas of science,

mathematics, and technology. Dr. Lawlis was nominated by Alex Frenett, a participant in the 2013 Summer Program.

A total of 328 high school students have participated in the program since it began in 1989. The students this year were selected from nearly 70 applicants. Each applicant submitted an essay describing their interests in science and technology, a copy of their transcript, and a letter of recommendation from a science or math teacher.

In the past, several participants of this program have gone on to become semifinalists and finalists in the prestigious, nationwide Intel Science Talent Search.

LLE plans to continue this program in future years. The program is strictly for students from Rochester-area high schools who have just completed their junior year. Application information is mailed to schools and placed on the LLE website in early February with an application deadline near the middle of March. For more information about the program, please contact Dr. R. Stephen Craxton at LLE.

High School Students and Projects (Summer 2014)

Name	High School	Supervisor	Project Title
Ryan Dens	Allendale Columbia	D. W. Jacobs-Perkins	Display of Scientific Image Sources with Mobile Devices
Pranav Devarakonda	Brighton	R. Epstein	The Use of Rosseland- and Planck-Averaged Opacities in Multigroup Radiation Diffusion
William Franceschi	Victor	B. E. Kruschwitz and A. Kalb	Optimization of Wavefront Control Using a High-Resolution Wavefront Sensor
Emma Garcia	Penfield	R. S. Craxton	Optimization of Uniformity for Current Polar Drive Implosion Experiments on the National Ignition Facility
Jack Gumina	Harley	K. L. Marshall	Next-Generation Polymers for High Power UV Replicated Optics
Krishna Patel	Webster Schroeder	W. T. Shmayda	Capturing Hydrogen on Chilled Molecular Sieve
Sophia Rogalskyj	Mercy	W. T. Shmayda	Water Collection on a Platinum-Coated Molecular Sieve
Liam Smith	Webster Schroeder	R. W. Kidder	Evaluation of a Collaborative Networking Environment for Experimental Configurations
Jeremy Weed	Victor	D. Hassett, R. Peck, and D. Axman	Creating an Open Source LLE-Based Ethernet to LonTalk Adapter
Felix Weilacher	Penfield	P. B. Radha	Optimizing Beam Profiles for Polar Drive Implosions on the National Ignition Facility
Kyle Xiao	Webster Schroeder	K. L. Marshall	Computational Modeling of Azobenzenes for Optically Addressable Liquid Crystal Alignment
Nathan Xu	Pittsford Sutherland	S. X. Hu	Effects of Alpha Particle Stopping-Power Models on Inertial Confinement Fusion Implosions
Christopher Ye	Webster Schroeder	J. A. Delettrez	Limits on the Level of Fast Electron Preheat in Direct-Drive Ignition Designs
Robin Zhang	Webster Schroeder	C. Kingsley	Statistical Investigation of Cryogenic Target Defects
Roger Zhang	Webster Schroeder	R. S. Craxton	Polar-Driven X-Ray Backlighter Targets for the National Ignition Facility
Junhong Sam Zhou	Victor	C. Stoeckl	Analyzing the Sensitivity of a Hard X-Ray Detector Using Monte Carlo Methods

Display of Scientific Image Sources With Mobile Devices

Ryan Dens

Allendale Columbia School

Rochester, New York

Advisor: Douglas Jacobs-Perkins

Laboratory for Laser Energetics

University of Rochester

Rochester, New York

December 2014

1. Abstract

Software infrastructure is being developed for mobile devices to enable scientists and technicians to view live images captured by cameras in the experimental areas of the Laboratory for Laser Energetics (LLE). Mobile display devices are desirable because users can see the images wherever wireless connectivity is available. However, they present significant software design challenges for efficient bandwidth management, visual presentation and ease of use. A rudimentary application was developed for Android devices. The application can display static images with captions and extract and graph line intensities from the image. This application provides the foundation to acquire and display live images and provide basic image analysis tools. The availability of live image display on mobile devices would allow the result of any repair or adjustment to be viewed nearly instantaneously.

2. Introduction

Currently, there is no secure way for LLE scientists and technicians to access live image and video feeds quickly and efficiently from a mobile device. LLE is developing many of its image acquisition software applications, such as the SI-800 scientific-grade camera service, as "services" that share data using ZeroC's Internet Communications Engine (ICE). ICE is available for many operating systems, including common mobile devices, and allows cross-platform communication. This enabling technology is being pursued as the basis for real-time image display on mobile devices at LLE.

Through this research, an Android application was developed. The application, with an appropriate username and password, accesses images from the OMEGA Shot Images and

Reports, based on a Uniform Resource Locator (URL). With an appropriate URL, username, and password, the application can load a static image, generate relevant graphs and add meta-data, such as image and graph captions. This application is the foundation for a comprehensive application for the selection and display of live image sources on mobile devices.

Sections 3 and 4 discuss the choice of platform for the application development, followed by an examination of the engineering of the application in section 5. Sections 5.1 and 5.2 specifically relate to how common issues, such as data transfer within the application and asynchronous image downloading, were resolved.

3. Determination of the Optimum Platform for the Application

A variety of decisions had to be made in order to determine how the application was to be developed. Considerations included taking advantage of the benefits of smartphones while minimizing the effect of their disadvantages, determining which programming language and operating system were best suited to the goals of the project, and how to develop the application in the decided manner.

3.1 Advantages and Disadvantages of Mobile Devices

The premise of the project was to enable display of scientific image sources on mobile devices. The advantages and disadvantages of mobile devices compared to a traditional personal computer had to be considered in order to determine the most effective manner to present the greatest amount of information possible with an intuitive interface. Compared to traditional personal computers, mobile devices often have much smaller screens, slower hardware, and

limited bandwidth over wireless internet networks. But, mobile devices also have touch screens and many built in sensors, such as accelerometers, that personal computers do not have that could be used to create a more intuitive interface for the user. Additionally, developing an application for mobile devices is useful because the devices can be taken anywhere due to their small size and long battery life.

This in particular offers the greatest advantage to technicians in the target bays of OMEGA and OMEGA EP. The laser and target bays are clean room work areas without many computers. Since not all available computers can access images from all cameras, live image display capabilities on mobile devices would be useful for performing tasks such as alignment operations. Additionally, it would also offer faster and mobile access for scientists running experiments at the LLE.

3.2 Determination of a Suitable Programming Language

Three different programming languages were considered when determining what language the application was to be initially developed in: HTML5, Java, and Objective-C. Java and Objective-C can be used to develop native applications for Android and iOS operating systems, respectively. HTML5 is a markup language that can be used to develop a web-based application.

First, the advantages and disadvantages of a web-based application compared to a native application were considered. Web-based applications offer a broader range of supported devices and higher inherent security, whereas native applications offer faster rendering of the application,

smoother response to touch gestures, and direct access to the mobile device's built-in hardware resources and sensors. Both of the advantages of web-based applications simply reduce the amount of work required for the final product, since the application could be re-developed in additional languages to support more devices and, with the proper tools, the security advantages of a web-based application over a native application would be minimal or nonexistent. Therefore, it was determined that a native application could offer a better user experience than a web-based application. Of the two types of programming languages considered for developing a native application, an Android application programmed in Java was chosen due to the developers' familiarity with Java and the cost associated with developing Objective-C applications.

4. Application Development tools

Since LLE does not have an in-house expert on mobile device programming, software tools for the development of Android applications were first explored. First, the Eclipse Integrated Development Environment (IDE) was installed along with Android Developer Tools (ADT) and the Android Software Development Kit (SDK). Some additional libraries were required to be installed in order to support the Android SDK on a 64-Bit operating system, as described on the Android developer webpage. Since the project's completion, the Android Studio has become the official IDE for Android application development. While this was tested on an LLE laptop, seemingly without any issues, Eclipse was used because, at the time, it was the IDE used by a vast majority of Android developers. However, for those involved in extending this

project at LLE, it is recommended that the existing project be transferred from Eclipse to Android Studio in order to stay current with respect to the Android SDK.

The first task undertaken was to understand how basic Android applications are developed. Several applications were developed, such as a to-do list, in order to explore some aspects of the design philosophy of mobile applications. Due to the limited processing resources available on mobile devices, the Android operating system is relatively strict, when compared to personal computers, with regards to which applications are allocated resources. If an application is using too many resources, it will crash. Or, if the application has not been accessed for a significant amount of time, the application will stop.

The foundation of an Android application is its activities, which make up the user interface. In general, an Android activity is specified by a Java class and an XML file. The Java class specifies how the activity reacts to the user input, while the XML file specifies the layout of that screen of the application, including buttons, text, sliders, and most other static features of the application. Multiple activities can make up an application. For example, in the case of the application developed for LLE, there are four: Main, Image, Graph, and Edit Image.

5. Application Activities

Figure 1 shows the Main Activity, which consists of three Edit Text boxes, declared in the XML file, and a button. The first Edit Text allows the user to specify the image source with a URL. If that URL requires a secure login to access the image, the user can input his or her appropriate username and password.
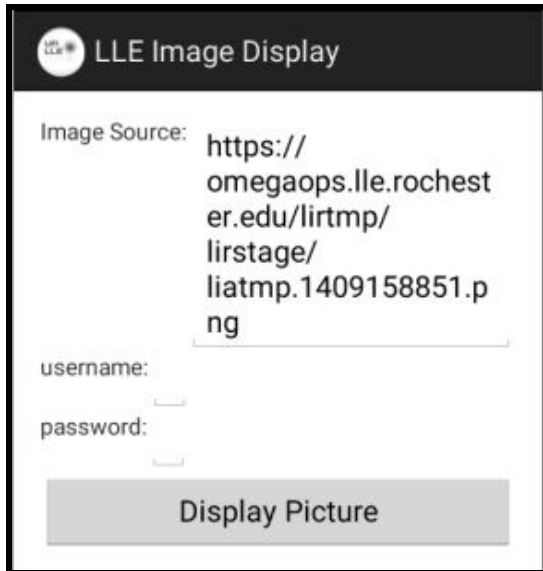
Figure 1. Screenshot of the Main Activity of the Android application.
The activity consists of three Text Views, three Text Edits, and one button.

Figure 2 shows the Image Activity. While the view itself is relatively simplistic, the bulk

of the system resources are consumed by this activity because, if required, high resolution

images can be downloaded from the internet to the device. Due to their resolution, the image

files downloaded are large and take up the majority of the processor time. The activity consists

of a Web View, which displays the image, and a Text View, which holds the caption overlayed

onto the image.
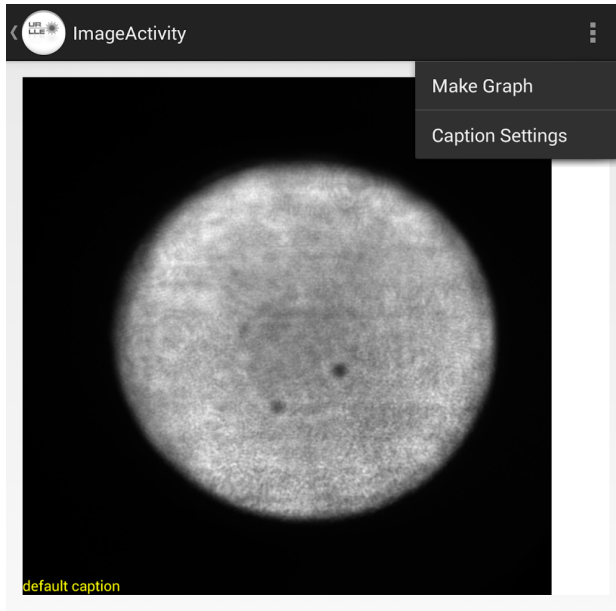
Figure 2. Screenshot of the Image Activity from the Android application.
The activity consists of a Web View and a Text View. The settings menu has options to start the Edit Image Activity and the Graph Activity,

Figure 3 shows the Edit Image Activity. Here, the user has the option to change the URL that points to the image source, overlay a caption onto the image, and position the caption. Since the user has already logged in, the option to input a new username and password is not provided. The new URL and caption are input using Edit Text boxes, as the URL, username, and password were specified before. However, in order to change the position of the caption over the image, the user must utilize the three Seek Bars, again provided by the Android SDK. One Seek bar specifies the width of the text box that contains the caption. If the user wished to split the caption into multiple rows, or to make it one single row, he or she must increase or decrease the width of the caption. The remaining two seek bars set the distance from the left and bottom sides of the screen. The indentation is based on a percent of pixels in a given column or row. For instance, changing the left margin Seek Bar's position to the exactly half ensures that the first letter of the

caption will be in the middle of the screen. This ensures compatibility across many devices, from

small smart phones to large tablets.
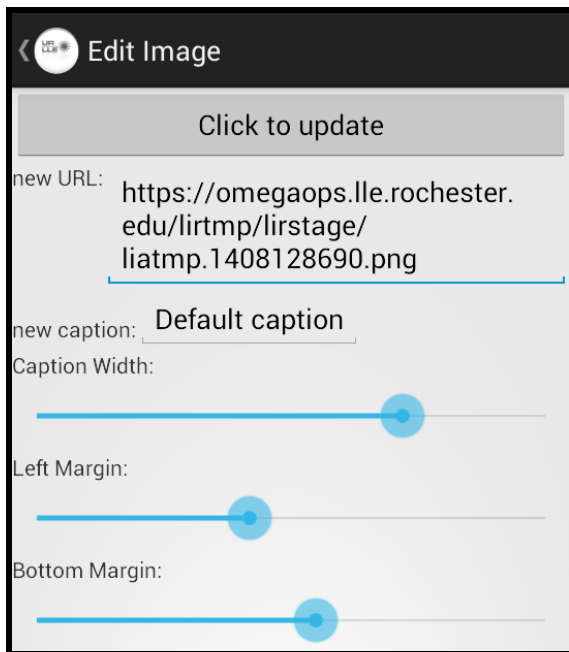
Figure 3. Screenshot of the Edit Image Activity from the Android application
The activity consists of one button, five Text View boxes, two Edit Text boxes, and three Seek
Bars.

Figure 4 shows the Graph Activity. The graph is a chart of pixel intensity for the image

specified by the URL. The Graph Activity is instantiated from the settings menu in Image

Activity from an Alert Dialog. Users can set which column or row they wish to analyze in this

dialog. The title of the graph can also be set from a secondary Alert Dialog. In order for the

graph to be generated, the image displayed in the Web View of Image Activity is saved as a

BitMap. The bitmap, column or row specifications, and graph title are then pushed to the Graph

Activity. The specified row or column of the image can be easily analyzed by analyzing the

two-dimensional array of the BitMap. In order to display the data on a graph, the Graph View

library was implemented. The Graph View library is an open source library for plotting graphs

on Android devices. A line graph was created, and the data obtained from the BitMap was

transferred to the Graph View and displayed.
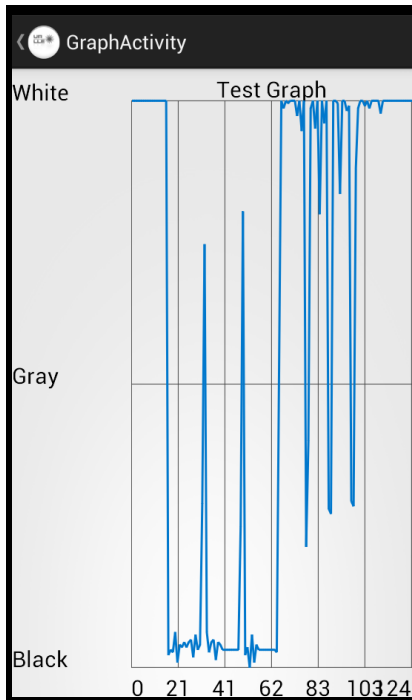
Figure 4. Screenshot of Graph View Activity from the Android application

5.1 Starting Activities and Transferring Data

Developers must be particular in the way they allow the user to travel from one activity to

the next in order to not lose data or crash the application. The best manner to travel from one

activity to another is using the "Intent" class, provided by the Android SDK. A basic diagram of

how an intent is primarily used is shown in Figure 5. Here, the Intent instantiated in Activity 1 is

being used to start and transfer information to either Activity 2 or Activity 3. As stated by the

class documentation for the Intent class, "An intent is an abstract description of an operation to

be performed". From the Main Activity, all other activities were instantiated using the functions

of the Intent class.
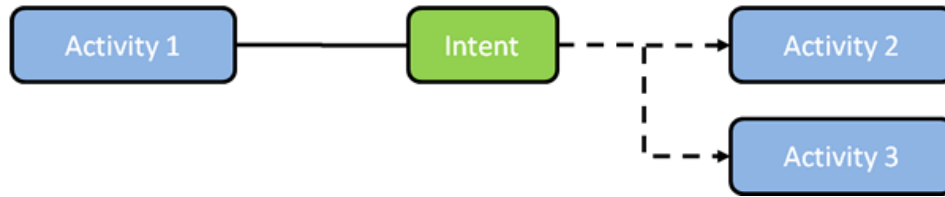
Figure 5. Diagram Showing an Intent Starting Multiple Activities

By following the instantiation of the Image Activity from the Main Activity, the capabilities of the Intent class can be better understood. First, upon the creation of Main Activity, a new instance of an Intent is created. The constructor used takes two variables: the activity, specified by the class from which the Intent is being created, and the activity, again specified by the class, that the Intent will start. By calling the function "startActivity", the current activity is safely and efficiently left while the new activity is created. If the developer were to simply attempt to change the view of the application, referring to the XML file, the application would crash. This occurs because the XML file specifying the layout of an activity is tied to the Java class that specifies how the activity functions. When only the view is changed, the Java class remains open and the application crashes.

The Intent class is not only able to safely and efficiently start new activities. It can also carry along user input from the previous activity to the new activity. This is done by calling the function "putExtra". At the most basic level, the function takes two arguments, represented as strings. One string is used as a key, while the other holds the data that the developer wishes to transfer. The key must be globally unique with respect to the project to ensure that the right data is transferred. All keys were instantiated as public, static, and final. This method must be called before the "startActivity" method in order to ensure that all data is transferred. There are several

other variations of the "putExtra" function that take booleans, integers, and even arrays. The function that passes arrays is used in the instantiation of the Graph Activity, but in the case of the instantiation of the Image Activity, only the function passing strings is utilized.

Again, examining the case of the instantiation of the Image Activity, once the function startActivity is called, the Main Activity is closed and the Image Activity is opened. From Main Activity, three values were passed to the Image Activity using the function "putExtra": the URL, the username, and the password. However, these will not automatically be transferred, and therefore be able to be directly referred to, in the Image Activity class. Upon the creation of Image Activity, the function "getIntent" is called. This function takes no arguments, but simply searches for an Intent that was sent to it. The intent is found upon the creation of Image Activity because an Intent was required to create it. The function returns the Intent that was sent to it. From that, the intent can now be referred to in the new activity. Likewise, the new activity reads data by calling the function "getStringExtra" with a key. For instance, if one were to call the function with the key value that corresponds to the key for the URL, the string representing the URL would be returned.

5.2 Proper Image Download on Android Devices

While the views and actions of an Android application are divided by activities, the execution of a task is divided into threads. Tasks can be executed synchronously or asynchronously. Synchronous tasks are executed one at a time, in sequence. When the processor has executed one task, it moves to the next. These tasks are executed on the same thread, which is generally referred to as the user interface thread. This thread handles all the input from the user

including typing on the keyboard, reaction to physical buttons, or the touch screen.

Asynchronous tasks, however, are executed on separate threads, so one task can begin before a

task on a separate thread ends. Since there is generally only one processor, all threads are given a

piece of processor time and are alternated between, allowing all threads to remain active.

As previously discussed, downloading an image from the web demands a large portion of

processor time. Because of this, time-consuming operations must not be done while running an

activity, or they will make the activity slow or become unresponsive. Therefore, the image must

be downloaded on a separate thread, or asynchronously. On Android devices, asynchronous tasks

are primarily executed by implementing the class AsyncTask, provided by the Android SDK.

When an instantiation of AsyncTask is executed, three methods are called: onPreExecute,

doInBackground, and onPostExecute, as shown in figure 6.
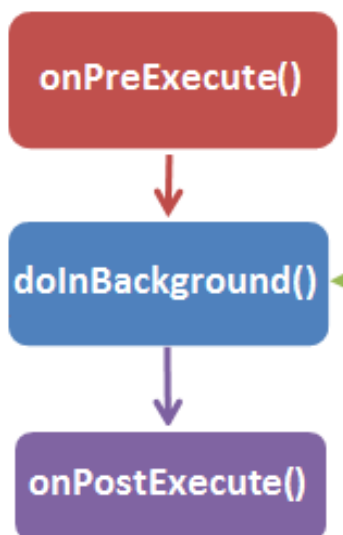
Figure 6. Flow chart of methods for the class AsyncTask.
The diagram represents the order in which the three methods, onPreExecute, doInBackground,
and onPostExecute, are called.

In order to download the image asynchronously, AsyncTask was overridden as a private

class inside the Image Activity. All three methods, onPreExecute, doInBackground, and

onPostExecute, are overridden inside this class. The function onPreExecute is executed first on the user interface thread. This method is used to set up the task that will be done on a separate thread. Next, the function doInBackground is called. This occurs on a new thread, separate from the user interface thread. This is also where the primary part of the task is executed. In the case of the Android application developed for LLE, this is where the image is downloaded as a Bitmap. Finally, the function onPostExecute is called, again on the user interface thread. This uses the result of the task executed in the background, in this case, to display the image to the user.

6. Conclusion

An Android application was developed for the display of static image sources on mobile devices. The application currently can access images specified by a URL from the OMEGA Shot Images and Reports webpage by an LLE employee with access to the OMEGA Shot Images and Reports. The application can generate a graph of pixel intensity with appropriate captions as well as overlay meta-data onto the downloaded images. This application is the foundation for a comprehensive application for the selection and display of images from live sources, such as the SI-800 Streak camera, with mobile devices.

Although there were security concerns, two-way communications between an Android device and image sources at the LLE can be achieved by utilizing ZeroC's Internet Communications Engine, referred to as ICE. ICE allows secure communication between client and server applications across multiple operating systems, including Android and iOS, the most popular mobile operating systems. ZeroC's ICE is already widely used at LLE. A client

application, similar to the Android application already created, will be able to communicate with an image service housed on a server at LLE using ICE. The image service will compress images and execute other resource intensive tasks that could not be executed on a smartphone. The image service will also prepare meta-data such as image and graph captions. The client application will be able to select and display image sources, including live image sources. It will also generate relevant graphs, apply colormaps to transferred images, and execute related image processing tasks.

7. Acknowledgements

I would first like to thank Dr. Stephen Craxton for interviewing me for and inviting me to LLE's Summer Research Program for High School Juniors**.** I would also like to thank Michael Charissis for providing technical support for setting up the Android IDE on the LLE computers. Additionally, I would like to thank Mr. Richard Kidder and Tyler Meyer for assisting with accessing ICE at LLE. Finally, I would like to thank Dr. Douglas Jacobs-Perkins for his endless support and guidance, as well as the idea for this project.

The Use of Rosseland- and Planck-Averaged Opacities in

Multigroup Radiation Diffusion

Pranav Devarakonda

Brighton High School, 1150 Winton Road, Rochester, NY

LLE Advisor: Dr. Reuben Epstein

Laboratory for Laser Energetics, University of Rochester, Rochester, NY

August 2015

Abstract

Opacity quantifies how strongly radiation is absorbed while passing through a material. Hydrocodes at LLE and elsewhere use opacity values averaged over large intervals of the radiation spectrum to calculate radiation energy diffusion transport within plasmas. This work compares two-opacity modeling, where Planck averages are used for emission and absorption and Rosseland averages are used for transport, with the treatment in LLE hydrocodes where a single opacity (typically the Planck average) is used. Planck and Rosseland interval-averaged opacities for Si were obtained by running the Prism detailed atomic model *PROPACEOS*. An analytic solution was then derived for the radiation diffusion equation in a slab-source problem in which separate opacities were used for absorption and transport. Results for the emitted spectral flux were compared for the preferred two-opacity case and for the case where a single, Planck opacity was used. Even when the Planck and Rosseland averages differed, the differences in flux were minimal except for spectral intervals where the optical depth was approximately 1.

1. Introduction

At the University of Rochester's Laboratory for Laser Energetics (LLE) and the National Ignition Facility (NIF),[1] research is done on laser fusion where laser energy is used to compress a capsule, bringing its fuel contents to thermonuclear fusion conditions.[2] There are two main types of laser fusion: direct drive and indirect drive. The Laboratory for Laser Energetics deals mainly with direct drive. In direct drive, a capsule's outer surface is irradiated directly by the laser beams, as opposed to indirect drive, where the inner surface of a small container enclosing the capsule is irradiated by laser beams entering the enclosure through laser entrance holes, generating thermal radiation that implodes the capsule.

The target is a spherical cryogenic capsule approximately 10 μm thick with a diameter of ~860 μm, coated on the inside with approximately 65 μm of deuterium-tritium (DT) ice, and filled with three atmospheres of DT.[3] The laser is the 60 beam OMEGA laser system,[4] one of the most powerful in the world. During direct-drive inertial confinement fusion, the laser pulses partially ablate the surface of the capsule, causing it to rocket off, and compress the capsule, along with its DT contents, to conditions of high temperature and density. At a sufficiently high temperature, the deuterium and tritium undergo fusion reactions to form helium, a neutron, and large amounts of energy. A large amount of thermal energy is needed to give the colliding nuclei the large thermal velocities needed to overcome their large electrostatic repulsion.

The amount of energy produced by the inertial confinement fusion process can be inferred from the measured neutron yield. LLE uses simulation programs, such as the one-dimensional hydrodynamics code LILAC,[5] to predict the outcome of these experiments. A significant factor affecting the outcome of inertial confinement fusion experiments is the x-ray opacity of the imploding capsule. Opacity is a measure of impenetrability of electromagnetic or

other kinds of radiation.[6,7] The current hydrodynamic codes use one type of averaged spectral-interval opacity, the Planck-averaged opacity. This work explores whether Rosseland-averaged opacity should also be used in the computational codes.[8]

2. Equations of Radiative Transfer

The hydrodynamic simulation code LILAC[5] is one of several used at the Laboratory for Laser Energetics that includes a radiation diffusion transport model. The codes are all similar, in that they all compute several important quantities such as radiation energy density U_ν, the spectral flux F_ν, scale length λ_ν, and optical depth τ_ν. These quantities are functions of the spectral frequency ν of the radiation and the local temperature T and material density. LILAC is unique in that it models plasma flow with spherical, cylindrical, or planar symmetry and spatial variation in only one dimension. Consequently, in this work, where we consider how radiation transport might be done differently, 1D radiation transport, as LILAC does it, is a logical point of reference. Other simulation codes at LLE use radiative opacity in similar ways, so the lessons learned in this work will have relevance to them as well.

Opacity is defined as the quantitative measure of how strongly radiation is absorbed while passing through a material. Optical depth is a dimensionless quantity defined as the integral of opacity with respect to distance. If the optical depth is much greater than 1, the source is considered to be optically thick, and, conversely, if the optical depth of the source is much less than 1, the source is considered to be optically thin. The following equation expresses the optical depth at the spectral frequency ν:

$$\tau_\nu = \int \kappa_\nu ds, \qquad (2.1)$$

where κ_ν is the opacity at frequency ν and s is the distance along a path through the source. The value of the optical depth depends on the choice of this path.[6,7] The quantities of spectral flux F_ν and radiation energy density U_ν are closely related in the time-independent diffusion approximation by the following equations,

$$F_\nu = -\frac{c}{3\kappa_\nu}\frac{dU_\nu}{ds} \tag{2.2a}$$

$$\frac{dF_\nu}{ds} = \varepsilon_\nu - c\kappa_\nu U_\nu, \tag{2.2b}$$

where c is the speed of light and ε_ν is emissivity (emitted spectral power per unit volume) at frequency ν.[8] Equations (2.2) are written for 1D plane-parallel geometry where the path length parameter s is the spatial coordinate in the one spatial dimension. The diffusion approximation arises from the assumption that radiation is defined as a locally isotropic spectral energy density of photons plus a small flux in a single direction along the gradient of U_ν. Equation (2.2a) gives the magnitude of this radiation flux in terms of this gradient of the radiation energy density, and Eq. (2.2b) equates the divergence of this radiation flux to the total radiation emission-minus-absorption at a given point. Equations (2.2a) and (2.2b) can be solved simultaneously for U_ν and F_ν. These two equations can be combined into one by eliminating F_ν, leaving the more familiar diffusion equation, a 2nd-order differential equation for U_ν,[8]

$$0 = -\frac{d}{ds}\left(\frac{c}{3\kappa_\nu}\frac{dU_\nu}{ds}\right) + \varepsilon_\nu - c\kappa_\nu U_\nu. \tag{2.3}$$

When calculating radiation transport numerically over the whole spectrum, the spectrum is divided into a finite number of frequency intervals or "groups," where the spectral frequency group index k refers to the frequency interval from ν_k to ν_{k+1}. This frequency grouping should

be as fine as necessary to resolve the spectrum, but there should also be as few groups as possible to minimize the time and other computational resources required to complete the calculation. This "multigroup" formulation is constructed by replacing the frequency-dependent flux, energy density, emissivity, and opacity quantities in Eqs. 2.2a, 2.2b, and 2.3 with group-averaged quantities:

$$F_k = -\frac{c}{3\kappa_{R,k}}\frac{dU_k}{ds} \tag{2.4a}$$

$$\frac{dF_k}{ds} = \varepsilon_k - c\kappa_{P,k}U_k. \tag{2.4b}$$

The group-averaged emissivity is obtained using

$$\varepsilon_k = \frac{\int_{v_k}^{v_{k+1}} \varepsilon_v dv}{v_{k+1}-v_k}, \tag{2.5}$$

and the flux F_k and energy density U_k averages are obtained by the same method.[6,8]

For Eq. (2.4a) to be consistent with Eq. (2.2a), the group-average opacity $\kappa_{R,k}$ must be

$$\frac{1}{\kappa_{R,k}} = \frac{\int_{v_k}^{v_{k+1}}\frac{1}{\kappa_v}\frac{dU_v}{ds}dv}{\int_{v_k}^{v_{k+1}}\frac{dU_v}{ds}dv} , \tag{2.6a}$$

and for Eq. (2.4b) to be consistent with Eq. (2.2b), the group-average opacity $\kappa_{P,k}$ must be

$$\kappa_{P,k} = \frac{\int_{v_k}^{v_{k+1}} U_v\kappa_v dv}{\int_{v_k}^{v_{k+1}} U_v dv}. \tag{2.6b}$$

Equations (2.6) show that calculating the multigroup average opacity quantities requires that the radiation energy density U_v frequency dependence be known in sub-group detail, i.e., in finer

6

spectral detail than the multigroup spectral resolution can provide. We can proceed with the

multigroup method by approximating the weighting functions in Eqs. (2.6) with the radiation

energy density known to exist under conditions of local thermodynamic equilibrium,[8]

$$U_\nu = \frac{4\pi}{c} B_\nu(T),$$
(2.7a)

where $B_\nu(T)$ is the Planck function

$$B_\nu(T) = \frac{2h\nu^3}{c^2} \frac{1}{e^{h\nu/k_B T} - 1},$$
(2.8)

and where h is the Planck constant and k_B is the Boltzmann constant. This approximation was

originally devised for the deep interior of stars, where it is an excellent approximation.[7] Other

than this precedent, we have no well-developed justification for using this approximation in laser

fusion. We can also write

$$\frac{dU_\nu}{ds} = \frac{4\pi}{c} \frac{dB_\nu(T)}{dT} \frac{dT}{ds}.$$
(2.7b)

The two kinds of opacity average which we will explore are the Planck-averaged opacity,

obtained from Eqs. (2.6b) and (2.7a), computed as an arithmetic mean weighted by the Planck

function,

$$\kappa_{P,k} \equiv \frac{\int_{\nu_k}^{\nu_{k+1}} B_\nu \kappa_\nu d\nu}{\int_{\nu_k}^{\nu_{k+1}} B_\nu d\nu},$$
(2.9a)

and the Rosseland-averaged opacity, obtained from Eqs. (2.6a) and (2.7b), computed as a

harmonic mean weighted by the derivative of the Planck function with respect to temperature,[8]

7

$$\frac{1}{\kappa_{R,k}} \equiv \frac{\int_{\nu_k}^{\nu_{k+1}} \frac{1}{\kappa_\nu} \frac{dB_\nu}{dT} d\nu}{\int_{\nu_k}^{\nu_{k+1}} \frac{dB_\nu}{dT} d\nu} \ . \tag{2.9b}$$

The temperature gradient *dT/ds* in Eq. (2.7b) cancels out of the quotient in Eq. (2.6a).

Just as the arithmetic mean of a set of data is always greater than or equal to the harmonic mean, the Planck-averaged opacity is generally greater than or equal to the Rosseland-averaged opacity, assuming that the weighting functions do not greatly impact the averages. As the number of groups increases and as the individual groups narrow to the point where the spectral features of the opacity begin to be resolved by the frequency groups, the differences between the Planck and Rosseland averages become less important, and the choice of the weighting functions becomes less critical. Unfortunately, computational limits on spectral resolution may not allow a number of frequency groups large enough to achieve this.

The tabulated group-averaged emissivity $\mathcal{E}_k$ is generally obtained as part of the same atomic-physics calculation used to obtain the group-averaged opacity or opacities. Under conditions of local thermodynamic equilibrium, which is assumed here, the emissivity is related to the opacity by the Kirchoff relationship[9]

$$\varepsilon_\nu = 4\pi\kappa_\nu B_\nu(T). \tag{2.10}$$

Equation (2.7a) is, in part, a consequence of Eq. (2.10). Using Eq. (2.10) in Eq. (2.5) and applying Eq. (2.9a) gives the expression

$$\varepsilon_k = \frac{4\pi\kappa_{P,k} \int_{\nu_k}^{\nu_{k+1}} B_\nu(T) d\nu}{\nu_{k+1} - \nu_k}, \tag{2.11}$$

which relates the group-averaged emissivity $\mathcal{E}_k$ to the Planck-averaged opacity $\kappa_{P,k}$.

Consequently, $\mathcal{E}_k$ will not be changed by varying $\kappa_{R,k}$, as long as $\kappa_{P,k}$ is left constant.
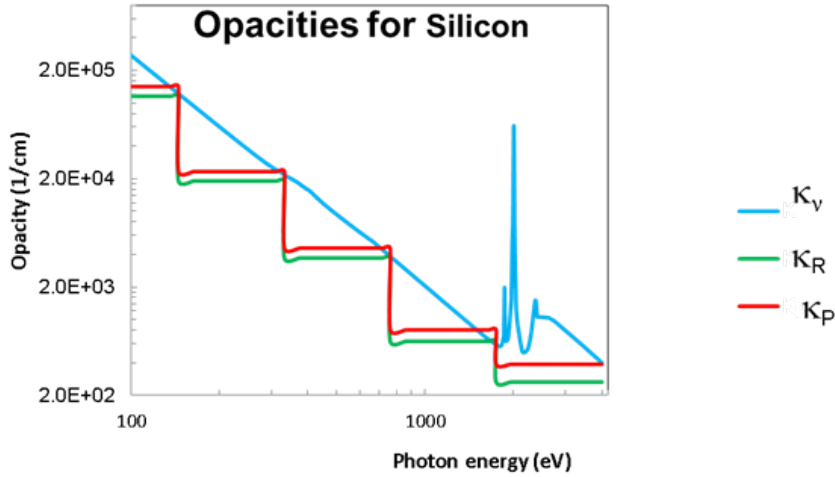
Fig. 1: A graph of the opacity (κ_ν) of silicon and the Planck (κ_P) and Rosseland (κ_R) group-averaged opacities as functions of photon energy, for a density n_i of 1.68×10^{23} ions/cm^3 and a temperature of 1.93 keV.

Figure 1 shows the opacity κ_ν of silicon,[10] which is a possible target material, for typical laser-fusion values of ion density and temperature. The Planck and Rosseland-averaged opacities are in the form of step functions in Fig. 1 where the horizontal segments represent the opacity averaged over a photon energy interval. Photon energy and frequency are essentially equivalent terms, related through the Planck equation $E = h\nu$. In the regions where the opacity varies smoothly, the Planck and Rosseland-averaged opacities are roughly equal. However, when there is a spectral line, as is seen in the highest energy group at the right end of the ordinate where the opacity value spikes markedly, the Planck-averaged opacity is significantly larger than the Rosseland-averaged opacity.

In this work, two-opacity modeling, where the Planck average is used for emission (through Eq. (2.11)) and absorption in Eq. (2.4b) and the Rosseland average is used for transport in Eq. (2.4a), is compared with the single-opacity treatment in LLE hydrocodes where a single opacity (typically the Planck average) is used for all purposes.

3. The Slab Source Problem

The slab source problem is a common illustrative example in radiation transport literature. The slab source problem assumes a uniform slab of thickness L under conditions of uniform composition, temperature, and density. This provides a slab with spatially uniform opacity and emissivity where the general solution to Eqs. (2.4a) and (2.4b) is

$$U_k(x) = C_0 - C_1 e^{\sqrt{3\kappa_{P,k}\kappa_{R,k}}\,x} - C_2 e^{-\sqrt{3\kappa_{P,k}\kappa_{R,k}}\,x}, \tag{3.1a}$$

and, by Eq. (2.4a),

$$F_k(x) = c\sqrt{\frac{\kappa_{P,k}}{3\kappa_{R,k}}}\left(C_1 e^{\sqrt{3\kappa_{P,k}\kappa_{R,k}}\,x} - C_2 e^{-\sqrt{3\kappa_{P,k}\kappa_{R,k}}\,x}\right), \tag{3.1b}$$

where x is the spatial coordinate in the direction normal to the slab. The constant C_0 is determined by substitution into Eqs (2.4a) and (2.4b),

$$C_0 = \frac{\varepsilon_k}{c\kappa_{P,k}}, \tag{3.1c}$$

and the constants C_1 and C_2 are set by a zero-flux condition at the center plane of the slab and by a surface flux boundary condition. At the center plane of the slab, $x=0$, there is no net flux in either direction because the positive and negative x directions are equivalent, so $C_1 = C_2$ from Eq. (3.1b). At the outer surfaces of the slab, $x = \pm L/2$, the only flux is that of the radiation energy density at the surface escaping freely at the speed of light along all possible directions, distributed uniformly into the outgoing hemisphere of directions. This is expressed as

10

$$F_k\left(\pm\frac{L}{2}\right) = \pm\frac{c}{2}U_k\left(\pm\frac{L}{2}\right), \tag{3.1d}$$

which, using Eqs. (3.1a), (3.1b), and (3.1c), completes the solution with

$$C_1 = C_2 = C_0 \frac{1}{\left(\frac{2}{\sqrt{3}}\sqrt{\frac{\kappa_{P,k}}{\kappa_{R,k}}}+1\right)e^{\sqrt{3\kappa_{P,k}\kappa_{R,k}}\frac{L}{2}}-\left(\frac{2}{\sqrt{3}}\sqrt{\frac{\kappa_{P,k}}{\kappa_{R,k}}}-1\right)e^{-\sqrt{3\kappa_{P,k}\kappa_{R,k}}\frac{L}{2}}}. \tag{3.1e}$$

Examination of Eqs. (3.1a) and (3.1b) reveals that the spatial dependence of the flux and energy density in one photon energy group is entirely exponential of the form $e^{\pm x/\lambda_{PR,k}}$ with a single scale length $\lambda_{PR,k}$ where

$$\lambda_{PR,k} \equiv 1/\sqrt{3\kappa_{P,k}\kappa_{R,k}}, \tag{3.2}$$

and an optical thickness

$$\tau_{PR,k} \equiv L/\lambda_{PR,k}. \tag{3.3}$$

For sources that are optically thick, Eq. (3.1e) shows that the coefficients C_1 and C_2 vanish exponentially, relative to C_0, for large $\tau_{PR,k}$. This means that U_k is very nearly equal to C_0 everywhere, except within a distance less than about one scale length inside of each of the outer surfaces of the slab. This is consistent with the interpretation that the energy density deep (optically) within a slab is determined almost completely by the balance of absorption and emission, leaving a flat energy density profile and, locally, a negligible flux, according to Eq. (2.4a), and, therefore, a negligible divergence of flux on the left-hand side of Eq. (2.4b) to modify the balance of absorption and emission expressed by the right-hand side of this equation.

By applying Eqs. (3.1) to the slab source problem, we can determine the spectral flux and energy density at various points in the source, most importantly at the outer surfaces. The material that we have chosen to explore as part of the slab source problem is silicon. This is

because other elements commonly used in laser fusion capsule shells such as hydrogen and carbon do not have spectral lines at typical temperatures because their electrons have already been freed and no longer undergo frequent transitions between discrete bound states. The sample temperature and ionic density which we have chosen to use is a temperature of 1.93 keV and an ionic density of 2.67×10^{23} ions/cm^3 as these values correspond to typical conditions in which the silicon spectrum contains interesting features, including some spectral lines. [10]

The majority of the simulation codes at the Laboratory for Laser Energetics do not simultaneously use both the Rosseland-averaged and Planck-averaged opacities, a relic from the days of limited storage and processing capacity. One simulation code, Helios, by Prism Computational Sciences, Inc.,[11] uses both Planck-averaged and Rosseland-averaged opacities in its multigroup radiation transport model. The modeling of the radiation diffusion equations typically uses the Planck-averaged opacity in place of the Rosseland-averaged opacity for flux. The effect of the resulting inaccuracy on the results of radiation simulation can be assessed by repeating the simulation with successively finer frequency groupings until the results are no longer changed by further refinement. This process will eventually converge, since the Rosseland and Planck averages are equal in the limit of fine spectral resolution.

To demonstrate the impact of using a single-opacity (or one-opacity) Planck-averaged opacity instead of the more correct two-opacity model on the calculated radiation energy density and spectral flux, we explored two cases of a single energy group with Planck optical thicknesses $\tau_{P,k} = 3$ and 1, where

$$\tau_{P,k} \equiv L/\lambda_{P,k}, \tag{3.4}$$

expressed in terms of a Planck scale length

$$\lambda_{P,k} \equiv 1/\left(\sqrt{3}\kappa_{P,k}\right), \tag{3.5}$$

to illustrate what happens when the slab is of moderate optical thickness. Results are shown in Fig. 2 for various ratios of the Rosseland-averaged opacity to the Planck-averaged opacity. In these figures, x represents the position across the thickness of the slab, plotted as the dimensionless quantity x/L, energy density is plotted in units of C_0, and flux is plotted in units of cC_0.

Figure 2(a) shows energy density profiles, and Fig. 2(b) shows radiation flux profiles of a slab of Planck optical thickness 3 for different values of the Rosseland-to-Planck opacity ratio. It is seen that there is little change in either graph when the Rosseland-averaged opacity is reduced to only half of the Planck-averaged opacity. Figure 2(c) shows the corresponding energy density profiles, and Fig. 2(d) shows the corresponding radiation flux profiles of a slab of Planck optical thickness 1. It is seen that by having reduced the optical thickness from 3 to 1, significantly less energy is bottled up in the slab, and the changes in the energy density and radiation flux with the reduction in the Rosseland opacity are still small. The more optically thin slab confines the escaping radiation less than in the more optically thick case, so the flux in Fig. 2(d) is more uniformly diverging and less affected by the Rosseland opacity value than in Fig. 2(b). In the examples studied thus far, no stronger or more dramatic effects than these of varying the Rosseland-to-Planck average opacity ratio have been found.
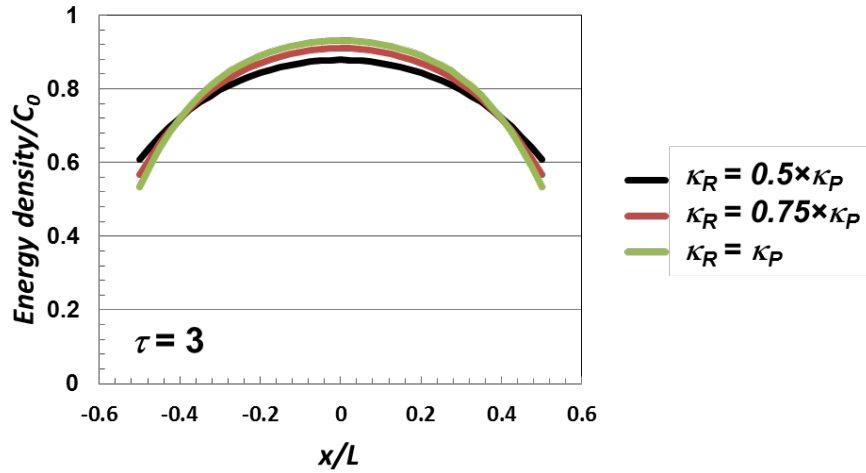
Fig. 2a: Energy density, in units of C_0, plotted as a function of position across the slab in units of the slab thickness L, within a slab of Planck optical thickness 3, for various ratios of κ_R/κ_P.
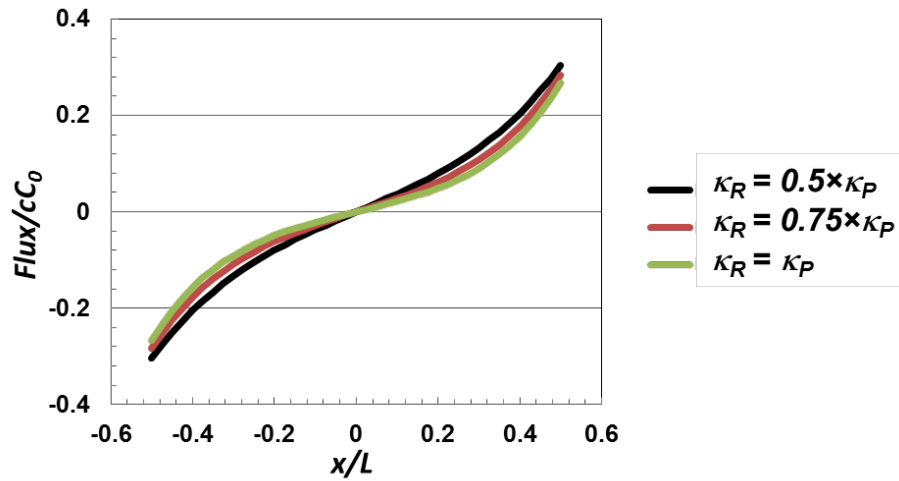
Fig. 2b: As Fig. 2a, but for spectral flux, plotted in units of cC_0.
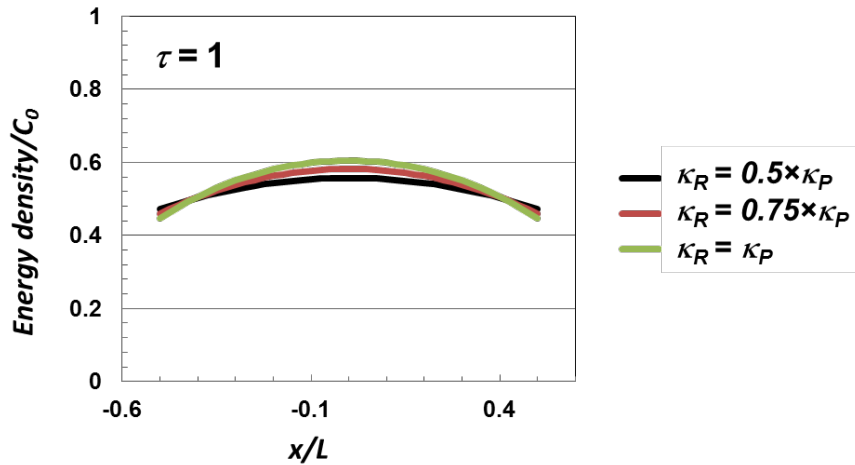
Fig. 2c: As Fig. 2a, but for a slab of Planck optical thickness 1.
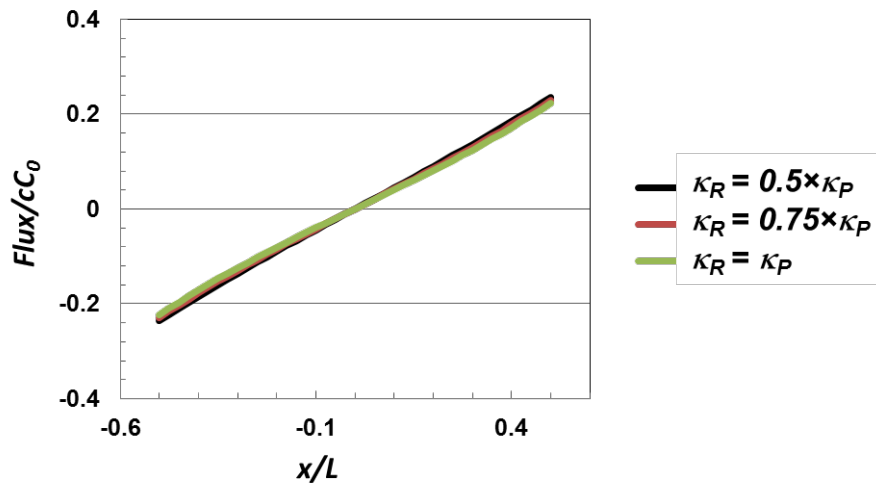
Fig. 2d: As Fig. 2c, but for spectral flux, plotted in units of cC_0.

4. Determining the Impact of the Rosseland-Averaged vs. Planck-Averaged Opacity

We will now analyze the impact of replacing the Rosseland-averaged opacity with the Planck-averaged opacity in a multigroup solution to the slab-source problem. We will set the

15

thickness of the slab to be 40 microns. The opacity, temperature, and ionic density are the same as those used to create Figure 1.

Figure 3 shows the ratio of the two-opacity to the one-opacity scale lengths λ_{PR}/λ_P obtained using Eqs. (3.2) and (3.5), plotted as a function of photon energy. The opacities are group-averaged, which accounts for the step-function appearance. The variation in the scale length stays at around 10% until the final group where it rises to 20%. This is because the final group has a silicon spectral line, causing the Planck-averaged opacity to be significantly larger, thereby causing the scale length computed using solely the Planck-averaged opacity to be significantly smaller.
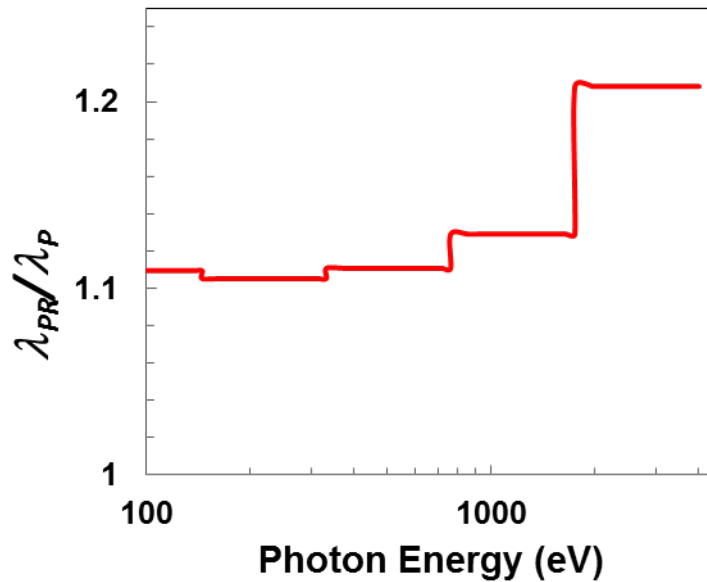
Figure 3: A graph of the ratios of the scale lengths λ_{PR}/λ_P computed using a 1-opacity vs. a 2-opacity model.

We now evaluate Eqs. (3.1) for the radiation spectral flux for the same slab and the same conditions for each of the energy groups shown in Fig. 3, first with distinct κ_P and κ_R, and then

substituting κ_P for κ_R. The difference in the two flux spectra plotted in Figure 4(a) shows the impact of using the Planck-averaged opacity in both Eqs. (2.4), rather than both the Planck and Rosseland averages, where indicated.

The spectral fluxes, plotted in Fig. 4(a) in arbitrary units, do not appear as step functions, as they would if Eqs. (3.1) had been evaluated entirely in terms of group-averaged quantities, as has been described thus far. The actual calculation was performed using a frequency-dependent emissivity $\varepsilon(\nu)_k$,

$$\varepsilon(\nu)_k = 4\pi\kappa_{P,k}B_\nu(T), \tag{4.1}$$

where the frequency ν lies within the group boundaries ν_{k+1} and ν_k. This is an attempt to restore some of the frequency dependence of the emissivity lost in the group-averaging process by using the Planck function itself, rather than its group average, as in Eq. (2.11). This does not recover all the spectral detail of the opacity within the frequency groups, particularly the strong spectral line seen in Fig. 1 in the highest energy group near 2000 eV.

The ratio of the one-opacity flux to the two-opacity flux plotted in Fig. 4(a) is plotted in Fig. 4(b). The sub-group frequency dependence of the emissivity, given by Eq. (4.1), cancels out of this flux ratio, restoring the step-function result that would have been obtained had Eq. (2.5) been used. It can be seen that the spectral flux computed by using solely the Planck-averaged opacity is greater by a small percentage for the smaller photon energy groups. However, for the higher energies, the flux computed using solely the Planck-averaged opacities is significantly, 15-25%, lower. This is due to the spectral lines of silicon appearing in this photon energy range

17
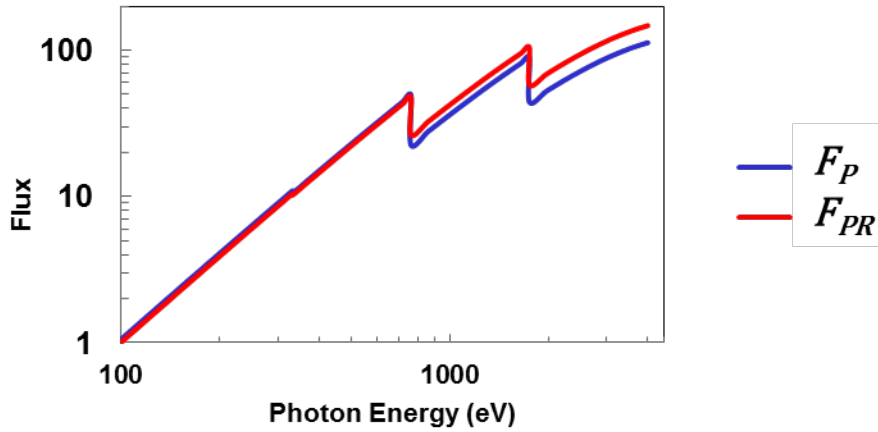
Figure 4a: Graphs of fluxes, expressed in arbitrary units, as functions of photon energy, comparing 1-opacity (blue curve) and 2-opacity (red curve) models.
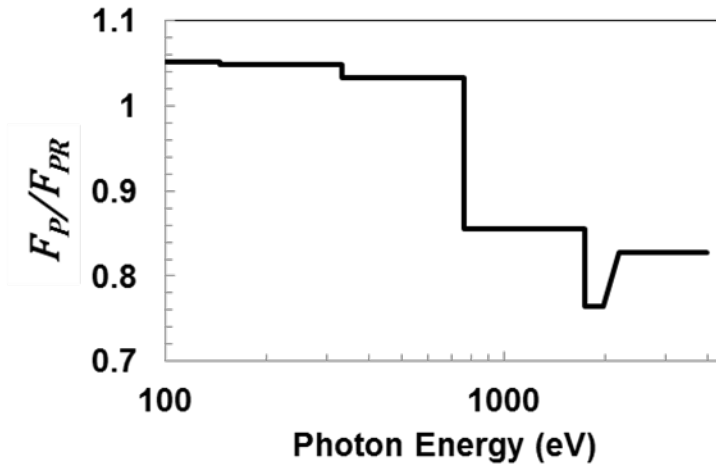
Figure 4b: Graph of the ratio of the fluxes computed by the one-opacity and two-opacity models as a function of photon energy.

lowering the Rosseland-averaged opacity, resulting in a longer scale length with less of the

emitted photons being absorbed before they escape.

A 15-25% error is clearly too large to be ignored and calls into question the accuracy of

one-opacity calculations in general, particularly if there is concern that an insufficient number of

photon energy groups are being used. Our preliminary results suggest that upgrading a one-opacity calculation to a two-opacity calculation may be an efficient complement to increasing the accuracy of calculations by increasing the number of energy groups. This conclusion is based only on our experience with the one example shown above. Before recommending that a simulation code be upgraded to include a two-opacity model, other examples will have to be studied, including realistic simulations of relevant experiments, as well as idealized configurations in addition to the slab model considered here.

5.   Conclusions

In conclusion, we have demonstrated, by example, the possible benefit of upgrading from a one-opacity to a two-opacity model. Planck and interval-averaged opacities for Si were obtained by running the Prism detailed atomic model in the code *PROPACEOS*. An analytic solution was then derived for the radiation diffusion equation in a slab-source problem in which either the same or separate opacities were used for absorption and transport, and the calculated emitted spectral fluxes were compared. Even when the Planck and Rosseland averages differed, the differences in flux were minimal except for spectral intervals where the optical depth was approximately 1. There, it was shown that the values for flux can differ by ~10% - 20%. A broad range of conditions with a larger set of test cases will be necessary to establish the importance of changing from one-opacity to two-opacity modeling, but this work has laid some of the groundwork for how this is to be done, particularly the solution to the slab problem expressed in terms of both the Rosseland- and Planck-averaged opacities, which will allow a

broad range of cases to be considered. Thus far, it appears that upgrading to two-opacity

modeling merits serious consideration.

References

1. C. A. Haynam, P. J. Wegner, J. Auerbach, M.W. Bowers, S. N. Dixit, G. V. Erbert, G. M. Heestand, M. A. Henesian, M. R. Hermann, K. S. Jancaitis, K. R. Manes, C. D. Marshall, N. C. Mehta, J. Menapace, E. Moses, J. R. Murray, M. C. Nostrand, C. D. Orth, R. Patterson, R. A. Sacks, M. J. Shaw, M. Spaeth, S. B. Sutton, W. H. Williams, C. C. Widmayer, R. K. White, S. T. Yang, and B. M. Van Wonterghem, Appl. Opt. **46**, 3276-3303 (2007).

2. J. Nuckolls, L. Wood, A. Thiessen, and G. Zimmerman, Nature **239**, 139 (1972); Lois H. Gresh, Robert L. McCrory, and John M. Soures, *Inertial Confinement Fusion: An Introduction,* Laboratory for Laser Energetics: Rochester, NY, 2009.

3. V. N. Goncharov, "Cryogenic Deuterium and Deuterium-Tritium Direct-Drive Implosions on Omega," in *Laser-Plasma Interactions and Applications,* Scottish Graduate Series **68**, Springer International Publishing, P. McKenna, D. Neely, R. Bingham, D. A. Jaroszynski, eds., 2013.

4. T. R. Boehly, D. L. Brown, R. S. Craxton, R. L. Keck, J. P. Knauer, J. H. Kelly, T. J. Kessler, S. A. Kumpan, S. J. Loucks, S. A. Letzring, F. J. Marshall, R. L. McCrory, S. F. B. Morse, W. Seka, J. M. Soures, and C. P. Verdon, Opt. Commun. **133**, 495 (1997).

5. J. Delettrez, R. Epstein, M. C. Richardson, P. A. Jaanimagi, and B. L. Henke, Phys. Rev. **A 36**, 3926 (1987).

6. R. Epstein, *Equation of Transfer*, privately circulated report, Laboratory for Laser Energetics, Rochester, 2009.

7. S. Chandrasekhar, *Radiative Transfer*, Dover Publications, New York, 1960; J. I. Castor, *Radiation Hydrodynamics*, Cambridge University Press, 2004.

8. G. C. Pomraning, *The Equations of Radiation Hydrodynamics*, Pergamon Press, Oxford, 1973.

9. H. R. Griem, *Principles of Plasma Spectroscopy*, Cambridge University Press, Cambridge, England, 1997.

10. J. J. MacFarlane *et al.*, *PrismSPECT and SPECT3D Tools for Simulating X-ray, UV, and Visible Spectra for Laboratory and Astrophysical Plasmas*, American Physical Society, 34th Meeting of the Division of Atomic, Molecular and Optical Physics, May 2003; PrismSPECT, Prism Computational Sciences, Inc., http://www.prism-cs.com/

11. J. J. MacFarlane, I. E. Golovkin, P. R. Woodruff, J. Quant. Spectrosc. Radiat. Transfer **99**, 381-397 (2006).

Acknowledgements

Optimization of Wavefront Control using a High Resolution Wavefront Sensor

Willie Franceschi
Victor Senior High School
Advisers: Brian Kruschwitz, Adam Kalb

1

Optimization of Wavefront Control using a High Resolution Wavefront Sensor

Abstract

The use of adaptive optics to correct the laser wavefront is a key component of the Omega EP laser. This correction is based on information provided by a wavefront sensor (WFS). Compared with the 77 resolution elements of the current wavefront control sensor, the high-resolution wavefront sensor (HRWS) contains 19,044 resolution elements (138 by 138), allowing for more accurate wavefront measurements and potentially improved wavefront correction. The incorporation of this sensor required modifications to previous software and writing of new MATLAB code for diagnostic and stability purposes. In order to solve the issue of a changing pupil area, a "global pupil" approach was developed and implemented in the calibration and correction processes. The testing of correction software, including the global pupil approach, was conducted in the deformable mirror (DM) testbed. The HRWS control algorithms were tested on a beamline of the Omega EP laser, and outperformed the existing Wavefront Control System with an 8% decrease in RMS wavefront error and a 5% decrease in focal spot size (80% encircled energy). The correction of two deformable mirrors simultaneously was also attempted, with mixed results.

Introduction

Due to a variety of factors, including aberrations in amplifiers and optics, the laser beam wavefront on the Omega EP laser system is not flat, resulting in poorly focused focal spots upon target. To minimize this effect, the Omega EP laser includes a series of wavefront control loops, or adaptive optics systems, that work to correct the wavefront aberrations (1). A simplified diagram of the wavefront control loop is shown in figure 1, demonstrating the process in which this aberrated wavefront is corrected. An adaptive optics system - in this case a deformable mirror - physically corrects the wavefront. The corrected laser beam continues on to the target (2).
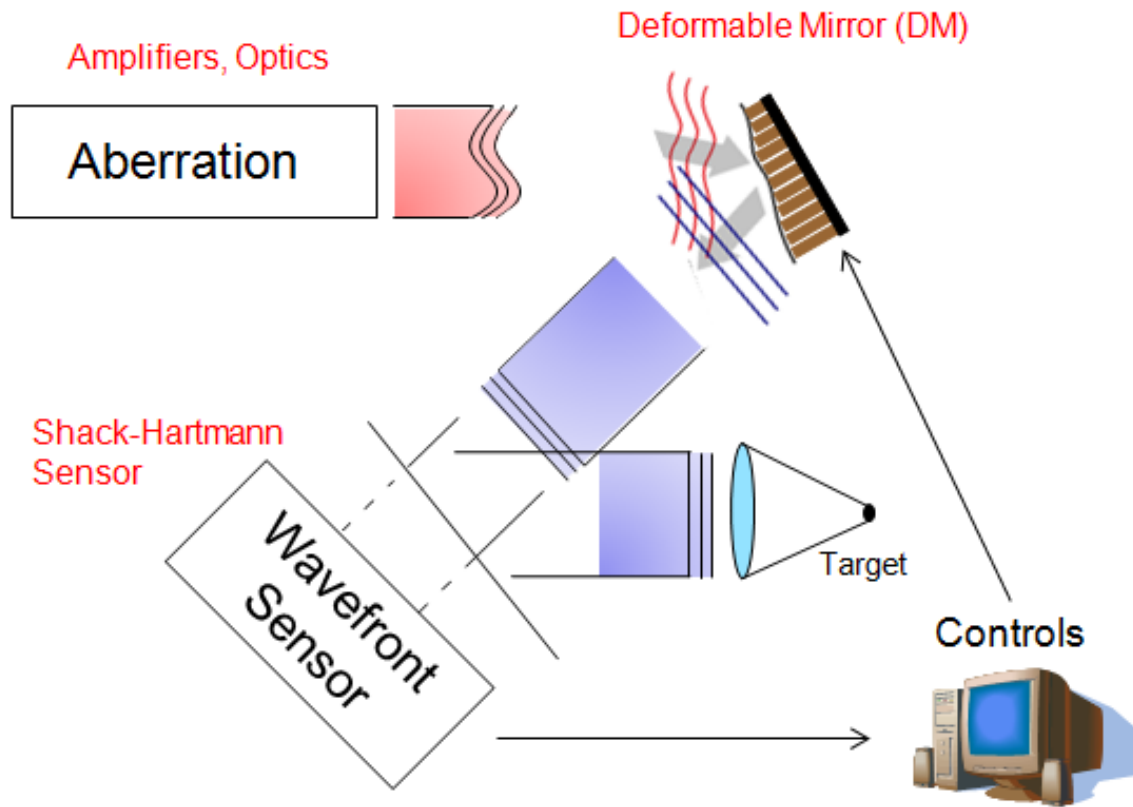
Figure 1: *An adaptive optics system used to correct the uneven wavefront produced by amplifiers and optics. A wavefront sensor measures the corrected wavefront and sends the data to a control system. The control system processes the data and adjusts the deformable mirror, further correcting the wavefront by altering the voltages of the 39 actuators spread out behind the mirror.*

The Omega EP DM has a reflective surface approximately 400 mm by 400 mm square. Actuators assembled in a hexagonal pattern push and pull on the backside of the mirror to create a deformed surface that corrects the uneven wavefront. Voltages are applied to these actuators, and the actuators move accordingly (104 nm per volt). All the actuators have lower and upper voltage limits at 30 and 150 volts respectively. Occasional issues with actuators reaching, and stalling, at upper and lower voltage limits were corrected through MATLAB software discussed later in the paper.

The wavefront sensors used in the Omega EP wavefront control system are Shack-Hartmann sensors (SHS). A SHS is composed of a two-dimensional array of lenses that focuses different parts of a beam of light onto a flat sensor. The sensor measures the offsets of these focused points (centroid locations or offsets) in the horizontal and vertical directions, relative to the centroid locations of a reference, flat wavefront (3). The sensor stores information about the horizontal and vertical offsets of the wavefront that the controls use in correction algorithms. Different wavefront aberrations cause varying centroid offsets.
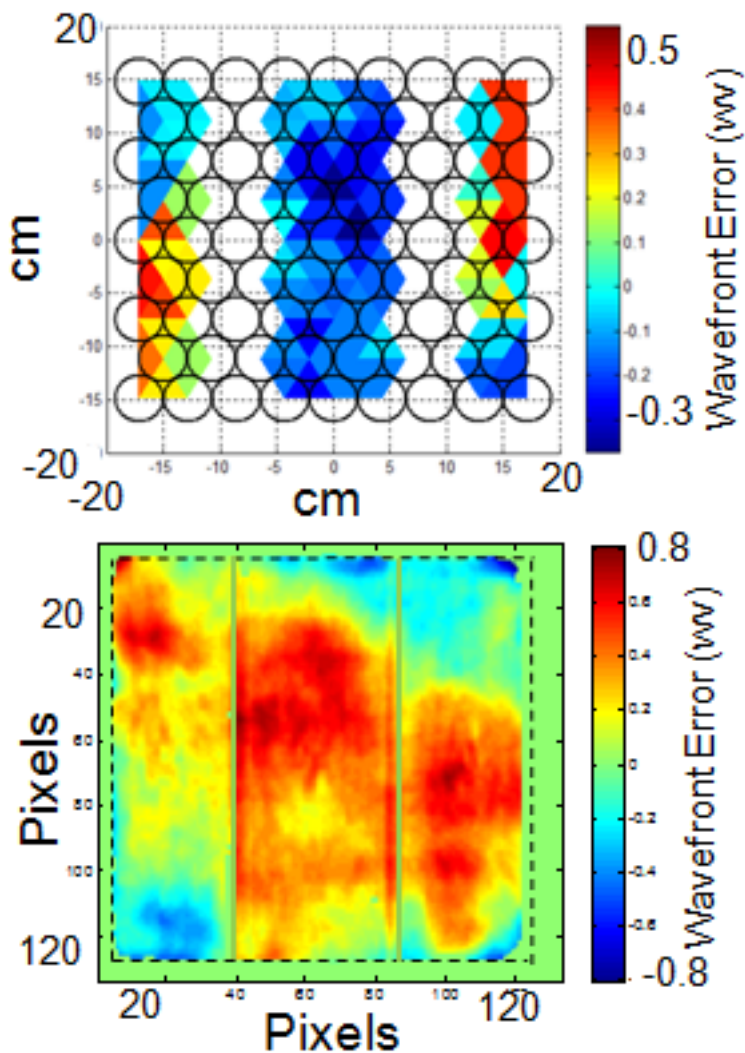
Figure 2: Wavefront images produced by the current, 77-resolution element sensor (top) and the HRWS (bottom). The superior wavefront imaging quality and resistance to tilted diffraction grating gaps (2 vertical lines missing light on both images) are shown in the bottom image.

Figure 2 shows a comparison of wavefront images produced by the current WFS and the HRWS. Aside from the clear advantages in the definition of the image of the wavefront, the HRWS image is less affected by the loss of light due to the tilted diffraction gratings (each grating is split into three "tiles"). The two vertical columns lacking light are caused by the gaps in the tiled diffraction grating assemblies in the lower compressor (the compartment at the latter end of the beam line in which the nanosecond input pulse is shortened to a picosecond output pulse) of the OMEGA EP laser. The current wavefront sensor shows a wavefront that is highly affected by the loss of light in those vertical areas, as seen by the missing light in a significant portion of the resolution elements. The diffraction grating gaps, however, do not affect the image of the HRWS wavefront nearly as badly. The loss of two vertical columns of resolution elements affects the wavefront image less when there are 138 columns of resolution elements.

Given a measured wavefront image, the 39 actuator voltages that need to be applied to the DM actuators to correct the wavefront are determined using a control matrix (C). The control matrix is formed in the calibration process. In this process, each actuator is pushed out a known amount and the response of the wavefront is stored into a response matrix (R) with 39 columns (39 actuators) and 38,088 rows (19,044 resolution elements with x and y displacements) when the HRWS is being used. The response matrix has one column filled each time an actuator is pushed out. After the response matrix is filled, it is pseudo-inverted to create a control matrix with 39 rows and 38,088 columns. Pseudo-inversion refers to the algorithm (described in ref. 4) whereby the control matrix is determined from the response matrix. The number of rows in the response matrix and the subsequent number of columns of the control matrix are dependent on the number of resolution elements in the wavefront sensor (4).

Matrix multiplication is used to determine the actuator voltages necessary for wavefront correction, as shown in figure 3. The control matrix is multiplied by an array (S) of centroid offsets. After a scalar multiplication by the "gain" which is a scalar value that enhances the stability of the correction process, a 39-element array of necessary voltage changes is produced.

Old:
- 39 x 154 matrix
- 154 element array
- Provided by DM WFS

$$\left(\text{Control Matrix} \right) \text{X} \left(\text{Centroid Offsets} \right) \text{X Gain} = \left(\text{Voltage Delta} \right)$$

New:
- 39 x **38088** matrix
- Made during **Calibration**

- **38088** element array
- Provided by HRWS

Scalar (stability)

39 element array
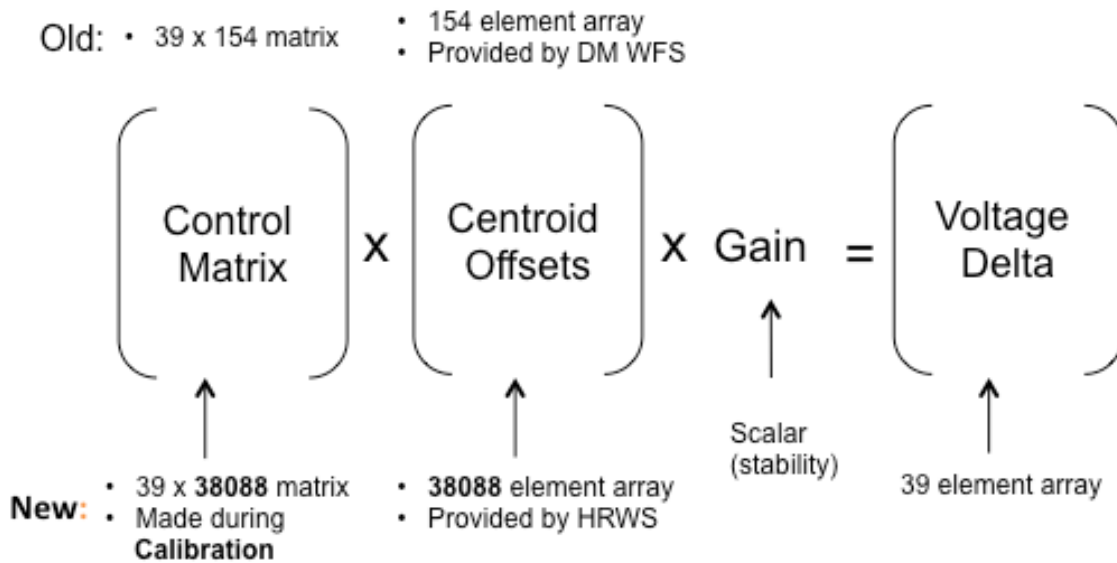
C = control matrix S = centroid offsets g = gain R = response matrix ΔV = voltage delta

$$C \cdot S \cdot g = \Delta V$$

Figure 3: *The matrix multiplication used in wavefront correction to determine the voltage changes ΔV to be applied to the actuators from the known matrices C and S. The dimensions labeled "old" correspond to the dimensions of the matrices when the 77-resolution element sensor was used.*

This project involved the writing of computer code using MATLAB to incorporate the HRWS into the wavefront control system. Various diagnostic and stability deficiencies required new code, as well as alterations to existing code. The new control system was tested and debugged on the deformable mirror testbed. Experiments on the Omega EP laser system were then conducted and showed improved wavefront correction.

MATLAB code

The following scripts and functions were written in this work: *fizeaudataanalysis*, *plotDMwavefront*, *tiltmonitoring*, *continuouswave*, *midTravel*, and *omegaepcontrol*. The first four functions and scripts have diagnostic purposes. The last two have stability purposes.

fizeaudataanalysis is a script that allows the user to obtain images and wavefront values from the Fizeau interferometer. *plotDMwavefront* is a function that uses the actuator voltages to calculate the wavefront of the deformable mirror. *tiltmonitoring* is a function that calculates the horizontal and vertical tilt of the deformable mirror based on the actuator voltages. *continuouswave* is a script with multiple parts that can display single or continuous images of the raw intensity or wavefront information obtained from the HRWS camera. These four functions and scripts were written for diagnostic purposes during the debugging of the control system. *midTravel* is a function that prevents the actuator voltages on the deformable mirror from reaching their upper or lower limits. This function increases or decreases all the actuator voltages by the same amount to prevent any gradual upward or downward shift in voltages after multiple correction iterations. *omegaepcontrol* is a script with multiple parts allowing user-specified correction of specific deformable mirrors on a beam line in the OMEGA EP laser. For example, there are two deformable mirrors in the first beamline of the OMEGA EP laser. *omegaepcontrol* is a script in which the user can run correction algorithms on a specific deformable mirror alone or on both DMs at the same time by running different sections of code, and record the RMS wavefront and gradient values of the corrected wavefront after each correction iteration.

The following alterations were made: controlling both deformable mirrors simultaneously and incorporating a "global pupil" algorithm into the calibration process. The global pupil algorithm is used to ensure that resolution elements typically near the edge of the beam that do not consistently record data throughout the calibration process are not used in the calculation of the control matrix. These alterations built upon previous code authored by Adam Kalb for the current wavefront system. The simultaneous controlling of both deformable mirrors in a beam line required various alterations to previous calibration, corrections, and voltage setting code. The specifics of these

alterations and their ultimate goal will be discussed below. Incorporating a global pupil was a solution to an issue with the HRWS of a changing pupil size.

Deformable Mirror Testbed and Troubleshooting

Before any new code could be tested, the DM testbed was set up and debugged. A top view of the DM testbed can be seen in figure 4. Much of the optics, specifically around the flip-up mirror and cameras, was set up and aligned. The HRWS was also installed and its optimal light intensity was found.
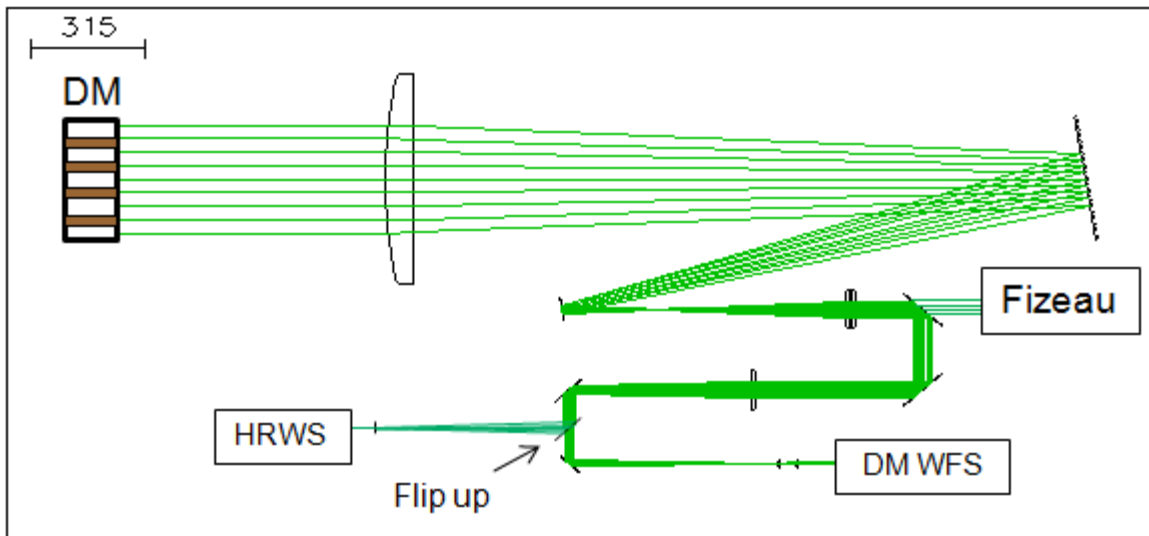
Figure 4: *The DM testbed setup. The light beam originates at the Fizeau interferometer. This beam continues on to a deformable mirror, and is then directed back through a series of mirrors and lenses to a wavefront sensor. Either the current wavefront sensor DM WFS or the HRWS receives light based on whether the flip-up mirror is up or down.*

A few lingering hardware problems made early testing of code difficult. The HRWS had some inaccuracies in imaging that complicated the calibration process. It is important to note that these inaccuracies did not impact the code testing. The minor inaccuracies were present during the whole process so all of the reference and corrected wavefront measurements had to deal with them. As testing progressed, these HRWS camera issues were mitigated.

The other, more prominent, hardware difficulty was a malfunctioning of the DM actuator electronics. As testing of code progressed, inconsistencies with wavefront correction persisted. For example, a correction iteration would adversely affect the quality of the wavefront instead of improving it. During the debugging process, it was discovered that some of the actuators were responding abnormally slowly. A longer pause was inserted into the calibration and correction processes with little improvement. Eventually, multiple failed resistors were discovered in the driver electronics. After replacement of these resistors in the drive board, code testing became much more consistent.

"Global Pupil Algorithm"

A "global pupil" algorithm was implemented to counter the issue of a changing pupil. A changing pupil means that light is present in a resolution element in the HRWS during the calibration of one actuator but not present during the calibration step of another actuator. This occurs primarily at the edges. This leads to inconsistent response matrix values corresponding to the inconsistent centroid locations. The control algorithms cannot accurately control the actuators. This issue with inconsistencies in the presence of light was not present with the current 77-resolution-element wavefront sensor. The current wavefront sensor has resolution elements of much greater size, decreasing the chance of inconsistent light fluctuations within each resolution element. Slight vibrations in the OMEGA EP laser would not affect the presence of light nearly as much as it would with the 19,044-resolution element HRWS. With the much smaller resolution elements in the HRWS, these slight vibrations cause light to shift in and out of resolution elements. This problem is illustrated in figure 5. The detailed view of the edge of the pupil shows how slight vibrations can easily alter the presence of light in certain resolution elements. A pupil is defined as a 138 by 138 element matrix, corresponding to resolution elements in the HRWS, with ones where there is light and zeros where there is no light.
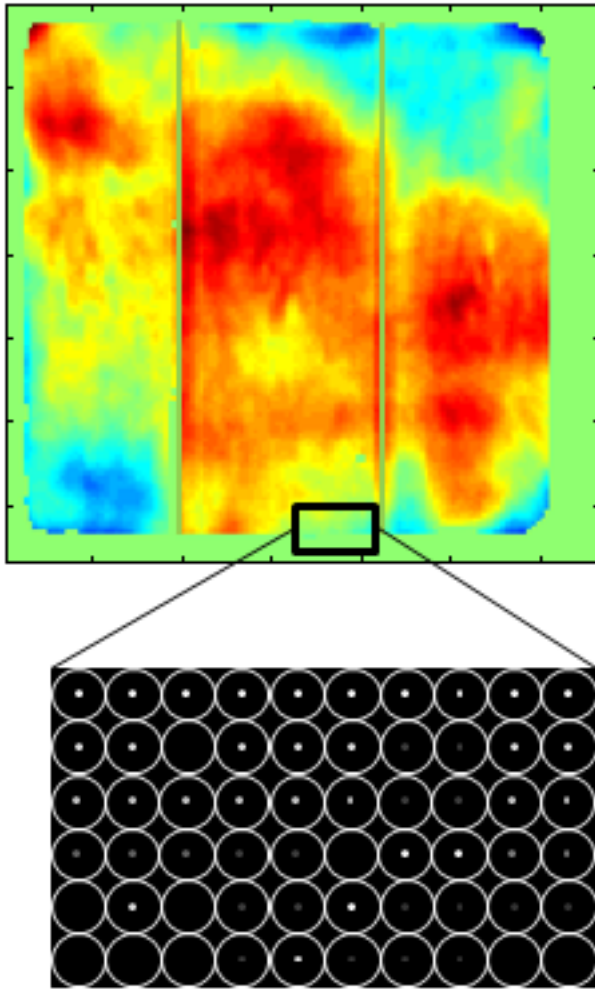
Figure 5: *A detailed diagram of the presence of light in resolution elements at the edge of the pupil (bottom). The wavefront image (top) is the same as in figure 2. The bottom diagram shows the lack of a definitive edge when a beam of light is captured by the HRWS. This allows slight vibrations to affect the distribution of light among these resolution elements.*

With the global pupil approach, only centroid locations with light present during the whole process are used in the correction process. This means that only offsets in these centroid locations would be corrected. This avoids any confusion between actuators concerning which centroids to correct. This approach was implemented through alterations to the calibration code. At the beginning of the calibration process, a pupil is obtained from the HRWS camera. Whenever a new wavefront image is obtained by the HRWS camera, a pupil is extracted and element-wise multiplied by the previous pupil. This new pupil is stored as an external variable that constantly gets smaller (some places with ones get replaced with zeros) as the calibration continues. A new pupil is obtained by the camera at least once every calibration step. After all the actuators have been calibrated and a response matrix has been formed, the new pupil, now known as the

global pupil, is made into a 38,088 element array. This global pupil matrix is element-wise multiplied by each column of the response matrix to remove any rows that correspond to inconsistent centroid locations. Any elements with a zero in the global pupil (centroid locations in which light was not present during the whole process) make the corresponding elements in the response matrix a zero. The response matrix is pseudo-inverted to create a 39 by 38,088 element control matrix. At this point, the DM actuators are able to correct consistent centroid locations.

It is important to note that filling a row of the response matrix with zeros before pseudo-inverting it (as done with the 38,088 by 39 response matrix to transform it into a 39 by 38,088 control matrix) does not adversely affect the resulting control matrix. With the many resolution elements without light in the HRWS, confirming resistance of the pseudo-inverting process to zeros was vital. To test this, a 4x4 matrix of random numbers was created. This was inversed, then multipled by a 4x1 matrix of random numbers. Next, a 12x4 matrix was created by inserting 2 rows of zeros after each row of the original 4x4 matrix. The 12x4 matrix was then pseudo-inverted and multiplied by a 12x1 matrix, which was created by inserting two rows of zeros after each row of the previous 4x1 matrix. The products from the first and second inversion tests were identical. This validated the pseudo-inverting process with the matrix multiplication using a HRWS.

In order to test the effectiveness of the global pupil approach, wavefront corrections were conducted with a control matrix generated using the global pupil in the calibration process and compared to wavefront corrections using a control matrix without the global pupil in the calibration algorithm. For consistency, the starting wavefront before correction was a reference flat wavefront. A flat mirror was set up in the place of the deformable mirror in the DM testbed and the wavefront was recorded in the HRWS, current wavefront sensor, and Fizeau interferometer software. After the reference wavefront was recorded, the deformable mirror replaced the flat mirror. Before a wavefront correction was tested, a known aberration was applied to the wavefront by manually changing the voltages of the DM actuators. Before each wavefront correction, 85 volts were applied to each DM actuator, producing a consistently biased wavefront for each correction test. The deformable mirror was then calibrated, producing a control matrix. Two calibrations were performed, one with the global pupil and one without.

Each control matrix was saved, and later loaded when wavefront correction tests were conducted.
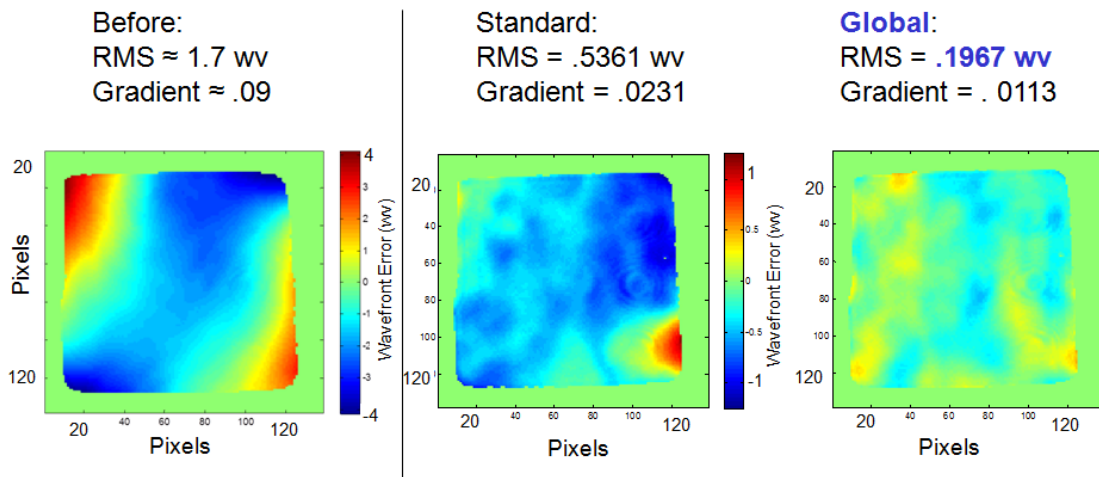
Figure 6: *The comparison between wavefront correction with and without the global pupil approach after 100 iterations. This test was conducted in the DM testbed. The lower RMS wavefront and gradient values attained with wavefront correction using the global pupil can be seen. The colorbar is four times greater in range in the biased wavefront image (on the left) compared to the two corrected wavefront images. The two corrected wavefronts use the same colorbar.*

The results of the global pupil tests can be seen in figure 6. The wavefront corrections using a control matrix generated without a global pupil, called a "standard" pupil in the figure, attained an RMS wavefront value of 0.5361 waves (wv) and a gradient (overall tilt) of 0.0231. Wavefront correction using the control matrix generated with the global pupil attained an RMS wavefront value of 0.1967 wv and a gradient of 0.0113. The aberrated wavefront applied before both corrections is shown on the left. The advantages of the global pupil are also seen in the wavefront images. The image after correction with the standard pupil control matrix has a red dot in the corner, which shows a DM actuator that did not correct properly. This was a common characteristic when correcting a wavefront with the standard pupil. When correcting the wavefront using the global pupil approach, however, the correction algorithm did not produce incorrect voltage changes, allowing the DM actuators to create a more uniform, flatter wavefront.

With 19,044 resolution elements in the HRWS, there was also some concern that errors accumulated during the matrix multiplication of the wavefront correction process could, after many iterations, cause the correction process to become unstable. This has occurred with the current system on a laser beamline where multiple corrections were consecutively applied throughout the day. 100 iterations of wavefront correction were conducted for the global pupil and standard pupil control matrices. The graph in figure 7 shows the stability of wavefront correction using the HRWS. The superiority of the global pupil control matrix can be seen on the graph as well. The RMS wavefront values attained through correction using the global pupil control matrix are clearly lower compared to wavefront correction using the standard pupil control matrix. Also, the global pupil correction algorithm converges to its final wavefront correction within 10 iterations.
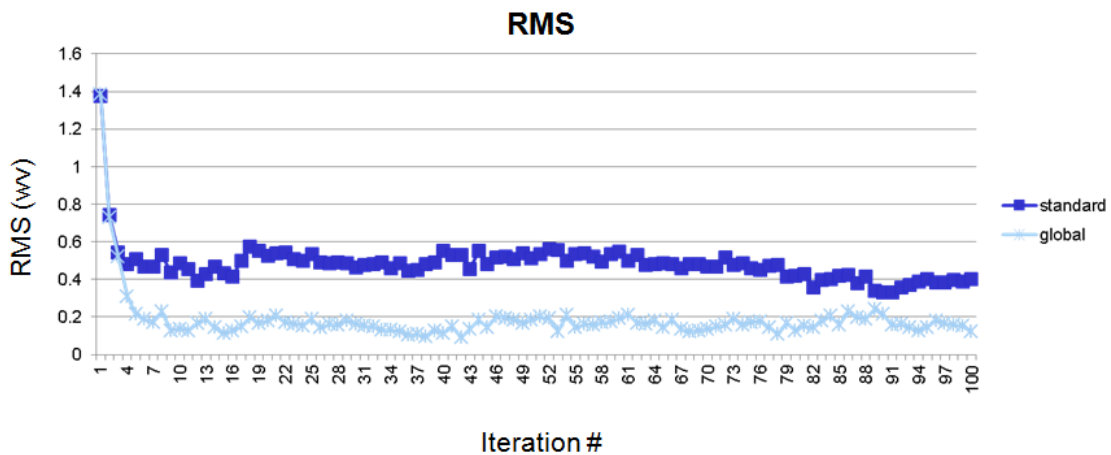
Figure 7: RMS wavefront error plotted against wavefront correction iteration number for standard and global pupil algorithms. 100 iterations of wavefront correction using the HRWS correction algorithms were conducted in the DM testbed. The correction algorithm without the global pupil (standard pupil) and the algorithm with the global pupil started with an initial aberration in the wavefront. Both correction algorithms approached and hovered around a certain RMS wavefront value, confirming that wavefront correction using the HRWS is stable.

Once wavefront correction using a HRWS was optimized (using the global pupil method), the optimized MATLAB software was tested on the OMEGA EP laser and its wavefront correction capabilities were compared to those obtained with the current 77 resolution element wavefront sensor using the current wavefront sensor correction software. The results can be seen in figure 8. Using the current 77-element wavefront sensor, the correction algorithm attained a wavefront with an RMS wavefront value of 0.27 wv and an R80 focal spot radius (radius of focused laser beam where 80% of energy is encircled) of 19.0 micrometers. Wavefront correction using the HRWS attained a RMS wavefront value of 0.25 wv and an R80 radius of 18.2 micrometers. Using the HRWS for wavefront correction decreased the RMS wavefront and R80 focal spot values by approximately 8% and 5% respectively. Ideally, this increases the average on-target intensity by approximately 10%. More tests are required to increase confidence in these findings.
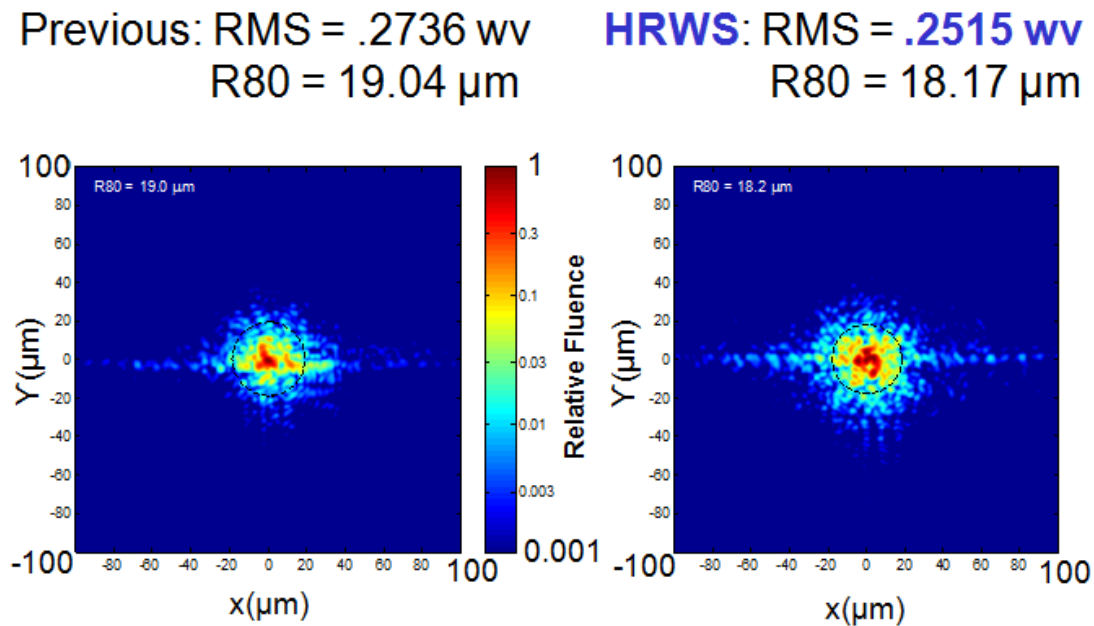
Figure 8: *Focal Spot on Omega EP using (left) wavefront correction with the current, 77-resolution element sensor and (right) wavefront correction with the HRWS.*
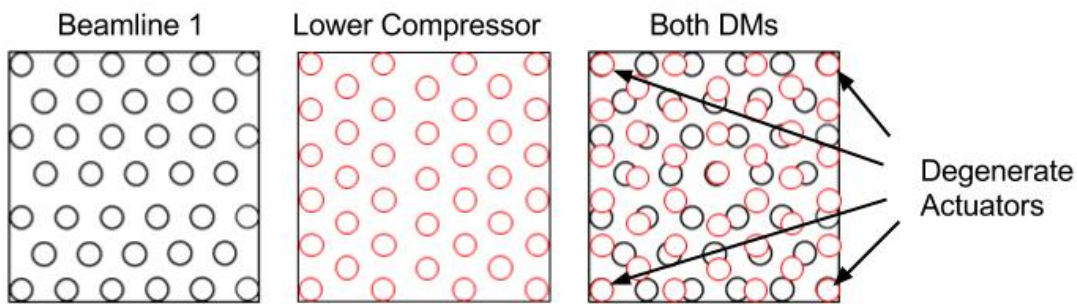
Figure 9: *The arrangement of actuators for each DM. The overlapped arrangement of actuators - when both DMs are corrected simultaneously - is shown on the right. The primary degenerate actuators are labeled.*

Simultaneous Correction of Two Deformable Mirrors

On the two short-pulse beamlines of the OMEGA EP laser, two deformable mirrors are configured in the laser path for each beam. One of these deformable mirrors is located in the amplifier line, and the other is in the compressor. Currently, each deformable mirror is corrected separately. A possible way to improve wavefront correction is to correct both deformable mirrors simultaneously. This means that one correction algorithm would correct both DMs using a control matrix with twice as many rows (78 combined actuators). The reason that simultaneous correction can improve wavefront correction is that the two DMs are oriented at 90° to each other as shown in figure 9. This causes more actuators to physically cover the wavefront. If the 78 actuators correct at the same time, there are more actuators per surface area, theoretically increasing the quality of wavefront correction. After a few correction iterations, the results are shown in figure 10. As was expected, simultaneous correction slightly improved wavefront correction compared to the previous method of separate deformable mirror correction.

After more than a few iterations, the simultaneous correction of both deformable mirrors caused problems due to the spacing of the two mirrors. The first deformable mirror began to apply a large wavefront error that was being corrected by the second

mirror, until the wavefront slope became too large to pass through the beamline. Starting at the corners and edges, parts of the beam were lost due to clipping by pinholes in the

(a) Beamline 1 DM
RMS = .1614 wv

(b) Lower Compressor DM
RMS = .1789 wv

(c) Both DMs
RMS = .1442 wv
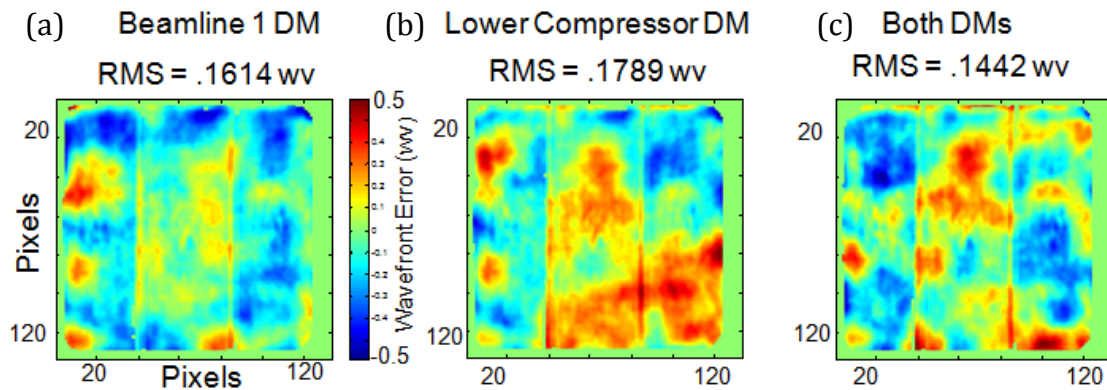
Figure 10: *Comparison of wavefronts obtained by correcting just the beamline 1 DM (a), the Lower Compressor DM (b), and both DMs simultaneously (c). Using the omegaepcorrect script, the deformable mirror in beamline number one of the OMEGA EP laser system underwent 5 correction iterations, and then the lower compressor deformable mirror underwent 5 correction iterations, and finally both deformable mirrors underwent 3 simultaneous correction iterations.*

laser beamline. Upon closer investigation of the actuator diagrams in figure 9, some actuators (corners and middle actuator) overlap; i.e. the actuators are "degenerate" and act on the wavefront identically. The result is one actuator pushing out while the corresponding actuator on the other deformable mirror pulls in. The HRWS at the end of the laser path does not realize this until the wavefront tilt from the first mirror's actuators causes the wavefront to be lost in the beamline. As significant portions of the centroid locations are lost, further correction iterations increasingly degrade the quality of the beam.

After unsuccessful attempts at containing actuator voltage values within a certain range, a more specific attempt was made. The primary dysfunctional areas of degradation, the corners, would be fixed by removing the four corner actuators of the beamline number one deformable mirror from the calibration and correction steps. This would mean that only the lower compressor deformable mirror would correct the corners of the

wavefront, avoiding the issues with overlapping corner actuators. The columns in the response matrix corresponding to the four corner actuators were set to zero. When the resulting control matrix was used in wavefront correction, the four corner actuators of the beamline number one deformable mirror remained stationary. Unfortunately, this provided little benefit to the stability of the simultaneous wavefront correction. Instead of three or four iterations, it now took five or six correction iterations before the wavefront began to degrade. The issue at the corners was resolved, but the actuators by the edges also began to experience similar issues of antagonistic displacement with their corresponding actuators. Although these actuators did not overlap, it is likely that nearly overlapping actuators experienced similar issues as the corner actuators.

It is important to note that while the center actuators overlapped between both deformable mirrors, the center of the wavefront did not degrade. This is most likely due to the abundance of information in centroid locations surrounding the center actuators - unlike the corner actuators where fewer surrounding resolution elements contain light - that would be greatly affected by the inaccurate correction caused by detrimental information provided to the center actuator. Also, nearby actuators influence the wavefront differently on each deformable mirror, meaning that the center actuators were not totally "degenerate". Simultaneous correction of both deformable mirrors is a potentially beneficial process, but it requires further investigation to solve the significant issues with antagonistic actuator voltage wandering.

Conclusion

Wavefront correction on the OMEGA EP laser system has been improved by the incorporation of the HRWS and optimization of the correction algorithms, leading to a decrease in the RMS wavefront of the laser beam and the R80 radius by ~8% and ~5%, respectively. This corresponds to an increase in the on-target average intensity by ~10%.

Acknowledgements

I would like to thank Dr. Craxton for granting me the opportunity to take part in the 2014 High School Summer Research Program. Furthermore, I would like to thank my advisors, Dr. Brian Kruschwitz and Adam Kalb, as well as Kyle Gibney for providing tremendous amounts of knowledge, resources and support during the program.

References

1. B. Kruschwitz, "Wavefront Control System for Omega EP," 9 Mar. 2007. *Microsoft Powerpoint* file.

2. S. S. Olivier, "Wavefront Correction Technologies," Summer School for Adaptive Optics. 11 Aug. 2004. Reading.

    http://cfao.ucolick.org/aosummer/archive/aosummer2004/lectures.php

3. B.C. Platt and R. Shack, "History and Principles of Shack-Hartmann Wavefront Sensing," *J. Refr. Surgery* **17**, S573 - S577 (2001)

4. R. Zacharias, E. Bliss, S. Winters, R. Sacks, M. Feldman, A. Grey, J. Koch, C. Stolz, J. Toeppen, L. Van Atta, and B. Woods, "Wavefront Control of High-Power Laser Beams in the National Ignition Facility (NIF)," in *Advanced High-Power Lasers*, ed. M. Osinski, H.T. Powell, K. Toyoda, Proc. SPIE vol. 3889, 332 - 343 (2000)

Emma Garcia

Optimization of Uniformity for Current Polar Drive Implosion Experiments on the

National Ignition Facility

E. M. Garcia

Penfield High School

Advisor: Dr. R. S. Craxton

Laboratory for Laser Energetics

University of Rochester

Rochester, NY

October 2014

Emma Garcia

1. Abstract

Several types of alternative designs for the current series of polar drive implosions on the National Ignition Facility (NIF) have been developed using the hydrodynamics simulation code *SAGE*. Polar drive is a method of repointing the NIF beams, which are configured for indirect drive, away from the poles and towards the equator to create a uniform direct drive implosion. The current design produces implosions that are close to spherical but still show some nonuniformities. They are calculated to have a center-of-mass nonuniformity of 1.3% averaged over the whole sphere when the shell has compressed to approximately half its initial diameter. The first alternative design, the "defocus" design, utilizes greater defocuses than the current design on all of the beams along with small changes to the pointing shifts. This design has a lower nonuniformity of 0.64%. The second type of alternative design, the "oblique" design, uses large pointing shifts so that most beams encounter the target at oblique incidence. It is speculated that the large pointing shifts of oblique designs may help to reduce the nonuniformity associated with laser speckle that is not modeled in the simulations. All beams in the oblique designs have a minimum pointing shift of 45% of the target radius. One oblique design has an rms nonuniformity of 0.57% and the other an rms nonuniformity of 0.64%. The final two alternative designs are optimized to overdrive the equator of the target by a small amount to allow for fine tuning of NIF experiments and demonstrate the ability of polar drive to overdrive the equator of the target if desired.

2. Introduction

Controlled fusion is a potential abundant source of clean, safe energy. One method to create fusion is to irradiate a spherical target consisting of a plastic or glass shell filled with deuterium and tritium with powerful lasers. The energy from the lasers causes the shell of the

target to ablate outwards while at the same time compressing the deuterium fuel inside the target.

The high temperature and pressure at the core of the compressed target create an environment in

which Coulomb repulsion forces between nuclei can be overcome and fusion reactions can occur

for a short time until the target explodes. As deuterium and tritium nuclei fuse, they form a

helium nucleus and an energetic neutron, which carries most of the energy from the fusion

reaction. If the fuel has a great enough radius and density, the energy from the helium nucleus

will be redeposited in the fuel. This redeposition of energy is known as ignition and is the first

step towards breakeven, when the energy released by fusion is equal to the energy input of the

laser. Breakeven is a step towards high gain, which is when the energy output is substantially

higher than the energy input. High gain is necessary for laser fusion to be used as an abundant

energy source.
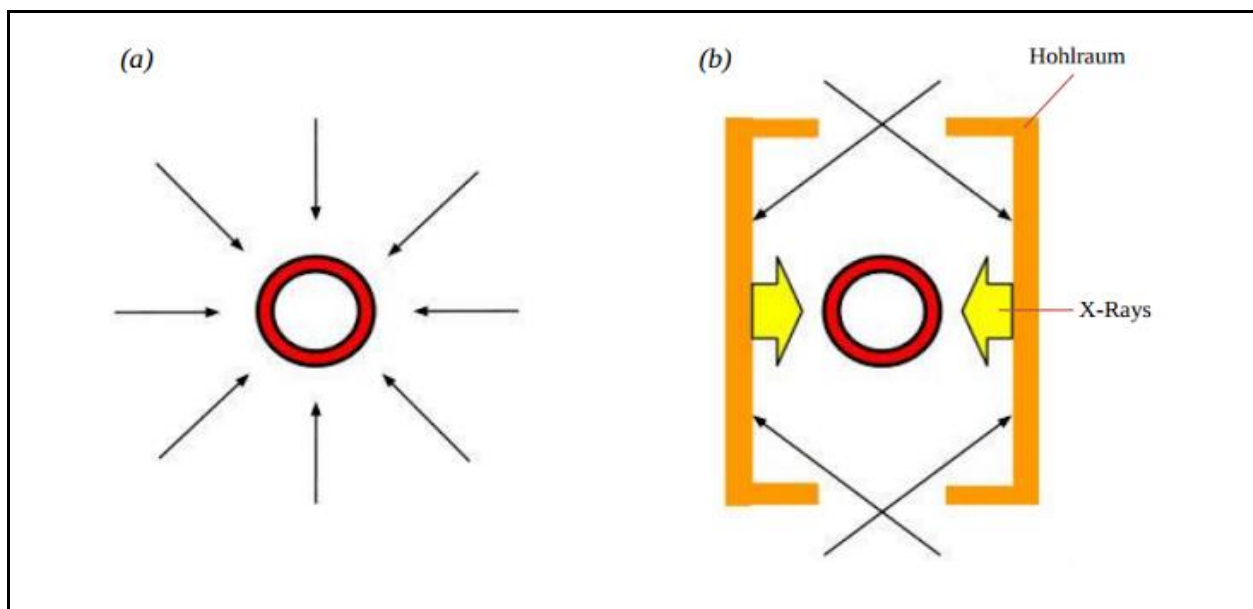
Figure 1: The two main approaches to inertial confinement fusion. (a) In direct drive, the target is irradiated directly by a symmetrical set of beams, represented by the black arrows. (b) In indirect drive, the laser beams irradiate a cylindrical hohlraum made of a metal with a high atomic number (usually gold) surrounding the target, which then emits x rays (yellow block arrows) that irradiate the target. (From Reference 1)

There are two main approaches to laser fusion currently being used: direct drive[2] and indirect drive[3]. In direct drive [Figure 1 (a)], a target is irradiated directly with laser beams coming in at normal incidence from all directions in a symmetrical configuration. The OMEGA laser at the University of Rochester's Laboratory for Laser Energetics (LLE) is configured to perform direct drive experiments. In the indirect drive approach, a cylindrical hohlraum made of a metal with a high atomic number, usually gold, is placed around the target, and the laser beams enter the hohlraum through holes at the top and bottom and irradiate the inside of the cylinder [Figure 1 (b)]. The hohlraum then re-emits about 80% of the energy it absorbed as x rays, some of which irradiate the target. This approach has the advantage of irradiating the target with good uniformity. However, only 20% of the energy from the laser beams is actually absorbed by the target, making this an inefficient method of fusion. The National Ignition Facility (NIF) at Lawrence Livermore National Laboratory is configured for indirect drive.

Because the NIF is set up to perform indirect drive experiments, the beam ports aren't located in ideal places to perform direct drive experiments. The NIF has 48 beam ports available evenly spaced around the azimuth (Φ) at angles of $\Theta = 23.5°$, $30.0°$, $44.5°$, and $50.0°$ from the poles, with corresponding angles in the lower hemisphere. Each port is used by 4 beams called a quad, for a total of 192 beams. If the NIF beams are pointed at the center of the target in a direct drive experiment, the poles are drastically overdriven in comparison to the equator, which is inadequate as it doesn't provide enough compression of the fuel to generate a lot of fusion reactions [Figure 2 (a)]. To create uniform direct drive implosions on the NIF, a method of repointing the beams called polar drive[4,5,6,7] is used [Figure 2 (b)]. In this method, some of the beams are pointed towards the equator so that they no longer encounter the target at normal incidence and instead deposit their energy near the equator.

Figure 2: Possible pointings of NIF beams for direct drive implosions. Quads are indicated by the numbers next to the arrows. Quad 1=23.5°from the z axis, Quad 2=30.0°, Quad 3=44.5°, and Quad 4=50.0°. (a) When all beams are aimed at the center of the target, the shell implodes faster at the poles than at the equator. (b) Repointing the beams away from the center of the target and towards the equator creates a more uniform implosion. Based on figure 2 of reference 8.

This type of pointing scheme has been effective in current direct drive experiments on the NIF carried out by LLE[7]. The purpose of this work was to improve upon the uniformity of the existing polar drive design using a variety of approaches, as nonuniformities are still observed in different types of images of current polar drive implosions.

3. Current Design

The target that is being used for current polar drive implosions on the NIF is a 1100 μm radius target with a plastic shell that is 100 μm thick [Figure 3 (a)]. The shell is filled with deuterium. The laser pulse shapes for each quad were already optimized for the current design[7] and were different for each ring of quads. The pulse shapes were not changed in this work. A diagram of the average pulse shape as well as the absorption for the current design is shown in Figure 3 (b).While good absorption is obtained at early times, it is difficult to keep a high

absorption percentage at later times because some energy misses the target as the shell

compresses.
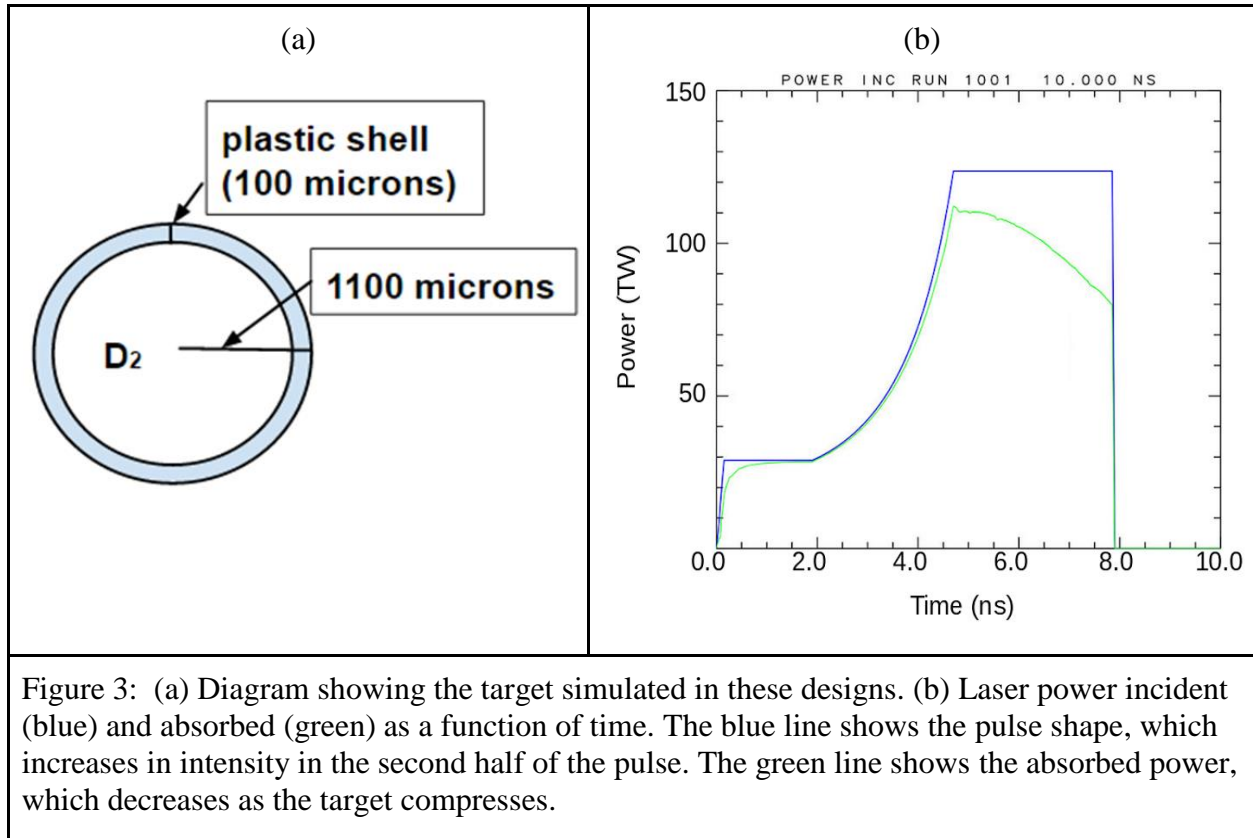
Figure 3: (a) Diagram showing the target simulated in these designs. (b) Laser power incident (blue) and absorbed (green) as a function of time. The blue line shows the pulse shape, which increases in intensity in the second half of the pulse. The green line shows the absorbed power, which decreases as the target compresses.

Three main parameters can be manipulated in developing a design [figure 4]. The defocus

of a beam can be changed by moving the lens towards the target, which creates a larger laser

spot. Some degree of defocus is required for polar drive designs because NIF phase plates create

a tighter focus in order to allow the beams to pass through the hole in the hohlraum. The aim

point of a beam can be changed by moving a mirror. Finally, the energy in each beam can also be

specified. The use of these parameters to make polar drive implosions viable on the NIF using

indirect drive phase plates was first described in Reference 8. The hydrodynamics code SAGE

was used to model these parameters and their effects on the target implosion.
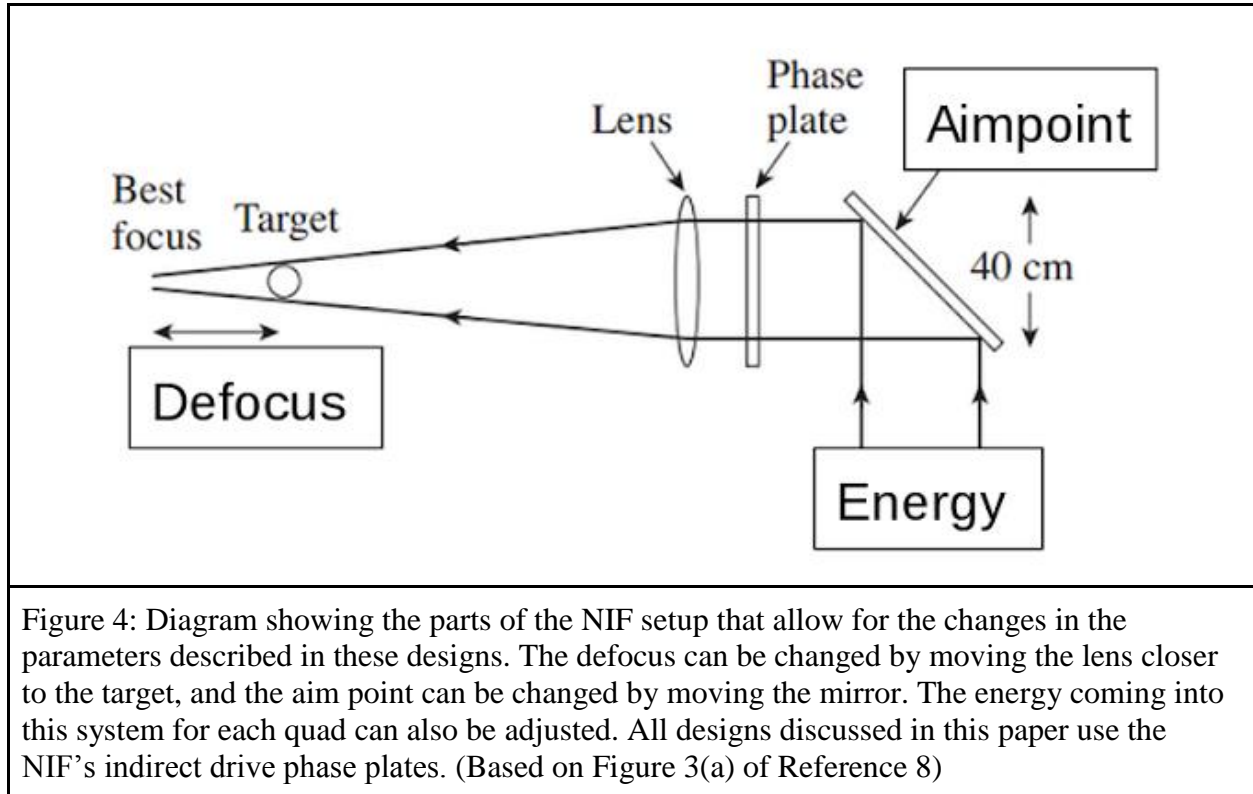
Figure 4: Diagram showing the parts of the NIF setup that allow for the changes in the parameters described in these designs. The defocus can be changed by moving the lens closer to the target, and the aim point can be changed by moving the mirror. The energy coming into this system for each quad can also be adjusted. All designs discussed in this paper use the NIF's indirect drive phase plates. (Based on Figure 3(a) of Reference 8)

The design currently being used for the polar drive implosions carried out by LLE on the NIF uses small defocuses on all beams and pointings that are close to the laser ports, especially for quads 1, 2, and the top beams of quad 3. It has several good qualities. First, it has a high absorption of 85.7% [Figure 3]. It also achieves good uniformity and has an rms of 1.30%. It is possible to see the potential source of some remaining nonuniformities by looking at the *SAGE* model of these implosions. Figure 5 shows a center-of-mass radius contour plot of the current design. Contours show deviations from the average center-of-mass radius, squares show the location of beam ports, dots show the beam aim points, and arrows show a selection of beam pointings. It can be observed from this plot that this design still contains some prominent features such as azimuthal nonuniformities around $\Theta=60°$. Even with these features, the overall nonuniformity of this design as modeled by *SAGE* is only 1.30%. However, it is believed that an

rms of at most 1.0% is required for ignition, so there was a need for improvements to the current design.
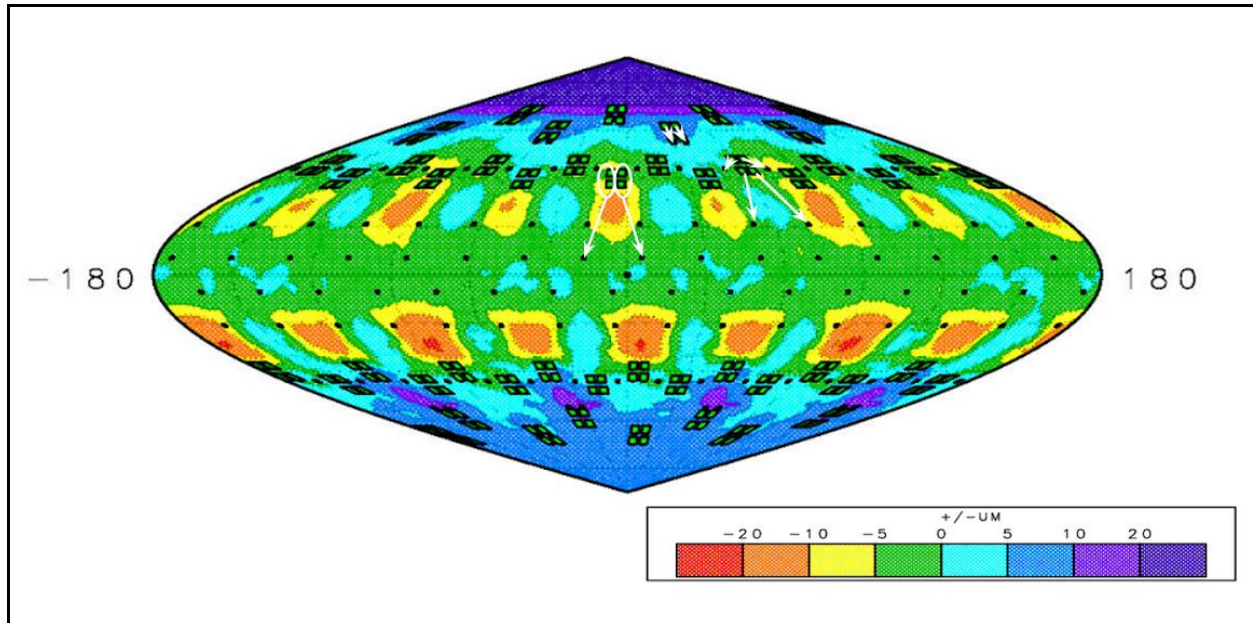
Figure 5: *SAGE* center-of-mass radius contour plot showing deviations from the mean radius in μm and pointings of the current design at 6 nanoseconds when the target's radius has been compressed from 1100 to 631 μm. The quad 1, quad 2, and upper quad 3 beams are pointed close to their origin, but the lower quad 3 and all quad 4 beams have large repointings towards the equator as well as horizontal shifts. These are specified as aim points on the target surface. The most visible features in this plot are the large fluctuations in radius around $\Theta=60°$, which are likely caused by the small defocuses. This design has an RMS nonuniformity of 1.30%.

Nonuniformities in the current design are also evident in different types of images of current polar drive implosions.   One type of diagnostic imaging that has been used on the NIF to determine how uniformly the targets for the current design implode is self-emission. Self emission captures the x rays given off by the outside of the shell as it implodes. In self emission imaging [Figure 6 (a)] the implosion seems to be fairly uniform, but it is evident that the areas around $\Theta=60°$ and $\Theta=120°$ appear to be slightly under compressed, creating a slight hexagonal shape. However, when another type of imaging known as x ray backlighting is used, nonuniformities become much more prominent [Figure 6 (b)]. In x ray backlighting, a secondary

target is shot to produce x rays, which pass through the primary target and reach a detector. The bright areas in the image are where x rays are being detected, and the dark shadow traced by the white line is where the shell of the primary target is blocking the x rays, allowing the nonuniformities in the dense shell to be seen. The nonuniformities visible from this type of imaging warrant further improvements to the uniformity of polar drive designs.

Figure 6: Images of the current design on the NIF viewed from the equator. (a) Self emission image[9]. While close to spherical, it is still possible to see a slight hexagonal shape. (b) X ray backlighter image[10]. In a backlit implosion of the current design, it is much easier to see some nonuniformities in the imploding shell.
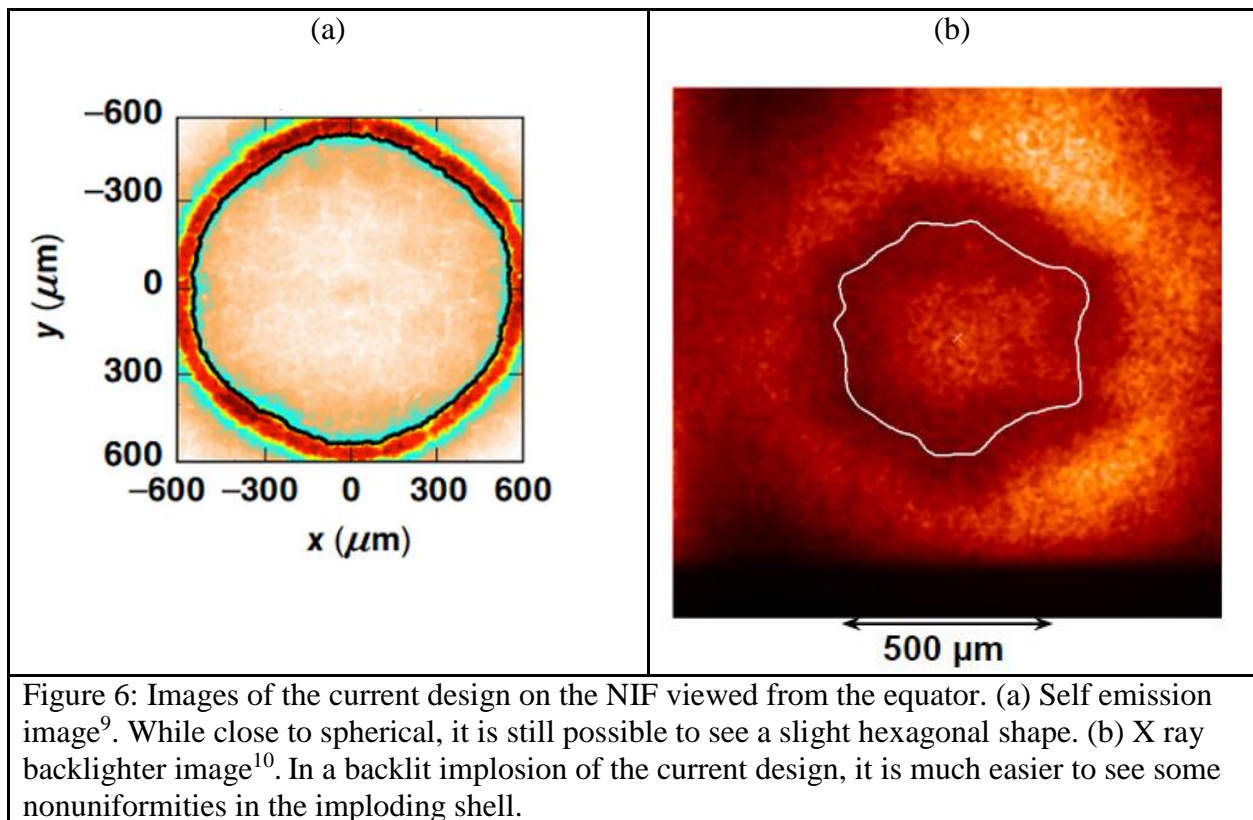
4. Optimized Designs

Three types of optimized designs were developed, each with a different goal. The defocused design had a goal of reducing the RMS nonuniformity of the original design using similar pointings and larger defocuses. The oblique designs had the goal of creating a pointing scheme that gives every beam as big of a shift as possible while maintaining good uniformity. Finally, the overdriven equator designs had a goal of overdriving the equator by a certain

amount. Because nonuniformities in the shell seeded at early times grow as time goes on, measurements of rms nonuniformity were taken at 6 nanoseconds when the target had been compressed to about half its initial radius (about 630 μm).

Every beam in each quad could be given its own shift in both the Θ and Φ directions. This allowed for flexibility in the distribution of energy. Because designs that are symmetrical around the azimuth were desired, parameters were specified for one quad in each ring and copied to the other quads in each ring.

4 a. Defocused Design

The first goal of the optimization process was to create a design that used bigger defocuses to spread out the energy from each beam more and therefore increase the overall uniformity. The effect of larger defocuses can be seen in Figure 7, which shows the energy deposition of a single beam with a small (1 cm) and large (2.6 cm) defocus, and Figure 8, which shows how the shape of a beam changes as it is defocused.   In addition to spreading the energy over a larger area, defocusing the beams creates a more gradual falloff from the maximum deposited energy for each beam and a lower maximum energy. Both of these features make it much easier to overlap beam energies to create a smoother implosion overall. In the process of optimizing this type of design it was observed that simply increasing the defocuses of the current design without any repointings resulted in an overdriven equator, which led to the group of designs meant to overdrive the equator discussed in section 4 c. Because of this, small pointing shifts from the current design were used in the defocused design along with the larger defocuses. Larger defocuses cause some loss of energy, so a 7% increase in energy from the current design was applied to all beams to ensure that the target is imploded to the same radius at the same time for both designs.
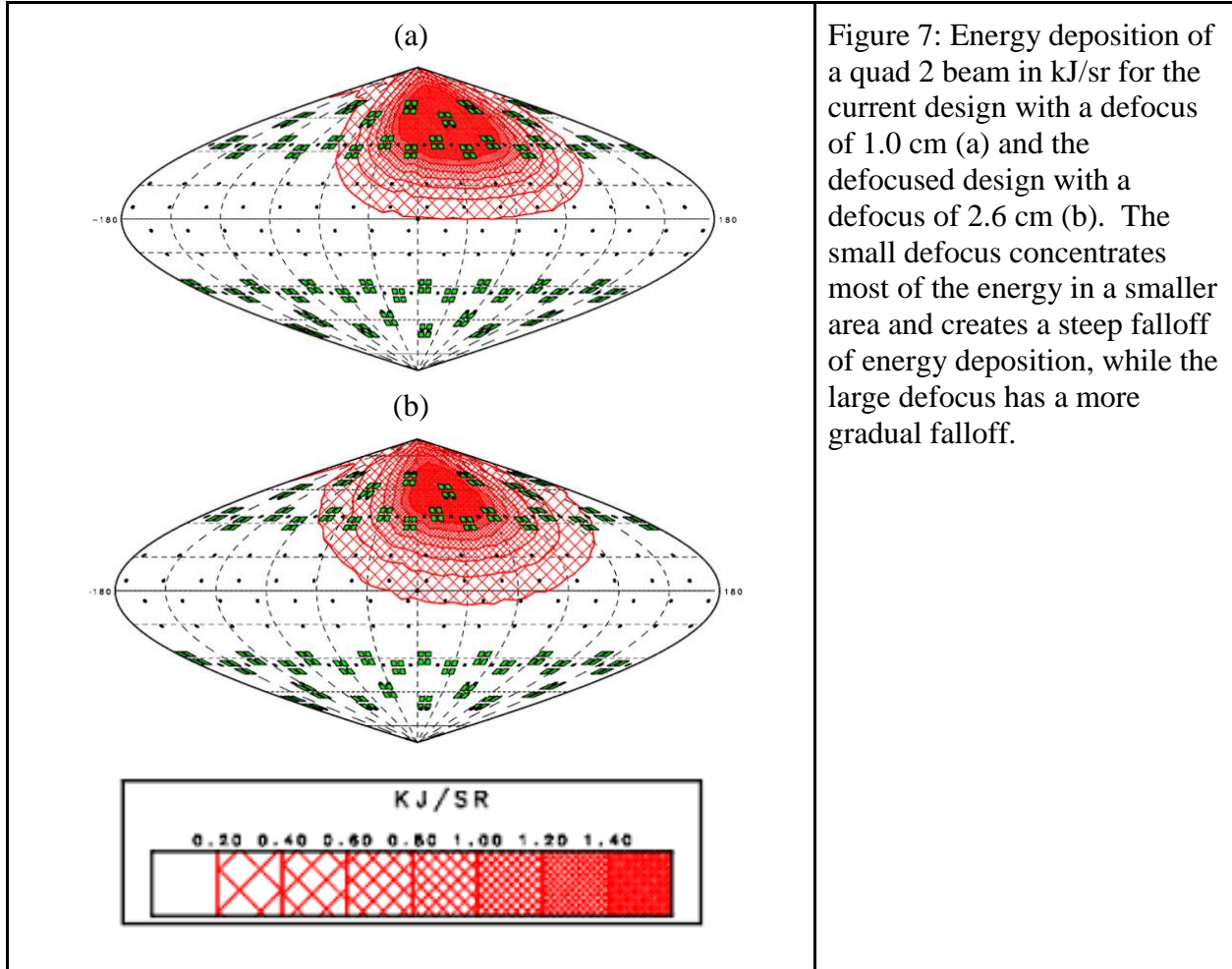
Figure 7: Energy deposition of a quad 2 beam in kJ/sr for the current design with a defocus of 1.0 cm (a) and the defocused design with a defocus of 2.6 cm (b). The small defocus concentrates most of the energy in a smaller area and creates a steep falloff of energy deposition, while the large defocus has a more gradual falloff.
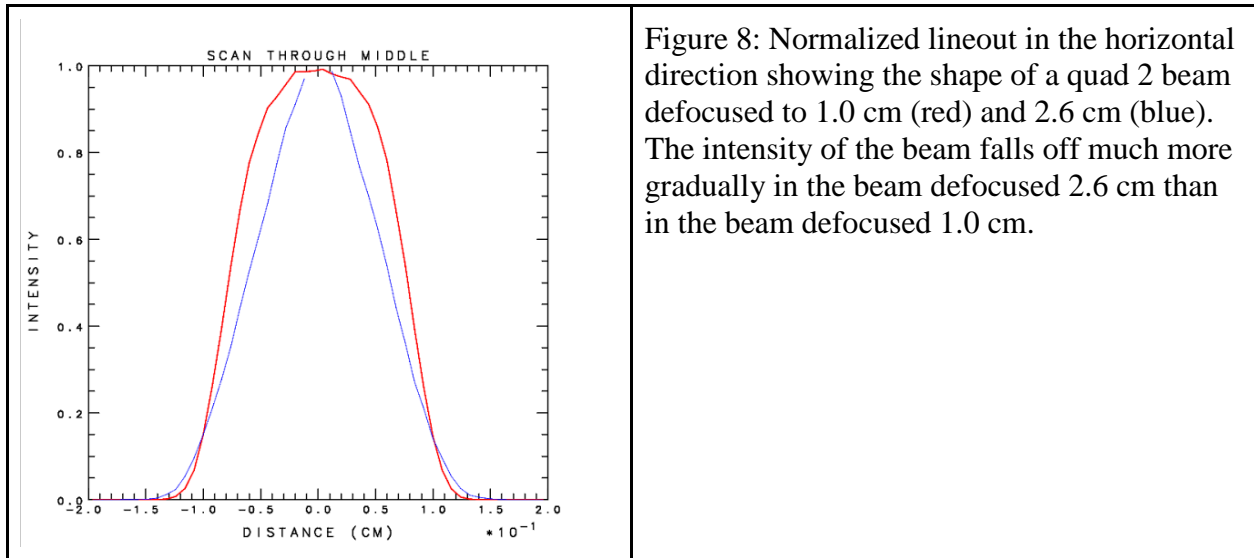
Figure 8: Normalized lineout in the horizontal direction showing the shape of a quad 2 beam defocused to 1.0 cm (red) and 2.6 cm (blue). The intensity of the beam falls off much more gradually in the beam defocused 2.6 cm than in the beam defocused 1.0 cm.
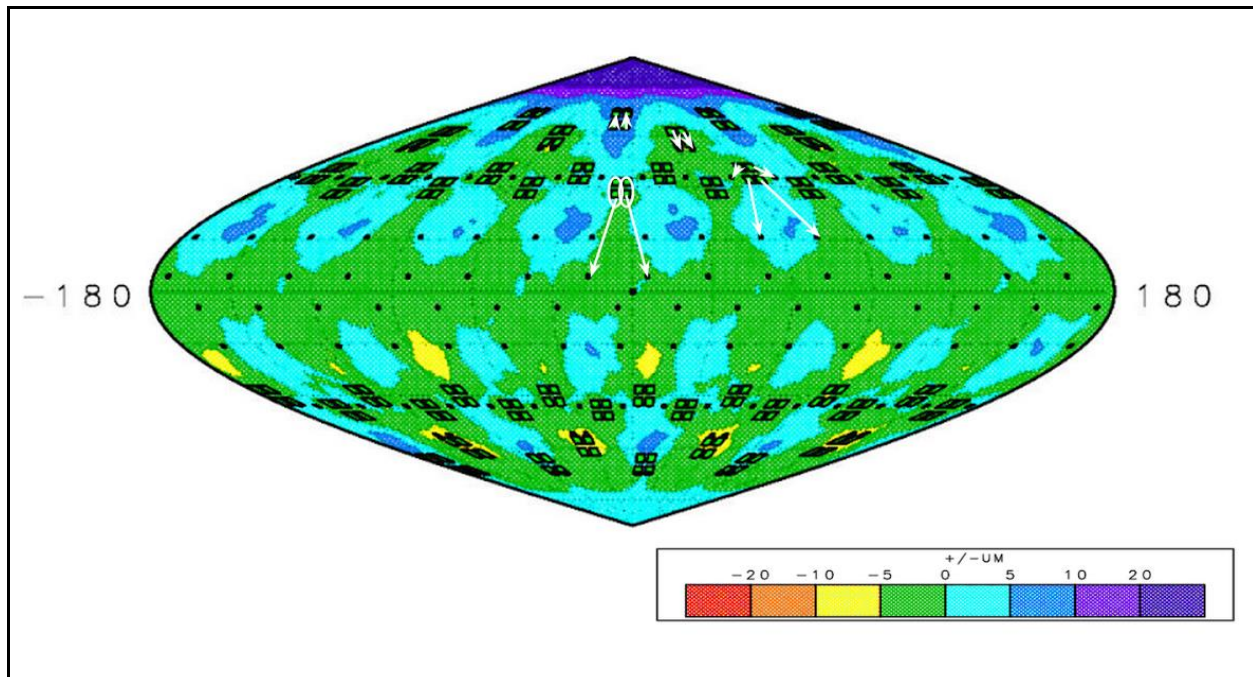
Figure 9: *SAGE* center-of-mass radius contour plot showing deviations from the average radius in μm and pointings of the defocused design at 6 nanoseconds when the target has been compressed to 629 μm. The defocused design has an rms nonuniformity of 0.64%. Top/bottom asymmetries are caused by noise in the code.

The defocused design is shown in figure 9 at 6 nanoseconds. The azimuthal nonuniformity around Θ=60° is greatly reduced in this design. The uniformity in the Θ direction is also much better in this design. The slight difference between the northern and southern hemispheres is caused by noise in the code and the fact that the contour levels have very small increments. Overall, this design has an rms nonuniformity of 0.64%. This is well below the 1.0% rms thought to be required for ignition. The parameters used in the defocused design are shown in Table 1.

	Defocused Design			Oblique Design		
Beam	Defocus (cm)	Theta (°)	Delta Phi (°)	Defocus (cm)	Theta (°)	Delta Phi (°)
1	2.4	20	0	3.0	23	70
2	2.4	20	0	3.0	23	115
3	2.4	20	0	3.0	23	-115
4	2.4	20	0	3.0	23	-70
5	2.6	35	0	2.7	39	70
6	2.6	35	0	2.7	39	115
7	2.6	35	0	2.7	39	-115
8	2.6	35	0	2.7	39	-70
9	2.0	46	-11.25	1.8	48	35
10	2.0	46	11.25	1.8	48	60
11	2.0	69	-11.25	1.8	68	-60
12	2.0	69	11.25	1.8	68	-35
13	1.8	84	-11.25	1.8	81	-11.25
14	1.8	84	11.25	1.8	81	11.25
15	1.6	84	-11.25	1.8	81	-11.25
16	1.6	84	11.25	1.8	81	11.25
17-32	all parameters a reflection of upper hemisphere			all parameters a reflection of upper hemisphere		

Table 1: Parameters of the defocused and first oblique designs. All beams in the defocused design also have an energy increase of 7% from the current design, and beams in the first oblique design have an energy increase of 25% from the current design. Beam 1 is the top left beam in Quad 1, Beam 2 is the top right beam in Quad 1, Beam 3 is the bottom left, etc.

4 b. Oblique Designs

One source of nonuniformities that isn't accounted for in the *SAGE* models is laser speckle. As illustrated in Figure 10, laser beams have areas of higher and lower intensity caused by the way the beam focuses and interferes with itself after going through a phase plate. At late times this speckle is smoothed out more by thermal conduction because the energy is absorbed farther out in the corona of the target, but at early times this speckle can create divots in the target surface known as imprint that don't smooth out as the target implodes [Figure 10 (a)]. It is speculated that having beams encounter the target at oblique incidence could help reduce this imprint by spreading energy over a larger area and by depositing energy farther from the critical surface even at early times [Figure 10 (b)]. In addition, oblique rays will deposit their energy over a larger area as they refract through the plasma, in contrast to normal incidence rays which deposit their energy at a single point on the target shell.

Figure 10: Diagram showing how laser speckle influences uniformity. (a) A normal incidence beam creates an exaggerated imprint pattern. (b) An oblique incidence beam is speculated to reduce imprint on the target surface.
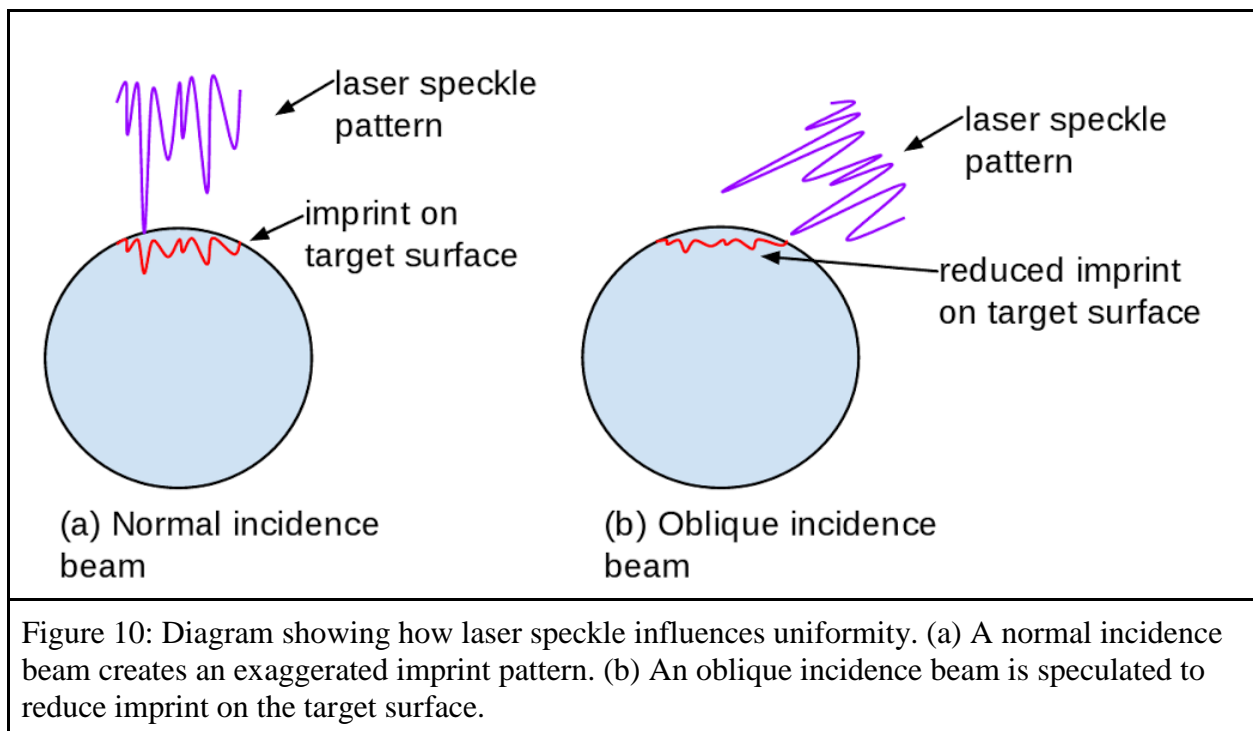
The first oblique design was developed with the goal of having large total pointing shifts for all beams. In the design, all beams have a total pointing shift between 495 and 932 μm, or at least 45% of the target radius. This design has similar defocuses to the defocused design. To gain the benefits of the oblique beams with respect to speckle, every beam in quads 1-3 was given a shift in the Φ direction, spreading out the energy and increasing the uniformity of the energy deposition on the target. Quad 4 beams weren't given an additional azimuthal shift because they already have a large shift in the Θ direction. As seen in figure 11, this design gives a good overall uniformity of 0.57%.

Figure 11: *SAGE* center-of-mass radius contour plot showing deviations from the mean radius in μm and pointings of the first oblique design when the target has been compressed to 632 μm. This design has an rms nonuniformity of 0.57%.
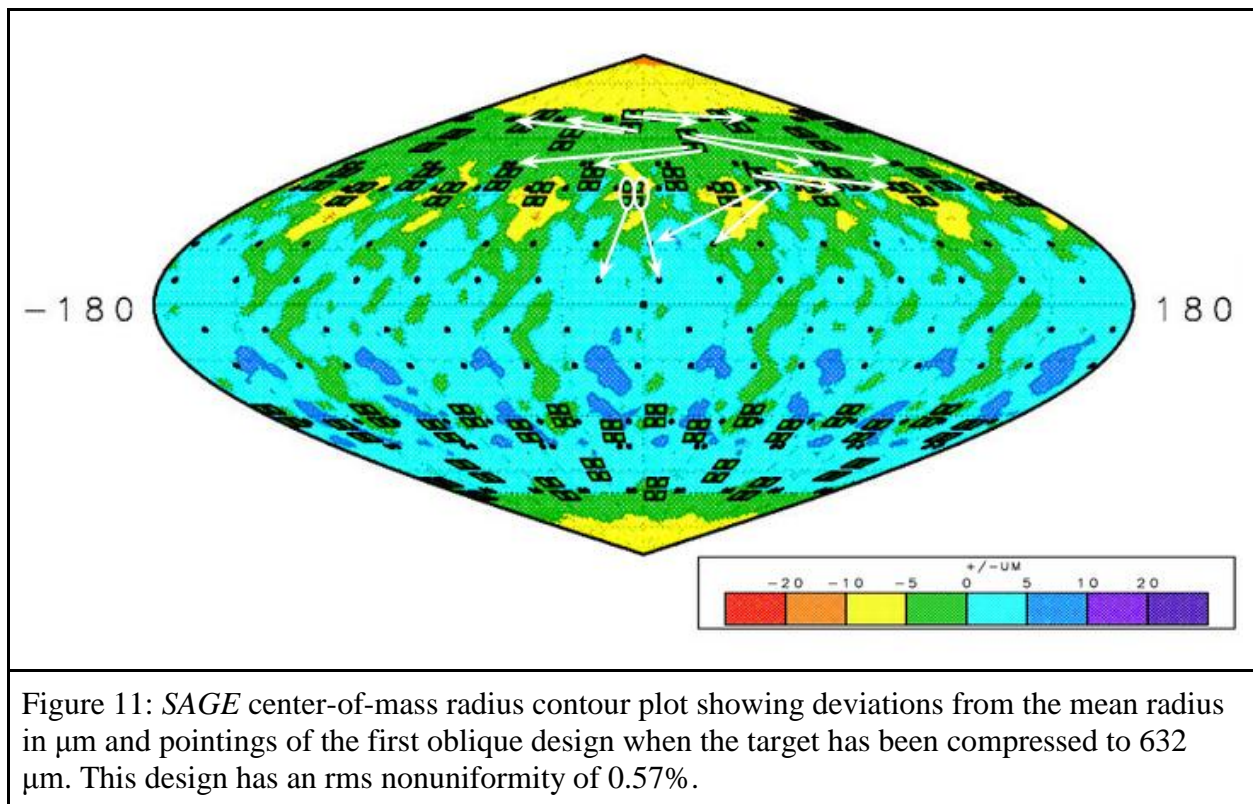
The effects of an oblique pointing on energy deposition can be seen in Figure 12, which shows the energy deposition pattern of a repointed beam in kJ/sr. With an oblique pointing, the majority of the laser's energy is deposited far away from the laser port, and very little energy

encounters the target at normal incidence. The one disadvantage to this design is that it requires a

25% increase in energy from the original design to compress to the same radius at the same time,

since oblique beams with large defocuses experience reduced absorption. This occurs because

while most of the energy hits the target at early times, as the target implodes it decreases in size

and some energy will miss the target [Figure 13].

Figure 12: Energy deposition of a quad 2 beam in the first oblique design in kJ/sr. The blue arrow shows the pointing shift of the beam. The majority of the energy is deposited far away from the laser port, with very little energy encountering the target at normal incidence.

Figure 13: Raytrace plots of a quad 2 beam on the first oblique design at (a) 2 nanoseconds and (b) 6 nanoseconds. (a) At early times, this beam with a large defocus and oblique pointing still transfers most of its energy to the target. (b) As time progresses, more of the energy from this beam misses the target, contributing to lower absorption. With oblique shifts, each ray is depositing its energy over a larger portion of the target as it refracts through the plasma, which may help to reduce the effects of laser speckle on uniformity.

A second oblique design was developed using large pointing shifts with smaller defocuses in an attempt to increase the energy absorption of the implosion. For example, the quad 1 defocuses are 2.0 cm in this design, in comparison with 3.0 cm in the first oblique design. While only about 1% energy absorption was regained with this type of design, the smaller defocuses may help to reduce the speckle present in each beam, because individual beam speckle gets worse as the defocus increases. Therefore, smaller defocuses are also advantageous for creating a uniform implosion. Because there wasn't much gain in absorption with this design, a 25% increase in energy on all beams was still used. If this type of design proves viable on the NIF, phase plates could be developed that allow oblique beams with greater absorption. This design is shown in Figure 14 and has an RMS nonuniformity of 0.64%.
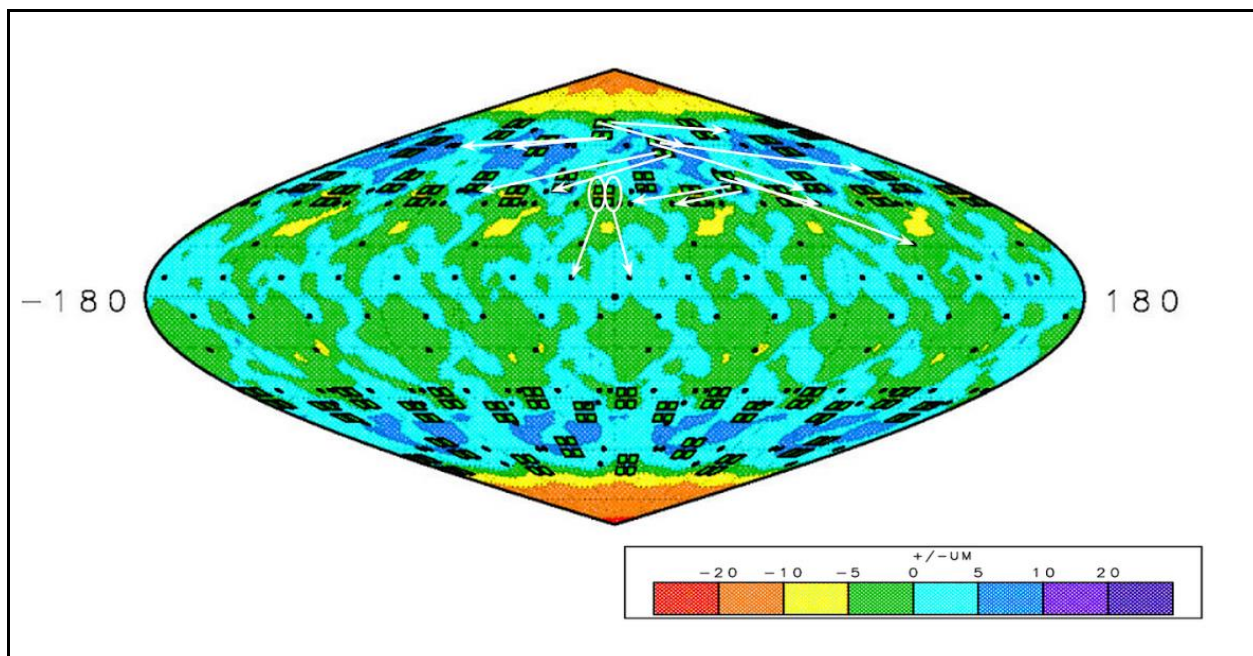
Figure 14: *SAGE* center-of-mass radius contour plot showing deviations from the mean radius in μm and pointings of the second oblique design when the target has been compressed to 631 μm. This design has an RMS nonuniformity of 0.64%.

One significant advantage of all of these designs is the reduction of the azimuthal nonuniformity at $\Theta=60°$ seen in the current design. As seen in figure 15, both the defocused and the first oblique design decrease the azimuthal rms nonuniformity at $\Theta=60°$ by close to a factor of two, significantly improving the overall uniformity of the implosion.

Figure 15: Lineout at $\Theta=60°$ of deposited energy vs Φ for the current design (red, rms = 1.84%), the defocused design (green, rms = 0.91%), and the first oblique design (blue, rms = 0.97%). Both the defocused design and the oblique design improve upon the rms nonuniformity of the current design at this Θ by a factor of 2.
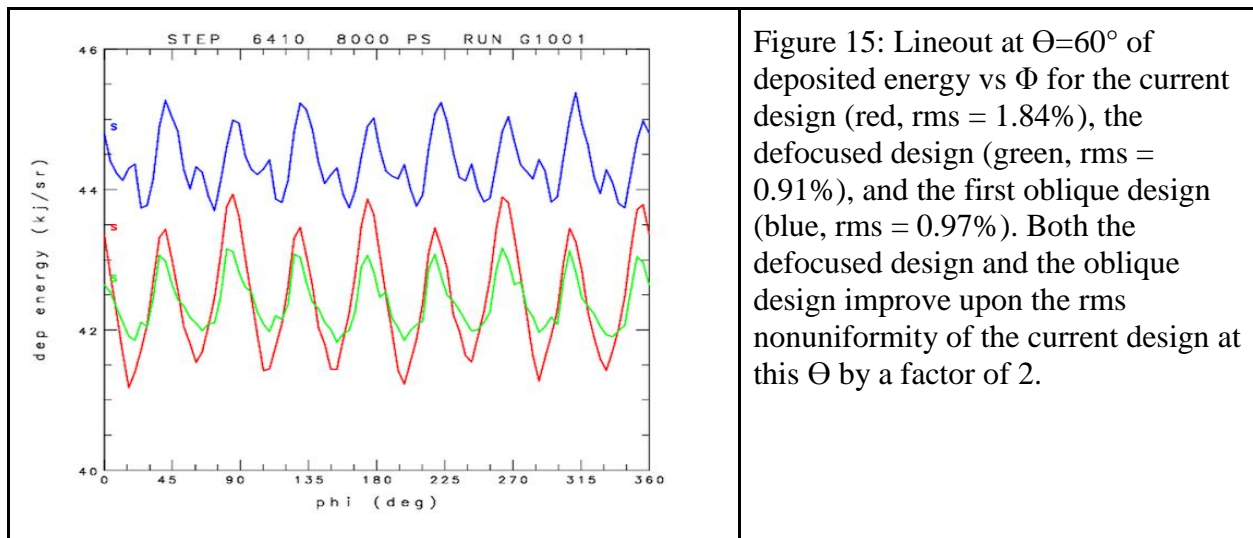
4 c. Overdriven Equator Designs

A final set of designs was developed with the goal of overdriving the equator of the target. Adequately driving the equator has been a persistent problem with polar drive experiments. In order to test the accuracy of the *SAGE* and *DRACO* hydrodynamics codes in modeling the amount of drive at the equator and to allow for adjustments to the equatorial drive based on experimental data, two designs were developed that overdrive the equator. These designs also demonstrate the ability of polar drive to significantly overdrive the equator. The first design overdrives the equator by about 5%, and the second design overdrives the equator by about 10%. Both of these designs use large defocuses on the poles and small defocuses on the equator along with comparatively more energy on the quad 4 beams. As seen in figure 16, both designs overdrive the equator in a relatively smooth manner, and the design that overdrives the

equator by 5% overdrives the equator more gently than the second design. It hasn't been

observed in experiments that the equator is 10% under compressed in relation to the poles

[Figure 6], but the purpose of the 10% overdriven design is to show that the equator can be over

compressed in a polar drive experiment.

Figure 16: Center-of-mass radius in cm vs Θ, averaged over Φ, for both overdriven equator designs. (a) The equator is overdriven by about 5%. (b) The equator is overdriven by about 10%.
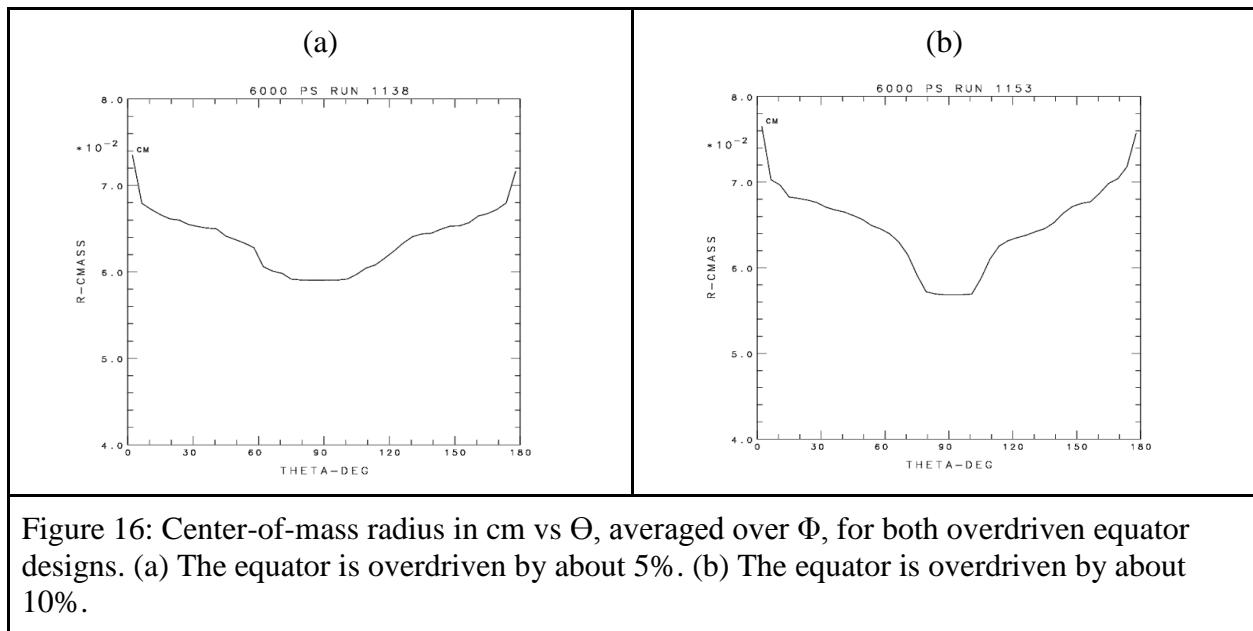
5. Conclusion

Several new designs for polar drive implosions on the NIF were developed using the

hydrodynamics code *SAGE*. A design utilizing larger defocuses to improve uniformity gave an

rms nonuniformity of 0.64%. Two oblique designs, one with larger defocuses and one with

smaller defocuses, were also developed that gave good uniformity using large pointing shifts. It

is speculated that these large pointing shifts could help reduce the effect of laser speckle on the

uniformity of NIF polar drive implosions. Additionally, two designs were developed that

overdrive the equator of the target to allow for tuning of polar drive implosions based on

experimental data. All of the designs are straightforward to test on the NIF.

6. Acknowledgements

First, I would like to thank Mrs. Shayne Watterson for telling me about the High School Program and for encouraging me to apply. I would also like to thank my parents for their support. Finally, I would like to thank Dr. Craxton both for organizing the High School Program and for all of his help and support with my project.

7. References

1.   Yifan Kong, *"Beam-Pointing Optimization for Proton Backlighting on the NIF,"* Laboratory for Laser Energetics High School Summer Research Program (2013).

2.   J. Nuckolls et al., *"Laser Compression of Matter to Super-High Densities: Thermonuclear (CTR) Applications,"* Nature 239, 139 (1972).

3.   J. D. Lindl, *"Development of the Indirect-Drive Approach to Inertial Confinement Fusion and the Target Basis for Ignition and Gain,"* Phys. Plasmas 2, 3933 (1995).

4.   S. Skupsky et al., *"Polar Direct Drive on the National Ignition Facility,"* Phys. Plasmas 11, 2763 (2004).

5.   A. M. Cok et al., *"Polar-drive designs for optimizing neutron yields on the National Ignition Facility,"* Phys. Plasmas 15, 082705 (2008).

6.   R. S. Craxton et al., *"Polar direct drive: Proof-of-principle experiments on OMEGA and prospects for ignition on the National Ignition Facility,"* Phys. Plasmas 12, 056304 (2005).

7.   P. B. Radha et al., *"Polar-drive implosions on OMEGA and the National Ignition Facility,"* Phys. Plasmas 20, 056306 (2013).

8.   Alexandra M. Cok, *"Development of Polar Direct Drive Designs for Initial NIF Targets,"* Laboratory for Laser Energetics High School Summer Research Program (2006).

9.   D. T. Michel, private communication.

10.   F. J. Marshall, private communication.

Next-Generation Polymers for High Power UV Replicated Optics

Jack Gumina

The Harley School

Advisor: Kenneth L. Marshall

University of Rochester

Laboratory for Laser Energetics

Summer High School Research Program 2014

1. Abstract

Several polymers were evaluated as candidate materials for UV laser optics. The manufacture of glass optics such as distributed phase plates and diffractive axicons by conventional optical fabrication techniques is costly and time-consuming. The use of moldable polymers instead of glass in these applications would greatly decrease cost and production time.

For a polymer optic to be viable, it would need to have high transmission at an optical path length of several hundred microns and a high laser damage threshold (>2 J/cm^2) at 351 nm. Polymers were blade-coated onto glass substrates at varying film thickness, and their optical transmission was measured in the UV. Two polymers (Sol Epoxy NB2908-51C and Resin Design 071607-D2) were found to have absorption coefficients that correspond to a transmission of > 98% at 351 nm for a 20 μm thick polymer layer. The Resin Design material was found to have a laser damage threshold of 2.8 J/cm^2 at 351 nm; the laser damage threshold of the Sol Epoxy material has yet to be determined. Both polymers have been shown to release cleanly from Teflon$^®$. Future research will look more closely at the moldability of current materials and expand the search for additional new materials.

2. Introduction

The concept of a polymer-based optic is not a new idea. Over 20 years ago, an effort was made at LLE to fabricate distributed phase plates (DPP's) for use on the OMEGA laser at 351 nm using thermosetting epoxy materials, but these devices suffered from insufficiently high laser damage threshold upon scale-up to large aperture fabrication for a variety of reasons [1]. Advances in materials technology in the area of UV-transparent polymers now make it feasible

to re-examine the viability of making such devices for diffractive/refractive optics for use in the Omega Laser Facility.

There are many methods for patterning optics; one of the fastest and cheapest is optical replication. This process involves patterning an optic from a master mold. Patterning of glass-based optics is accomplished by techniques such as laser writing, multiple mask lithography, or small-tool deterministic polishing, all of which utilize a piece-by-piece process that is costly and time consuming. Polymer-based optics can be produced by optical replication, which is a process that lends itself well to rapid and cost-effective manufacture of optics on a large scale [2]. The ideal polymer material for such an application needs to have a number of important physical properties: (1) as high a transmission at 351 nm as possible at long optical path lengths (up to several hundred microns); (2) excellent laser damage resistance in the UV; (3) mechanical properties amenable to surface pattern generation and replication by molding or stamping, and (4) commercial availability with low raw materials cost. This work concentrated on a survey of commercially available materials for the purpose of identifying which candidates were capable of meeting these key requirements.

3. Background

There are many chemical classes that can undergo polymerization reactions; some typical examples include carbonates, urethanes, epoxides, alkenes, and halogenated alkenes. To achieve high UV transparency, polymers need to have certain chemical properties. Most polymers are composed of long chains of carbon-carbon bonds, which can differ in bond order (e.g., single, double, or triple- bonds between each carbon atom). Molecular structures composed entirely of carbon-carbon single bonds (C-C) are highly UV transmissive down to ~ 200 nm; carbon-carbon double bonds (C=C) that are isolated from each other in a carbon chain by <u>multiple intervening</u> carbon-carbon single bonds (e.g., -C=C-C-C-C-C=C-) also absorb deep in the UV (~204 nm) [3]. However, when C=C bonds are separated by only <u>one</u> C-C unit, (e.g. –C=C-C=C-) they are termed to be in "conjugation" and the absorption spectrum is shifted to longer wavelengths. From the quantum chemistry viewpoint, conjugation of double bonds is manifested by the overlap of available p-orbitals across a sigma bond. When a double bond exists only one sigma bond away from another double bond, the p-orbitals can overlap. This overlap allows the electrons in the overlapping orbitals to be delocalized between each other, forming a π-bond. This electron delocalization results in stabilization of the molecule; the more extensive the delocalization, the more thermodynamically stable the molecule is. However, this more extensive electron delocalization also results in an increased optical absorption in the UV, which would be undesirable for the intended application. Ideally, a completely aliphatic (free of double bonds) material would be the most desirable [3]. Two examples of these cases are shown below in Fig 1. Polyethylene (structure "a") is aliphatic and has almost no absorption in the UV, whereas polystyrene (structure "b") has benzene rings that contain double bonds in conjugation, and has an appreciably higher UV absorbance.

4

(a)   (b)

Polyethylene   polystyrene
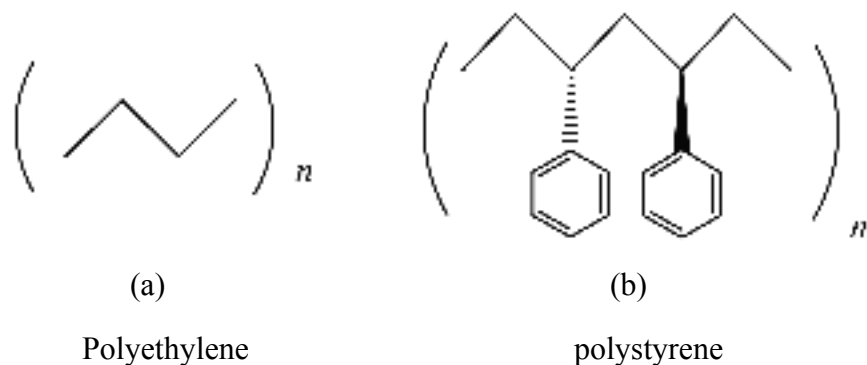
Fig. 1: The molecular structures of polyethylene (a) and polystyrene (b). The fully saturated (aliphatic) carbon skeleton of polyethylene makes it absorb significantly less in the UV than does polystyrene.

Materials with carbon-halide bonds are also to be avoided, as many of these bonds absorb in the UV. The very common commercial polymer polyvinyl chloride (PVC), shown in Fig. 2, is prepared by polymerization from a halogenated alkene. The carbon-chlorine bond is sensitive to UV light, and breaks down to form chlorine as a free radical, which is highly reactive and causes structural rearrangements and degradation of the polymer. These molecular rearrangements produce an increase in both UV and visible absorption, causing the material to become yellow.
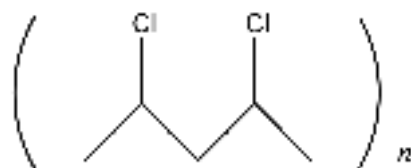
Fig. 2: The molecular structure of polyvinyl chloride.

The polymers evaluated in this study were all commercially available epoxide and urethane formulations. Urethanes are produced by the reaction of an isocyanate [Fig 3(a)] and a *polyol* (a hydrocarbon chain containing a large number of –OH groups as substituents); epoxy

5

materials are formed by polymerization of an epoxide ring [Fig 3(b)] with an amine or similar nucleophile. The properties of both types of polymers are highly dependent on the molecular structure of the reactants [3].
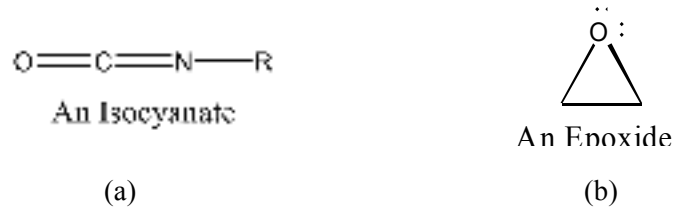
Fig. 3: The molecular structures of some of the monomeric "building blocks" used to prepare urethanes and epoxy materials: (a) an isocyanate; (b) an epoxide.

Ordinary polymers are formed from only two reactive species (e.g., one type of isocyanate and one type of polyol). When a mixture of two or more of one reactive species is used (e.g., one type of isocyanate and two different polyol structures), co-polymers are formed. Co-polymers are often employed to make further adjustments to the properties of the desired polymer (e.g., mechanical, thermal, chemical) than would be possible from using only two reactants.

Figure 4 shows the reaction mechanism for the formation of an epoxy polymer. Epichlorohydrin, a common epoxide, polymerizes with a nucleophilic monomer (e.g., an amine). The reaction occurs at room temperature and is exothermic (releases heat), and thus proceeds by a thermal mechanism. The extent to which the reaction proceeds to completion to form a solid polymer is termed the *degree of cure*.
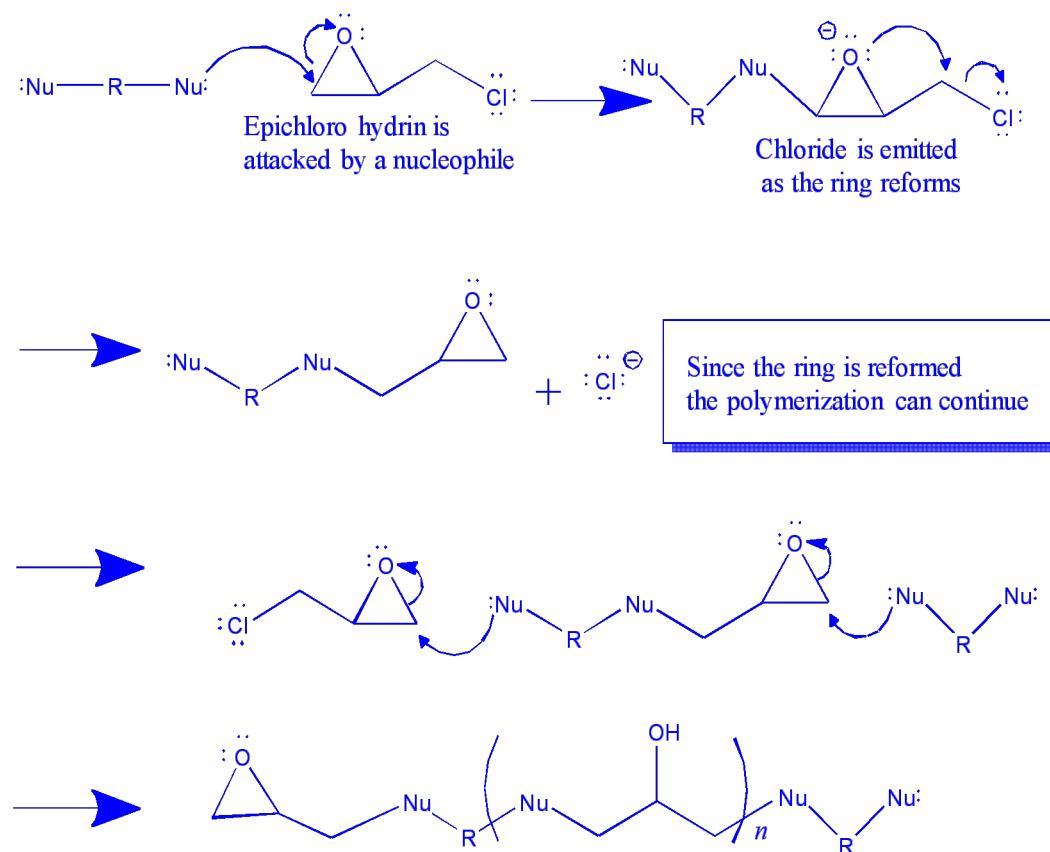
Fig. 4: Polymerization mechanism for reaction of an epoxide with a nucleophile to form an epoxy polymer.

Most thermal-curing systems will proceed to an 85% degree of cure on their own, but as the concentration of reactants begins to drop off, the rate of reaction decreases to a point where additional heat may be required to achieve a fully-cured system with all of the desired physical properties. Employing reactants with multiple functional groups that can participate in the same reaction (e.g., a di-isocyanate) results in a polymer that is *cross-linked* (i.e., bonds are formed laterally between adjacent polymer chains) to form a polymer network. The degree of cross-linking controls the stiffness and rigidity of the polymer network, and is an important element

often used when designing engineering materials and optical polymers. Figure 5 compares the molecular packing of a normal polymer network to a cross-linked one.
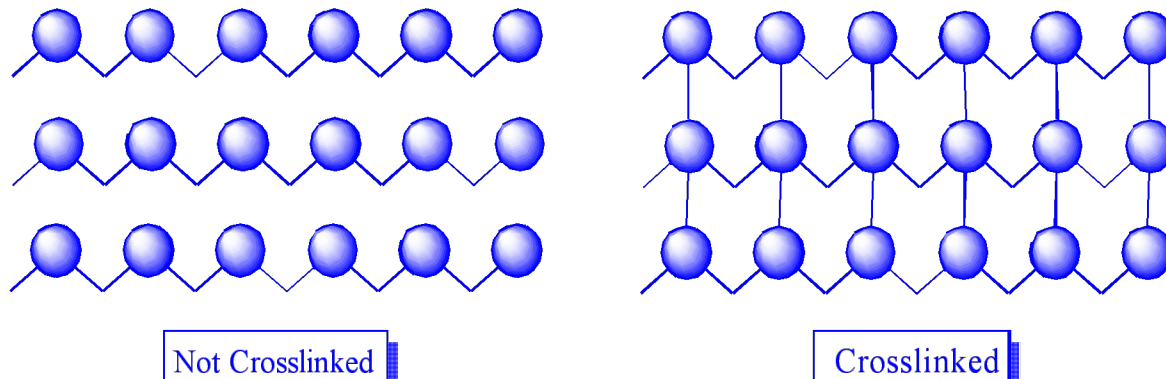
Fig 5: Comparison of a non-crosslinked polymer network to one that is cross-linked.

Certain co-polymer systems can also be cured using UV light. Because these materials contain UV chromophores by necessity in order to initiate the photoreaction (either intrinsically as part of the monomers or in the form of photoinitiators that have been added to produce transient species to initiate the reaction), they are not good candidates for high peak power laser applications in the UV, as there is always the possibility that not all traces of these UV chromophores will be converted into the desired product and some may remain behind to initiate laser damage. For this reason, only materials following a thermal cure route were considered at this time.

4. **Sample preparation**

Three commercially available thermosetting polymer materials, Masterbond EP21LSC1 Epoxy, Sol Epoxy NB2908-51C and Resin Designs 071607-D2 (urethane), were chosen for evaluation after an exhaustive search of available materials. After samples were obtained from the respective manufacturers, the relative rate of cure for each polymer system was tested. The

curing protocol supplied by the manufacturer of each polymer formulation was used as a starting point, with some variations applied in order to produce samples that were as completely cured as possible. The cure schedules developed involved heating a sample that had been coated qualitatively onto a piece of glass using a spatula from 30 min to 3 hrs at various temperatures, depending on the material's formulation. Once the right cure method was found, the samples were coated onto a glass substrate in a Class 10,000 clean room using a knife coater equipped with micrometers for controlling the coating layer thickness. The thickness of the coatings was determined using a Taylor-Hobson Talysurf stylus profilometer; the optical transmission at 351 nm was determined using a UV-VIS-near IR spectrophotometer (Perkin Elmer Lambda 900). These two values were used to calculate the absorption coefficient μ using the formula

$$I = I_0 e^{-\mu x}$$

where

      I = light intensity after passing through the sample
      I_0 = Initial intensity of light
      μ = linear absorption coefficient
      x = sample thickness (optical pathlength)

The absorption coefficient values were then used to calculate the expected transmission for a 20 μm path length, which is the minimum desired film thickness for this application.

5. Laser Damage Testing

Laser damage testing was conducted on cast sample films of the three thermosetting polymer formulations described in Section 4 at 351 nm with a 0.9 ns pulse width. Only the 1-on-1 testing protocol (where different sites are tested at increasing laser fluence levels until damage is observed) was used for these samples. Damage testing was also conducted on a fourth polymer formulation supplied by Rochester Photonics Inc. (RPC) that had already been deposited on a substrate. This proprietary material is reported to have a laser damage threshold at 351 nm of 6.2 J/cm^2 (in very thin films) and originally was intended as a benchmark. Optical absorption measurements on the supplied sample showed that this material had an absorption coefficient of 1.6 X 10^{-3} μm^{-1}, which indicates that at the targeted 20 μm film thickness the resulting transmission would be only 96.9%. Because the material is proprietary, RPC would not release any information on its composition without a signed agreement to purchase parts made with this material.

6. Results

The sample processing conditions, linear absorption coefficients, optical transmission calculated from the optical absorption coefficients, and laser damage thresholds for the three candidate materials are shown in Table 1, along with relevant available information for the material from RPC. Figure 6 shows typical optical absorption spectra for the two best candidate materials (Sol Epoxy NB2908-51C and Resin Designs 071607-D2) in the UV-visible region between 265 nm and 450 nm. These spectra are shown for qualitative comparison of absorption coefficients, as it was not possible to make coatings of identical film thicknesses repeatedly with existing coating equipment.

Material	Chemical class	Cure method/ conditions	Absorption coefficient (μm^{-1})	Calculated transmission (20 μm)	Laser damage threshold	
					J/cm^2 (351 nm, 0.9ns)	Test path (μm)
MasterBond EP21LSCL-1	Epoxide	Thermal 65^oC, 3 hrs	1.7 X 10-2	64%	0.14 ± 0.01	100
Resin Design 071607-D2	Urethane	Thermal 65^oC, 1 hr	5.9 X 10-4	98.8%	2.8 ± 0.50	34
SolEpoxy NB2908-51C	Epoxide	Thermal 150^oC, 30 min	9.4 X 10-5	99.8%	TBD	
RPC	Proprietary	Unknown	1.6 x 10-3	96.9%	6.2 ± 0.05	< 5

Table 1: A compilation of the data generated for the polymer formulations tested. The data for the RPC material is also included as a qualitative benchmark. Note that the damage threshold data for the RPC material was for a very thin path length on a device supplied by RPC
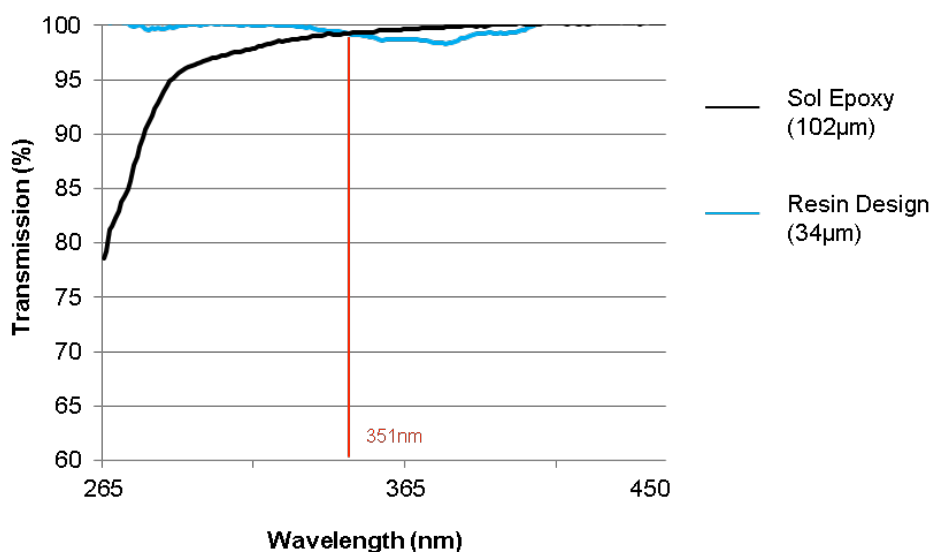
Fig. 6: Optical transmission of Sol Epoxy NB2908-51C and Resin Designs 071607-D2 in the UV-visible region. These spectra are shown for qualitative comparison of absorption coefficients, as it was not possible to make coatings of identical film thicknesses repeatedly with existing coating equipment. The high transparency of the Resin Designs urethane extending down to nearly 265 nm is remarkable.

Examination of the data in Table 1 reveals that only the Resin Designs and Sol Epoxy materials have sufficiently high transparency to be viable candidates for applications at 351 nm. The Masterbond material can be eliminated from consideration due to its relatively low 351 nm transmission (64%) and poor laser damage threshold (~0.14 J/cm^2). The Resin Design material has a higher laser damage threshold (2.8 J/cm^2) for a 20 μm path length than the 2.0 J/cm^2 required for the application. Due to insufficient time and schedule conflicts on the damage test system, it was not possible to determine the laser damage threshold for the Sol Epoxy during the time frame of this project; this data will be pursued in future studies.

Another requirement for a polymer material to be useful for optical replication is for it to be able to be released cleanly from the master mold used to generate the patterned optic. Preliminary experiments conducted with the Sol Epoxy and Resin Designs material showed that these two polymers release cleanly from a Teflon® mold. Because the surface of the available Teflon® mold used was not intended for optical replication and did not have a smooth finish, the surfaces of the polymer replicates in contact with the mold were rough and produced significant scattering when illuminated with visible laser light.

7. Conclusions

This study has identified two commercially available polymers, Sol Epoxy NB2908-51C and Resin Design urethane 071607-D2, which by virtue of their physical and optical properties are excellent candidates for polymer replicated optics for high-peak-power lasers operating at 351 nm. Both materials have linear absorption coefficients corresponding to an optical transmission of > 98% at 351 nm for a 20 μm thick polymer layer, and the Resin Designs material has a damage threshold at 351 nm that is 40% above the minimum required damage

threshold of 2 J/cm^2 at the same wavelength and pulse width. Both materials were also shown to release cleanly from a Teflon$^®$ mold, which is an important requirement for optical replication.

Considerable additional research needs to be conducted before the generation of replicated polymer optics can be fully realized using these materials. More work needs to be done in developing accurate curing protocols using thermal analysis techniques such as differential scanning calorimetry (DSC). This instrument can determine the glass transition temperature (T_g) of the polymer at different cure times. For polymers, T_g is the temperature at which the polymer backbone begins to become flexible, and can be used as a measure of how well-cured the material is. As the polymer cures, the T_g increases as a function of cure time and cure temperature until it reaches a constant value, at which point it is considered fully cured. Using the DSC allows quantitative determination of the optimum cure temperature and time to ensure that there are no residual monomers left behind that can adversely affect the polymer's optical and mechanical properties.

Although the coatings for laser damage testing were prepared in a Class 10,000 clean room, due to the high viscosity of the polymer materials no efforts were made to filter the polymer materials to remove suspended solids that might act as sites for promoting laser damage. Higher laser damage thresholds may be possible if the polymer materials could be dissolved in a suitable carrier solvent to reduce their viscosity sufficiently to allow filtration through a submicron particle filter, followed by evaporation of the carrier solvent. Further investigation into pattern replication from molds with optical-quality surfaces also needs to be conducted. This activity may require the use of different mold materials such as polished metals or, alternatively, a flexible mold material like polydimethylsiloxane (PDMS), along with mold release agents to

produce optical-quality replicated polymer optics for 351 nm applications in OMEGA or OMEGA EP.

Acknowledgements

I thank Dr. Stephen Craxton and the Laboratory for Laser Energetics for giving me this amazing opportunity. I have learned so much about research and how labs operate over these 8 weeks. I especially thank my advisor Kenneth L. Marshall for being very helpful with my symposium presentation and advising me for the eight weeks of the program. I thank Chemical Engineering PhD student Debbie Saulnier in the Materials Laboratory for helping me with both my abstract and my symposium slides. Lastly, I thank my project partner, Chemical Engineering undergraduate student Reid Desruisseaux, for working with me as a colleague for the duration of my project.

References

1. T. Kessler et al, "High-Efficiency Distributed Phase Plate Generation and Characterization", LLE Review Volume 65, pgs 1-8.

2. T. Kessler, private communication.

3. K. Marshall, private communication.

Capturing Hydrogen on Chilled Molecular Sieve

Krishna Patel

Webster Schroeder High School

Advisor: **Dr. W.T. Shmayda**

Laboratory for Laser Energetics

University of Rochester

Rochester, NY

November 2014

I. Abstract

LLE studies inertial confinement fusion using deuterium-tritium fuel mixtures. Tritium released from processing equipment is re-captured with *ZrFe* getter beds. These devices must be unloaded annually to recover their tritium collection efficiency. One approach to collecting the tritium released from *ZrFe* getter beds utilizes a cryotrap, a coil filled with crushed molecular sieve chilled to liquid nitrogen temperatures (77 K). The performance of a compact cryotrap was evaluated using hydrogen-helium mixtures. The hydrogen capacity of the cryotrap has been measured to be 5.99 sL, or 58.5 scc of hydrogen per gram of molecular sieve. At approximately one-fifth of the total capacity, the mean residence time of the hydrogen in the cryotrap is 170 minutes for a helium purge flow rate of 0.100 L/min. The residence time decreases logarithmically as the helium purge flow rate increases. The cryotrap releases deuterium before it releases hydrogen, and the deuterium residence time has a linear relationship with the helium purge flow rate.

II. Introduction

The University of Rochester's Laboratory for Laser Energetics (LLE) operates a 30 kJ laser to study inertial confinement fusion reactions that utilize deuterium-tritium (*DT*) fuel mixtures inside cryogenic targets. Typically, *DT* fuel needs to be pressurized to several hundred atmospheres and then cooled below the triple point of 19.8 K to form a layer of *DT* ice inside the thin plastic target shells. The tritium processing equipment required to generate these high pressures and low temperatures is encapsulated in a glovebox in order to minimize the release of tritium to the environment. This glovebox system *(see figure 1)* is continuously flushed with helium, which then encounters a series of adsorbent beds in order to remove tritium effluents

2
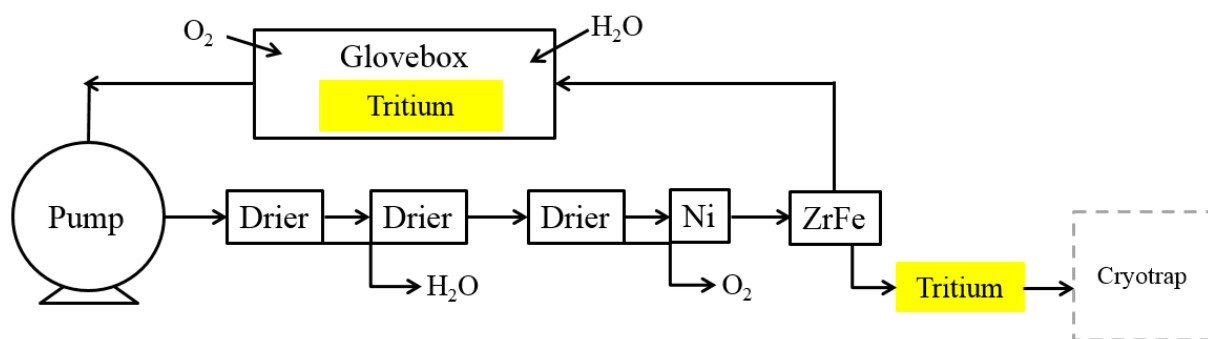
Figure 1. Schematic of the glovebox environment containing tritium processing equipment. The first two driers remove water from the helium stream and the next two beds remove oxygen from the stream in order to protect the ZrFe bed from oxidization. The ZrFe bed removes tritium, which could potentially be unloaded into a cryotrap.

from the helium stream. The first and second driers in this system remove water from the helium stream. The next two beds consist of a drier that contains room temperature molecular sieve and a nickel bed that remove the oxygen from the stream. These beds are necessary to protect from contaminants that cause passivation of the reactivity of the zirconium-iron (*ZrFe*) bed.[1] The helium stream then flows over the *ZrFe* bed, which removes any traces of tritium that are released from the processing equipment into the helium stream. The *ZrFe* bed must be regenerated annually in order to regain its tritium capturing efficiency. When heated to 450°C and back-flushed with a pure helium stream, the *ZrFe* bed will gradually release the tritium it contains at low concentrations. Currently, the tritium released from these beds is oxidized, transforming it into tritiated water, and collected on molecular sieve driers. These driers are heated off-site to recover the tritiated water that is then reduced in a catalyst column back into deuterium-tritium gas (*DT*). The *DT* is sent to an Isotope Separation System (ISS) where it is purified into tritium and reused. However, if the *DT* released from the *ZrFe* beds could be captured as deuterium-tritium gas without conversion to tritiated water first, then the *DT* gas

could be sent directly to an ISS, simplifying the tritium regeneration process while simultaneously saving money and processing time.

A possible approach to capturing the tritium released from the *ZrFe* beds as tritium gas is by using a cryotrap. A cryotrap is composed of three separate coils that are nested and brazed together. One side contains a heater, the other allows for liquid nitrogen flow, and the coil in the middle of the two contains crushed molecular sieve. When chilled to 90 K, the cryotrap will extract tritium from a helium stream at very low partial pressures and store it on the molecular sieve surface through physisorption. When heated above 110 K, the cryotrap will release the tritium back into the carrier stream at much higher partial pressures. At these higher concentrations, the tritium can be transferred from the cryotrap to a uranium bed for temporary storage or subsequently unloaded into an ISS.

In order to characterize the cryotrap, two sets of trials were conducted. The first consisted of loading hydrogen onto the cryotrap to calculate the cryotrap's maximum hydrogen capacity. The second set of trials measured the maximum residence time for hydrogen to elute from the cryotrap, i.e., the time it takes for the loaded hydrogen to be forced out of the cryotrap by a pure helium purge stream while still cooled at 90 K, at approximately 21% of its hydrogen capacity.

III. Characterization of the Pd/Ag Membrane

In order to determine the time of breakthrough, i.e., the time when the cryotrap stops adsorbing the hydrogen from the helium-hydrogen mixture, it is necessary measure the partial pressure of hydrogen exiting the cryotrap. Because residual gas analyzers and Bayard Alpert gauges are harmed at high pressures, the hydrogen must be separated from the helium stream and then measured. To do so, a heated palladium-silver (*Pd/Ag*) membrane (a permeator) is used.

When a hydrogen-helium mixture is exposed to such a membrane heated to 250°C, hydrogen

molecules disassociate into atoms on the membrane surface, are adsorbed into the membrane,

permeate through the membrane, re-associate, and are released on the downstream side.[2] Since

helium cannot diffuse through the membrane in this manner, the permeator can be used to

separate hydrogen from a helium stream. Testing hydrogen-helium mixtures at various concentrations confirmed that the pressure on the downstream side of the *Pd/Ag* membrane is sensitive to the hydrogen concentration of interest.[3] *Figure 2* shows that in the temperature range 250°C to 350°C the permeator is neither linearly dependent on upstream pressure nor dependent on the square root of pressure, but rather in transition between the

Figure 2. Downstream pressure as a function of upstream hydrogen concentration. As hydrogen concentration increases, so too does upstream pressure; hydrogen concentration in the carrier stream is therefore used as a measure for upstream hydrogen pressure. The relationship between the two proves that the Pd/Ag permeator is sensitive to hydrogen concentration, and therefore allows for the detection of hydrogen in helium streams.

two extremes.[2] Linear dependence on pressure implies that the quantity of hydrogen passing

through the permeator depends on the arrival of hydrogen at its surface while dependence on the

square root of upstream pressure implies that hydrogen permeation is limited by the diffusion

rate through the palladium-silver tubes. Therefore, during each trial the *Pd/Ag* membrane was

heated to 250°C or above, to prevent the system from falling into a $P^{1/2}$ dependent state.

IV. Experimental Setup

A typical cryotrap run begins by cooling the cryotrap to below approximately 103 K

(-170°C) by beginning the liquid nitrogen flow while flowing a pure helium stream through the

cryotrap. Concurrently, the *Pd/Ag* membrane is heated to approximately 250°C. The temperature

of the entire system is measured in five places using thermocouples. Once below the cyrotrap

temperature threshold, the bypass is closed, and hydrogen is added into the helium stream at a concentration set through the two mass flow controllers (MFCs) *(see figure 3).* The cryotrap is loaded until breakthrough occurs, i.e., until hydrogen stops being adsorbed by the cryotrap because its maximum capacity has

Figure 3. Schematic of experimental setup with the bypass in the closed position. Two separate mass flow controllers (MFCs) control the concentration of hydrogen in the helium stream. The hydrogen that permeates the Pd/Ag membrane enters a vacuum system where it is analyzed by a residual gas analyzer (RGA), which uses an RF-quadrupole mass spectrometer, a Bayard Alpert gauge (BAG), and pressure transducer gauges (PT Gauge). The vacuum system is maintained at approximately 10^{-6} Torr using scroll and turbomolecular pumps.

been reached. At this time, hydrogen comes in contact with the *Pd/Ag* membrane, traverses the

membrane, enters the vacuum system, and is detected by pressure gauges. Inside the vacuum

system, the data collected from a Bayard Alpert gauge (BAG), a 1 Torr pressure transducer gauge, and a 10 Torr pressure transducer gauge are used to create a hydrogen release profile for the run *(see figure 4a)*. The total volume of hydrogen loaded onto the cryotrap is calculated using the hydrogen flow rate and the loading time.

During certain trials, the cryotrap capacity decreased because of contact with impurities. However, by attaching heaters to the thermocouples on the cryotrap and heating it to 250°C with a pure helium purge, the cryogenic molecular sieve capacity can be regenerated.[1]

V. Results and Discussion

i. Full Capacity Cryotrap Run

The maximum capacity cryotrap run successfully loaded a total of 5.99 sL of hydrogen onto the cryotrap, giving a capacity of 58.5 scc of hydrogen per gram of molecular sieve contained in the cryotrap. The run began by heating the permeator to 250°C, with a pure helium stream flowing through the bypass at 0.103 L/min, and cooling the cryotrap to 91.0 K (-182.0°C) by starting liquid nitrogen flow. Once both temperature thresholds were reached, the bypass was closed and the cryotrap was opened. At 3 minutes, hydrogen was
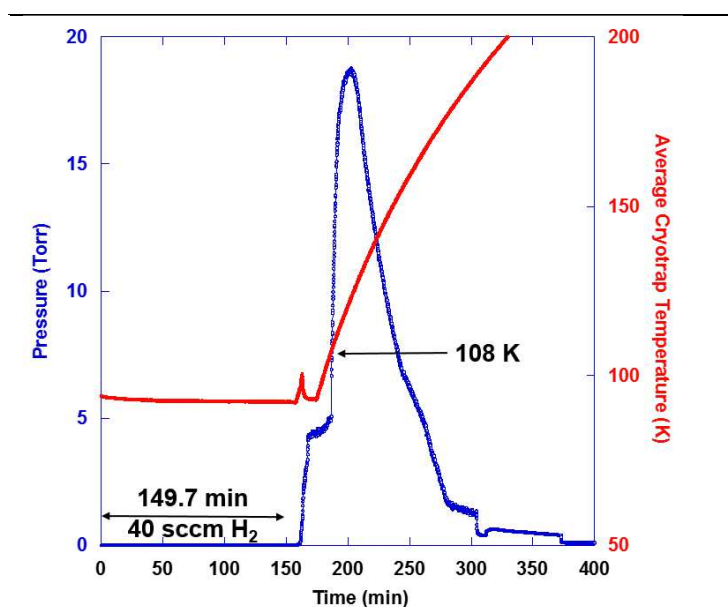
Figure 4a. Hydrogen pressure (Torr) as a function of time. The maximum capacity cyrotrap run was loaded at a flow rate of 40 sccm of hydrogen for 149.7 minutes. At 108 K, the majority of the hydrogen unloaded rapidly. The rapid pressure increase from 158-172 minutes levels at the new baseline pressure of 4.42 Torr.

added into the helium mixture at 40 sccm to create a concentration of approximately 40%. At

149.7 minutes, breakthrough occurred *(see figures 4a, 4b)*, i.e., the cryotrap reached maximum

capacity. The hydrogen flow was shut off at 152 minutes, and the turbomolecular pump was

shut down at 158 minutes to prevent it from overheating. After the pressure in the vacuum

system stabilized to a baseline of 4.42 Torr, at 172 minutes the liquid nitrogen flow was stopped,

and the helium flow rate was increased to 1.002 L/min to facilitate the hydrogen unloading cycle.

Because it proved unreliable at high pressures, the RGA was shut down at 185 minutes. The

cryotrap unloading cycle peaked at 187 minutes at a temperature of 108 K (-165°C). At 239

minutes, the helium purge rate was lowered to 0.100 L/min, and the system was allowed to

unload overnight.
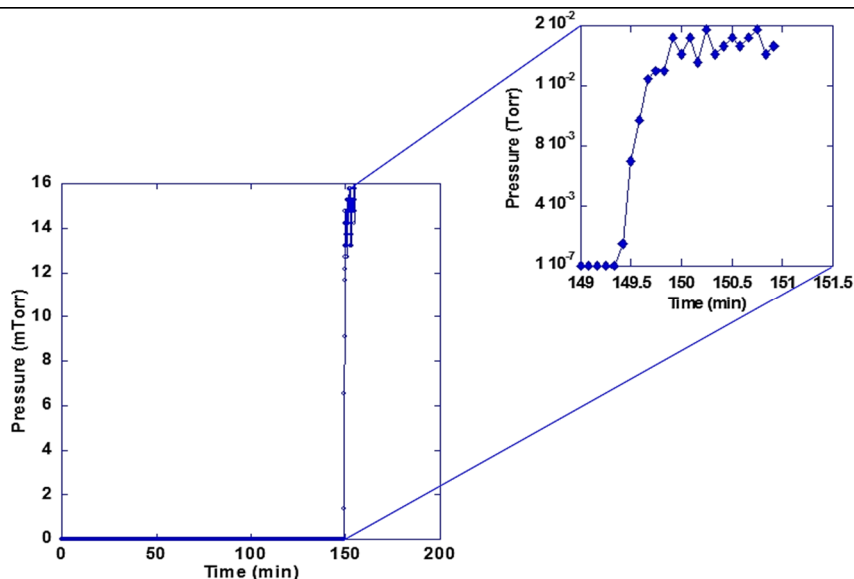
*Figure 4b. A close up of the breakthrough in figure 4a: hydrogen pressure as a
function of time. Until breakthrough, the cryotrap is completely efficient at
retaining hydrogen.*

At breakthrough, 149.7 minutes, no additional hydrogen is adsorbed by the cryotrap

because the cryotrap has reached its maximum capacity. As seen in *figure 4b*, the pressure

gauges initially register a hydrogen signature in the magnitude of 10^{-6} Torr. These pressures are well below the detection threshold of the pressure gauges monitoring the vacuum system. Therefore, it was concluded that until the point of hydrogen breakthrough, the cryotrap is 100% efficient at adsorbing hydrogen. Furthermore, the cryotrap was able to concentrate the release of hydrogen to a maximum of 18.6 Torr. The ability to concentrate tritium is ideal in a tritium recovery method.[4] For example, uranium beds have a high tritium storage capacity; however, they cannot be loaded at the low pressures that are produced when a *ZrFe* bed is purged.[1] Because of its capacity to concentrate, a cryotrap presents a model solution to this dilemma.

ii. Partial Capacity Cyrotrap Run

Tests with the cryotrap charged to full capacity lead to the hypothesis that the cryotrap cannot hold hydrogen indefinitely while cold, if a helium stream is still flowing through the coil. The cryogenic molecular sieve medium does eventually release hydrogen even while chilled to 77 K while being purged with helium.[1] Therefore, for these tests, the cyrotrap was loaded to approximately one-fifth its capacity (1.2 sL), the hydrogen stream was stopped, and a pure helium purge was continued while liquid nitrogen was flowed to maintain the cryotrap's temperature below the normal release threshold (approximately 113 K, or -160°C).
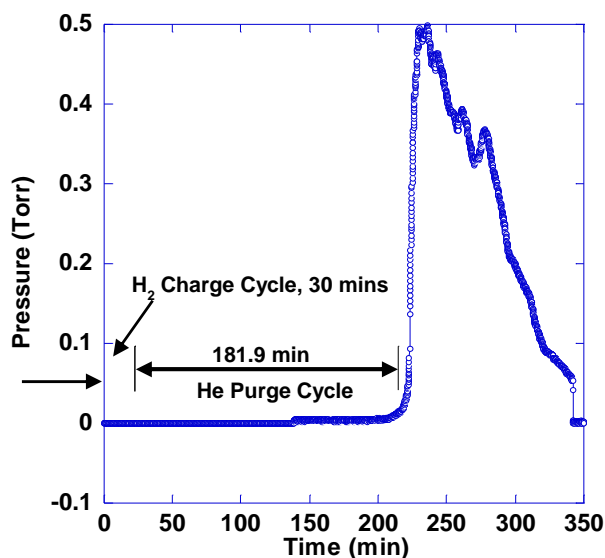
Figure 5. Hydrogen pressure as a function of time measured using pressure transducer gauges. After a 30-minute charge cycle, a pure helium stream at a flow rate of 0.200 L/min takes 181.9 minutes to begin the involuntary unloading of hydrogen from the cryotrap. Unloading was complete after 132.6 minutes.

For a helium purge rate of 0.200 L/min, the cryotrap bypass was opened, the liquid nitrogen flow began to bring the cryotrap temperature down to -178°C (95 K), and the permeator temperature was set to 250°C. The cryotrap bypass was then closed and the hydrogen was added to the helium stream at 40 sccm. At 30 minutes, after 1.2 L of hydrogen had been loaded, the hydrogen flow was stopped. With the cryotrap temperature below 95 K, the helium purge took 182 minutes to push the hydrogen through the entire length of the cryotrap and out the other end *(see He purge cycle in figure 5).* At 212 minutes, the helium purge forced hydrogen breakthrough. The hydrogen unloading cycle was completed at 345 minutes. Repeated partial capacity trials revealed a trend between hydrogen residence time (the time it takes for the hydrogen to exit the cryotrap), t_H, and helium purge flow rate, σ, given by the following equation, as illustrated in *figure 6*:

$$t_H = -131.9 \ log(\sigma) - 74.8 \qquad [1].$$
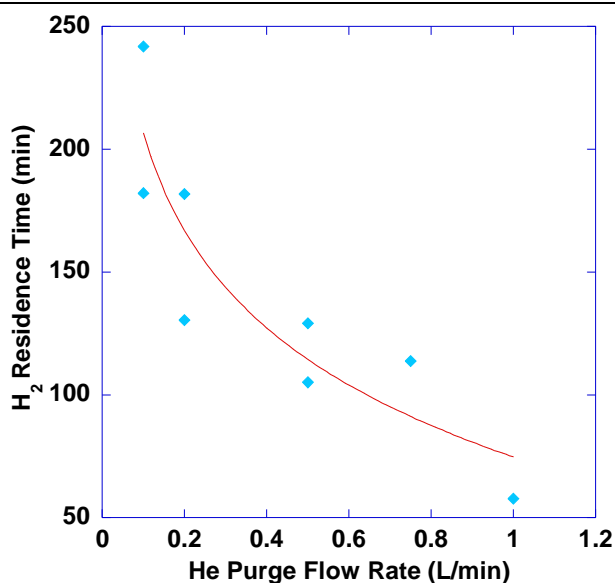
Figure 6. Hydrogen residence time as a function of helium purge flow rate. There is a noticeable logarithmic relationship between the helium purge rate and the residence time of the 1.2 L of hydrogen inside the cryotrap. $R^2 = 0.802$

Returning to the first partial capacity run, an unexpected increase in pressure *(too minute to be visible in figure 5)* was noticed at 115.5 minutes (85.5 minutes after the hydrogen loading cycle was completed). Cryogenic molecular sieves were once used to separate hydrogen isotopes, and there are approximately 150 ppm of deuterium naturally occurring in hydrogen. Therefore, hydrogen-deuterium traces were tested for during these runs to determine if deuterium was released first during this miniscule pressure increase. Hydrogen-deuterium (*HD*) was monitored because any deuterium passing through the permeator would be more likely to recombine with hydrogen atoms because of their relative abundance. Thus, by monitoring *HD* releases, the deuterium residence time can be determined. Using the RGA, it was confirmed that the initial breakthrough, i.e., the first pressure increase at 115.5 minutes, is a release of hydrogen-deuterium molecules (*HD*). As shown in *figure 7*, the concentration of *HD* overtakes the concentration of hydrogen entering the vacuum system. Furthermore, this initial breakthrough point was determined for multiple helium flow rates, revealing a linear dependence on helium purge flow rate modeled by the equation *(figure 8):*

$$t_D = -171.0\sigma + 146.7 \qquad [2]$$

where helium purge flow rate is σ and deuterium residence time is t_D.

These relationships between helium purge flow rate and deuterium residence time are significant for the cryotrap's implementation. Although deuterium is only a small fraction of naturally occurring hydrogen, there is importance in investigating its properties because the eventual application of the cryotrap will be storing both deuterium and tritium. These equations hypothetically give an estimated timeframe for handlers to set up a uranium bed or the ISS at the end of the cryotrap. After the set amount of time for the helium purge flow rate has elapsed, the

cryotrap will involuntarily release its contents. Therefore, the cryotrap must undergo further

tests using deuterium and tritium.
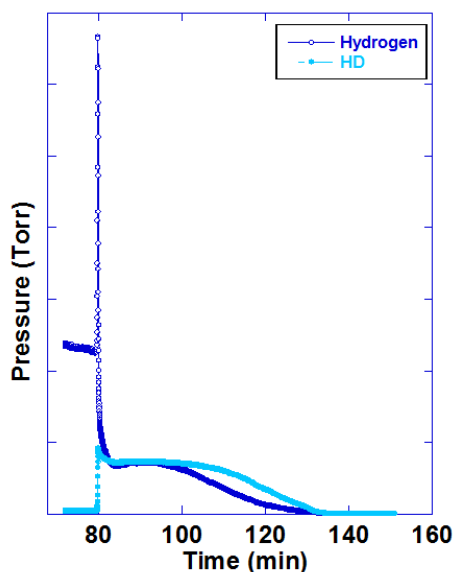
Figure 7. Pressure as a function of time. During the initial breakthrough (the pressure increase at 115.5 minutes), deuterium has a greater presence than hydrogen. Because the RGA is overloaded at high pressures, the pressure appears to decrease at breakthrough when it is actually increasing.
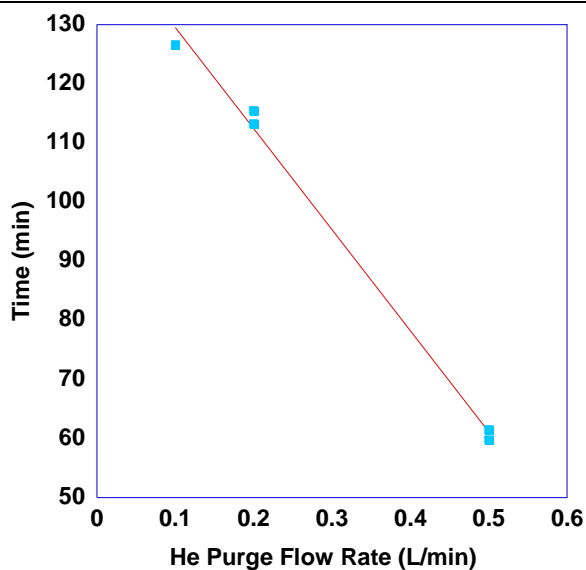
Figure 8. Deuterium residence time as a function of helium purge flow rate. The clearly linear relationship between initial breakthrough time and helium purge rate has an R^2-value of 0.961.

VI. Conclusion

Once the cryotrap was tested at full, its maximum capacity was calculated to be 5.99 sL

of hydrogen, or 58.5 scc hydrogen per gram of molecular sieve. The cryotrap's crushed

molecular sieve capacity can be regenerated after contacting impurities by heating the coil while

simultaneously pushing a pure helium purge through the coil. A *Pd/Ag* membrane can be used to

detect the pressures of hydrogen released from the cryotrap, and the cryotrap can serve as a

concentrator for the loading of tritium onto uranium beds. Furthermore, the cryotrap adsorbs all

hydrogen from the hydrogen-helium stream until breakthrough.

At one-fifth capacity, it was discovered that hydrogen will elute from a cold cryotrap, and there is a logarithmic relationship between the hydrogen residence time and helium purge flow rate. In addition, it was confirmed that the initial release of gas from the cryotrap is composed of deuterium molecules, and there is a linear relationship between this initial breakthrough time and the helium purge flow rate.

Before implementation, further experimentation must be conducted with deuterium and tritium to determine if the cryotrap acts in a similar manner with these isotopes.

VII. Acknowledgements

VIII. References

_____

[1] W. T. Shmayda, "*Technologies for Mitigating Tritium Releases to the Environment,*" LLE Review. **103**, 142 (2005).

[2] F. J. Ackerman, G. J. Koskinas, "*Permeation of Hydrogen and Deuterium Through Palladium-Silver Alloys,*" Journal of Chemical and Engineering Data. **17**, 51 (1972).

[3] S. Goodman, "*Detection of Hydrogen in Helium Streams,*" Laboratory for Laser Energetics High School Summer Research Program (2013).

[4] M. Nishikawa, K. Tanaka, and M. Uetake, "*Mass Transfer Coefficients in Cryosorption of Hydrogen Isotopes on Molecular Sieves or Activated Carbon at 77.4 K,*" Fusion Technology. **28**, 1738 (1995).

Water Collection on a Platinum-Coated Molecular Sieve

Sophia Rogalskyj

Our Lady of Mercy School for Young Women

LLE Advisor: Dr. Walter Shmayda

Laboratory for Laser Energetics

University of Rochester

Summer High School Research Program 2014

December 2014

Abstract

Tritium is a radioactive isotope of hydrogen gas that is used regularly in experiments at the Laboratory for Laser Energetics (LLE). To prevent emissions to the environment, capture and containment of tritium released from process systems is very important. Air detritiation systems oxidize elemental tritium to form tritiated water (HTO), which is then collected on a molecular sieve drier. Tests were conducted to determine whether or not a platinum-coated molecular sieve (Pt/4A MS) loaded with light water (H_2O) could serve as an alternative to the classical 'burn and dry' approach of capturing tritiated water currently employed (1). In these tests, deuterium was used as a surrogate for tritium. Deuterium gas in a helium carrier was converted to heavy water over a hot copper/zinc getter bed (2,3) and flowed over a platinum-coated 4A molecular sieve preloaded with light water. The dependence of the amount of heavy water captured in the molecular sieve on flow rate was measured.

1. Introduction

Currently, at LLE, the tritium removal from Omega and processes that contain tritiated air utilize the conventional "burn and dry" detritiation method (4). This comprises the conversion of elemental tritium to oxide using hot copper oxide, Hopcalite, or a precious metal catalyst (Pd, Pt), a molecular sieve drier and a tritium monitor. Although this system serves its purpose, conversion of HT to water over Hopcalite requires the presence of oxygen. A novel method of detritiation, explored in these experiments, may offer a simpler and more versatile solution. A platinized molecular sieve (Pt/4A MS) preloaded with light water (H_2O) may eliminate the need for an oxidizer and drier. These two options are illustrated in Figure 1. In cases where the water content in the air stream is high, a condenser can be installed in front of the drier to extend the operational lifetime of the drier as shown in Figure 1.

In this experiment, a Pt/4A MS was tested for its ability to remove tritiated water (T_2O) from an air stream with high humidity. The purpose of this experiment was to determine whether or not a Pt/4A MS, preloaded with H_2O, could adsorb a significant amount of T_2O, using D_2O as a surrogate. The efficiency and capacity at different flow rates of deuterium were also tested in the experiments.
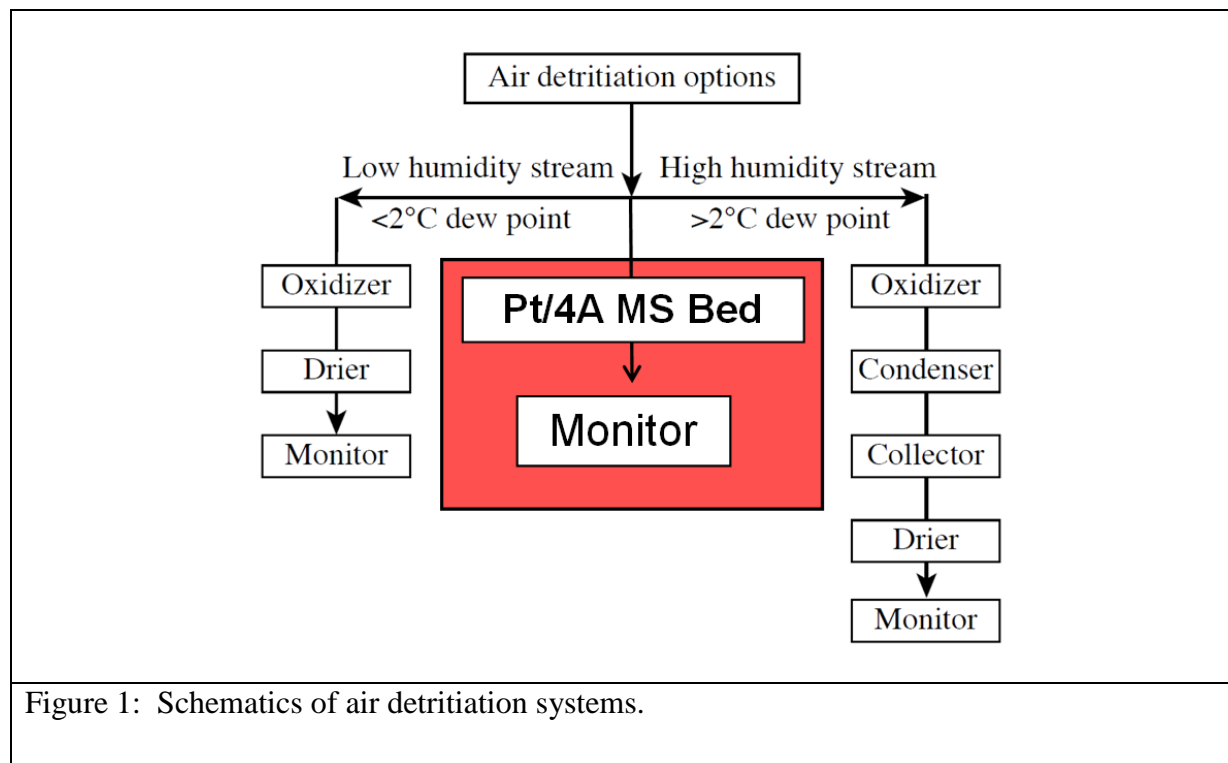
Figure 1: Schematics of air detritiation systems.

2. Experimental

2.1. System Configuration

A system was built to test how much D_2O could be loaded on to a Pt/4A MS, preloaded with H_2O. The system is organized into three sections: D_2O production, isotopic exchange, and hydrogen/deuterium detection. As seen in Figure 2, there are four gas cylinders containing He, 1% O_2 in He, D_2, and compressed air. The gases, whose flow rates are controlled by mass flow controllers (MFC), are flowed either through a bed or through a bypass. The gases are monitored

downstream of both beds by the atmospheric sampling system, including a diaphragm pump, a

turbomolecular pump, and a residual gas analyzer (RGA). An RGA measures the partial

pressures of gases in the system. The nitrogen partial pressure was measured to ensure that no

air leaked into the system during loading of the Cu/Zn getter bed. The total pressure could also

be measured. A dew point sensor measured the humidity of the compressed air being flowed

into the system. Thermocouples were used to control the temperatures of the Cu/Zn getter bed,

the Pt/4A MS bed, and the heating tape used around the capillary tubing as well as select areas of

piping. Capillary tubing connects the system with the RGA/ Atmospheric Sampling System and

allows sampling during the experiments.

Figure 2: Schematic of experimental system. Capillary tubing is represented with the bolded, squiggly line.
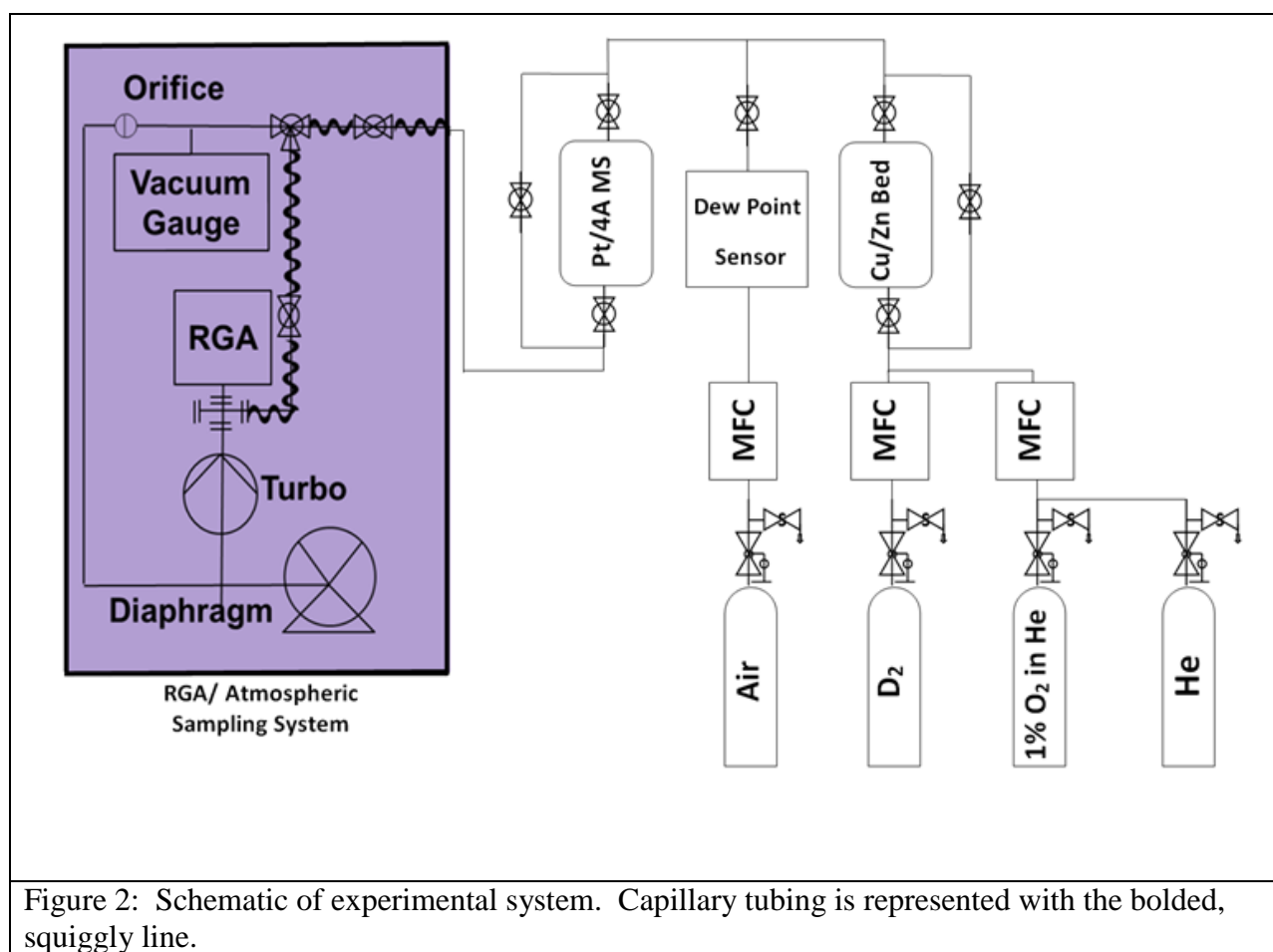
2.2. Experimental Procedure:

2.2.1 Formation of D_2O:

The Cu/Zn getter bed was heated to $200^{\circ}C$, and 1% O_2 in He was flowed at 5 LPM (liters per minute) through the bed. The Pt/4A MS bed was bypassed such that no oxygen flowed through it. Once filled to capacity, the getter bed was bypassed, and He was flowed at 5 LPM to purge the system. Once the system was purged, the Cu/Zn getter bed was re-opened and D_2 was flowed through it at 50 sccm (standard cubic centimeters per minute). As seen in Figure 3, a stream of D_2O was produced for approximately 500 minutes before D_2O production began to decrease. This occurred when the oxidized Cu/Zn was reduced to elemental Cu/Zn and no more O_2 was available. Because the stream of D_2O was not continuous over a long period of time, this method of D_2O production was referred to as the "limited production method".

Figure 3: H_2, H_2O, and D_2O partial pressures as functions of time when D_2 was flowed at 50 sccm through a Cu/Zn getter bed loaded with O_2. The Cu/Zn bed was heated at $200^{\circ}C$.
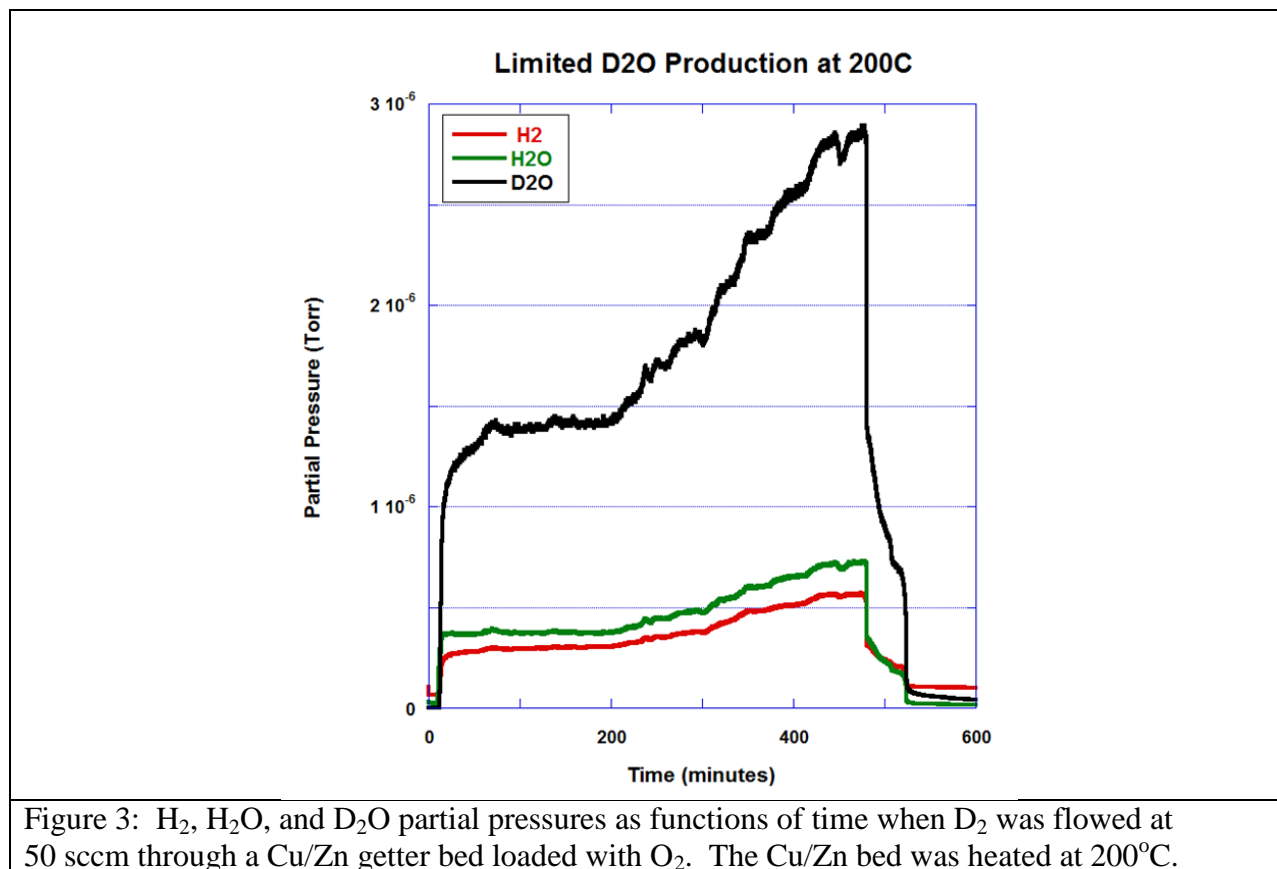
It was found that this method of D_2O production would not suffice for full runs, a full run meaning an experiment where D_2O is flowed through a Pt/4A MS bed preloaded with H_2O until complete D_2O breakthrough occurs from the Pt/4A MS bed without running out of D_2O on the Cu/Zn bed. Instead, it was determined that a constant stream of D_2O would be necessary. To produce a constant, unlimited flow of D_2O, D_2 and 1% O_2 in He were co-injected into the system through the Cu/Zn getter bed, which was preloaded to capacity with O_2. D_2 was flowed at 100 sccm and 1% O_2 was flowed at 5 LPM. This method, referred to as the "continuous production method," proved to be successful. As seen in Figure 4, a stable D_2O stream leaving the bed approaches a steady state level after approximately 300 minutes.

Figure 4: Partial pressures of D_2O and O_2 as functions of time when D_2 and O_2 were simultaneously flowed through the Cu/Zn getter bed. D_2 was flowed at 100 sccm. O_2 was flowed at 5 LPM. The Cu/Zn getter bed was preloaded with O_2 and kept at 200^oC.
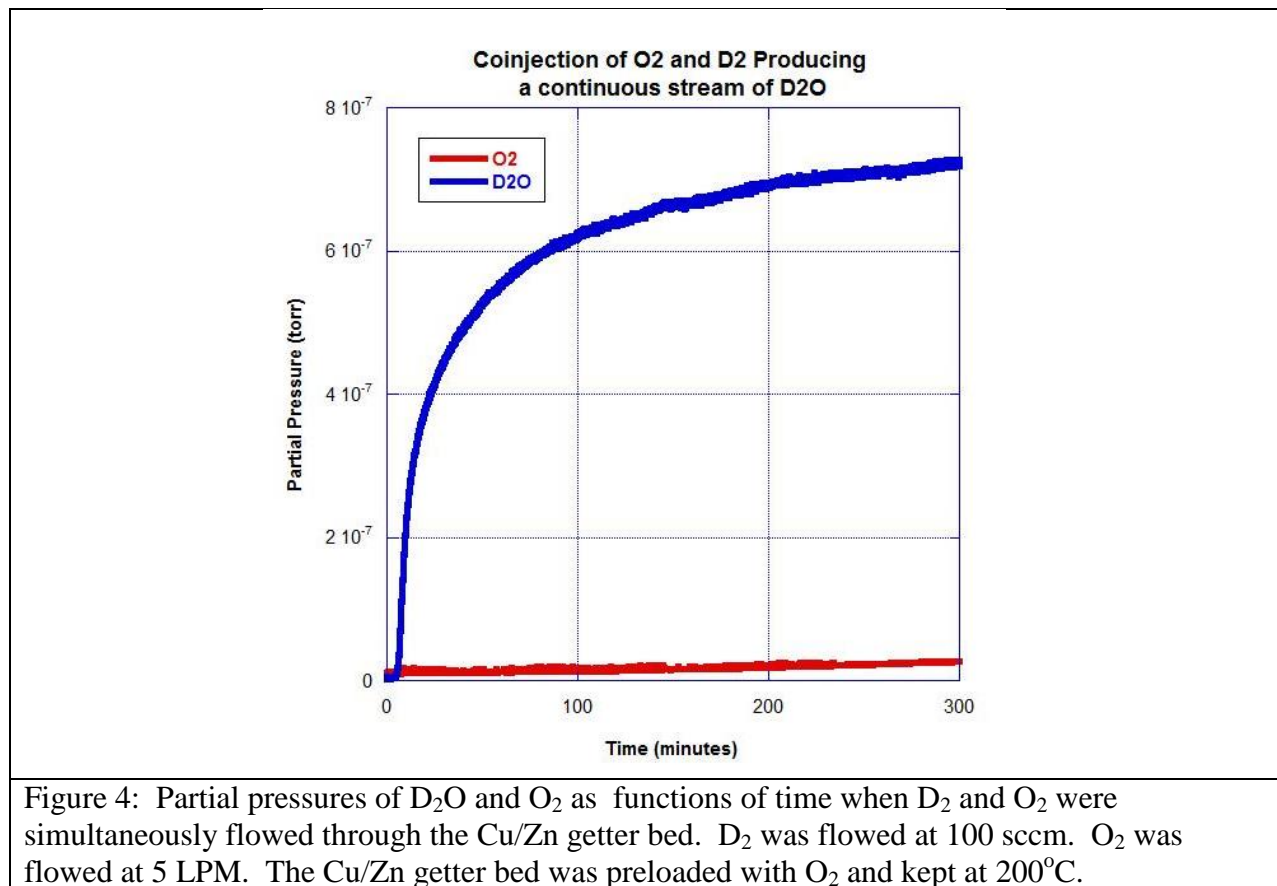
2.2.2 Loading Pt/4A MS with H_2O:

To prepare the Pt/4A MS for operation in humid air streams, the Pt/4A MS bed was pre-loaded with H_2O. This medium was chosen because of its ability to capture H_2O. The interatomic space between the neighbor cages of the molecular sieve is four-angstrom. Four angstrom molecular sieves have the ability to adsorb H_2O without altering its chemical composition, allowing it to extract H_2O from flowing gas streams. When loading the Pt/ 4A MS with H_2O, the Cu/Zn getter bed was valved so as to isolate the Cu/Zn getter from the H_2O. Initially, compressed air was flowed at 1 LPM, such that a 100% air flow pressure was recorded for later comparison. The air flow was turned off, and He was flowed at 1 LPM to purge the system. The Pt/4A MS bed was opened, still only flowing He at 1 LPM. Once air levels were back down to background levels, the He flow was stopped and the air flow was turned on at 1 LPM.

2.2.3 Full Experiment:

Once the system was set up for a full experiment (i.e. the Cu/Zn bed was loaded to capacity with O_2 and the Pt/4A MS was loaded with H_2O), co-injection of D_2 and 1% O_2 in He began through the Cu/Zn getter bed which was preheated to 200^oC . Once a stable maximum reading of D_2O production was recorded, the Pt/4A MS bed was opened and its bypass closed. Full runs were performed at three different flow rates of D_2. After a full run was completed, the system was purged and reset. To purge the system, the Pt/4A MS was heated to 150^oC, and He was flowed through it at 2 LPM. After 120 minutes, the temperature of the Pt/4A MS was increased to 200^oC.

3. Results:

The results of one run using the limited production method are shown in Figure 5. The results show that D_2O can, indeed, be stored on the loaded Pt/4A MS, and that the Pt/4A MS is capable of adsorbing significant amounts of D_2O. The amount of D_2O is comparable to the amount of H_2O that can be stored. Prior to a full test, approximately 8g H_2O /gMS was loaded onto the Pt/4A MS. When D_2O was flowed through the pre-loaded Pt/4A MS using the limited production method, approximately 5g of additional D_2O/g MS was loaded onto the Pt/4A MS.
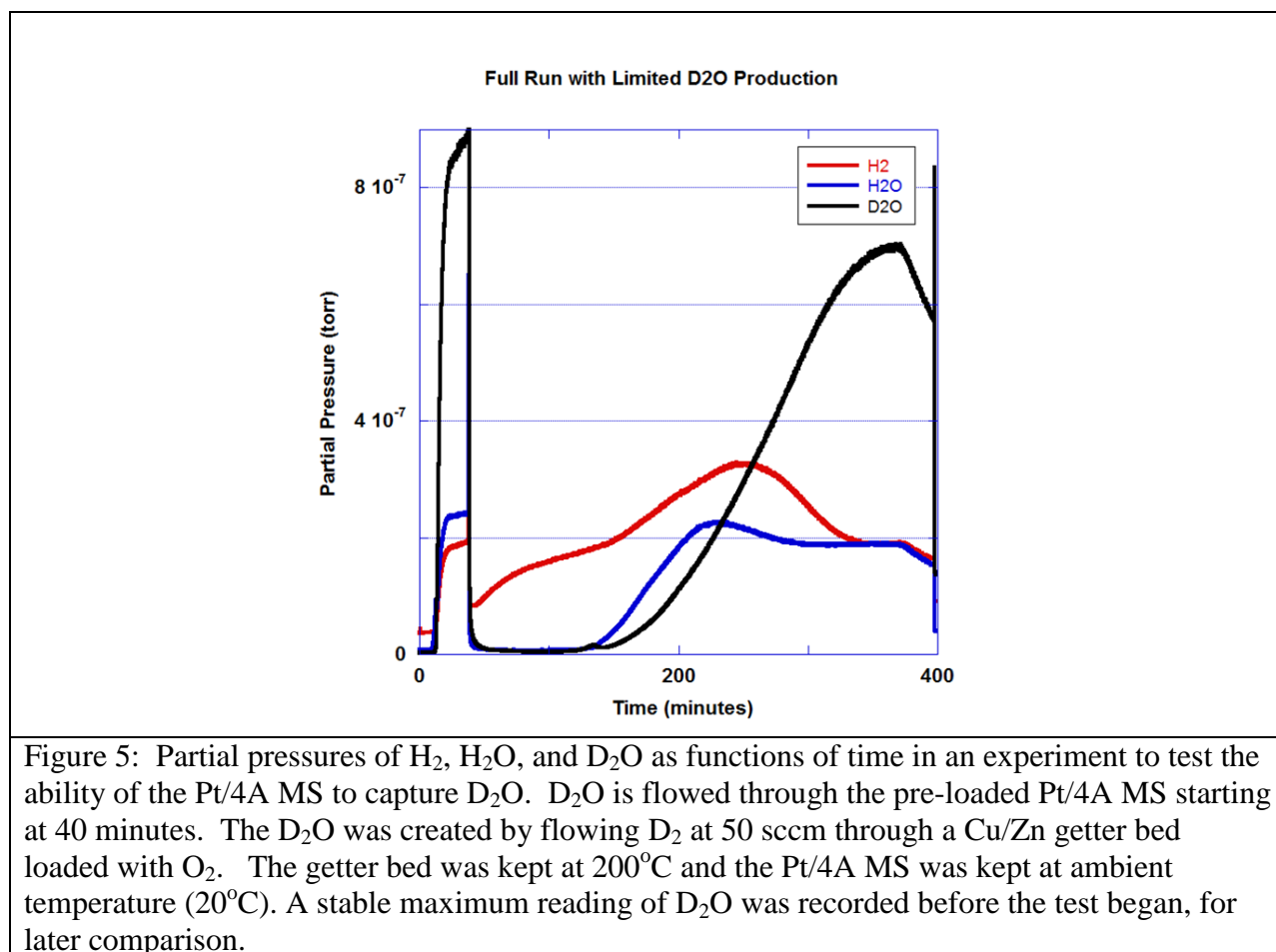
Figure 5: Partial pressures of H_2, H_2O, and D_2O as functions of time in an experiment to test the ability of the Pt/4A MS to capture D_2O. D_2O is flowed through the pre-loaded Pt/4A MS starting at 40 minutes. The D_2O was created by flowing D_2 at 50 sccm through a Cu/Zn getter bed loaded with O_2. The getter bed was kept at 200^oC and the Pt/4A MS was kept at ambient temperature (20^oC). A stable maximum reading of D_2O was recorded before the test began, for later comparison.
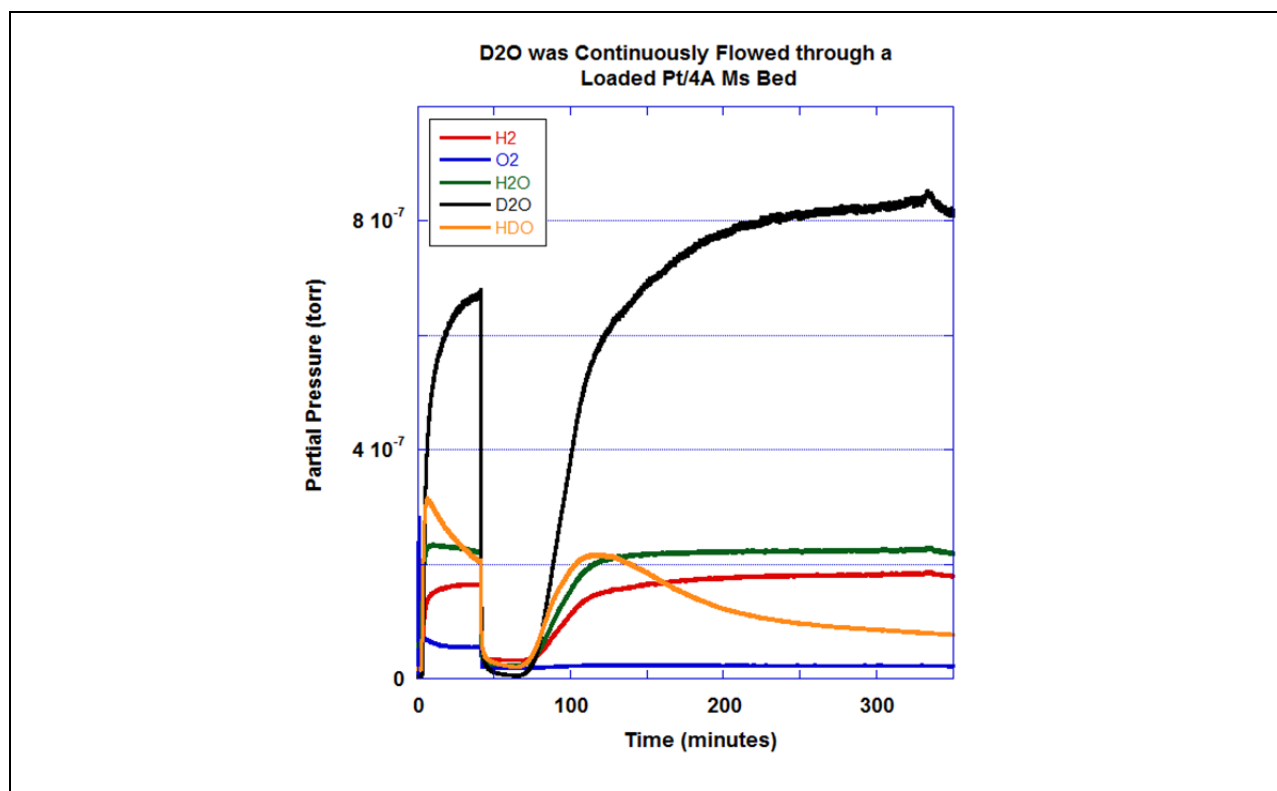
Figure 6: Partial pressures of H_2, O_2, H_2O, D_2O, and HDO as a function of time for an experiment similar to that of Figure 5 except that 1% O_2 in He was also flowed through the Cu/Zn getter bed. D_2 was flowed at 100 sccm. O_2 was flowed at 5 LPM. At 40 minutes, the Pt/4A MS was opened and D_2O was allowed to flow through the Pt/4A MS.

High capture efficiencies were realized at superficial flow rates up to 11 scc/min/cm^2. In Figure 6, D_2 was co-injected with 1% O_2 in He at the respective rates of 100 sccm and 5 LPM. For 27 minutes, no D_2O was recorded in the outlet stream, indicating that all D_2O being produced was being absorbed by the Pt/4A MS. 27 minutes into the experiment, however, breakthrough occurred. Breakthrough refers to the time at which the concentration of D_2O in the outlet stream reaches 1% of the value when the bed is bypassed, or, in this case, 2.31×10^{-9} torr. For the remainder of the experiment, the Pt/4A MS's ability to absorb D_2O decreased until the maximum reading in the outlet stream was reached.
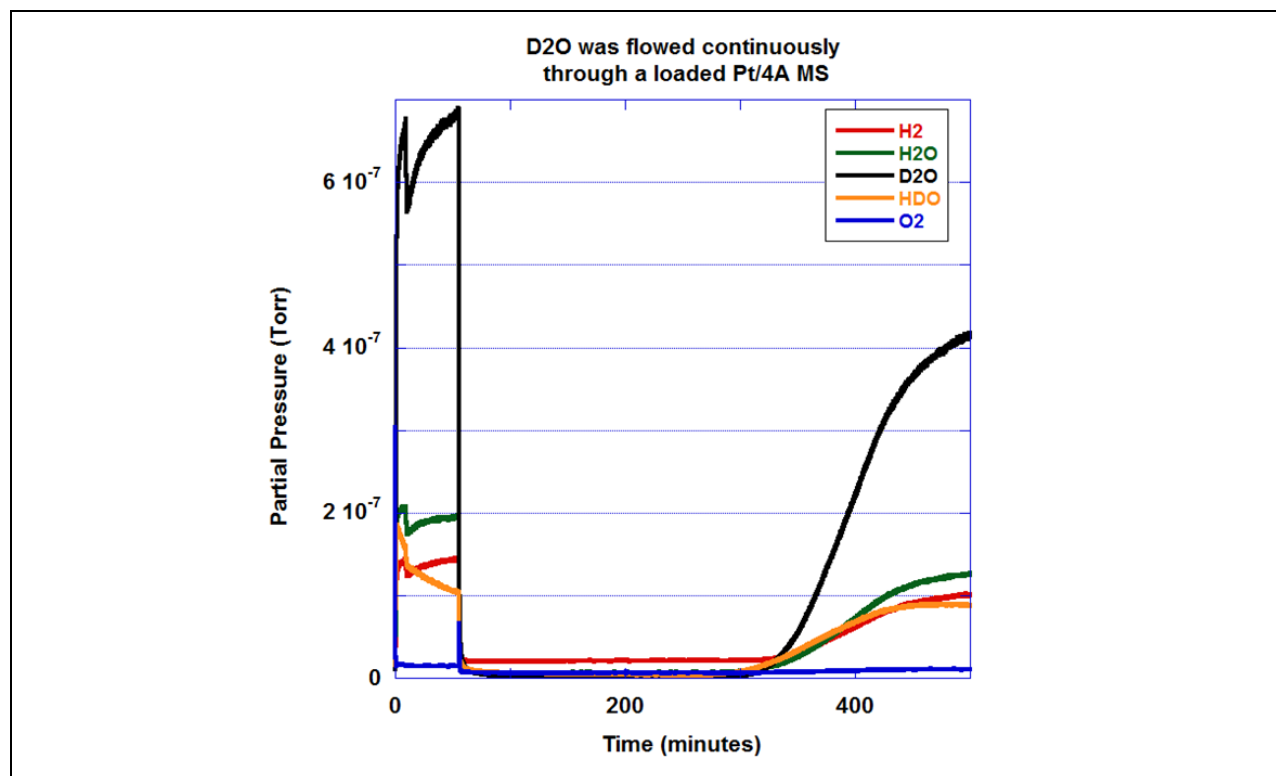
Figure 7:   Partial pressures of H_2, O_2, H_2O, D_2O, and HDO as a function of time for an experiment similar to that of Figure 6 but with lower D_2 and O_2 flow rates. D_2 was flowed at 20 sccm. O_2 was flowed at 1 LPM. At 40 minutes, the Pt/4A MS was opened and D_2O was allowed to flow through.

As shown in Figure 7, the same experiment was performed with D_2 flowing at a lower rate of 20 sccm, and 1% O_2 in He flowing at a rate of 1 LPM.   In this experiment, breakthrough occurred 260 minutes into the experiment.   The mass of D_2O loaded onto the Pt/4A MS is shown in Table 1. Reducing the D_2O residence time in the Pt/4A MS by a factor of 5 increases the storage capacity approximately two fold, even though the Pt/4A MS has been preloaded with H_2O to capacity.

Flow Rate of D_2O (sccm)	Mass of D_2O Loaded onto Pt/4A MS (gD_2O/gMS)
20	2.4
100	4.7

Table 1: Total mass of D_2O loaded onto Pt/4A MS for runs at both D_2O flow rates of 20 sccm and 100 sccm.

Conclusions

Experiments were performed to determine whether a Pt/4A MS could serve as a novel and alternative method to the conventional "burn and dry" method for tritium extraction from a humid air stream. Tests were completed by flowing D_2O through a Pt/4A MS preloaded with H_2O, to simulate the humid air stream. Superficial flow rates were realized up to 11 scc/min/cm^2. Results indicate that the Pt/4A MS has the capability of capturing up to 4.7g/g MS of D_2O on a bed preloaded to capacity with H_2O. These tests suggest that a simpler, more versatile technique of tritium capture and recovery can be implemented at LLE by preferential extractions of HTO from humid airstreams.

Acknowledgements

I would like to thank Dr. Craxton for giving me the opportunity to be part of the internship program, as it has been an eye-opening and invaluable experience. I would also like to thank my advisor, Dr. Shmayda, for the guidance and advice he has shared with me over the course of the program. Finally, I would like to thank my lab partners, Krishna Patel, Ian Gabalski, Sam Goodman, Sara Gnolek, and all of the other high school interns for their encouragement, help, and enthusiasm.

References

1. "Technologies for Mitigating Tritium Release to the Environment," LLE Review **103**, pp. 142-154 (2005).

2. MaryKate Hanchett, "Oxygen Uptake Using a Nickel Catalyst," Laboratory for Laser Energetics Summer High School Research Program (2012).

3. Sara Gnolek, "Catalytic Oxidation of Hydrogen in Air Streams." Laboratory for Laser Energetics Summer High School Research Program (2013).

4. W.T. Shmayda et al., "Tritium Operations at the Laboratory for Laser Energetics," Fusion Sci. Technol. **49**, pp. 851-856 (2006).

Evaluation of a Collaborative Networking Environment for Experimental Configurations

Liam Smith

Webster Schroeder High School

Webster, NY

Advisor: Richard Kidder

1. Abstract

A three-dimensional model of the OMEGA Target Chamber that was developed for web-based services to emulate interaction with large-scale laser facilities, specifically the OMEGA laser facility, has been improved upon to incorporate more collaborative options for the users. This design was created with the purpose of allowing users of the OMEGA laser system to collaborate in an interactive and visually intuitive environment to set up experimental configurations. Work has been done to increase the network collaborative capabilities of the web-based service to include tools that allow users to directly interact with one another in a real-time situation. Users can interact with the Target Chamber, by toggling diagnostics and Ten-Inch Manipulators. Users can also interact with other online users by sending messages or even watching the actions of another user in real-time. The three-dimensional virtual model of the OMEGA Target Chamber was expanded upon for use as an interactive platform for configuration creation and display as an alternative to the traditional text-based proposal tools.

2. Introduction

At the Laboratory for Laser Energetics (LLE) research proposals and setups are designed to be used for testing on the OMEGA laser system. Currently, scientists use a text-based method of campaign management and design proposal. This poses a few problems: first, the users cannot easily access information relevant to the laser system or current setup or quickly communicate with each other and relevant specialists, and second, the researchers can't easily and visually view the current setups to evaluate additional options. Additionally, researchers from facilities other than LLE who wish to use the laser facility for their own purposes have to use a system that isn't

the most user friendly. To help solve these problems, a sophisticated three-dimensional (3D) diagnostic, a laser semantic model of the 60-beam OMEGA laser system, has been created[1] and developed since. It aims to provide a straightforward and easier way to set up and communicate work and projects that use the laser system. This program's functionality isn't just in the third dimension; it has many visually hidden aspects that make up the heart of the program. In addition to showing what the laser system looks like, the program can relate information from projects and setups to a user's preference. Users can therefore work on experimental setups by viewing and adjusting settings for diagnostics, the target chamber's tools for data gathering and analysis [Figure 1]. This program, named SILICON (simulation of laser operations through collaborative networking), has been improved upon to work better with the collaborative aspects of shot design and discussion.
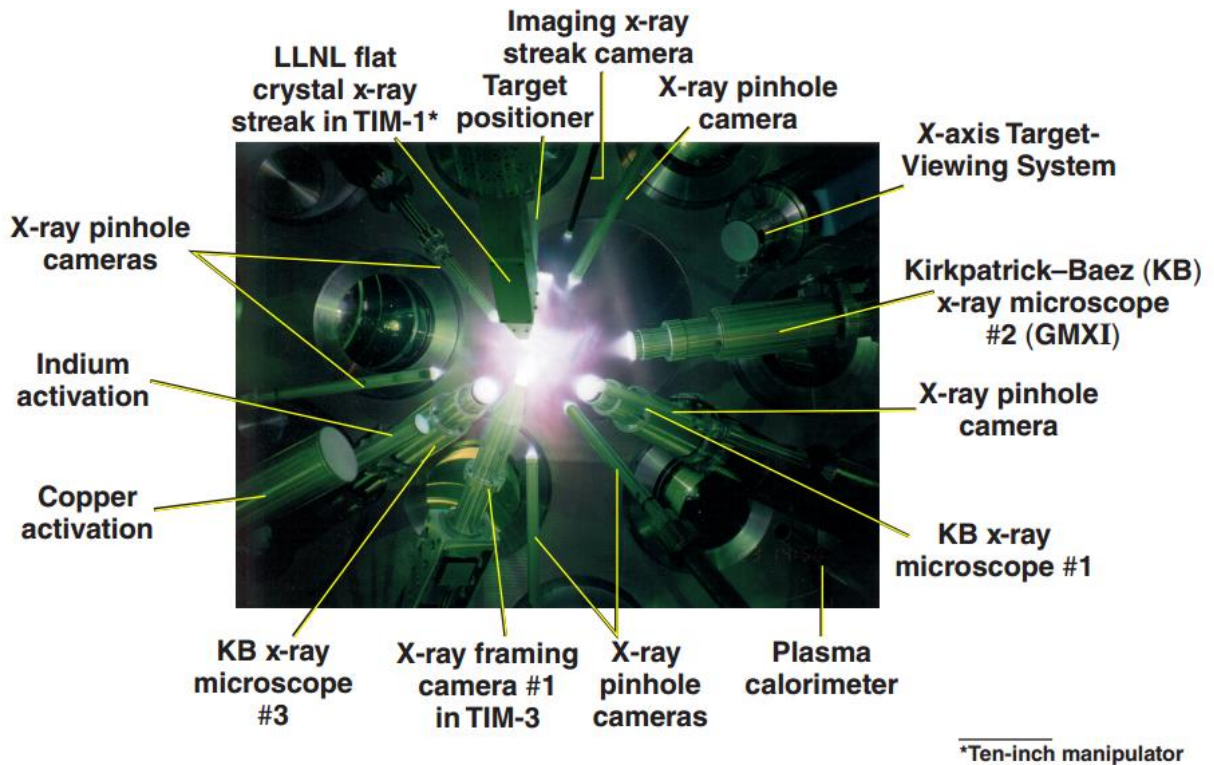
Figure 1: Typical selection of diagnostics on the 60-beam OMEGA target chamber. The target chamber also uses Ten-Inch Manipulators (TIMs), which allow for the insertion of a variety of different diagnostics in the vacuum chamber that are specific to certain shots and research aims.

3. SILICON

The interactive model of the target chamber has been created using JavaScript APIs (application program interfaces) including WebGL and three.js. These allow the rendering of 3D graphics, specifically interactive ones, in common internet browsers. This allows the creation of a more user-friendly program that doesn't require installation or setup by the user while remaining freely expandable. Since WebGL is based on OpenGL, which is a cross-platform API that implements shaders to generate 3D graphics, better looking and performing 3D environments can be created for the program.[2] WebGL differs from Canvas (another browser-based renderer) in that it is more focused on and optimized for 3D rendering instead of 2D rendering.

The usage of an ontology also allows for an expanded range of possible features. An ontology is essentially a web of data that is based on the properties of and relationships between objects. An ontology uses subjects and predicates, which are the objects and the links between them[3] [Figure 2]. Because an ontology can relate many properties together, this web-like data can be used to
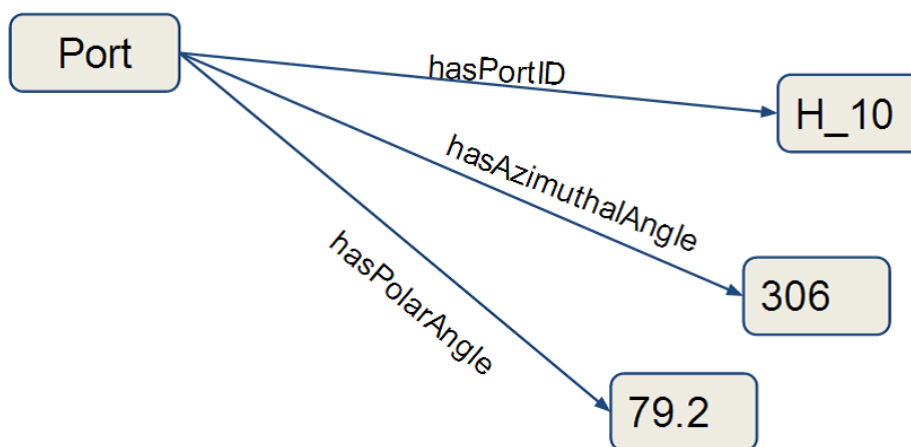
Figure 2: Illustration of how data is linked in an ontology by properties. Relationships are represented by the subject and predicate system. Shown here, the "Port" object has three properties: hasPortID, hasAzimuthalAngle, and hasPolarAngle. These properties contain values which can be used by the program to render, process, or obtain information.

infer relationships to gather relevant data more easily. Inferencing can be done based on a set of predefined rules; in SILICON's ontology OWL rules (the standards of languages for ontology mapping) are used. For example, the identification of a user could be used to find his or her relevant campaigns and the research proposals associated with them, which, in turn, could be used to find the specifics of that setup and other people who are either associated with it or that person (who could then be used to access more setups, and so on).

4. Node.js

Since the target chamber model had to be able to support multiple users connected at the same time with communication between both other users and the program itself, Node.js was selected as the base for the collaborative aspects. Node.js is an event-driven JavaScript API that has included extension support. It was selected because it is able to process
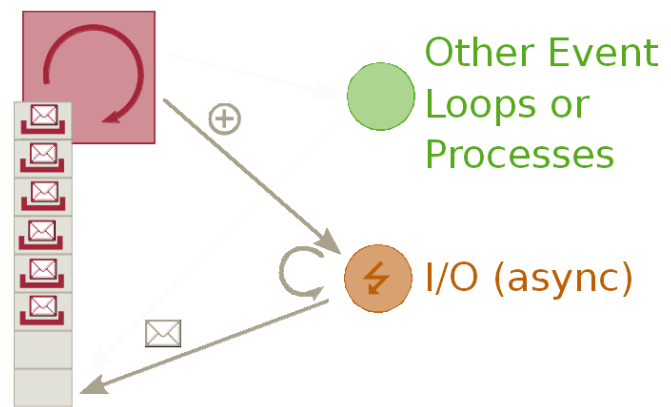
Figure 3: Visual example of how Node.js operates with an event loop. This allows inputs and output to be processed separately from the rest of execution while still allowing other processes to be dealt with.
Source: http://bert.github.io/

multiple inputs simultaneously and separately from each other in a way that allows for unrestricted communication (that is, without causing the inputs to impede the function of other inputs both from the same user and others) and future expandability. Node.js was also selected because it is based on JavaScript, which was what much of the program was written in, allowing for an easier integration with the existing code. Node.js is event-driven [Figure 3], which means

that when an input is received it is processed separately from the rest of the code execution, which allows for decreased hang-up in requests from multiple sources and also allows those same requests to be processed more quickly. Node.js also has its own built-in extension support so, since it is already part of the community of JavaScript APIs, it has a large range of future possibilities.[4] Of Node.js's many extensions, socket.io was chosen as the main network interface for Node.js, which, using Node.js's event-driven approach, allows for a real-time communication to be set up between multiple clients and a server. Using both Node.js and socket.io, the program was modified to allow real-time communication and collaboration so users could both chat with each other and view, load, and modify configurations.

5. Capabilities

The creation of a program such as SILICON requires certain capabilities to be met, such as an easy to use interface and the ability to view configurations. The configuration information is retrieved for each user, so someone can easily log in and see the current available projects that he or she is associated with. The interactive model has been constructed so that users can interact with campaigns and the selected diagnostics, as well as the current beam layouts [Figure 4]. The ability to visualize the beam layouts of the current configuration is
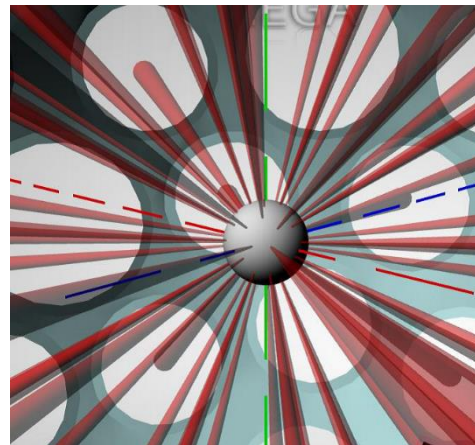
Figure 4: Laser beam pointings seen focused on a center target, which allows for users to more easily see and predict how the target will be hit by the lasers and how it may react.

one of the core functionalities in SILICON, providing users with visual feedback before

extensive testing is done. This allows researchers to visualize their setups and is intended to

assist in the reviewing of those setups before shots are done on the laser system itself. The

diagnostics that are selected for use and the ports of the target chamber are also noted in the

program so users can see which ones are used in the current configuration [Figure 5]. This can

help them see where a diagnostic will be pointing on a target, especially with the usage of the

three dimensional models of the diagnostics and other instrumentation associated with the OMEGA laser system. The application also provides a way for users to modify the current setup, allowing for the toggling of active
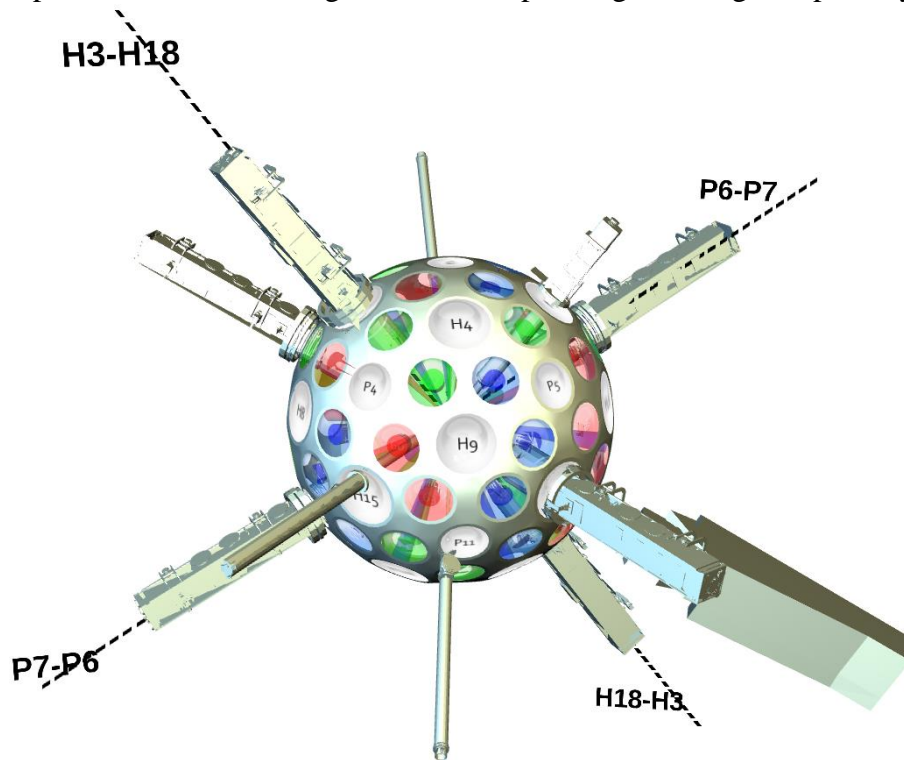
Figure 5: Sample view of SILICON. The 3D models of the target chamber and the diagnostics allow the visualization of the ones that are active and where they are pointing. The ports of both the diagnostics and lasers are labeled (although in this figure, the laser ports have been set transparent, which is another feature available to researchers using the program).

diagnostics on and off [Figure 6]. In addition, a chat interface has been provided to allow people

who are working together on the same setup to discuss options for the configuration of shots

while looking at the setup itself. This chat feature also allows for users to view the temporary, or

unsaved, setups of other users on the same configuration before decisions are made for the final

setup or to specify a certain area or subject, since the viewers can also see the current camera location and other aesthetic options in the application of the person being viewed.

6. Future Plans

Because of the need to have an easier to use configuration creation tool, the 60-beam OMEGA laser target chamber model has been developed. The program is planned to be used alongside, and eventually instead of, the current system of campaign creation and modification [Figure 7]. Work is also planned to fully integrate the program with the ontology database of configuration data so that it will become a useful tool for people who wish to use the OMEGA laser facility. The program will be able to load and save temporary files, that is, setups that a user creates before a version is finalized and then used for research. It is intended for this program to provide visual feedback and

Figure 6: The current user interface of SILICON. The program allows users to turn diagnostics on and off as well as make aesthetic changes that make it easier to see parts of the target chamber. Additional options are available to allow users to select setups and chat with others.

collaboration between users so that experiments can be set up more quickly in an easier and more user-friendly manner. The program also aims to provide an easy method of communication between instrument specialists (people who work with certain diagnostics or the laser system in general) and those who use the OMEGA system for research.

Figure 7: Currently, text-based shot request forms (SRFs) are used to set up or create plans for shots on the OMEGA laser system.

7. Conclusion

Work has been done on the 3D interactive model of the 60-beam OMEGA target chamber to create a better collaborative work environment at LLE. Visual interfaces with collaborative tools, like the one discussed here, are very helpful for researchers because they provide a research-oriented and specialized approach with an easy to use structure. This interactive model has multiple advantages when compared to the typical text-based forms of setup and data manipulation. The interactive environment developed further by this work increases the collaborative opportunities provided. SILICON is now able to establish and process both peer-to-peer and peer-to-server network connections for real-time communication. This allows the program to have both direct communication between users, such as messaging through a chat system, and data transfer between a central entity and the users, such as configuration retrieval. Additionally, SILICON's new collaborative networking capabilities have

been designed as a base for future network communication of varying degrees. This means that it has been set up so that new types of information can be sent through pre-established connections by using existing code. This research demonstrates not only a simpler and more efficient way of OMEGA shot planning and coordination but also a more accurate and informed one, as it aims to provide communication between instrument specialists and those who may be new to the OMEGA system.

6. Acknowledgements

7. References

1. Michael Hartman, "Emulating Laser Facility Operations Through a Real-Time Collaborative Network." Laboratory for Laser Energetics High School Summer Research Program (2013).
2. "Semantic Web - W3C." W3C. Web. Jan. 2015.
   http://www.w3.org/standards/semanticweb/
3. "OpenGL ES 2.0 for the Web." Khronos Group. Web. Jan. 2015.
   https://www.khronos.org/webgl/
4. "Node.js." Joyent Inc. Web. Jan. 2015.
   http://nodejs.org/

Creating an Open Source LLE-based Ethernet to LonTalk adapter

Jeremy Weed

Victor Senior High School

LLE Advisors: Dave Hassett, Robert Peck, Dustin Axman

1. Abstract

The OMEGA Laser System is currently controlled by a LonWorks distributed control system that includes over 1,600 Neuron 3150 chips running at 10 MHz. Communicating on more than 20 twisted pair channels, the Neurons control over 3,000 A/D channels, 2,000 DC servo motors and 4,000 digital I/O channels. All communications entering or exiting the network travel through LENA servers across an RS-232 serial bus to a Serial to LonTalk adapter and onto the LonTalk network. Creating a direct Ethernet to LonTalk adapter would allow for the retirement of the LENA computers used, provide physical connections to the LonTalk network, allow the servers to reside on virtual machines, and minimize any errors caused by high traffic volumes through the current RS-232 interface. Using a Netburner board and a Neuron card, a proof-of-concept Ethernet to LonTalk adapter was attempted. Using Neuron-to-Neuron network variables, data communication from the current firmware to an updated system was demonstrated. However, SPI data communication between the Netburner and Neuron was not achieved due to hardware limitations, so different protocols will be explored.

2. Introduction

The OMEGA Laser System currently operates over 10,000 control and acquisition points, consisting of over 3,000 A/D Channels, 2,000 DC servo motors and 4,000 digital I/O channels. A LonWorks distributed control system operates these points, and allows them to communicate across the network. The system consists of more than 1,600 Neuron 3150 chips, running at 10 MHz and communicating on over 20 twisted pair channels. To enter the LonWorks control network, data must travel through LENA servers and then across an RS-232 serial bus to a Serial

to LonTalk adapter, which then propagates the data across the LonWorks network, as shown in figure 1.

Fig 1. Diagram of current LonTalk network system.
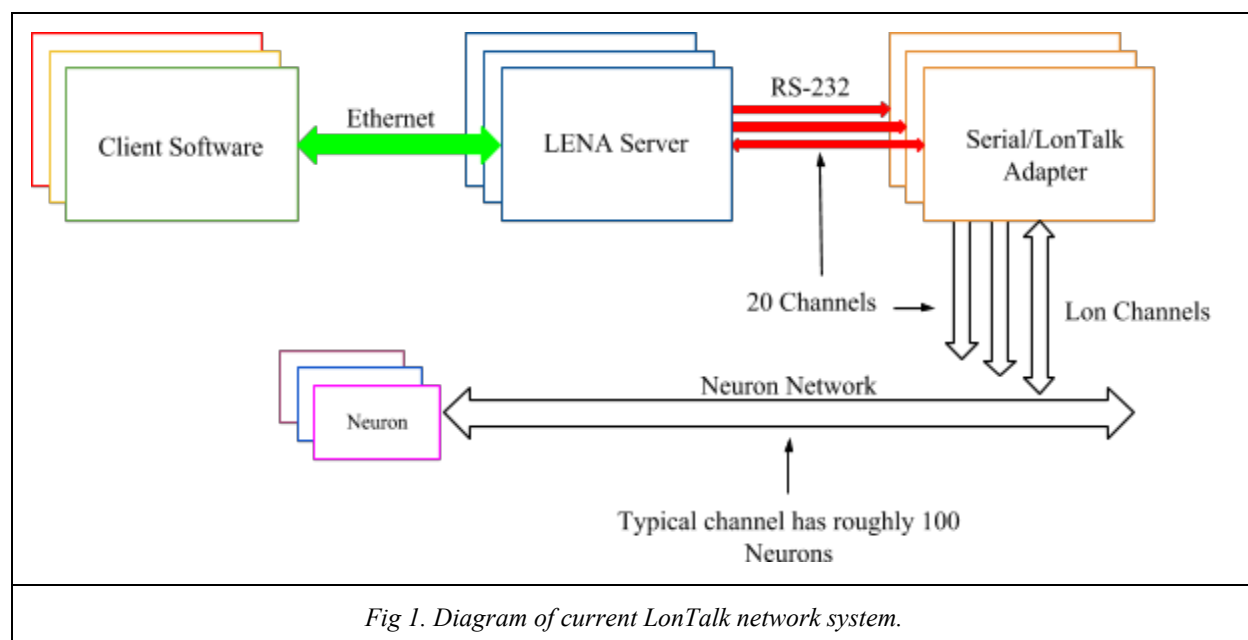
Each Neuron on the network, commonly referred to as a node, communicates to other nodes using the LonTalk communication protocol. The LonTalk protocol was designed for building automation and industrial control, and it allows the various nodes on the network to communicate in a decentralized fashion. Neuron chips can be programmed in Neuron C, an event-driven ANSI C based language that allows automated variable communication and synchronization using the LonTalk protocol. Neuron C allows for multiple modes of communication between nodes, anywhere from explicitly created and propagated messages to autonomously propagated network variables.

The current LonTalk control system on the OMEGA Laser has hardware limitations that can lead to data bottlenecks. To pass from the LonTalk system to external clients, the data must pass through one of twenty RS-232 serial connections. The RS-232 serial bus on the system can

currently transmit data at about 38,400 bits per second, much slower than the over 100 million bits per second transfer rate possible on current Ethernet systems. Data from the system and commands going to the control cards can become "backed up" at the RS-232 serial bus, causing data to be either lost or delayed.

3. Setup

The original proposed solution to the data bottlenecks in the LonTalk system involved the use of a Netburner web server to create the messages that would then be propagated across the LonTalk network, shown in figure 2. This would eliminate the existing bottleneck in the system, but would require all data going across the network to be translated by Netburner to a form that the Neuron cards could understand, and would require that the Netburner translate all data coming out of the network. There is currently no software written for a Netburner to interpret LonTalk communication, and with the multitude of ways the Neuron cards communicate over the LonTalk network, extensive work would be necessary to create a working prototype.

Fig 2. Diagram of Original Proposed Solution
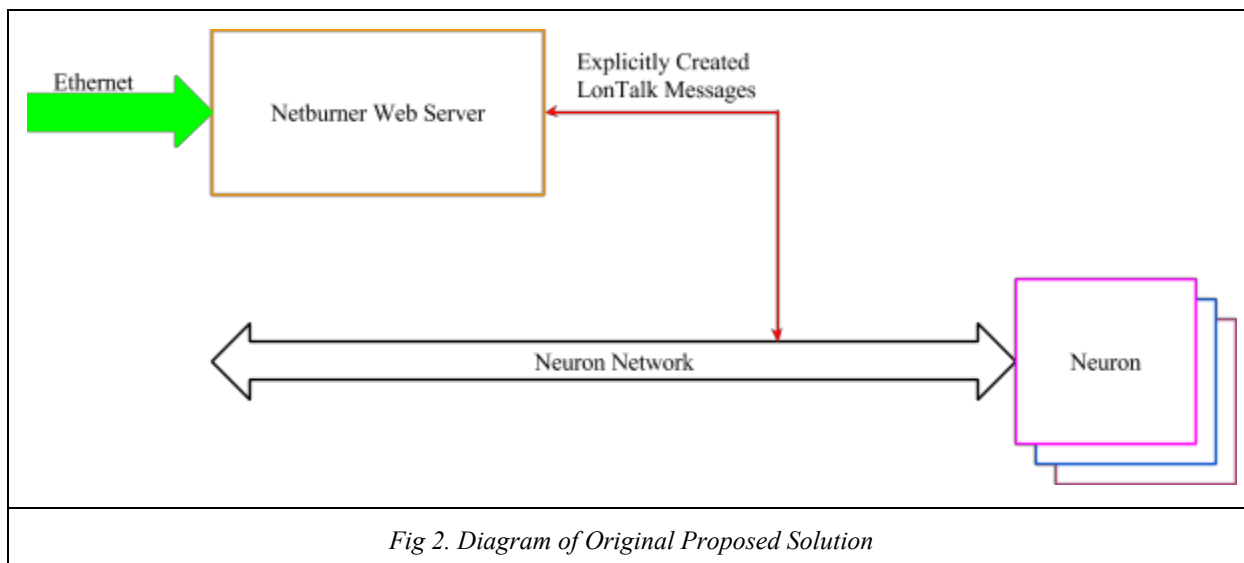
As a result of these challenges, other solutions were explored. The use of a Neuron card to translate messages to and from the LonTalk network was proposed. The Neuron C language, used to program the Neuron chips, includes implicit handling of all communication across the LonTalk network and would allow for simple and easy translation between the Ethernet and LonTalk networks. Neuron cards cannot interpret data from the Ethernet network, so it was proposed that a Netburner web server be used to collect and send data over Ethernet. This setup requires the data going between the two networks be transferred between the Netburner and Neuron card, so a data communication protocol had to be chosen to facilitate the transmission. SPI, or serial peripheral interface, was chosen as the protocol for transmission between the Neuron and Netburner. SPI was chosen because both devices support the protocol, and SPI data transfer is relatively easy to implement in a short amount of time. The final testing setup can seen in figure 3.

Fig 3. Diagram of Final Testing Setup
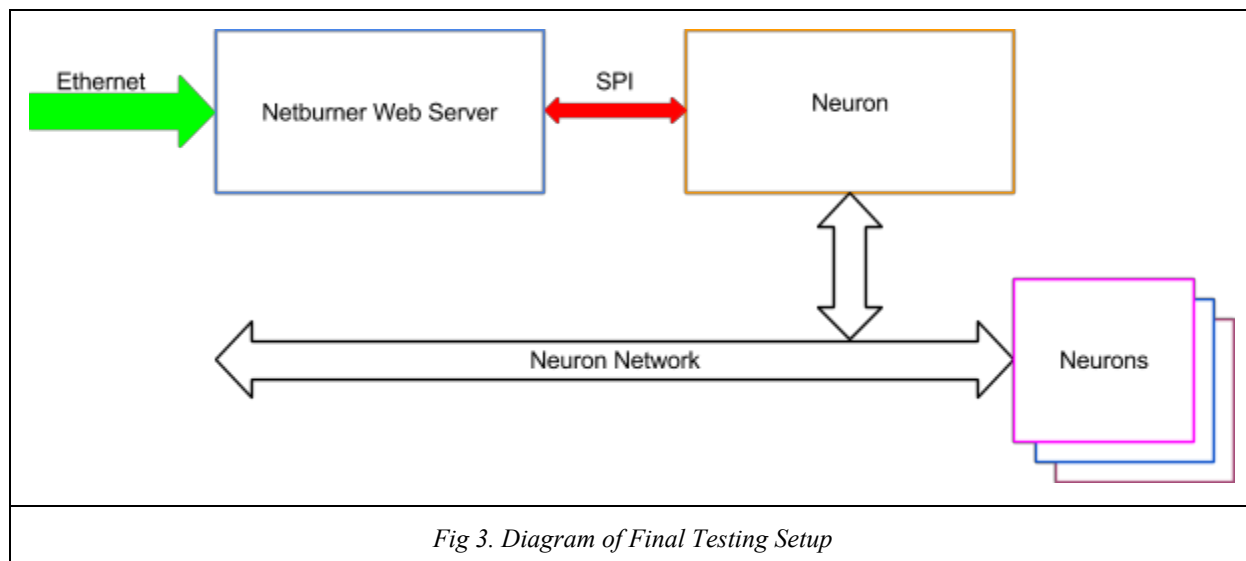
4. Data Communication

There are multiple ways to transmit information over the LonTalk network. Two different methods were explored, explicit messages and network variables. Both forms of communication require a form of binding between the recipient and the sender. Explicit messages can be bound in code, but it is recommended that network variables be bound with an external tool, such as the LonMaker Integration Tool.[1] For this reason, explicit messages were explored first for LonTalk data communication. Although easier to implement, explicit messages are not autonomously propagated like network variables and are more resource intensive.

Explicit messages were sent between two different Neuron cards in a test setup. Before sending the message, the destination must be bound. First, the type of message must be defined (i.e., is it domain-wide or directed for one specific node) and then the destination for the message is defined. For subnet-node type addressing, which was used in this demonstration, the domain, subnet, and node location of the message recipient must be defined. An example of a subnet-node addressed message can be found in figure 4. Further exploration of explicit messages in Neuron C showed that messages could request responses, and respond directly to messages received without defining a recipient explicitly. Neuron C also provides the ability to check whether a message has been received. Both of these abilities were successfully demonstrated.

```
                    msg_out.tag = test_message;
                    msg_out.data[0] = 0;
                    msg_out.dest_addr.snode.type = SUBNET_NODE;
                    msg_out.dest_addr.snode.domain = 0;
                    msg_out.dest_addr.snode.subnet = 1;
                    msg_out.dest_addr.snode.node = 3;
```

Fig 4. Example of Subnet-Node Type Addressing in Neuron. This example shows a message called `test_message` *that is destined for a Neuron Card located at domain 0, subnet 1, and node 3, containing the value 0. The structure definitions and typedefs can be found in the Neuron C header files ADDRDEFS.H and MSG_ADDR.H.*

After exploring explicit messages, Neuron C network variables were investigated. While faster and more powerful than explicit messaging, network variables require more setup than messages. It is recommended that network variables be bound with a separate tool, so as to leave the specific addresses and locations of other network variables ambiguous to the software on a Neuron chip. This tool was not available, so an operation called "self-binding" had to be performed on the variables. Shown in figure 5, binding a network variable requires two things: an address and a selector. Addresses work similarly to explicit messages, with multiple types defining where and to how many network variables the variable is synced with. Unlike explicit messages, multiple network variables can exist on one Neuron at a time. The selector allows network variables to specify the specific variable they are bound to, allowing multiple variables to coexist on one Neuron.

Fig 5. Example of Properly Configured Network Variable. In order for two network variables to communicate, two criteria must be met: that the address of the output variable matches that of the device with the input variable, and that their selector IDs match. If these two requirements are met, automatic data transmission can take place.
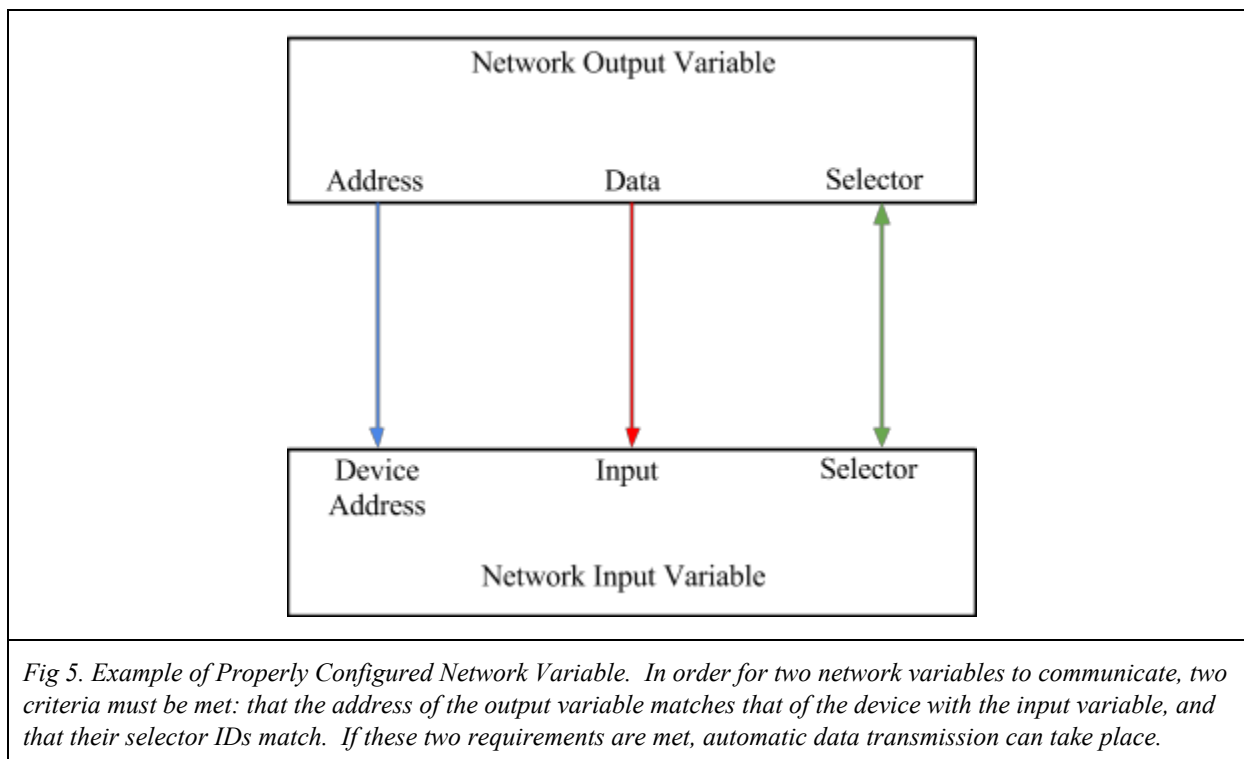
There are multiple types of network variables, and all require a slightly different binding process. At their most basic, there are two types of network variables: input and output. To bind an output variable to an input, the selector value for each variable must be the same, they must be of the same type, and the address of the output variable must match the address of the device that contains the input variable. Once these criteria are met, the value of the output variable can be changed, and the Neuron will automatically update the input variable on the other chip. Other types of network variables exist, such as propagated, which must be explicitly told to update, and polled, where the roles of the output and input variables are reversed, and the input variable must ask for the value of the output variable. On the test setup, basic, polled, and propagated network variable communication was demonstrated. Communication with a Neuron running firmware currently deployed on the OMEGA Laser system using network variables was also

demonstrated, which is not possible with explicit messages. Disregarding the initial bind, network variables were both faster and easier to implement than explicit messages, and were chosen as the communication protocol for this project.

For communication from Ethernet to the Neuron card, a Netburner web server[2] was used. A Netburner was chosen because it offered an easy and simple web interface and data output. A web interface was first created and tested on the Netburner. It allowed for simple, byte-sized data transfer from the web to the Netburner. The Neuron card and the Netburner were then connected to transmit data over an SPI bus. SPI, or Serial Peripheral Interface, was designed for simple, serial data transmission between one master and many slaves. SPI uses four wires, one to signal that a data transmission is occurring, two for data transmission, and one, called the clock, to specify the rate at which data will be transferred. Unfortunately, data communication between the Neuron and Netburner over SPI was not possible. The first issue that arose was that the Neuron operated with a 5V signal as high, and the Netburner interpreted 3V as high. This issue was resolved using level shifters integrated into the Netburner board, to allow it to communicate with 5V as high. After this was fixed, it was discovered that the lowest possible clock speed for SPI data communication for the Netburner was multiple magnitudes faster than the fastest clock speed available on the Neuron chip, and during the data transfer, both boards wished to be masters. To resolve these issues, bit-banging code, or code that explicitly created and interpreted SPI signals, was written for the Netburner web server. Unfortunately, this code was not successful in solving the issue in communication between the two devices. In the future, the SPI bus could easily be replaced with another communication protocol that is compatible with both the Netburner and Neuron.

5. Conclusion

To solve the current issues with the OMEGA Laser LonTalk system, an LLE-based Ethernet to LonTalk adapter was explored. Research into various methods of LonTalk communication protocols showed that network variables show the most promise for a future adapter. Several proof-of-concept ideas were also demonstrated, including integration with the current firmware on the laser. Due to incompatible hardware, a full Ethernet to LonTalk adapter was not possible, but with a few small changes, a proof-of-concept adapter could now be easily created.

Acknowledgements

I would like to thank Dr. Craxton for giving me this opportunity to participate in the internship program. I would also like to thank Dustin Axman for providing me with guidance and debugging help with the early stages of this project, Dave Hassett for helping me to understand the LonTalk system at the facility and providing me with the resources I needed to work on my project, and Robert Peck for overseeing my project and guiding me throughout the summer. Lastly, I would like to thank all of the teachers, mentors, and friends who have inspired me over the years, and provided me with the knowledge I needed to work on this project.

6. References

1. "Neuron C Programmer's Guide."
   "http://www.echelon.com/assets/blte1a7d6a3b37598bf/078-0002-02H_Neuron_C_Programmers_Guide.pdf "1990. PDF file.
2. "Netburner MOD5441X Datasheet.""http://www.netburner.com/mod54415/255-1-7/file "
   File last modified on 25 July 2014. PDF file.

Optimizing Beam Profiles for Polar Drive Implosions on the National Ignition Facility

Felix Weilacher

Penfield High School

Penfield, New York

Advisor: Radha Bahukutumbi

Laboratory for Laser Energetics

University of Rochester

Rochester, New York

August 29th, 2014

Abstract

In polar drive (PD) geometry, beams are displaced closer to the equator from their original on-target positions to achieve better implosion symmetry. Current direct-drive polar drive implosions for the National Ignition Facility (NIF) use phase plates - optics which define the shape of the laser beams or beam profiles - designed for indirect drive. The uniformity achieved in PD implosions is therefore limited. Optimal laser beam profiles have been identified using the hydrodynamics code DRACO. A combination of spherically symmetric and elliptical beam profiles are necessary for nearly uniform implosions. With the use of these optimized beam profiles, adjustments to laser temporal power histories can significantly improve symmetry and therefore target performance. These optimal beam profiles are also robust to model variations. For example, the same beam profiles can be used to optimize designs with different heat conduction models by requiring a relatively minor variation in laser power histories. The neutron yield increases by ~50% compared to designs using current NIF profiles.

I.   Introduction

In inertial confinement fusion (ICF),[1] many nominally identical laser beams are incident on a shell made of materials such as plastic containing a layer of solid cryogenic deuterium-tritium. This irradiation causes ablation of the outer regions of the target, driving the rest of the shell inward like a rocket.

A couple of different methods of delivering energy to the surface of the target are currently possible on laser facilities: direct drive,[1,2] where beams illuminate a target directly

Figure 1: (a) Original NIF beam pointing configuration. (b) Optimized polar drive beam pointings. Note that Ring 3 is split into two rings and that the quads of rings 3 and 4 are split in the azimuthal direction.
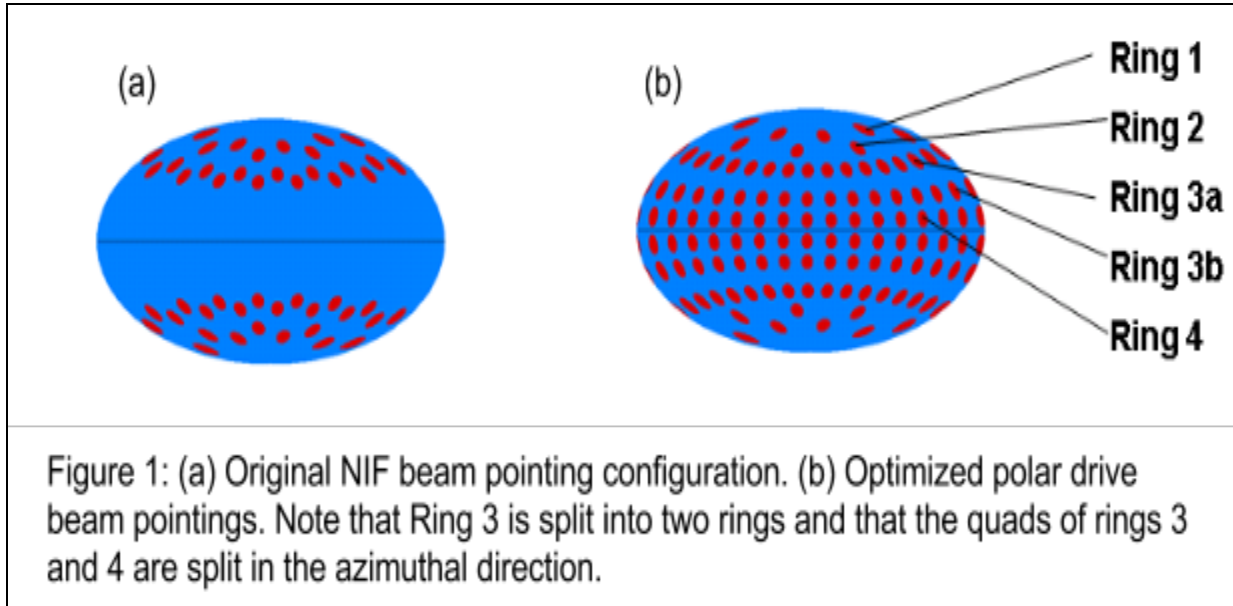
from all sides, and indirect drive,[3] where a target is placed inside a hohlraum (a gold cylindrical capsule with holes at the ends) and beams illuminate the sides of this hohlraum, causing the emission of x rays which then deliver energy to the target.

On facilities configured for direct drive, such as OMEGA,[4] beams are set up so that they strike the target with a nearly spherically uniform distribution at normal angles of incidence. The uniformity in beam placement leads to high uniformity in on-target intensity and creates a highly symmetric spherical implosion. On a facility such as the National Ignition Facility[5] (NIF), which is configured primarily for indirect drive, however, beam ports are concentrated around the poles of the target, corresponding to the two ends of the hohlraum (Fig. 1a). Thus, using the NIF for direct drive without displacing the beams from their centers of normal incidence results in a distribution of beams on target which is far from uniform. The solution to this is polar drive,[6] wherein beams are displaced from their original positions on the target surface; the resultant on-target positions of the beams are shown in in Fig. 1b. On the NIF, beams are organized into logical groupings of rings as shown in Fig. 1. These rings are displaced toward the equator or "repointed" to achieve better on-target symmetry.

Since beams are displaced laterally, beams which are repointed irradiate the target at more oblique angles of incidence. This results in the laser energy being deposited further away from the ablating shell and a reduction in drive. The equatorial beams must be repointed over the greatest polar angle from their original position and beam obliquity can significantly compromise drive at the equator. Thus, polar drive implosions tend to be underdriven at the equator.

Although the use of polar drive significantly improves the uniformity of the distribution of beams, and thus of on-target intensity, additional improvements to the irradiation uniformity can be made through the optimization of the laser pulse shapes and beam profiles, two additional sets of laser parameters which are introduced below.

The target considered in this paper (shown in Fig. 2) is a 1.1 mm radius sphere with a 100 μm-thick plastic (CH) shell filled with 20 atmospheres of deuterium (D_2) gas. This is typical of targets currently being used for polar drive experiments on the NIF.
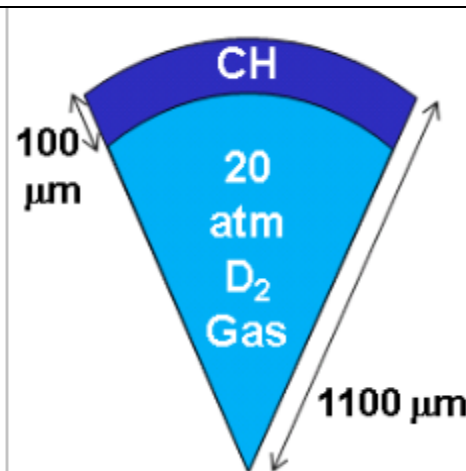
Figure 2: Cross section of a 1100 µm radius room temperature target with a 100 µm shell
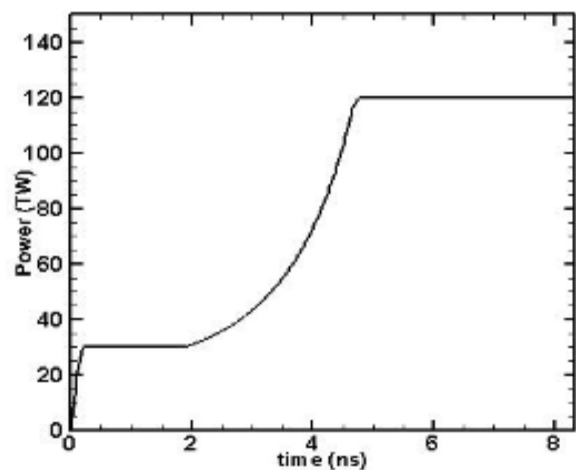
Figure 3: Example of a pulse shape, which gives laser power as a function of time over the course of an implosion. This pulse shape gives total laser power.

The design includes laser beam pulse shapes that describe the temporal power history of the beams. An example of a pulse shape is given in Fig. 3. In polar drive implosions on the NIF, these pulse shapes are characterized by a foot (between 0 and 2 ns), and then a slow rise (between 2 and 5 ns), to a main pulse (after 5ns).[7] During the initial rise to the foot a shock is launched into the shell. The length of the foot is fixed to correspond to when the shock breaks out of the shell into the gas. The overall length of the laser pulse is determined by the energy available on the laser system. Up to 700 kJ is normally available to implode a target on the NIF. Laser pulse shapes can be adjusted independently for each ring of beams, and also are easily mutable. They are thus an important tool for fine tuning polar drive implosions.

Figure 4: (a) Intensity contours of a circular beam profile. (b) Intensity contours of an elliptical beam profile. (c) Intensity contours of a profile which includes a secondary ellipse. The radius in the longest direction at 5% of peak intensity typically is equal to the target radius.
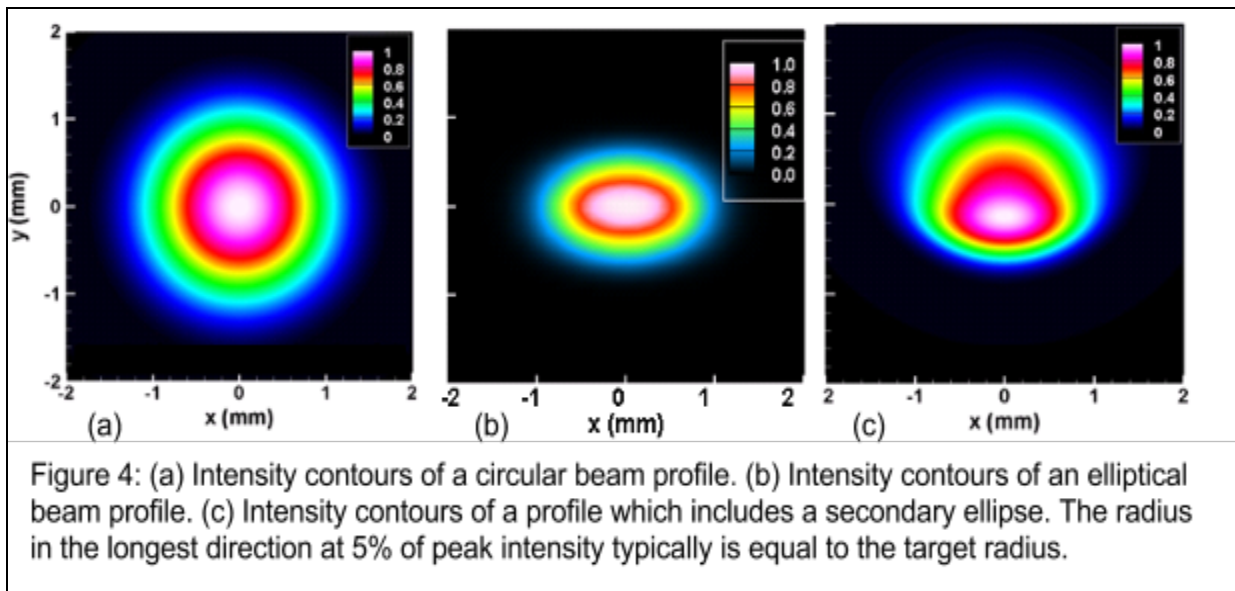
A third important set of laser parameters which can have a significant effect on the uniformity of an implosion are laser beam profiles, examples of which are shown in Figure 4. They are most intense at the center, with decreasing intensity toward the edges of the beam. The Intensity, $I(x,y)$, as a function of position for a simple, circular beam profile such as the one shown in Fig. 4a can be described as a super-Gaussian

$$I(x,y) = I_0 e^{-[(x^2+y^2)/\delta]^{n/2}}$$

[1.1]

where I_0 is the peak central intensity, which varies in time according to the pulse shape, δ is a constant which controls the width of the profile, and n is the super-Gaussian order. Larger values of n lead to beam profiles which are flatter at the center.

Beam profiles can take shapes with more complexity than a simple circle, however. This can have the effect of concentrating the intensity along certain directions. Fig. 4b shows an elliptical profile, given by

$$I(x,y) = I_0 e^{-[(x^2+(\eta y)^2)/\delta]^{n/2}}$$

[1.2]

where η is the ellipticity of the profile, defined as the ratio of the major axis to the minor axis of the ellipse. Note that elliptical beam profiles are oriented so that their major axes run latitudinally. Finally, Fig. 4c shows a complicated profile that can be described as a secondary ellipse superimposed on a primary profile;[8] this has the effect of offsetting the center of intensity from the center of the beam. This type of profile is given by

$$I(x,y) = I_0 \left[(1-a)\, e^{-[(x^2+(\eta y)^2)/\delta]^{n_1/2}} + a\, e^{-[(x^2+(\eta(y-o))^2)/\delta]^{n_2/2}} \right]$$

[1.3]

where o is the offset of the secondary ellipse from the center of the primary profile, and a, a fraction between 0 and 1, and $(1-a)$ define the relative intensities of the primary and secondary profiles. The ellipticity and Gaussian order for the secondary ellipse are not

necessarily the same as they are for the primary profile. These different beam profiles have advantages and disadvantages, and their merits are investigated in section II. While pulse shapes and pointings are easy to change, beam profiles are determined by phase plates, optics which are difficult and expensive to manufacture and cannot be changed.

The primary goal of this work is to identify beam profiles that can be used for experiments on the NIF devoted to studying the physics of ICF implosions. Simulations are a powerful tool to guide the design of experiments and model the conditions which predict ignition in ICF. Since the physics of laser deposition and the subsequent heat conduction to the ablation surface is extremely important to implosions, experiments are critical to test simulation codes and gain confidence in ignition predictions. Heat conduction is typically modeled using diffusion, and an empirical parameter, the flux limiter, is used to limit the simulated heat flux to match various observables in experiments. The motivation for a flux limiter is somewhat ad-hoc. An improved model in polar-drive geometry is a non-local model where heat is conducted by electrons that have long mean-free paths. It has been shown that non-local transport is an improvement over the flux-limited model based on several experiments in spherical geometry; however, rigorous comparisons with experiments in polar drive are outstanding. It is therefore critical that the experiments be designed carefully - expensive pieces of equipment such as phase plates should be robust to such uncertainties in the physics. It will be shown that the beam profiles designed in this work are robust to different models of heat conduction.

II. **Simulations**

Implosion simulations were carried out using the 2D hydrodynamics code DRACO[9] to determine optimal beam profiles. DRACO allows important parameters, such as beam

pointings, beam pulse shapes, and beam profiles, to be specified for all 5 rings of beams used in polar drive on the NIF and allows the effects of changes in these parameters to be tested.

Although the focus of this report is optimization of beam profiles, pointings and pulse shapes are also very important. All the simulations discussed in this report use the same polar drive pointing which gives an acceptable irradiation uniformity (Table 1). The original polar angle is shown in column 2, followed by the repointed polar angle in column 3.

Ring #	Original θ	Repointed θ
1	23.5	23.5
2	30	35
3a	44.5	49
3b	44.5	69
4	50	83

Table 1: Table showing the original and repointed polar angles for the design in this work. Rings 1 and 2 were displaced only in polar angle. Within the rings 3a, 3b, and 4, the beams were additionally moved so that they were equally spaced in the azimuthal direction.

Pulse shapes, discussed previously, are especially useful tools for fine tuning the uniformity of an implosion. The testing of various sets of beam profiles, outlined in this section, is always accompanied by adjustments to pulse shapes to identify an optimal level of uniformity. Throughout this report, when a simulated implosion using a set of beam profiles is said to have optimized pulse shapes, or to be an optimized implosion, it should be understood that there is not some universal optimal set of pulse shapes, but that pulse shapes for that implosion were tuned specifically to optimize uniformity with that set of beam profiles.

Since the NIF is designed for indirect drive, the currently installed phase plates produce elliptical beam profiles. This is because in indirect drive, beams pass through one of two laser entrance holes in the hohlraum at oblique angles. To clear a hole, the cross section

of a beam in the plane of the hole must fit the shape of the hole, which is circular. Therefore, all of the beams must be elliptically shaped. A significant interest of this work is the effect of circular beam profiles on target uniformity for polar drive ICF on the NIF when compared to these elliptical profiles.

Figure 5: (a) Initial normalized on-target Intensity for an optimized implosion using elliptical beam profiles. (b) Outer shell surface position relative to the mean at 1 ns for the implosion corresponding to (a). (c) and (d) Same as (a) and (b), except for an optimized implosion using circular (spherical) beam profiles for the higher latitude rings. The pole corresponds to 0 degrees, whereas the equator is at 90 degrees.

As is shown in Fig. 4, elliptical profiles have the effect of localizing laser intensity at a specific latitude. This localization can be a useful feature, as it permits the preferential irradiation of the equator relative to the pole. An optimal set of elliptical profiles for polar drive constitutes beams with increasing ellipticities from the pole to the equator. The on-target intensity at the initial target radius at the start of an optimized simulation using these profiles is shown in Fig. 5a. The accompanying plot in Fig. 5b shows the variation in the location of the ablation surface around the average location at a time of 1 ns into that simulation (during the foot). The troughs in the irradiation pattern correspond to an underdriven outer surface. When

9

the higher-latitude beam profiles for Rings 1, 2, 3a and 3b are replaced with circular profiles (Fig. 5c and 5d), and pulse shapes are re-optimized, the peaks and valleys in the irradiation pattern and the ablation surface decrease in amplitude resulting in a more uniform implosion. This is due to the better overlap provided by the circular beams. Note that the equator is still significantly underdriven. This is related to the choice of the heat conduction model (all the simulations described in section II used a flux limiter model as opposed to a nonlocal model) and will be discussed in section III. Therefore, the higher latitudes, which do not require the preferential irradiation delivered by the elliptical beam profiles, can be driven more uniformly with spherical beam profiles.

The equatorial region requires special attention. Ring 4, being the most oblique ring of beams, necessitates beam ellipticity to irradiate the equator effectively. The blue curve in Fig. 6 shows the position of the outer shell surface relative to the mean, versus polar angle with only circular beam profiles. The equator is significantly under-driven. This cannot be remedied with higher laser power for the equatorial ring. This is because a circular beam profile for ring 4 with a 5% radius equal to the target radius results in energy being deposited to a polar angle of nearly 30°. (An elliptical profile with a 5% semi-major axis equal to the target radius has a 5% semi-minor axis less than this radius and thus does not spread energy deposition as widely in the polar direction.) Thus it is difficult to sufficiently drive the equator without dangerously over-driving higher latitude portions of the target.

Figure 6: Outer shell surface position relative to the mean at 2 ns for optimized implosions using three different beam profiles for ring 4.
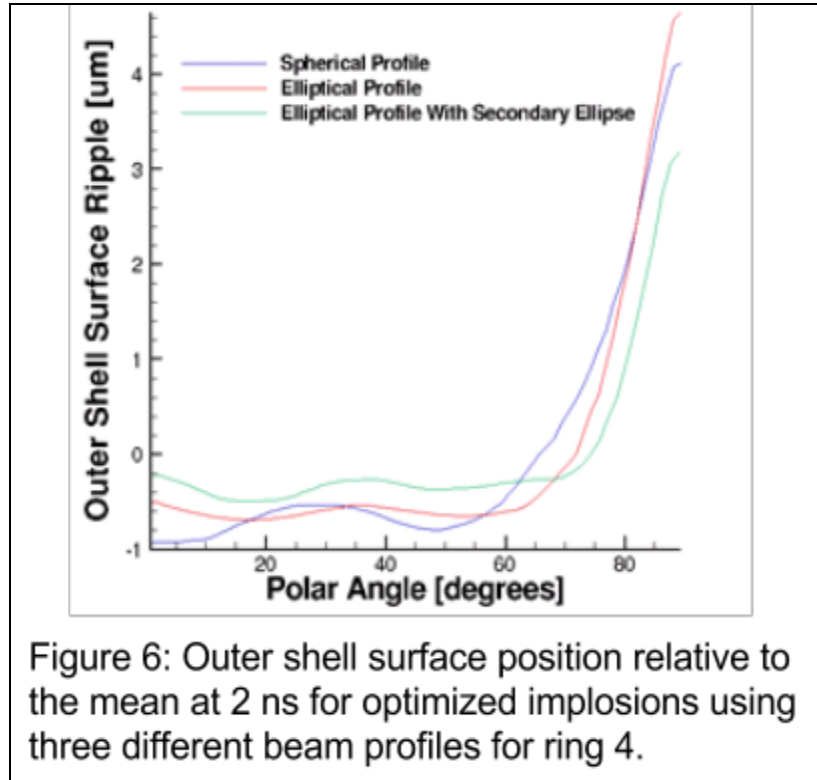
Localizing the energy distribution at the equator via use of an elliptical beam profile is doubly advantageous. First, this localization with respect to polar angle directly increases the amount of energy deposited at more-equatorial latitudes, providing greater drive. Second, it allows any laser power increases for ring 4 to preferentially drive the equator without overdriving the higher latitudes. The curves in Fig. 6 illustrate these effects. The case which uses ellipticity for ring 4 (red curve) shows a better-driven equatorial region (the range 60° to 75° is in particular improved), and a flatter surface northwards of 60°. Adding a secondary ellipse with an offset [Fig. 3c and Eq. (1.3)] iterated upon the benefits of this localization by further localizing the intensity and shifting the center of localization away from higher latitudes (green curve in Fig. 6).

The neutron yield from the fusion of deuterium ions is a good measure of target performance. Neutron yield can be increased by increases in drive velocity; however, when

two implosions have comparable velocities and incident energies, differences in uniformity can result in differences in neutron yield. As the target converges near the end of an implosion, the fuel becomes concentrated in a hot, dense area bound by the plastic shell and known as the hot spot. A more uniform implosion will feature a more uniform (close to spherical) hot spot, and higher hot spot uniformity generally leads to a higher neutron yield. The case featured in Fig. 6 using an elliptical profile for ring 4 has a 5.5% higher yield than the case using a circular profile, and adding the secondary ellipse brings a further 18.5% increase in yield compared to the case using a purely elliptical profile. Clearly, the equator was not sufficiently driven in any simulation, but the improvements brought by utilizing an elliptical beam profile which includes a secondary ellipse are encouraging.

Gaussian order is an additional parameter which can affect the overall shape and effect of a beam profile. Profiles with a lower Gaussian order are more sharply peaked, whereas higher-order profiles spread intensity out over a larger region. For this reason, lower Gaussian orders are more optimal for more equatorial rings as their localization can compensate somewhat the effects of obliquity. Therefore, in an optimal set of beam profiles, the order for each ring should get consistently lower moving from pole to the equator, i.e, from the less displaced to the most displaced rings of beams.

III.   Results

An optimal set of beam profiles was identified using the trends outlined in section II. Optimal beam profile parameters and the corresponding optimal pulse shapes are shown in Tables II and III and Fig. 7 respectively. The beam profile of ring 4 includes a moderate degree of ellipticity and a secondary ellipse, while the other rings have circular or close to circular beam profiles. Gaussian orders also decrease as was described previously. These

Ring	1	2	3a	3b	4
Gaussian Order	4.4	2.7	3.2	2.4	2.0
Ellipticity	1.0	1.0	1.0	1.2	1.6

Relative Amplitude of SE	0.5
Gaussian Order of SE	2.0
Relative offset of SE	0.15
Ellipticity of SE	2.1

Table II: Beam profile parameters used to obtain the uniform implosion shown in Figs. 8 and 9b.

Table III: Parameters of the Secondary Ellipse (SE) present in the profile used for ring 4. Offset is relative to the radius of the target

Figure 7: Pulse shapes for all 5 rings for optimized case. Note that the ratio between the Powers of Ring 3a and 3b must remain constant throughout the implosion
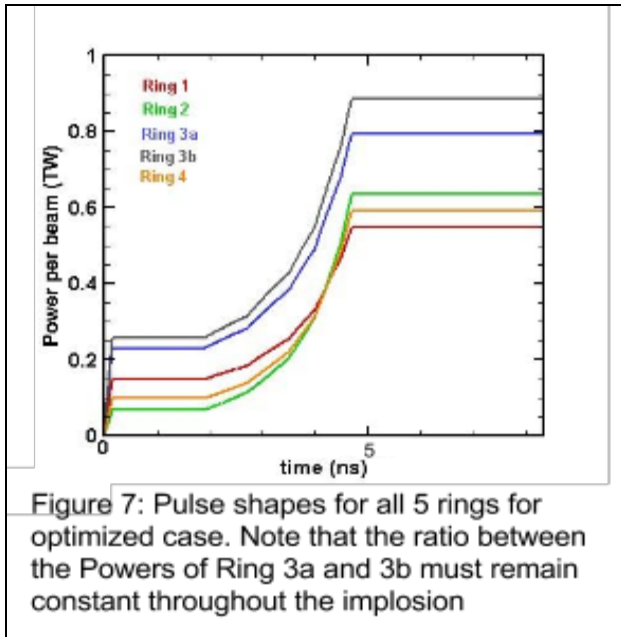
optimized profiles and parameters achieve an implosion with high levels of uniformity, as is detailed below in Figs. 8 and 9b.

Note that while section II suggested that more oblique rings' profiles should have higher Gaussian orders and that rings 1-3b should have circular profiles, the super-Gaussian order for the rings does not monotonically decrease with increasing polar angle, and Ring 3b has a small ellipticity of 1.2. These deviations come from a specific constraint applied to the pulse shapes for rings 3a and 3b. As is seen in Fig. 1, ring 3 is split into rings 3a and 3b for polar drive. Due to the organization of beam lines on the NIF, the pulse shapes for rings 3a and 3b must be the same, although an energy ratio close to 1.0 between the two rings is tolerable. For the optimal pulse shapes shown in Fig. 7, the pulse shape of ring 3b has a 12% higher energy than the pulse shape of ring 3a. This constraint on the pulse shapes for rings 3a and 3b reduces

13

control over symmetry in the 40° - 70° region where these rings are most influential. Generally, due to the increased obliquity, more energy is required around 70°, or where ring 3b is most influential. The ellipticity in the profile for ring 3b helps to localize energy there, and the higher super-Gaussian order for ring 3a lessens the drive near the 45° region and instead spreads energy out to regions which include the 70° area. These choices of beam profile help to restore symmetry which could otherwise be compromised by the pulse shape constraint for rings 3a and 3b.

In designing uniform ICF implosions, it is vitally important to maintain a high degree of uniformity until shock breakout, which occurs around 2 ns for this pulse shape. Non-uniformities introduced early on in an implosion will tend to grow as time continues, and, in particular, non-uniformities in the shock which is launched at the initial time of laser irradiation can give rise to hot spot non-uniformities near the time of peak compression which compromise target performance. The implosion whose parameters are described in Fig. 7 and Tables II and III has a shock strength that is very uniform, as is shown in Fig. 8.

Figure 8: Density contour at shock breakout for optimized implosion. 0° corresponds to the pole, while 90° corresponds to the equator
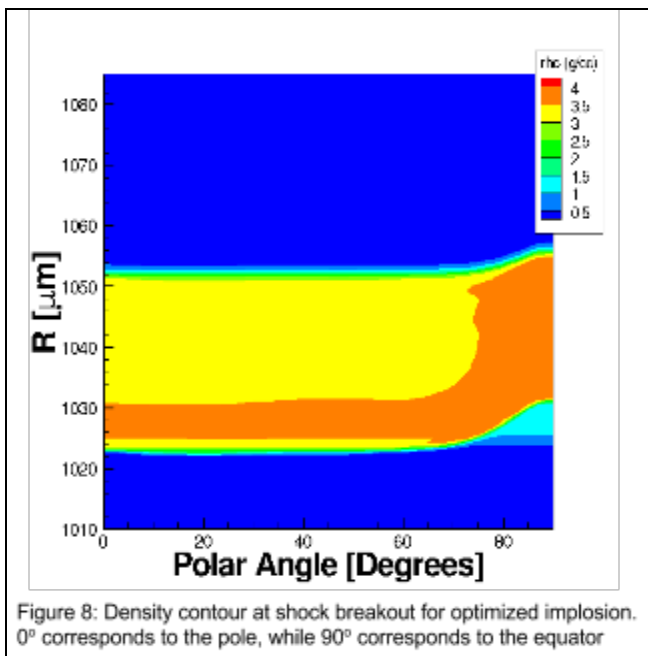
Optimizing past shock breakout is generally accomplished by optimizing the power of each ring during the main pulse. The late-time results of the implosion shown in Fig. 8 are shown in Fig. 9b, which shows mass density contours at peak neutron production, when the target has converged by roughly a factor of 10 from the initial radius. Mass density contours from a simulation of current NIF implosions with existing NIF indirect-drive

14

Figure 9: Density contours at a convergence ratio of 10 (8.1 ns) for (a) an optimized implosion using current NIF beam profiles and (b) an implosion which uses the optimized set of beam profiles identified in Tables I and II
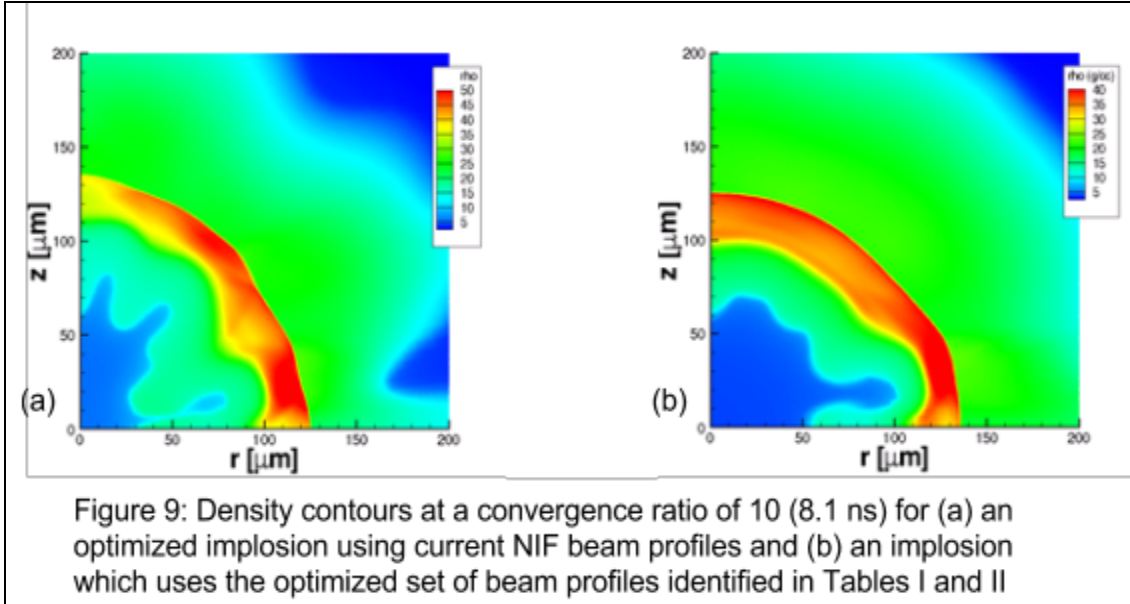
beam profiles are shown in Fig. 9a next to those of the simulation with optimized beam profiles shown in Fig. 9b. The inner fuel-shell interface (shown by the contours separating the blue and green regions inside the shell) for the simulation of the implosion which uses the optimized set of beam profiles has a much higher degree of uniformity than that of the simulation which uses the existing set of beam profiles. Quantitatively, table IV shows that the distortion of this interface for the implosion shown in Fig. 9a is twice as high as that of the implosion in Fig. 9b which uses an optimized set of beam profiles. Table IV also compares the neutron yields of these two implosions, and shows that use of the optimized set of beam profiles increases the neutron yield by more than 50%.

	Current NIF beam profiles	Optimized beam profiles
Hot Spot Distortion	12.5%	6.2%
Neutron Yield	1.7×10^{12}	2.6×10^{12}

Table IV: Target performance for implosions visualized in Fig. 9a and 9b, (columns 2 and 3 respectively). Hot spot distortion is defined as the ratio of the rms of the inner fuel-shell interface to the average radius of the interface.

When modeling implosions with a simulation code such as DRACO, there are questions as to the accuracy of certain aspects of this modeling. In some cases, multiple models exist for one aspect of the hydrodynamic simulation. One example is heat conduction, and uncertainty in the heat conduction model is one model variation that can be explored. Since the corona of the NIF has temperatures of ~4 keV, the electrons that conduct heat have energies ~20 keV and large mean-free paths that permit them to reach the ablation surface. Heat conduction is typically modeled using diffusion, which assumes small electron mean free paths; however, it is expected that the non-local effects of large mean-free paths will alter the drive at the ablation surface.

Because the phase plates which determine beam profiles are fixed and expensive, it is desirable that a set of beam profiles optimized and shown to be successful (compared to current NIF profiles) with one heat conduction model not have that success compromised by the use of alternate models. The optimal set of profiles previously identified was used in

Figure 10: Mass density contours at a convergence of ~10 for a simulation with the optimal beam profiles and a non-local heat conduction model.
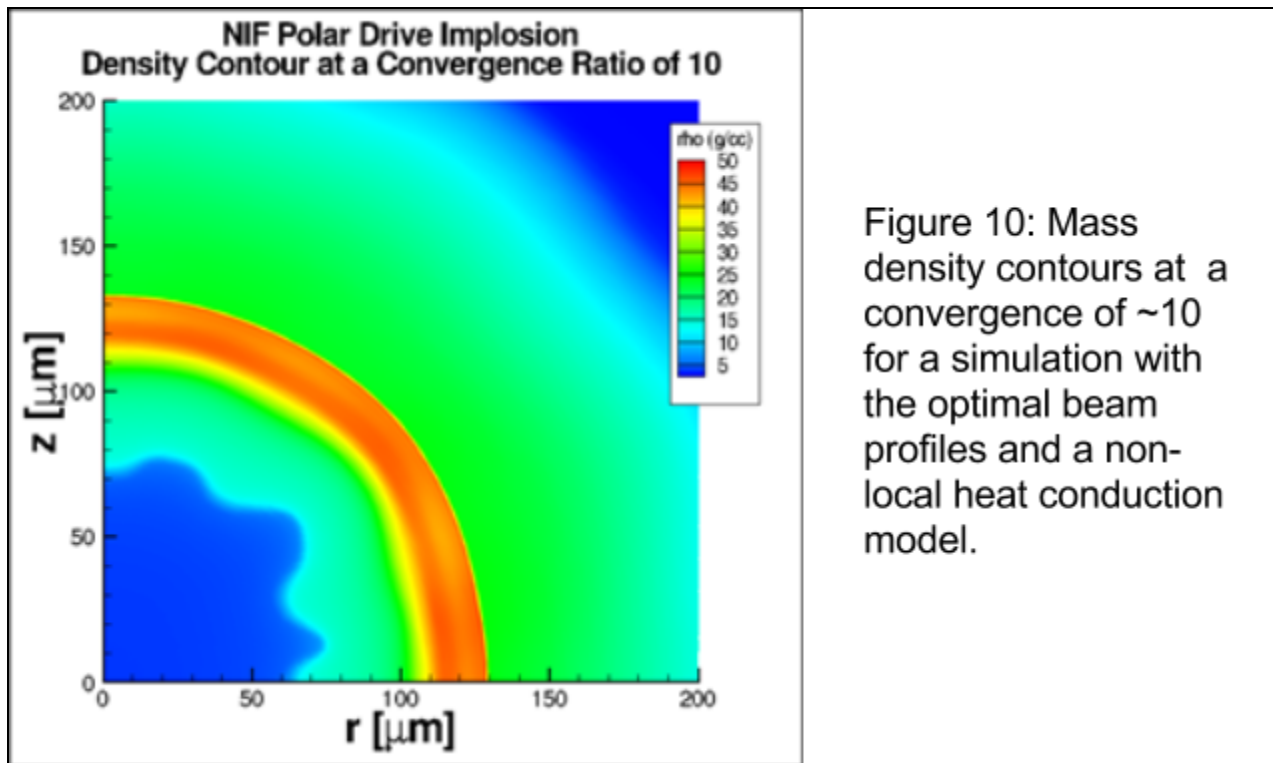
simulations with a non-local heat conduction model instead of a flux-limited model as is used in the majority of this work. Excellent symmetry was recovered with minor changes to the ring laser pulse shapes for the same set of beam profiles. (Fig. 10)

IV. Conclusion

Current experiments on the National Ignition Facility which explore the use of direct drive ICF via polar drive use a set of phase plates designed for indirect drive. Simulations were carried out using the 2D hydrodynamics code DRACO which aimed to identify an optimal set of beam profiles and compare the performance of these profiles to that of the current NIF profiles. By varying Gaussian orders and ellipticities and exploring the use of secondary ellipses, and ultimately by fine tuning pulse shapes, a set of optimal beam profiles was identified which had the capability to significantly improve the uniformity of a polar drive implosion, increasing the simulated fusion yield by more than 50%, and whose benefits are robust to variations in the heat conduction model.

V. Acknowledgements

I would like to extend thanks to the amazing people who contributed to the successful completion of this project and this report and who made my all too brief summer sojourn at LLE one of the greatest experiences I've had. I'd like to thank every member of the lab in addition to all the participants in this year's high school program for creating such a fantastic environment to work in. In particular, I'd like to thank Dr. Stephen Craxton, for providing me with the opportunity to carry out this research and for doing so much work to give other high

school students this experience every year, Michael Charissis, for providing me with the technical support necessary for this project, and Ian Gabalski, for sharing with me so much of his knowledge, work, and expertise in this area of study. I'd especially like to thank my advisor, Dr. Radha P. Bahukutumbi. She poured a huge amount of effort into both creating this project and guiding me through it, and did a fantastic job providing me with the perfect amount of guidance to make this project such a success.

References

1. J. Nuckolls, L. Wood, A Thiessen, and G. Zimmerman, Nature 239, 139 (1972).

2. S. Atzeni and J. Meyer-ter-Vehn, *The Physics of Inertial Fusion: Beam Plasma Interaction, Hydrodynamics, Hot-Dense Matter*, International Series of Monographs on Physics (Clarendon, Oxford, 2004).

3. J. D. Lindl, Phys. Plasmas 2, 3933 (1995).

4. T. R. Boehly et al., Opt. Commun. 133, 495 (1997).

5. J. D. Lindl and E. I. Moses, Phys. Plasmas 18, 050901 (2011).

6. S. Skupsky et al., Phys. Plasmas 11, 2763 (2004).

7. P. B. Radha et al., Phys. Plasmas 20, 056306 (2013).

8. T. J. B. Collins et al., Phys. Plasmas 19, 056308 (2012).

9. P. B. Radha et al., Phys. Plasmas 12, 032702 (2005).

Computational Modeling of Azobenzenes for Optically Addressable Liquid Crystal Alignment

Kyle Xiao

Webster Schroeder High School

Webster, NY

Advisor: Kenneth L. Marshall

Laboratory for Laser Energetics

University of Rochester

Rochester, NY

December 2014

Abstract

Photoisomerization of azobenzene between its rod-like *trans* and bent *cis* forms can be used to control liquid crystal alignment. This property makes azobenzenes useful in optically addressable liquid crystal beam shapers. Rather than using the costly trial-and-error synthesis method to synthesize a large array of compounds in order to identify unique characteristics of certain azobenzenes, computational modeling was performed. Density functional theory (DFT) and time-dependent DFT calculations were performed in this study using Schrodinger's Materials Science Suite to model azobenzenes tethered to a polymer backbone. The length of the spacer chain tethering the azobenzene to the polymer was shown to affect the energy difference between the *trans* and *cis* states. The addition of terminal groups was also explored and yielded interesting results. A cyanate ester terminal group increased the energy difference between isomers by 50% and 2-methoxy-N-(2-methylphenyl) acetamide group decreased the energy difference by 75%. Adding terminal groups tended to increase the wavelength of light required to initiate *trans-cis* isomerization. The addition of terminal groups also resulted in fluctuations in the HOMO-LUMO bandgap.

1. Introduction

Azobenzenes are defined by the double bond between the two nitrogens at their centers. Composed of two phenyl rings along with a nitrogen double bond, azobenzenes are noted for their ability to *photoisomerize* (i.e., photomechanically switch between the rod-like *trans* isomer and the bent *cis* isomer) when irradiated with the appropriate wavelength of UV or visible light. Under UV irradiation, *trans-cis* isomerization is

initiated, whereas *cis-trans* isomerization occurs when the material is exposed to visible region light of the appropriate intensity (Fig. 1).
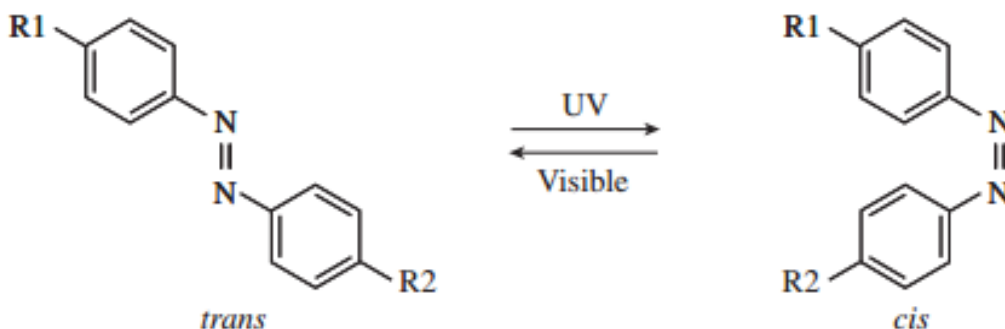
Fig. 1: Photochemically induced isomerization of azobenzene derivatives. R_1 and R_2 are terminal groups.

Beam shaping is required in high-peak-power laser systems for a variety of applications. The beam shapers currently used in OMEGA EP are composed of metal pixels deposited on a fused silica substrate.[1] Once the pattern has been generated, it cannot be changed; a new beam shaper needs to be fabricated. These metal-mask beam shapers are also limited to only the lowest-fluence areas of OMEGA EP due to their low laser damage threshold (250-500 mJ/cm^2 at 1054 nm, 1 ns pulse width). Electro-optical liquid crystal (LC) programmable spatial light modulators (PSLIM's) are also used in OMEGA EP to actively control the beam profile, but these devices suffer from the same low damage threshold as metal mask beam shapers due to the need for conductive-oxide electrodes required for their operation. A new alternative to these beam shapers would be an LC beam shaping device similar to the PSLIM except that the conductive oxide electrodes are replaced with a photoswitchable alignment coating composed of azobenzene "pendants" tethered to a polymer backbone. Because LC molecules are anisotropic in shape, they can exhibit differing optical properties depending on the

3

direction light is incident on the molecular structure. This difference in optical properties can be used to modulate or attenuate the intensity or phase of a light beam that is incident on the LC material or device. The major axes of the liquid crystals have a tendency to align with long axes of the azobenzene pendants, and will change their orientation in response to a change in the orientation of the azobenzene pendants as they undergo photoinduced *trans-cis* (and *cis-trans*) isomerization, resulting in an optically-induced change in the intensity or phase of the incident light. Figure 2 shows the molecular reorientation of LC molecules in contact with photoswitchable alignment layer that are designed to produce LC reorientation either out-of-plane (Fig 2, top) or in-plane (Fig 2, bottom) with respect to the device substrates. Testing at LLE has demonstrated that these azobenzene alignment layers have 1054-nm laser damage thresholds ranging from 28 to 67 J/cm^2 at 1054 nm, 1 ns pulse width, which is well above the minimum requirement to be a viable alternative to the currently used PSLIM beam shapers.[2]
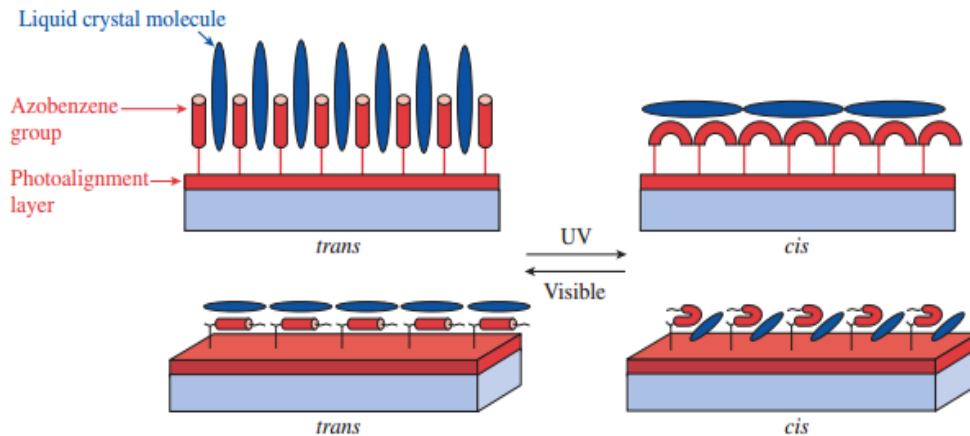
Fig. 2: Optically-addressed switching of LC devices using photoswitchable azobenzene alignment layers designed to induce out of plane (top) or in-plane (bottom) switching. The LC molecules follow the reorientation of the azobenzene "command surface" to produce a change in intensity or phase of the incident light.

Computational modeling is a quick and cost effective alternative to trial and error synthesis. In the past, when scientists wanted to develop a new compound to serve their purposes, they would need to synthesize a large array of compounds. Not only can this work be resource intensive, but it also can be time-intensive as each synthesis and purification process can take weeks or even months. More recently, as computers have become more powerful, many researchers have been relying on computational chemical modeling to determine which proposed molecules would have favorable predicted results. Researchers then only have to synthesize the much smaller set of viable compounds rather than the large set containing every molecule. Computational modeling has already been used heavily by the pharmaceutical and optics industries to help synthesize new drugs and liquid crystals.

There are many different algorithms and methods available for chemical modeling, the fastest of which is semi-empirical. As the name suggests, this method relies on some previously obtained experimental data. Semi-empirical methods are very fast because they parameterize the calculation, but are not very accurate. Hartree-Fock is also a very common method. It is an *ab initio* method, meaning that it is not based on previous experimental data, but rather on simulations that are run from the beginning using physical principles. This method is extremely accurate, but also comes with a large computational cost.[3] Electron orbitals are expressed as one-electron functions, and the multi-electron calculation is based on the sum of the single-electron functions.[4] Density functional theory (DFT) and time-dependent density functional theory (TDDFT) try to provide a middle ground that is both fast and accurate. They use a 3-D electron density function rather than a many-electron wave function (Figure 3). TDDFT differs from DFT

in that it accounts for how the system responds to an outside disturbance.
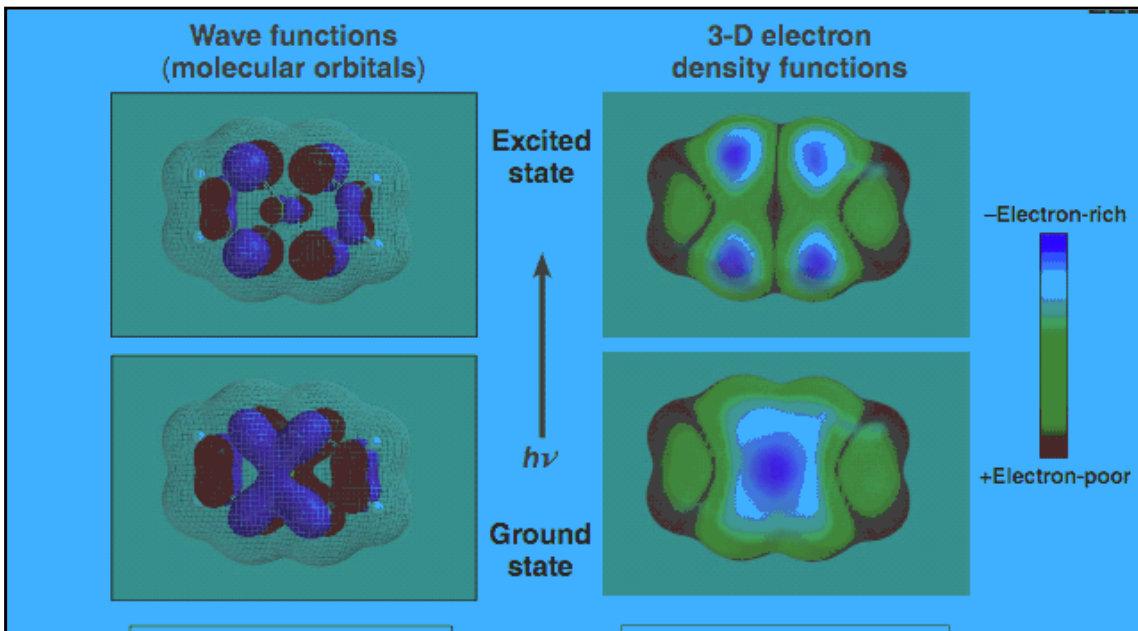
Fig. 3: A comparison of computed visualizations of wave functions vs electron density functions for the same molecule.

In this study, DFT and TDDFT were used to study the impact of molecular structure on optical switching properties in photoswitchable azobenzenes. Forty-two molecules were tested as possible components of photoalignment layers with low switching energies, enhanced bistability (the ability of a device or material to remain in one state indefinitely after the "writing" energy is removed), write/erase fatigue resistance, and high laser damage resistance.

2. Methodology

All calculations performed in this study were done using Schrödinger's Materials Science Suite software. The process is detailed in Fig. 4.
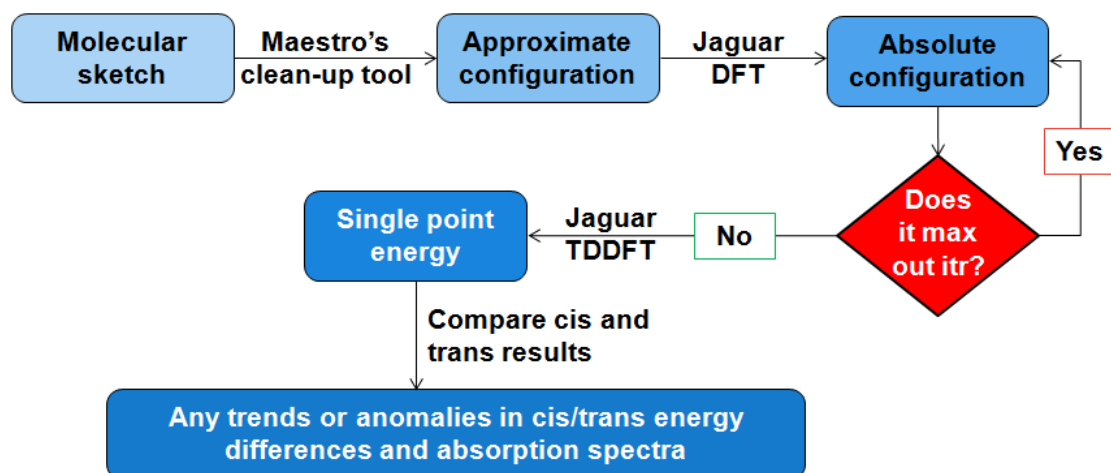
Fig. 4: Flowchart that portrays the methodology used in the computational analysis of candidate photoswitchable alignment layers employing azobenzenes.

Maestro is a visualization component of the Material Science Suite that allows the creation and visualization of molecules; it also includes a quick optimization routine that provides an approximate minimum-energy configuration of the molecular structure. Files generated by Maestro can be directly input into Jaguar computational engine for a more accurate geometry optimization using DFT. This optimization often had to be repeated as the molecules reach complexities at which they began to max out the iteration limits. Finally, the results of this optimization were input into TDDFT calculations that modeled the excited state absorption spectra.

One goal of the simulations was to find azobenzene structures that would impart high bistability to the photoswitchable alignment layer. In order for an azobenzene molecule to be bistable, there needs to be a significantly large difference between the activation energy required for it to undergo isomerization and the potential energies of the molecule in both its *cis* and *trans* states. However, if the energy barrier between the two states is too large, then optical switching will be difficult to achieve (Fig. 5).
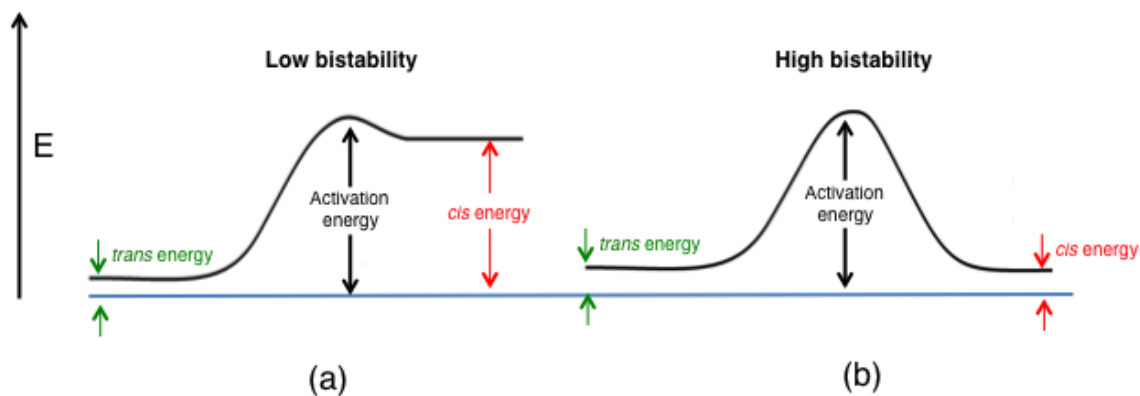
Fig. 5: Comparison of energy diagrams for photoswitchable azobenzene alignment layers. (a) a system with low bistability; the activation energy barrier required to switch from the *trans* state to the *cis* state is large, while the energy barrier for the reverse transition from *cis* to *trans* is relatively shallow, making conversion back to the *trans* isomer easy. (b) a system with high bistability; here, the energy barrier between both the *trans-cis* and *cis-trans* states is large, and once switched into the *cis* state the material will remain in that state indefinitely. The large activation energy barrier also means that a larger amount of optical energy will be needed to induce switching.

The initial model compound employed an alkyl spacer chain to tether a single azobenzene molecule with various kinds of terminal groups to a methacrylate *oligomer* (a "mini-polymer" with $\leq$ 10 to 15 repeat units); the example shown in Fig. 6 has an oligomeric backbone consisting of four repeat units of methacrylate groups. Computations were done using this short backbone rather than a fully polymerized chain to reduce the very large computational time and resources that would be required to compute energy levels for the complete polymer system.
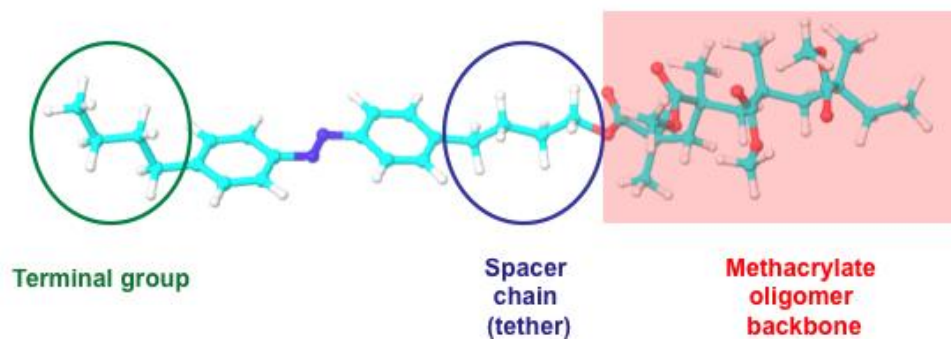
Fig. 6: An example of a single azobenzene repeat unit used in the simulations. This azobenzene contains a 4-carbon alkyl *terminal group* and is connected to the methacrylate oligomer on the right of the Figure by a 4-carbon spacer chain, or *tether*. A large number of these short backbones consisting of such "repeat units" would be linked together to form the polymer backbone by polymerization of the methacrylate groups at the ends of the oligomer chain.

3. Results and Discussion

Computational efforts focused on the effects of two different factors: (1) the length of the alkyl spacer chain (tether), and (2) the composition of the terminal group attached to the opposite end of the azobenzene structure (in Fig. 6, the 4-carbon chain on the left side of the molecule). Testing on the effects of spacer chain lengths was conducted with methoxy ($-OCH_3$) terminal groups to simplify the computations. Spacer chain lengths ranging from 1 to 12 were examined (Table 1). Figure 7 gives the difference between the *trans* and *cis* energies as a function of spacer length. At lengths of 4, 7, 10, and 12 there seem to be noticeable peaks in the difference in energies. In order to determine whether or not a pattern exists, however, additional alkyl spacer chain lengths

9

need to be tested. One possible reason for the degradation of the pattern that seems to exist for spacer lengths 4, 7, and 10 is that the spacer chain eventually reached lengths (12 or higher) that are sufficiently long to began to fold itself into a convoluted shape, thus altering the energy values. Spacer chains of lengths 5, 6, 8, and 9 appear to be the best choices for azobenzenes designed to be bistable.

Spacer Length	*trans* Energy (hartrees)	*cis* Energy (hartrees)	Energy Difference (hartrees)	Energy Difference (kJ/mol)
1	-2149.203653	-2149.175137	0.028516	74.86874774
2	-2188.527937	-2188.50071	0.027227	71.48447871
3	-2227.843367	-2227.816239	0.027128	71.22455424
4	-2267.160542	-2267.12571	0.034832	91.45140347
5	-2306.474972	-2306.4509	0.024072	63.20102734
6	-2345.783562	-2345.762786	0.020776	54.54738053
7	-2385.110183	-2385.075182	0.035001	91.89511291
8	-2424.400884	-2424.375819	0.025065	65.80814849
9	-2463.734154	-2463.714671	0.019483	51.15260949
10	-2503.0624	-2503.031431	0.030969	81.30909836
11	-2542.366776	-2542.348358	0.018418	48.35645238
12	-2581.689842	-2581.6579	0.031942	83.86370951

Table 1: Calculated values of *trans-cis* isomerization energy for tethered azobenzenes with various spacer lengths. All materials had –OCH$_3$ as the terminal group.
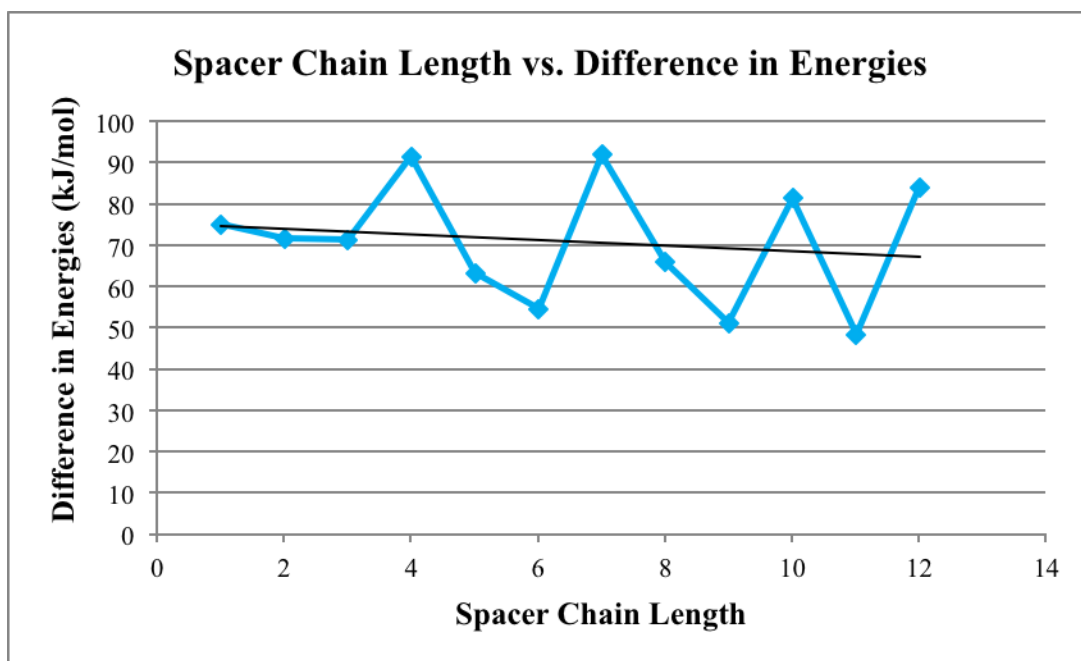
Fig. 7: Plot of the difference in energy between *trans* and *cis* states vs spacer chain length for the
data shown in Table 1.

Alkyl chains ranging in length from 1 to 9 comprised a large portion of the

terminal groups tested using the methods detailed earlier; the results are displayed below

in Table 2 and Fig. 8.

Terminal group	*trans* Energy (hartrees)	*cis* Energy (hartrees)	Energy Difference (hartrees)	Energy Difference (kJ/mol)
Methyl	-2191.954981	-2191.920787	0.034194	89.7763347
Ethyl	-2231.27128	-2231.238445	0.032835	86.20828069
Propyl	-2270.588028	-2270.554955	0.033073	86.83314961
Butyl	-2309.903743	-2309.870307	0.033436	87.78620597
Pentyl	-2349.221007	-2349.187397	0.03361	88.24304291
Hexyl	-2388.537727	-2388.502606	0.035121	92.21017287
Heptyl	-2427.853855	-2427.817284	0.036571	96.01714735
Octyl	-2467.170722	-2467.133454	0.037268	97.8471206
Nonyl	-2506.486855	-2506.452856	0.033999	89.26436227

Table 2: Calculated values of *trans-cis* isomerization energy for tethered azobenzenes with
various alkyl terminal group lengths.
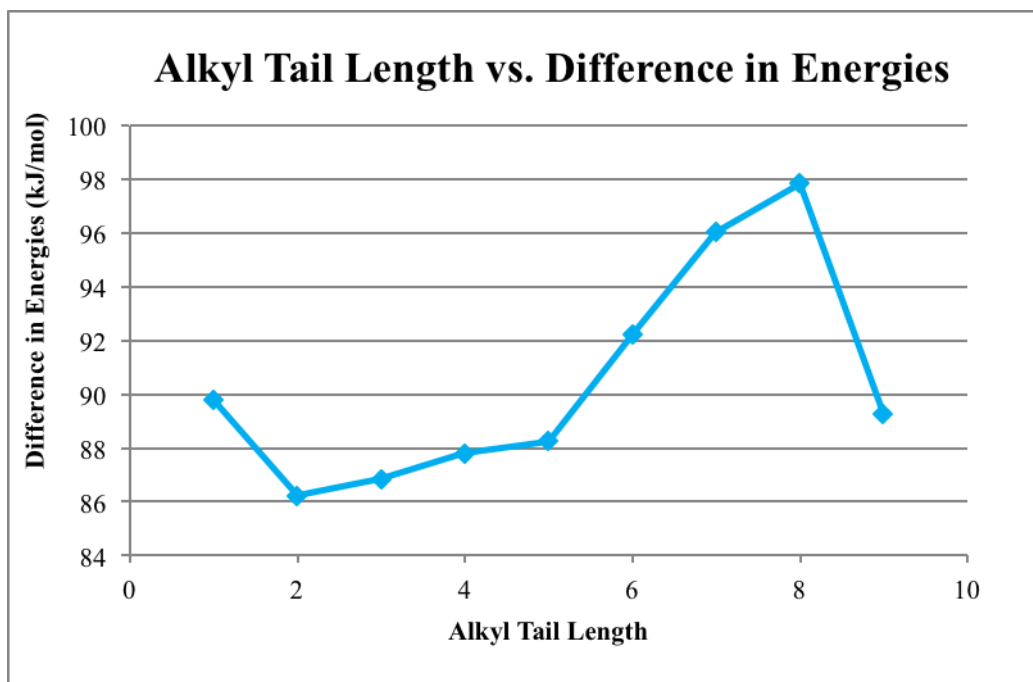
Fig. 8: Plot of the difference in energy between *trans* and *cis* states vs alkyl terminal group length for the data shown in Table 2.

These simulations clearly show that the energy difference increases steadily as the alkyl tail's length increases. The fact that the energy difference begins to decrease when the alkyl terminal group reaches a length of 9 can be attributed to folding of the carbon chain upon itself as was observed earlier for the alkyl tethering chains; the terminal groups contort themselves into a position that alters the chemical properties of the molecule significantly.

The remaining molecules that were tested contained a variety of other terminal groups, as well as some heteroaromatic rings. A complete listing of these terminal groups and the resulting *trans-cis* isomerization energies that result when they are attached to the azobenzene core can be seen in Tables 3 and 4. The energy differences between *trans* and *cis* isomers for the cyanate ester terminal group and the 2-methoxy-N-(2-methylphenyl) acetamide group were lower than that for an un-substituted azobenzene core by 16% and

72%, respectively. Additional work needs to be done, but this initial information points to terminal groups containing ester and acetamide functionalities as being potentially valuable for producing a bistable photoswitchable azobenzene. Chloromethyl acetamide, another terminal group in this class, was observed to increase the *trans-cis* isomerization energy difference by 43%.

Terminal group	*trans* Energy (hartrees)	*cis* Energy (hartrees)	Energy Difference (hartrees)	Energy Difference (kJ/mol)
None	-2152.634056	-2152.600728	0.033328	87.50265
Chloroalkane	-2612.228515	-2612.194726	0.033789	88.71301
Fluoroalkane	-2251.866129	-2251.832568	0.033561	88.11439
Trichloromethyl	-3570.708575	-3570.676345	0.03223	84.61985
Triflurormethyl	-2489.666375	-2489.636063	0.030312	79.58415
Cyanate ester	-2320.060921	-2320.033091	0.02783	73.06765
Isocyanate	-2320.116235	-2320.082803	0.033432	87.7757
Alcohol	-2227.855194	-2227.821613	0.033581	88.1669
2-methoxy-N-(2-methylphenyl) acetamide	-2706.243346	-2706.233957	0.009389	24.65082
Amine	-2207.994625	-2207.961011	0.033614	88.25354
Nitrile	-2244.875016	-2244.841972	0.033044	86.75701
Chloromethyl acetamide	-2820.248755	-2820.200977	0.047778	125.4411
NHOC2	-2360.652447	-2360.619731	0.032716	85.89585
CSSO2C	-3178.026333	-3177.994327	0.032006	84.03174

Table 3: Calculated values of *trans-cis* isomerization energy for tethered azobenzenes with a wide variety of terminal groups

Terminal group (rings)	*trans* Energy (hartrees)	*cis* Energy (hartrees)	Energy Difference (hartrees)	Energy Difference (kJ/mol)
6–membered	-2403.35558	-2403.321033	0.034547	90.70313608
5–membered	-2364.03914	-2364.005146	0.033994	89.25123477
Open 5–membered	-2365.23989	-2365.209427	0.030463	79.98059554

Table 4: Calculated values of *trans-cis* isomerization energy for tethered azobenzenes with heteroaliphatic rings as terminal groups.

The absorption spectra of the candidate molecules were calculated and analyzed; spectra for both the *cis* and *trans* isomers are shown in Figs. 9-18. The addition of terminal groups does not significantly alter the absorption spectra in most cases, which means that a narrow-band light source can be used to optically switch a wide variety of azobenzene photoalignment coatings. Only for the heteoraliphatic ring terminal groups was a bathochromic (red) shift in the absorption spectra observed.
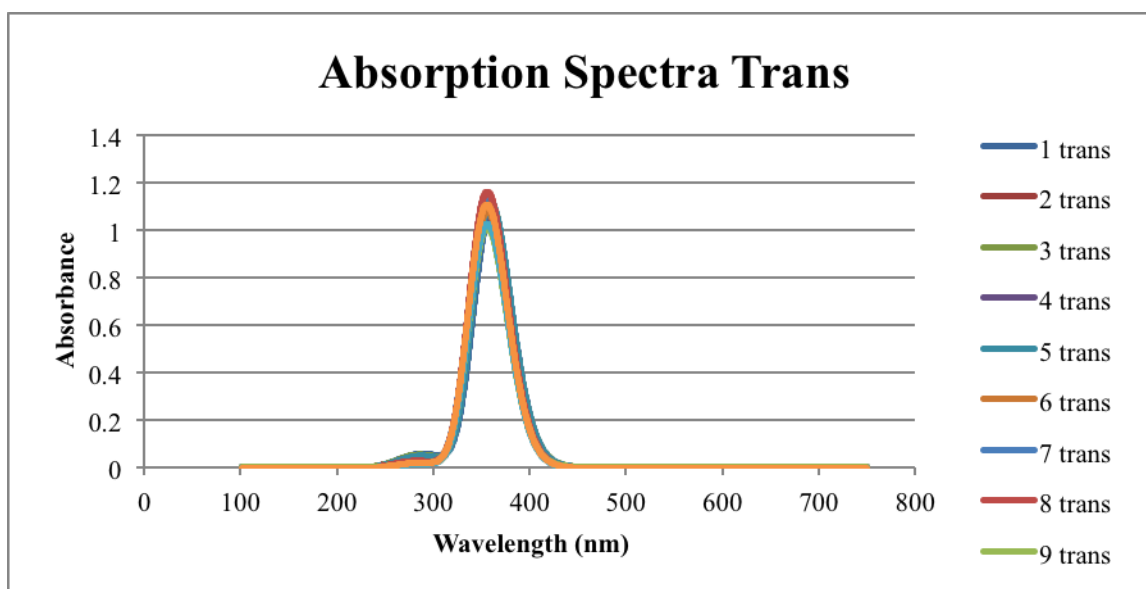
Fig. 9: Calculated absorption spectra for the *trans* isomer with spacer chain (tether) lengths ranging from 1-9.
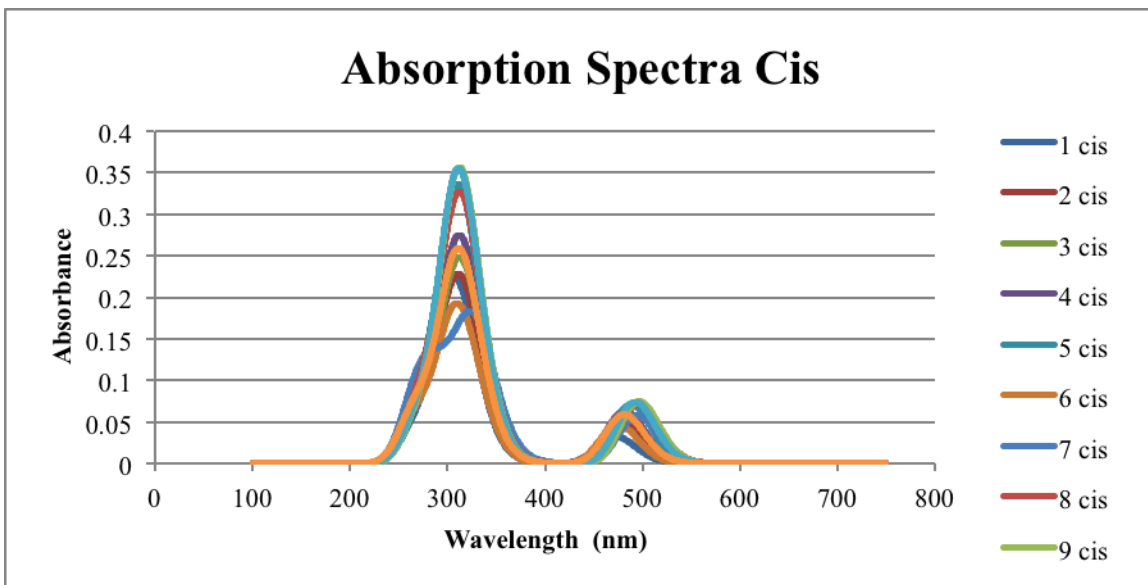
Fig. 10: Calculated absorption spectra for the *cis* isomer with spacer chain (tether) lengths ranging from 1-9.
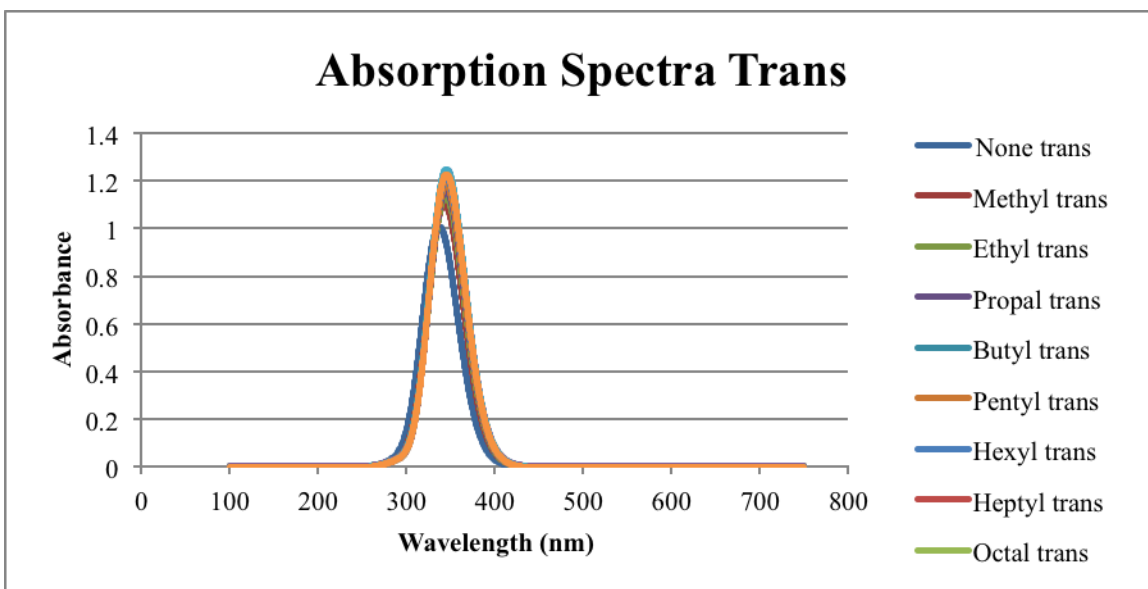
Fig. 11: Calculated absorption spectra for the *trans* isomer with alkyl terminal groups ranging from 1-8.
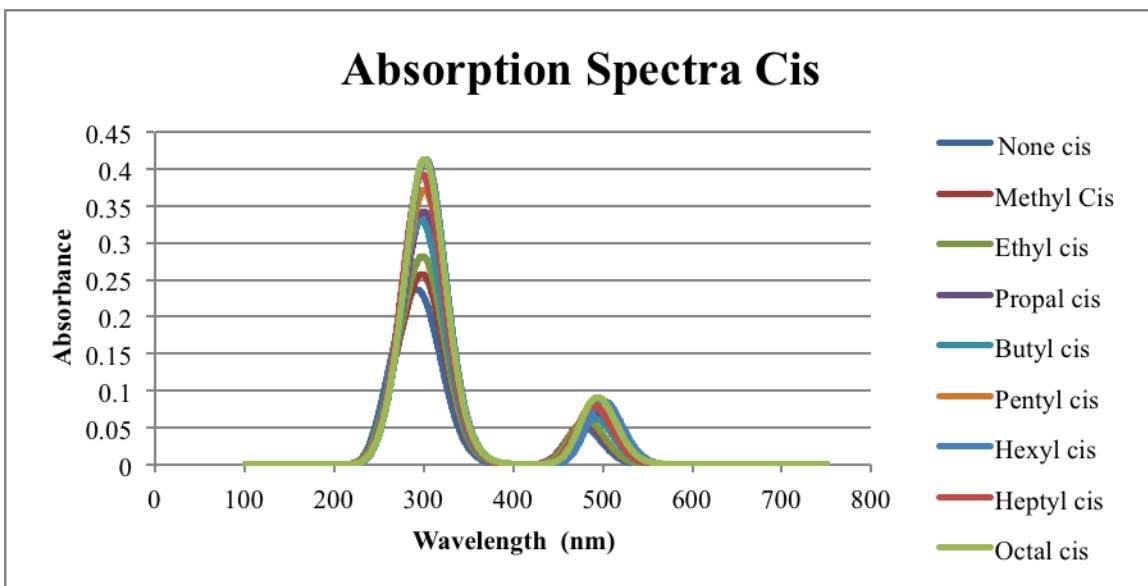
Fig. 12: Calculated absorption spectra for the *cis* isomer with alkyl terminal groups ranging from 1-8
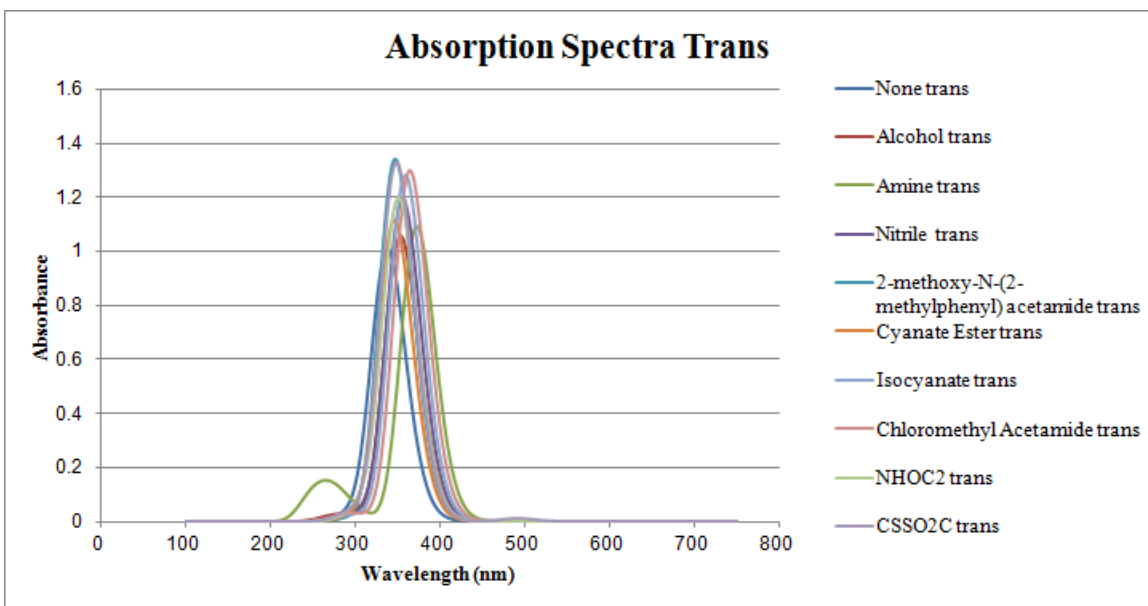
Fig. 13: Calculated absorption spectra for the *trans* isomer with various terminal groups
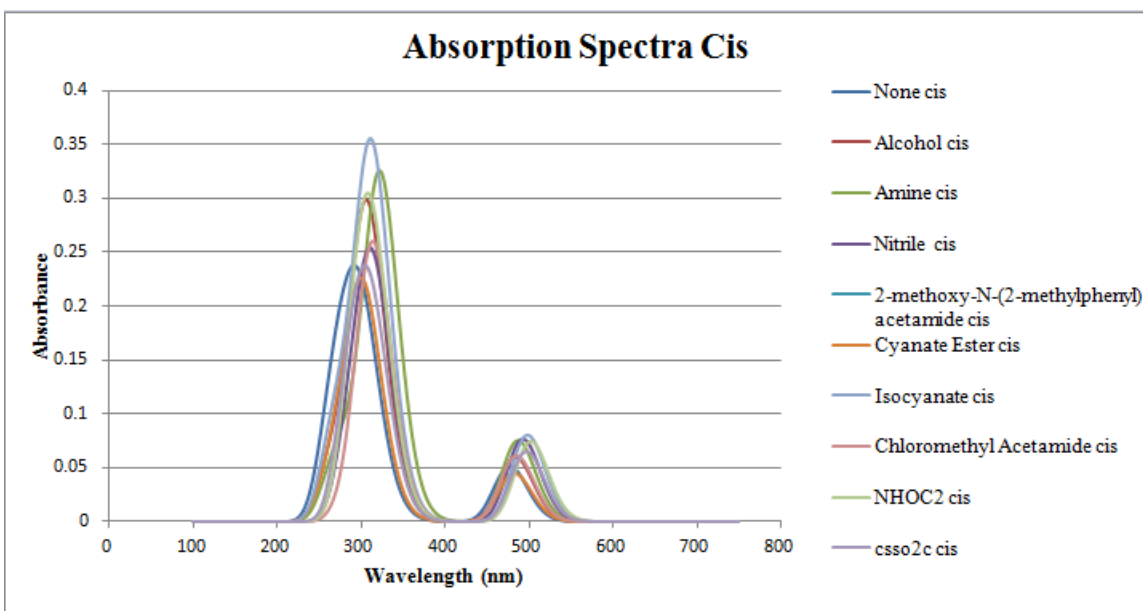
Fig. 14: Calculated absorption spectra for the *cis* isomer with various terminal groups.
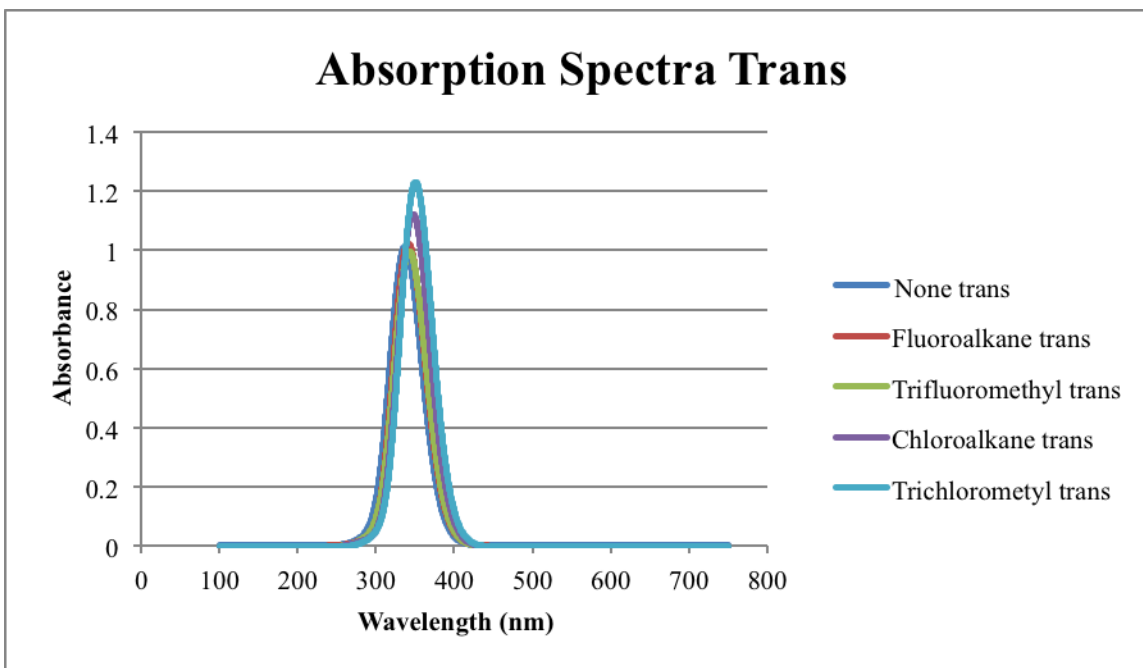
Fig. 15: Calculated absorption spectra for the *trans* isomer of azobenzenes with halogenated terminal groups
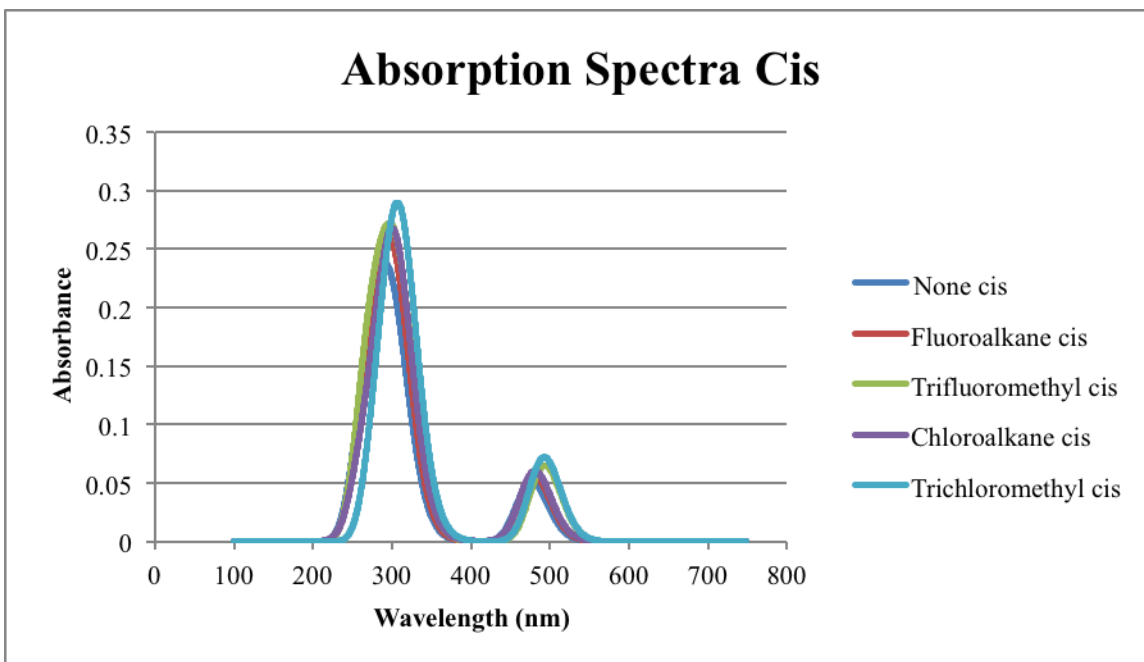
Fig. 16: Calculated absorption spectra for the *cis* isomer of azobenzenes with halogenated terminal groups.
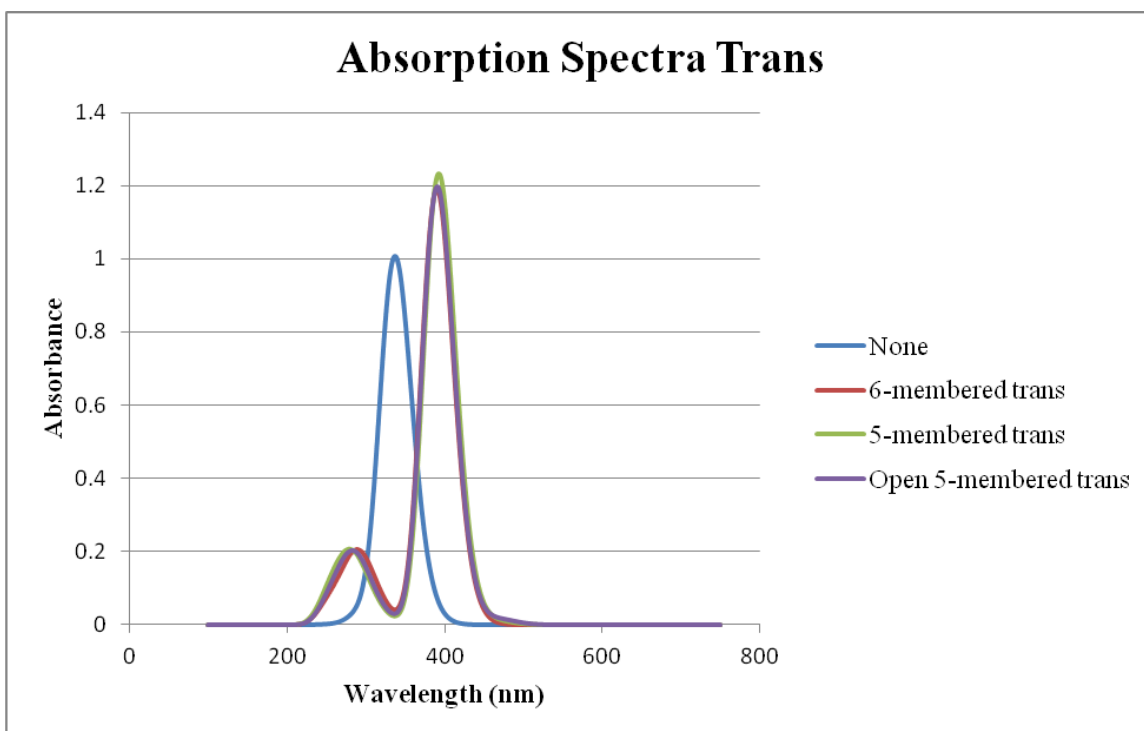
Fig. 17: Calculated absorption spectra for the *trans* isomer of various azobenzenes with terminal groups containing heteoaliphatic rings.

18
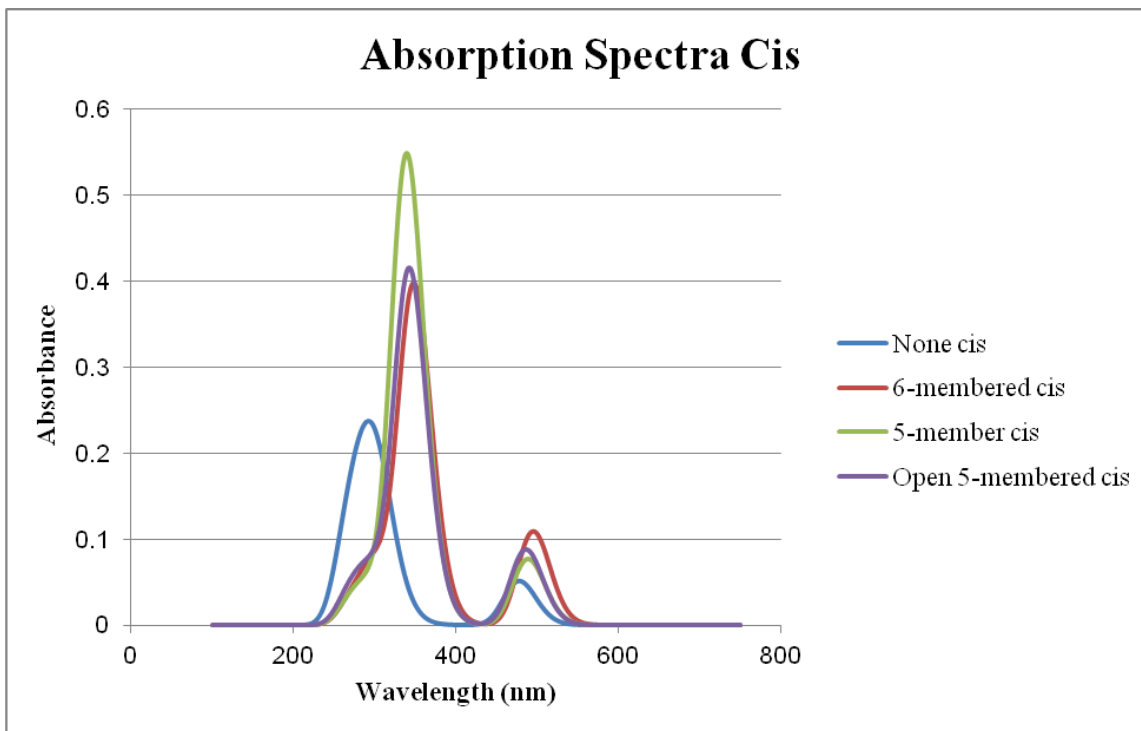
Fig. 18: Calculated absorption spectra for the *cis* isomer of various azobenzenes with terminal groups containing heteoaliphatic rings.

4. Conclusions

Using computational modeling, a azobenzene cores substituted with various terminal groups and tethered to a methacrylate oligomer by flexible alkyl chains were evaluated as potential candidates for photoswitchable alignment layers for an optically-switchable LC beam shaper. Both *trans-cis* isomerization energies and electronic absorption spectra for the various materials were calculated using Schrodinger's Materials Science Suite software using DFT and TDDFT computational methods. Alkyl spacer chains containing 5, 6, 8, and 9 carbons appear to be the optimal length for tethering the azobenzene to the methacrylate monomer to promote bistability; terminal groups containing ester and acetamide functionalities also appear to be valuable

components in this regard. With the exception of heteroaromatic rings, most of the terminal groups evaluated did not significantly alter the calculated absorption spectra of the materials. Future investigations will center around the more computationally intensive task of conducting an in-depth study of the effect of the most favorable terminal groups and alkyl spacer chains determined in this preliminary study on the *trans-cis* isomerization energies in photoswitchable polymeric systems employing from 3 to 15 or more monomeric repeat units.

5. Acknowledgements

6. References

1. Marshall, K. L. et al., "Liquid crystal beam-shaping devices employing patterned photoalignment layers for high-peak-power laser applications," Proc. SPIE 8114, Paper 81140P, (2011).

2. Marshall, K. L. et al., "Liquid crystal near-IR laser beam shapers employing photoaddressable alignment layers for high-peak-power applications," Proc. SPIE 8828, Paper 88280N (2013).

3. Levine, Ira N. (1991). Quantum Chemistry,: Prentice Hall, Englewood Cliffs, New Jersey , pp. 455–544.

4. Cramer, Christopher J. (2002). Essentials of Computational Chemistry. John Wiley & Sons Ltd ,Chichester, UK: pp. 153–189.

Effects of Alpha Particle Stopping-Power Models

on Inertial Confinement Fusion Implosions

Nathan Xu

Pittsford Sutherland High School, 55 Sutherland Street, Pittsford, NY, 14534

Advisor: Dr. S. X. Hu

Laboratory for Laser Energetics, University of Rochester, Rochester NY

October 2014

Abstract

An important issue in the design of inertial confinement fusion (ICF) implosion experiments is calculating the proper energy-deposition rate of the alpha particles as they travel through the plasma. In this project, four different models of stopping power (energy deposition), based on different physics approximations, have been examined: the Skupsky model (currently used in Laboratory for Laser Energetics' hydrocodes), the Li-Petrasso model, the quantum molecular dynamics model, and the Brown-Preston-Singleton model. These models have been tested for different deuterium-tritium (DT) plasma conditions such as temperature, density, and initial alpha particle energy. The models have been implemented into the one-dimensional hydro-code *LILAC*, allowing their effects on National Ignition Facility-scale ignition implosions to be investigated. Contrary to what was expected, the results show significant differences in the overall target performance depending on which model is used; differences in target gain vary by a factor of two. Finally, an experiment has been suggested to verify which model, if any, is truly valid.

1. Introduction

Around the world, nuclear fusion, a virtually inexhaustible source of power, has been studied for the past few decades. Inertial confinement fusion (ICF), using powerful lasers, is one way to make nuclear fusion a viable clean energy source [1]. During laser-driven ICF implosion experiments, laser pulses ablate the surface of a layered target and implode the target through the "rocket" effect [2]. The target is a spherical plastic capsule (Figure 1a) with a layer of deuterium-tritium (DT) ice, and filled with DT gas. The powerful laser-driven shocks and the spherical convergence, as shown in Figure 1b, compress the DT, creating extreme temperatures and pressures. The high temperatures and densities cause the DT to fuse together to produce energetic alpha (α) particles and neutrons (D+T=α+n+17.6 MeV). The alpha particle is created with an energy of 3.54 MeV.
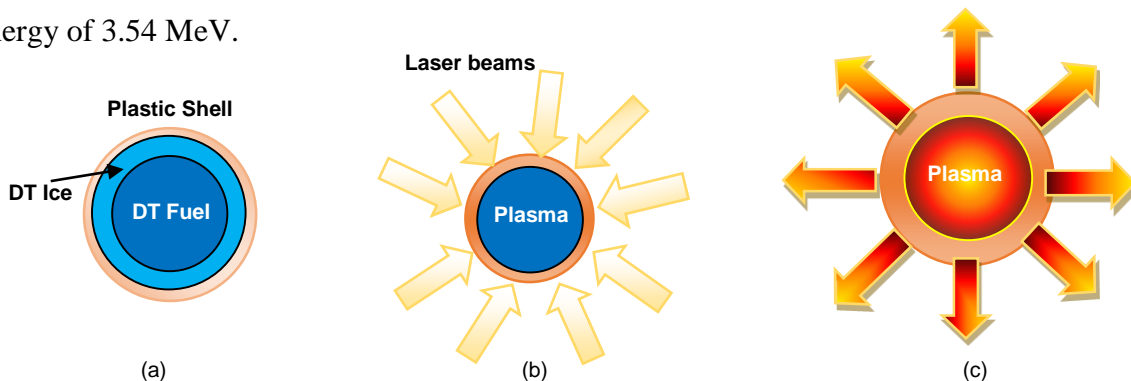
Figure 1: Illustration of the direct-drive ICF implosion
(a) The target is a spherical plastic capsule 1 to 3 mm in diameter; (b) The fuel target is compressed by the implosion of the hot surface material caused by laser shocks; c) The compressed hot fuel core ignites and the "bootstrapping" process occurs. Thermonuclear burn spreads, yielding many times the input energy.

The implosion generates a relatively low-temperature and high-density shell and a high-temperature and medium-density hotspot center. The alpha particles that are created from the reaction in the target center carry the energy that is necessary to further heat DT plasmas for more fusion reactions to occur, which is called a "bootstrapping" process. This "bootstrapping" process eventually leads to ignition and energy gain. Ignition is when output energy equals input energy or gain =1; gain is the ratio of output energy to input energy.

As the positively charged alpha particles travel through the plasma, they deposit their energies; the neutrons do not deposit a significant amount of energy in the plasma because neutrons are uncharged and marginally influenced by the plasma. Stopping power, the rate at which energy is transferred from the alpha particles back to the plasma, is directly involved in determining the

effectiveness of the "bootstrapping" process. In ICF simulation codes, stopping power is calculated by using a physics model that approximates the interaction process between traveling particles (i.e., alpha particles) and matter (i.e., the plasma). Several stopping power models have been proposed.

One of the purposes of this study is to evaluate four proposed models of stopping power in the one-dimensional simulation code LILAC currently used for ICF implosion experiments at the Laboratory for Laser Energetics (LLE), University of Rochester. The four models are the Brown-Preston-Singleton (BPS) model [3], the Li-Petrasso (LP) model [4], the Skupsky model [5], and the Quantum Molecular Dynamics (QMD) model [6]. The Skupsky model is currently used in the hydro-code *LILAC* [7]. In this study, the other three models were implemented into *LILAC* in order to estimate the stopping power in different DT plasma conditions such as temperature, density, and initial alpha particle energy. A comparison of results was performed to show the variations among the four models. Contrary to what was expected, the results show significant differences in the overall target performance depending on which model is used; differences in target gain varied by a factor of two. Finally, an experiment has been suggested to verify which model, if any, is truly valid.

The paper is organized as follows: In Section 2, the four stopping power models are described. In Section 3, results are presented for the comparisons of these four models. The stopping power effects are examined in hydro-simulations in Section 4. In Section 5, a future experiment to test the four models in measurable plasma conditions is suggested. Finally, a conclusion is presented in Section 6.

2. Models of Stopping Power

2.1. Stopping Power

Stopping power describes the rate of energy loss by charged particles or the energy deposited in the matter. It can be expressed in a generic formula as shown in equation 2.1.1.

$$S(E) = -dE/dx \qquad\qquad 2.1.1$$

The stopping power, $S(E)$, of the matter is equal to the loss of energy E per unit path length, x. The mean travel range of the particle, Δx, can be calculated by integrating the reciprocal stopping power over energy shown in equation 2.1.2.

$$\Delta x = \int_0^{E_0} \frac{1}{S(E)} dE \qquad\qquad 2.1.2$$

where E_0 is the initial kinetic energy of the particle. The total deposited energy can be obtained by integrating the stopping power over the entire path length of the particle while it moves in the matter.

In plasma physics, stopping power is defined as the retarding force acting on charged particles due to interaction with matter, resulting in loss of particle energy [8]. In the beginning of the slowing-down process at high energies, the charged particle is slowed down mainly by electrons and moves in a nearly straight path. When the particle has slowed down sufficiently, its collisions with ions dominate the slowing down process while its path becomes more erratic [9]. In direct-drive ICF implosion experiments, an alpha particle from DT fusion encounters various conditions while traveling from the hot spot center towards the outside, e.g., hot and cold temperatures and low and high densities [2]. When the DT fuel absorbs enough α-particle energy so that the plasma temperature increases, more fusion reactions are started and the burn process begins. The stopping power determines the number of subsequent fusion reactions that occur within the target. Thus, the stopping power is directly involved in determining the energy output. The stopping power of a particle depends on the temperature and density of the matter and the energy of the particle passing through the matter.

2.2. Models of Stopping Power

The stopping power of a charged particle is usually attributed to two major types of interactions between the charged particle and the plasma: electron and ion stopping power. Electron stopping power refers to the slowing down of a traveling ion due to inelastic collisions between bound electrons in the matter and the ion moving through it. Ion stopping power refers to the elastic collisions between the traveling ion and ions in the plasma. The interaction between the ions and plasma is a rather complex process. It is very difficult to describe all possible interactions for all possible ion charge states. Analytic models have been proposed based on these major interactions under certain assumptions. For example, a Coulomb logarithm is used in each model discussed below to model the Coulomb interactions between charged particles. The Coulomb logarithm is a unit-less parameter fundamental to many plasma properties; it helps to determine charged particle stopping in the plasma.

These models differ to some degree in their assumptions. These assumptions are often related to the condition of the plasma. For example, the differing physics assumptions of each model affect the pre-factor and parameters used in the Coulomb logarithm.

A. Brown-Preston-Singleton (BPS) model

Brown, Preston and Singleton introduced the BPS model in 2005 [3]. The BPS model utilizes the dimensional continuation method, which is related to the quantum mechanical description of dense plasmas, to compute the energy loss rate for a non-relativistic particle moving through fully ionized plasma. The model worked out a formula for the electron-ion energy transfer rate in a wide range of plasma conditions including quantum and coupling effects. The BPS model puts no restriction on the charge, mass, or speed of a particle. It assumes that the plasma is not strongly coupled in the sense that the dimensionless plasma coupling parameter is small.

The total stopping power for BPS is the sum of the following two formulas:

$$\frac{dE_p}{dx} = \frac{e_p^2}{4\pi}\frac{\omega_b^2}{v_p^2}(\ln\Lambda) \qquad\qquad 2.2.A1$$

$$\frac{dE_p}{dx} = \frac{e_p^2}{4\pi}\kappa_e^2(\ln\Lambda)\frac{2}{3}\left(\frac{\beta m_e v_p^2}{2\pi}\right)^{\frac{1}{2}} \qquad\qquad 2.2.A2$$

where the ionic plasma frequency is $\omega_b^2 = 4\pi e_b^2 n_b/m_b$, n_b is the ion density, m_b is the ion mass, m_e is the electron mass, e_b is the background ion charge, e_p and v_p are the charge and velocity of the projectile particle, $\ln\Lambda$ is the Coulomb logarithm, β is $1/k_B T$, k_B is the Boltzmann constant, and κ_e is the electron Debye wave number. Subscript p is used when describing the projectile particle; subscript b is used when describing the background plasma ions. Equation 2.2.A1 gives the stopping power due to ions and equation 2.2.A2 gives the stopping power due to electrons.

The Coulomb logarithm $\ln\Lambda$ in the BPS model is comprised of three terms [3], a main term and two correction factors, shown here:

$$\ln\Lambda_{BPS} = \ln\Lambda_{BPS}^{QM} + \ln\Lambda_{BPS}^{\Delta C} + \ln\Lambda_{BPS}^{FD} \qquad\qquad 2.2.A3$$

The leading term incorporates quantum mechanics effects, while the second term is a correction for the case where the plasma coupling parameter is no longer near the quantum limit; the third term takes the many-body electron degeneracy effect into account when Fermi-Dirac statistics become relevant. Each term, ignoring small electron-ion mass ratio effects, is given as:

$$\ln\Lambda_{BPS}^{QM} = \frac{1}{2}\left[\ln\left(\frac{8k_B^2 T_e^2}{\hbar^2\omega_e^2}\right) - \gamma - 1\right] \qquad\qquad 2.2.A3.1$$

$$\ln\Lambda_{BPS}^{\Delta C} = \frac{e_H}{k_B T_e}\sum_i\frac{\omega_i^2 Z_i^2}{\omega_I^2}\left\{1.20205\left[\ln\left(\frac{k_B T_e}{Z_i^2 e_H}\right) - \gamma\right] + 0.39624\right\} \qquad 2.2.A3.2$$

$$\ln\Lambda_{BPS}^{FD} = \frac{n_e\lambda_e^3}{2}\left\{-\frac{1}{2}\left(1 - \frac{1}{2^{3/2}}\right)\times\left[\ln\left(\frac{8k_B^2 T_e^2}{\hbar^2\omega_e^2}\right) - \gamma - 1\right] + \left(\frac{\ln 2}{2} + \frac{1}{2^{5/2}}\right)\right\} \quad 2.2.A3.3$$

where e_H is the binding energy of hydrogen, $\hbar = h/2\pi$, h is the Planck constant, Z_i is the effective charge number, n_e is the electron density, and γ is the Euler constant (0.57721). The electron and ion plasma frequencies are given by ω_e and ω_i, respectively; ω_I is the average ion frequency. The BPS model also includes the electron thermal wavelength, λ_e [3].

B. Li-Petrasso (LP) model

Li and Petrasso proposed their analytic model for charged-particle stopping powers for inertial confinement fusion plasmas in 1993[4]. Previously, ion stopping power for large-angle scattering was not considered or treated properly in the analytic models. Collective plasma effects were ignored and the plasma Fokker-Planck equation was limited to an upper limit. The LP model includes important effects, such as plasma ion stopping effects, collective plasma oscillation effects, and quantum effects. The LP model also generalizes the use of the Fokker-Planck equation, which properly treats the effects of large-angle scattering as well as small-angle collisions[4]. It was the first time that the effects of scattering had been properly treated in the calculation of charged-particle stopping power in inertial confinement fusion plasmas.

The LP stopping power formula for test particles (t) by field particles (f) is

$$\frac{dE_{(t,f)}}{dx} = -\frac{(Z_t e)^2}{v_t^2}\,\omega_{pf}^2\, G\left(x^{\frac{t}{f}}\right) ln\Lambda_b \qquad\qquad 2.2.\,B1$$

where $G\left(x^{\frac{t}{f}}\right)$ is given by

$$G\left(x^{\frac{t}{f}}\right) = \mu\left(x^{\frac{t}{f}}\right) - \frac{m_f}{m_t}\left\{\frac{d\mu\left(x^{\frac{t}{f}}\right)}{dx^{\frac{t}{f}}} - \frac{1}{ln\Lambda_b}\left[\mu\left(x^{\frac{t}{f}}\right) + \frac{d\mu\left(x^{\frac{t}{f}}\right)}{dx^{\frac{t}{f}}}\right]\right\} \qquad 2.2.\,B2$$

$$x^{\frac{t}{f}} = v_t^2/v_f^2 \qquad\qquad 2.2.\,B2.1$$

$$v_f^2 = \frac{2k_B T_f}{m_f} \qquad\qquad 2.2.\,B2.2$$

$$\omega_{pf} = (4\pi n_f e_f^2/m_f)^{1/2} \qquad\qquad 2.2.\,B2.3$$

$$\mu(x^{\frac{t}{f}}) = 2\int_0^{x^{\frac{t}{f}}} \frac{e^{-\xi}\sqrt{\xi}d\xi}{\sqrt{\pi}} \qquad\qquad 2.2.\,B2.4$$

The Coulomb logarithm is given by

$$ln\Lambda_b = ln\left(\frac{\lambda_D}{p_{min}}\right) \qquad\qquad 2.2.\,B3$$

$$p_{min} = [p_\perp^2 + (h/2m_r u)^2]^{1/2} \qquad\qquad 2.2.\,B3.1$$

$$p_\perp = e_t e_f / m_r u^2 \qquad\qquad 2.2.B3.2$$

$$m_r = (m_t m_f) / (m_t + m_f) \qquad\qquad 2.2.B3.3$$

The constants are defined here: $Z_t e$ is the test charge, e is the electron charge, v_t (v_f) is the test (field) velocity, m_t (m_f) is the test (field) mass, w_{pf} is the field plasma frequency, $\mu(x^{t/f})$ is the Maxwell integral; λ_D is the Debye length, m_r is the reduced mass and u is the relative velocity, n_t (n_f) is the test (field) density, e_t (e_f) is the test (field) charge. Test parameters are similar to projectile particle parameters and field parameters are similar to plasma parameters.

C. *Skupsky model*

Skupsky [5] was the first to examine the Coulomb logarithm for inverse-bremsstrahlung laser absorption for plasmas of different ionic charge, spanning the classical and quantum-mechanical limits. Previously, this term had not been calculated exactly for the conditions of interest in laser fusion experiments; it had only been estimated from physical considerations.

For short-wavelength irradiation (e.g., 0.35 μm), uncertainties in the "logarithmic" factor can produce variations of 20–50 % in the laser absorption coefficient. A more exact treatment of this term is presented here. For low-Z plasmas, a modified approximation is used that reproduces previous results for long-range interactions that cannot be described by a single electron-ion collision, and it simultaneously treats the short-range electron-ion encounters. For high-Z plasmas, the Coulomb logarithm is calculated in terms of the classical, nonlinear electron trajectory in a self-consistent electrostatic potential; strong ion-ion correlations are treated by the nonlinear Debye-Hückel model.

$$\frac{dW}{dx} = -\sqrt{W} n_e \frac{Z^2 e^4}{(k_B T)^{\frac{3}{2}}} \left(\frac{m_e}{M}\right)^{\frac{1}{2}} \sqrt{\pi}\, \frac{8}{3} \left(\frac{\sqrt{\pi}}{2F_{\frac{1}{2}}(\eta)} \frac{1}{e^{-\eta}+1}\right) \ln\Lambda_{RPA} \qquad\qquad 2.2.C1$$

where $F_{\frac{1}{2}}(\eta)$ is the Fermi integral

$$F_{\frac{1}{2}}(\eta) = \frac{1}{\Gamma\left(\frac{3}{2}\right)} \int_0^\infty \frac{t^{\frac{1}{2}}}{e^{t-\eta}+1} dt \qquad\qquad 2.2.C2$$

and where the Coulomb logarithm is defined as

$$\ln\Lambda_{RPA} = (1+e^{-\eta}) \int_0^\infty dk\, \frac{k^3}{(k^2+k_0^2)^2} \left[\exp\left(\frac{\hbar^2 k^2}{8 m_e k_B T}\right) - \eta\right]^{-1}. \qquad\qquad 2.2.C3$$

Equation 2.2.C1 is simplified into

$$\frac{dW}{dx} = \frac{Z^2 e^2}{2\pi^2 v_0} \int \frac{d\vec{k}(\vec{k}\cdot\vec{v}_0)}{k_D^2} Im \frac{1}{\epsilon(\vec{k},\vec{k}\cdot\vec{v}_0)} \qquad\qquad 2.2.C4$$

$$\epsilon\left(\vec{k}, \vec{k}\cdot\vec{v}_0\right) = 1 + \sum_s \frac{4\pi Z_s^2 e^2}{m_s k_D^2} \int d\vec{v} \frac{\vec{k}\cdot\partial f_s/\partial \vec{v}}{\omega - \vec{k}\cdot\vec{v}_0 + i\delta} \qquad 2.2.\,C5$$

where W is the particle energy, n_e is the electron number density, Z_s is the background ion charge, Z is the charge of the particle projectile, $\vec{v}_0$ is the velocity, k is the wave number of plasma electrons, η is the electron degeneracy parameter, f_s is the Fermi-Dirac single-particle distribution function, $k_0^2 = k_D^2 F'_{\frac{1}{2}}(\eta)/F_{\frac{1}{2}}(\eta)$, k_D is the Debye wave number, and $k_D^2 = 4\pi n_e e^2/k_B T$.

D. Quantum Molecular Dynamics (QMD) model

The QMD model is the same as the Skupsky model except that its Coulomb logarithm is replaced by the QMD-calculated one and the model considers many-body physics [6]. This means that the interactions between charged particles take into account all of a particle's nearby surroundings, rather than just the two particles directly involved in the collision.

The QMD stopping power is given by

$$\frac{dW}{dx} = -\sqrt{W} n_e \frac{Z_{eff}^2 e^4}{(k_B T)^{\frac{3}{2}}} \left(\frac{m_e}{M}\right)^{\frac{1}{2}} \sqrt{\pi}\, \frac{8}{3} \left(\frac{\sqrt{\pi}}{2F_{\frac{1}{2}}(\eta)} \frac{1}{e^{-\eta}+1}\right) \times (ln\Lambda)_{QMD} \qquad 2.2.\,D1$$

$$\left(\ln\Lambda\right)_{QMD} = \exp\left\{\alpha_0 + \sum_{i=1}^{5}\left[\alpha_i\left(\ln\Gamma\right)^i + \beta_i\left(\ln\theta\right)^i\right]\right\} \qquad 2.2.\,D2$$

where Z_{eff} is the effective charge number, $\theta = T/T_F$ is the degeneracy parameter (T_F is the Fermi temperature) and the values of α_i and β_i in $\ln\Lambda_{QMD}$ are listed in Table 1.

i	α_i	β_i
0	-0.74014809257279	
1	-0.18145905042211	+0.861554200945883
2	+6.39644338111 x 10^{-4}	-0.105703692158405
3	+1.47954277819 x 10^{-3}	-6.757828681522 x 10^{-3}
4	-1.23361568162 x 10^{-4}	-1.690070651236 x 10^{-4}
5	-2.58107191013 x 10^{-5}	+3.492008487199 x 10^{-4}

Table 1 The values of α_i and β_i used in the QMD model

3. Comparison of the Stopping Power Models

Within these equations, variables such as temperature, plasma density, and initial energy of a projectile can be varied to model different mediums. Each model was run through a simulation

code, with ICF-relevant electron and ion temperatures and plasma densities, to calculate the stopping power from each model as well as the distance traveled by an alpha particle starting with 3.54 MeV of energy. The greater the alpha particle distance traveled, the less the average stopping power. The most optimistic model for each specific condition is the model that predicts that the distance traveled by the alpha particle is the smallest; in other words, the alpha particle energy is deposited closer to the DT fuel (in the center).

3.1 Stopping Power in Hot Spot Plasma Condition

First, the stopping power was calculated from each of the four models at different alpha particle energy levels (0 to 3.54 MeV) in the plasma at a low DT density of 50 g/cc and a high temperature of 6000 eV. Note that the 3.54 MeV is the normal birth energy of alpha particles created by DT fusion and it is usually used as a starting energy for alpha particles in ICF implosion simulations. The models were compared for the stopping power of alpha particles traveling in the hot spot plasma. The stopping power (dE/dx) is calculated and plotted as a function of initial alpha particle energy as shown in Figure 2. In addition, the decrease of energy with distance traveled is plotted for an alpha particle with initial energy 3.54 MeV.
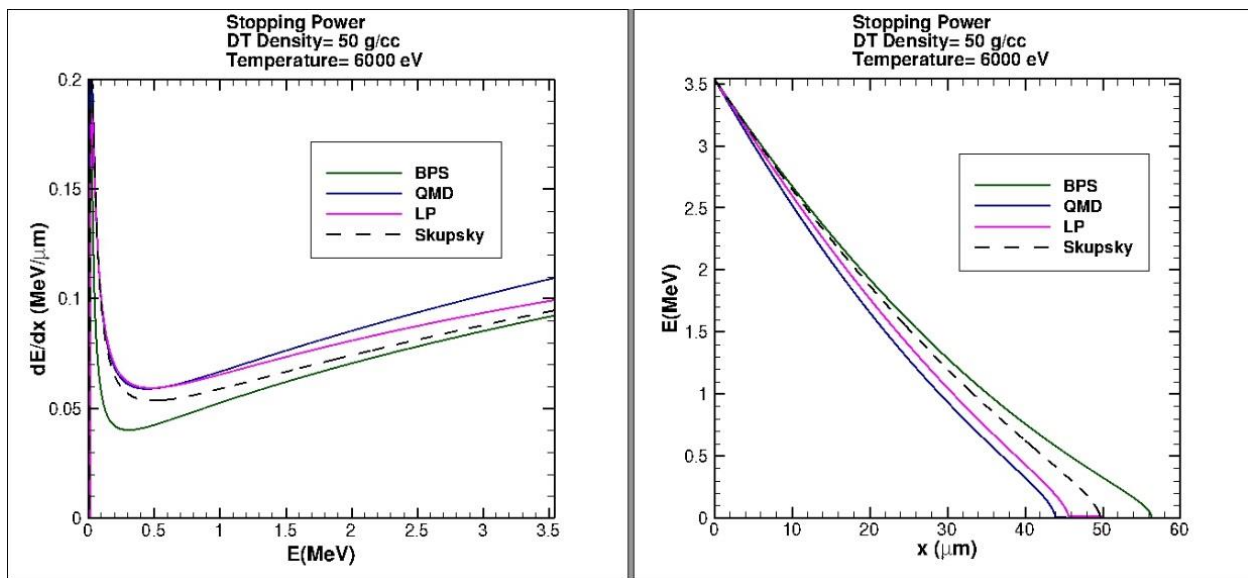
Figure 2: Stopping power calculated in the low-density and high-temperature plasma condition The stopping power is plotted as a function of alpha particle energy in the left panel. The right panel shows how far the alpha particle will travel in the hot spot plasma. The two figures are related in that the higher stopping power means a shorter distance traveled.

As shown in Figure 2, there is not much variation between the four models for stopping power or alpha particle distance traveled when the DT density is 50 g/cc and the temperature is 6000 eV. In hot spot DT-plasma conditions, the stopping power can vary by a maximum of 19% among the four models at a particle energy level of 3.54 MeV as shown in Figure 2.

3.2 Stopping Power in Lower Temperature and Dense Plasma Condition (DT shell)

The stopping power was also calculated from each of the four models at different energy levels (0 to 3.5 MeV) in the plasma at a higher DT density (400 g/cc) and a lower temperature (1000 eV). This combination of temperature and density simulates conditions similar to those of the DT shell.
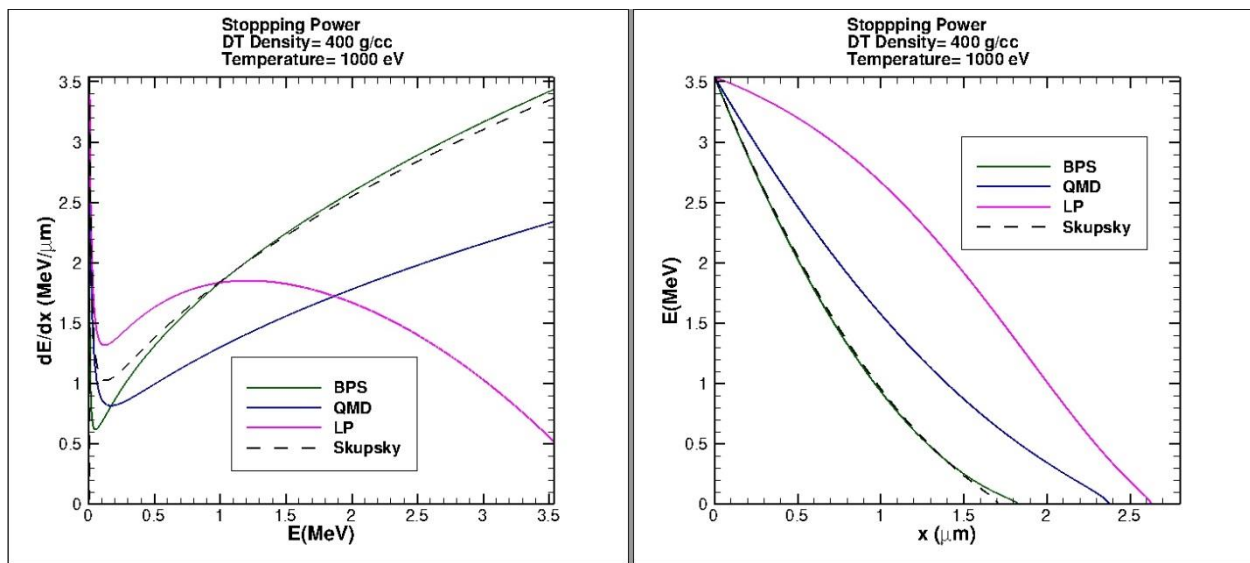
Figure 3: Calculated stopping power in a low temperature and high density plasma condition Stopping power is plotted as a function of alpha particle energy in the left panel. The right panel shows how far the alpha particle will travel in low temperature and dense plasma conditions. The two are related in that the higher stopping power means a shorter distance traveled.

The variations among the four models for stopping power and alpha particle distance traveled are rather significant for a low temperature and dense plasma condition as shown in Figure 3. The BPS and Skupsky models yield similar results for the stopping power at all energy levels. The stopping power calculated from the BPS model (3.4 MeV/μm) is roughly seven fold greater than the LP model stopping power (0.5 MeV/μm) when the alpha particle energy is 3.54 MeV. The right panel of Fig. 3 shows that the alpha particle distances traveled as calculated by the four

models vary from 1.7 μm to 2.6 μm. The Skupsky model predicted the smallest distance, making it the most optimistic model for these DT shell conditions.

In general, the stopping power decreases and the distance traveled by an alpha particle increases as the temperature increases. The opposite is true as the density increases, when the stopping power increases and the distance traveled by an alpha particle decreases. An increase in the stopping power leads to more energy being deposited closer to the DT fuel in the center, which allows more fusion reactions to occur.

Some interesting results are found from careful inspection of the stopping power models. First, the models are affected differently by changes in the initial energy of alpha particles, as seen in Figures 2 and 3. Second, a comparison of the figures shows that the order of the stopping power models in terms of the distance traveled from the least to greatest changes when the plasma conditions (temperature and density) are changed.

	% change in distance traveled Temperature (300eV → 1000 eV)		% change in distance traveled Temperature (1000 eV→5000 eV)	
	Density= 400 g/cc	Density= 1000 g/cc	Density=400 g/cc	Density=1000 g/cc
BPS	4450	8525.0	339.6	455.1
QMD	17.5	45.5	152.1	71.3
LP	-	-	151.9	-
Skupsky	486.2	1100.0	233.6	275.0

Table 2 Percent change in the distance traveled by an alpha particle at the conditions of plasma density at 400 g/cc and 1000 g/cc when the temperature changes from 300 eV to 1000 eV and from 1000 eV to 5000 eV, respectively. The percent change of distance traveled by an alpha particle as shown in this table is positive.

Tables 2 and 3 show the change (%) in distance traveled by an alpha particle when the temperature and density change. Table 2 shows the change in distance when the temperature changes from 300 to 1000 eV and from 1000 to 5000 eV at 400 g/cc and 1000 g/cc, respectively. The BPS and Skupsky models are affected more by temperature than the QMD model.

	% change in distance traveled Density (400 g/cc→1000 g/cc)	% change in distance traveled Density (400 g/cc→1000 g/cc)
	Temperature= 5000 eV	Temperature= 1000 eV
BPS	-52.1	-62.1
QMD	-54.7	-32.7
LP	-46.8	-
Skupsky	-53.3	-50.6

Table 3 Percent change in the distance traveled by an alpha particle at the temperature conditions of 5000 eV and 1000 eV, respectively, when the plasma density changes from 400 g/cc to 1000 g/cc. The percent changes for both conditions as shown in this table are negative changes (decreases).

At a temperature of 5000 eV, a density change as shown in Table 3 appears to affect all the models similarly; all models have about a 50% decrease in distance traveled. However, at a temperature of 1000 eV, the QMD model predicts a distance traveled that differs from the other models, which appear to be grouped together. The LP model only produces results for low DT density and high temperature conditions. There were many cases in Tables 2 and 3 where the LP model did not produce any data, indicating that the conditions were not applicable to the LP equation.

Overall, it appears that the alpha particle distance traveled is more sensitive to a change in temperature (Table 2) than a change in density (Table 3). A larger variation is seen at the lower temperature range (300 eV to 1000 eV).

4. Effects of Stopping Power Models in Hydro-Simulations

All four models were implemented into the one-dimensional hydrocode, *LILAC*, as a subroutine using the FORTRAN programming language. *LILAC* is used to simulate implosions. The effects of the different stopping power models were examined on National Ignition Facility (NIF)-scale ignition implosions through hydro-simulations. Results output by *LILAC*, such as total neutron yield, neutron-averaged ion temperature, and gain (the ratio of output energy to input energy) were used for analysis.

Two simulations were performed to examine the four proposed models in terms of the output gain, neutron yields and ion temperature. The simulations have different adiabats, which is the ratio of plasma pressure to the Fermi degeneracy pressure. The adiabat is a measure of how cold the target is.

The cross session of the target used in the simulations is shown in Figure 4. The target is a spherical plastic (CH) capsule (37 μm thick) with a layer of 150 μm of deuterium-tritium (DT) ice, and is filled with three atmospheres of DT gas (radius of 1500 μm).
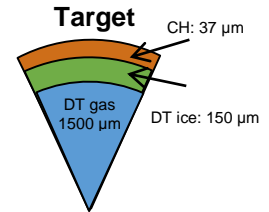
Figure 4: Cross section of the simulation target.

4.1 *LILAC* Simulation at a Moderate Adiabat (α=2)

The first simulation was performed at a moderate adiabat (α=2). A laser beam, with its pulse shape described in Figure 5a, is fired at the target. Figure 5b is the snapshot of density and ion temperature distributions in the target within the radius of 150 um from the target center at 11.361 nanoseconds (soon after the beginning of the burn process) of the implosion. It is evident, as shown in Figure 5b, that there are large differences among the four models while the Skupsky model and LP model are nearly identical. Table 4 shows how the ion temperature differences affect the output performance.

(a)   (b)
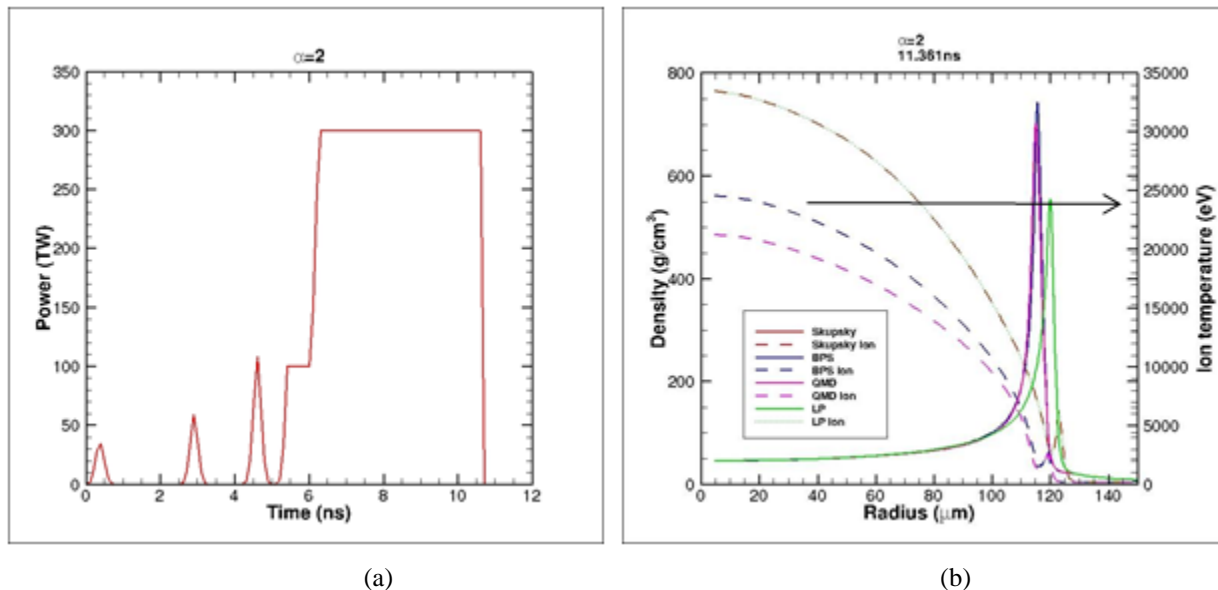
Figure 5: (a) Pulse shape in terms of power (TW) for the α=2 design. (b) Snapshot of density (solid curves) and ion temperature (dotted curves) distributions at 11.361 nanoseconds (beginning of the burn process) of the implosion in the *LILAC* simulation at an adiabat of 2.0.

14

The goal of the NIF is to maximize the outputs (Table 4) of an implosion, especially the gain. The total neutron yield, ion temperature, and gain are important in determining the effectiveness of an implosion. In Table 4, the results of the different stopping power models show significant changes in the overall target performance, in which the target gain could vary by a factor of nearly two, 1.87 to be exact.

Outputs from simulation Moderate adiabat (α=2)	BPS	LP	QMD	Skupsky
Total neutron yield	1.78E+19	2.35E+19	1.25E+19	2.35E+19
Neutron-averaged ion temperature	20.68 keV	28.88 keV	15.14 keV	28.88 keV
Gain (output energy/ input energy)	33.263	43.924	23.482	43.922

Table 4 The total neutron yield, the ion temperature, and the gain from all four models in the LILAC simulation at adiabat of 2.0.

4.2 *LILAC* Simulation at a Low Adiabat (α=1.7)

In the second simulation, the same target shown in Figure 4 is used but in a low (α=1.7) adiabat condition. In Figure 6a, the pulse shape for the low adiabat is different than that for the moderate adiabat. The low adiabat pulse is in a linear ramp shape. It is designed to avoid hot electron generation and electron preheating by slowly increasing the power.

Similar to moderate adiabat conditions, there are large differences in the density (solid lines) and ion temperature (dotted lines) distributions in the target among the models as shown in Figure 6b, while the Skupsky model and LP models are again nearly identical. In Table 5, the results show even larger changes in overall target performance, a difference by a factor of 2.66.

For both low and moderate adiabats, there are significant differences in the predictions of gain from the four stopping-power models that warrant further investigation. Accurate gain predictions allow for better nuclear fusion implosion experiments to be designed in the future. The gain from the implosion is the ultimate goal of nuclear fusion as an energy resource, so it is important to find a model that can accurately predict target performance.

(a)   (b)
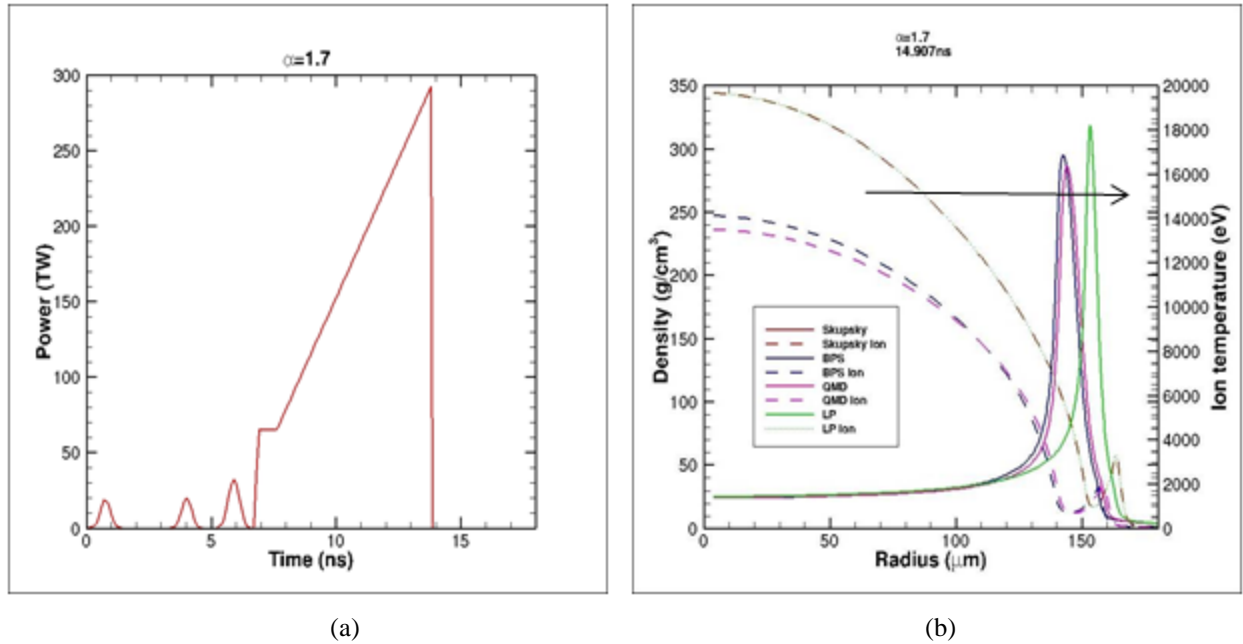
Figure 6: (a) Pulse shape in terms of power (TW). (b) Snapshot of density (solid lines) and ion temperature (dotted lines) distributions at 11.361 nanoseconds (soon after the beginning of the burn process) of the implosion in *LILAC* simulations at an adiabat of 1.7.

Outputs from simulation Moderate adiabat (α=1.7)	BPS	LP	QMD	Skupsky
Total neutron yield	2.29E+18	5.64E+18	2.12E+18	5.64E+18
Neutron-averaged ion temperature	8.81 keV	11.95 keV	8.57 keV	11.95 keV
Gain (output energy/ input energy)	5.374	13.218	4.966	13.216

Table 5 The total neutron yield, the ion temperature, and the gain from all four models in the *LILAC* simulation at an adiabat of 1.7.

5. Suggested Future Validation Experiments

The *LILAC* simulations above, although representative of ICF implosions in terms of density and ion temperature levels, do not have testable conditions—as it is very hard to make uniform plasma under such conditions. More measurable plasma conditions are proposed, i.e., density= 1 g/cc and temperature=10 eV, which can be used to validate which one of the four stopping-power models best represents reality. Protons, which are more viable and manageable particles compared to alpha particles, are proposed for this experiment. The stopping power and distance traveled by a proton calculated from the four models are shown in Figure 7.
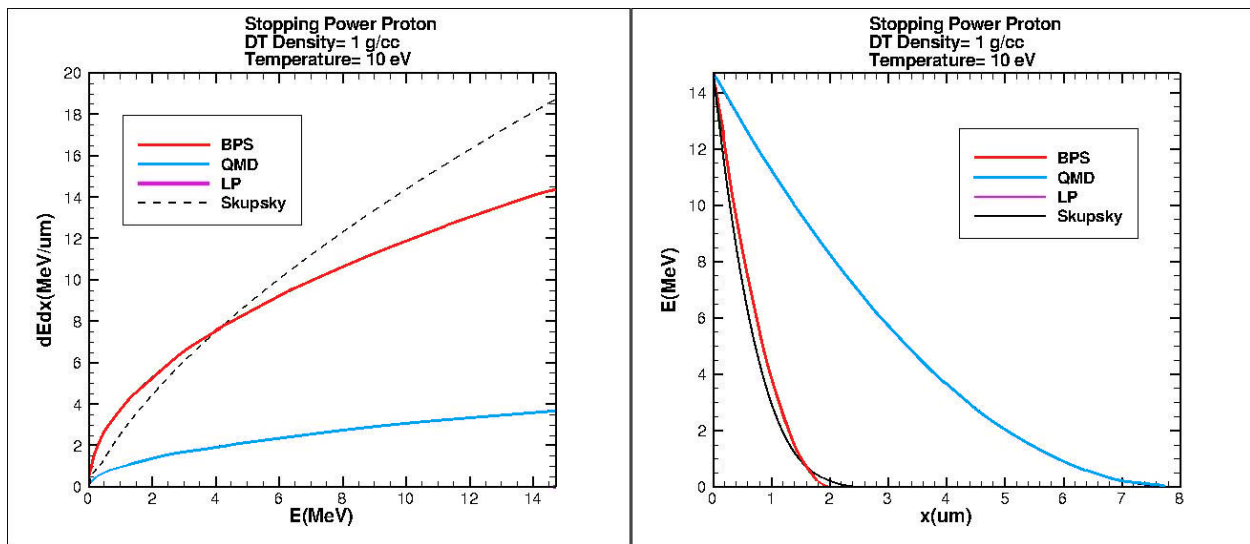
Figure 7: Calculated stopping power for a density of 1 g/cc and temperature of 10 eV
Stopping power is plotted as a function of proton particle energy in the left panel. The right panel shows how far the proton particle will travel in the plasma when the DT density is 1 g/cc and the temperature is 10 eV. On the left panel, the LP model predicts a stopping power curve that is very close to 0 MeV/μm or negative; this makes the curve invisible. This translates into the LP model predicting a curve, on the right panel, that does not fit in the limits of the right panel.

In an ideal case, the actual physical measurements from this experiment would validate which stopping power model is the most accurate: there would be a model that closely coincides with the experiment's results. However, the actual physical measurements may not match any of the models. All in all, the experimental results may guide researchers in finding future improvements of stopping power models. But even so, being able to predict the stopping power at 1 g/cc and 10 eV does not necessarily allow one to validate models at 50 g/cc and 6 keV or 400 g/cc and 1 keV.

6. Conclusion

The stopping power models, Brown-Preston-Singleton (BPS), Li-Petrasso (LP), Quantum Molecular Dynamics (QMD), and Skupsky (currently used in LLE's hydro-codes), have been examined in ICF plasmas. These models have been tested for different deuterium-tritium (DT) plasma conditions such as temperature, density, and initial alpha particle energy. The four stopping power models vary due to the different physics in each model. The results have been analyzed for similarities, differences, and patterns between these four models. An important discovery is that these models show large differences in DT-shell conditions. The results show that as temperature increases, the distance traveled by an alpha particle increases—in other words, the average stopping power decreases.

The stopping power effects are further examined in hydro-simulations using the program *LILAC* to predict ICF performance. The results show significant changes in the overall target performance depending on which model is used; changes in target gain varied by a factor of two. Finally, a future experiment for testing the four models in measurable plasma conditions was suggested. This experiment could help determine if any of the models agree or closely coincide with experimental results.

Acknowledgements

References

1. S. Atzeni and J. Meyer-ter-Vehn, "The Physics of Inertial Fusion: Beam Plasma Interaction, Hydrodynamics, Hot Dense Matter," International Series of Monographs on Physics (Clarendon Press, Oxford, 2004).

2. J. H. Nuckolls, L. Wood, A. Thiessen, and G. B. Zimmerman, "Laser Compression of Matter to Super-High Densities: Thermonuclear (CTR) Applications," *Nature* 239, 139 (1972).

3. L.S. Brown, D. L. Preston, and R.L. Singleton, Jr., "Charged Particle Motion in a Highly Ionized Plasma," Phys. Rep. 410, 237 (2005).

4. C.K. Li and R.D. Petrasso, "Charged-Particle Stopping Powers in Inertial Confinement Fusion Plasmas," Phys. Rev. Lett. 70, 3059 (1993).

5. S. Skupsky, "Energy Loss of Ions Moving Through High-Density Matter," Phys. Rev. A 36, 5701 (1987).

6. S.X. Hu, L.A, Collins, T.R. Boechly, J.D. Kress, V.N. Goncharov, and S. Skupsky, "First-Principles Thermal Conductivity of Warm-Dense Deuterium Plasmas for Inertial Confinement Fusion Applications," Phys. Rev. E 89, 043105 (2014).

7. J. Delettrez, R. Epstein, M. C. Richardson, P. A. Jaanimagi, and B. L. Henke, "Effect of Laser Illumination Nonuniformity on the Analysis of Time- Resolved X-Ray Measurements in UV Spherical Transport Experiments," Phys. Rev. A 36, 3926 (1987).

8. International Commission on Radiation Units and Measurements Report 73: "Stopping of Ions Heavier than Helium," Journal of the ICRU, 5 No. 1 (2005), Oxford Univ.

9. International Commission on Radiation Units and Measurements (October 2011). "Fundamental Quantities and Units for Ionizing Radiation," in Seltzer, Stephen M. *Journal of the International Commission on Radiation Units and Measurements* (Revised ed.) 11 (1).

Limits on the Level of Fast Electron Preheat In Direct-Drive Ignition Designs

Christopher Ye

Webster Schroeder High School

Advisor: **Dr. Jacques Delettrez**

Laboratory for Laser Energetics

University of Rochester

Rochester, NY

January 2015

1. Abstract

Inertial confinement ignition designs are characterized by their gains (energy produced over energy input), which can be reduced by preheat of the fuel. High intensity lasers like the ones used in direct-drive ignition create plasma instabilities, producing fast electrons. When fast electrons penetrate the cold fuel shell, they preheat the target, increasing the adiabat (a measure of the preheat) and decreasing the gain. The one-dimensional hydrodynamic code LILAC was used to simulate target implosions affected by the fast electrons. The optimizing code TELIOS adjusted the picket timings and levels in the laser pulse for the implosions in an attempt to decrease the preheat and counteract the decrease in gain caused by fast electrons. Optimization with TELIOS was able to partially recover the gain by varying the picket timings and powers.

2. Introduction

Direct-drive ignition is one of two ways that inertial confinement fusion (ICF) is carried out.[1] Direct-drive ICF uses high intensity lasers focused directly on the surface of a target, which contains the fuel used in fusion, in order to compress it. The laser energy heats up the outside shell of the target, usually composed of a carbon-hydrogen compound, which then ablates outwards and compresses the fuel in the center of the target. The energy of this compression triggers fusion, which releases energy. The DT fuel is composed of a mix of deuterium and tritium, two isotopes of hydrogen. Deuterium contains one neutron and tritium contains two, whereas normal hydrogen atoms have none. When deuterium and tritium are combined, an atom of helium is produced along with a neutron, accompanied by a release of energy. This released energy, divided by the energy input by the laser, is known as the gain. A high gain is required for fusion to be an efficient energy source.

One of the methods used to improve the gain is using cryogenic targets. While normal targets contain DT gas only, cryogenic targets contain a layer of frozen DT ice with a low-density DT gas inside. The frozen DT is denser than the DT gas, so it is possible to fit more fuel into the target. In the simulations used in this project, a high-gain target designed for the National Ignition Facility (NIF), composed of a 1,338 μm layer of DT gas, a 199 μm layer of DT ice, and a 39 μm layer of CH plastic [Fig. 1] was irradiated with a 1.6 MJ laser pulse [Fig. 2]. This target requires low preheat of the fuel before implosion, as preheat reduces the fuel compressibility and the energy gained from fusion.
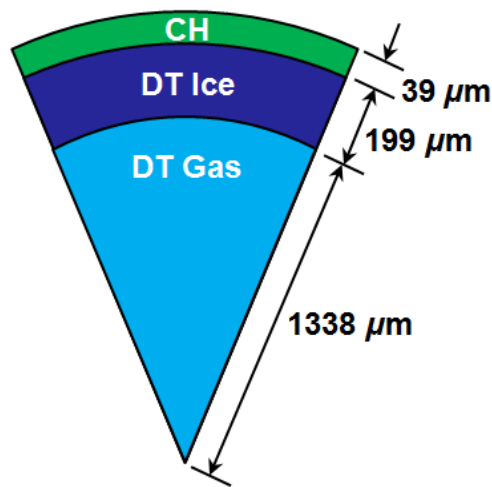
Figure 1: Structure of a typical high gain cryogenic target. The ice layer is much thinner than the gas layer, and is deposited inside the CH shell.
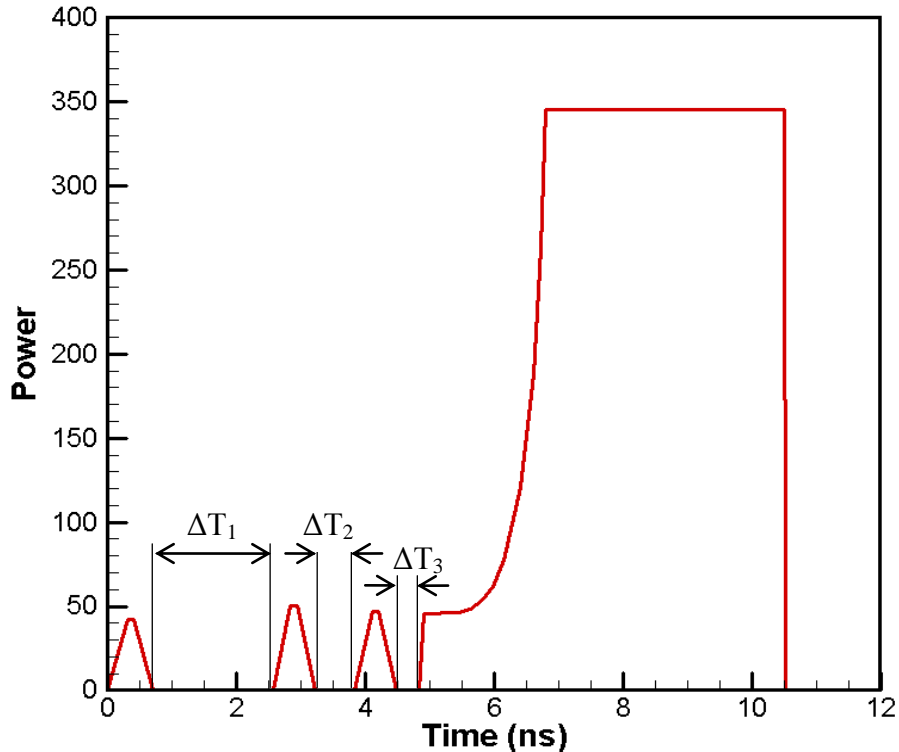
Figure 2: Typical laser pulse (power in TW) used in an ICF high gain design. The three small spikes are the pickets, and the much larger shape is the main pulse, which contains the majority of the laser's energy.

A primary cause of preheat in the targets is from the fast electrons that are created by laser-plasma instabilities. When the natural plasma frequency is resonant with (typically) half the laser frequency, instabilities occur which produce fast electrons. They can reach temperatures of 60 keV, compared to 3 keV in the corona of the target. These fast electrons penetrate the cold fuel and lose their energy, heating up the fuel. This preheat can prevent the fuel from being compressed to a sufficiently high density to reach ignition. Preheat was measured in this project as the percentage of the laser energy that is deposited by the fast electrons into the cold fuel shell. The gain was plotted in Fig. 3 as a function of preheat. As a result of density changes, increases in preheat result in a steep drop-off in the gain.

4

The compressibility of the fuel can be measured using the concept of adiabat (defined as the electron pressure divided by the pressure that the shell would have at a temperature of absolute zero). Lower adiabat values correspond to low preheat and higher levels of compressibility. The adiabat of the target must have a value under around 3 before the target is compressed by the main pulse in order for the implosion to reach high gains. But, when the target experiences high enough levels of preheat, the adiabat before compression becomes too large for effective fusion reactions [Fig. 4].
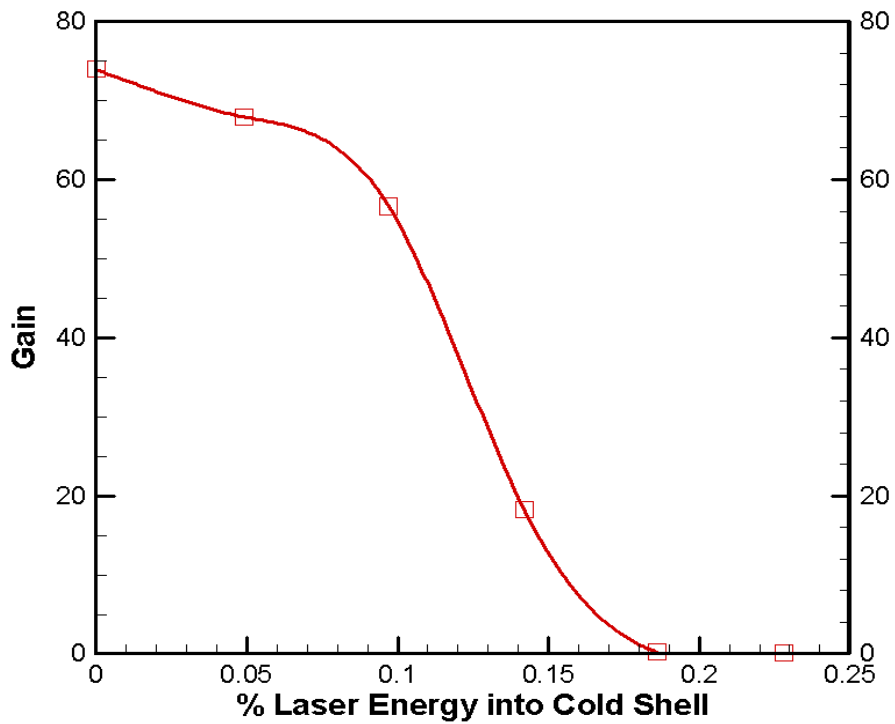
Figure 3: The effect of preheat on gain in ICF. Preheat is measured by the percentage of laser energy deposited in the cold fuel shell.

Effect of fast electron energy deposition in the cold shell on the minimum adiabat
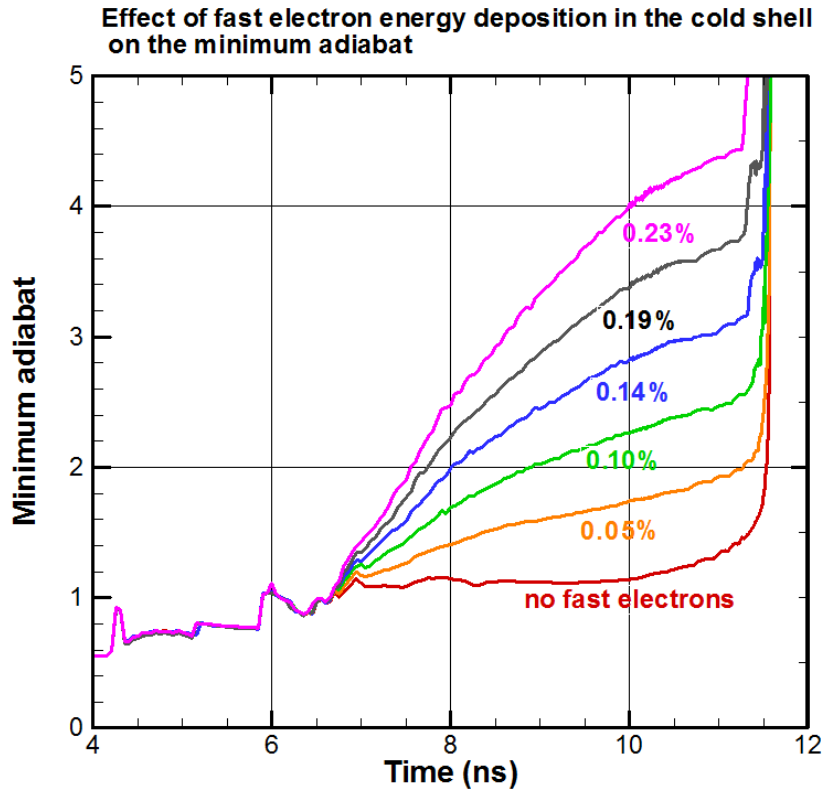
Figure 4: Effect of fast electron energy deposition in the cold shell on the minimum adiabat. The six lines correspond to the six preheat conditions in Fig. 3.

Because the NIF is normally able to fire its laser only one to three times a day, this study would have been impossible to conduct using an actual laser and target. Instead, the one-dimensional hydrodynamic code LILAC[2] was used to simulate the implosions. LILAC takes input decks including the parameters of the shot and runs through the implosion, computing conditions in the target for each time step.

In this project, the amount of preheat was manipulated by changing the parameters of the laser pulse. The laser pulse (Fig. 2) is composed of a main pulse preceded by three "pickets," which are smaller laser pulses that deliver small shocks to the target and prepare it for the main pulse. The times between pickets and the powers of the pickets were the six variables used to adjust the level of preheat.

Since there were an unlimited number of possible combinations of different parameters for the pickets, an optimizer was used to find the right set of parameters which resulted in the highest gain. The optimizing code TELIOS[3] was used to find the picket timings and powers that gave the highest gain, and therefore were affected the least by preheating. The code required an input of all the laser pulse and target parameters for the basic simulation. Then TELIOS modified each picket parameter slightly using a downhill simplex method (Nelder-Mead method) until it found the highest possible gain. This saved the time that would have been required to enter new input decks and manually decide how to adjust the variables.

3. Initial Attempts

At first, only the timings of the pickets were adjusted in an attempt to reduce the effects of preheat on the gain. TELIOS was given an input deck for the LILAC simulation discussed previously, and was allowed to manipulate only the time between the first and second picket, the time between the second and third picket, and the time between the third picket and the main pulse. From this initial "guess," it ran subsequent LILAC simulations in an attempt to obtain the maximum possible gain. TELIOS was given input decks with the six preheat conditions presented above to optimize, each with an increasing amount of preheat. The goal was to reduce the steep drop-off in gain that occurs once the percentage of laser energy into the cold fuel shell reaches about 0.1% (see Fig. 3). But TELIOS was unable to recover the gain in any significant manner when more than 0.1% of the laser energy entered the cold shell [Fig. 5]. At around 0.14% of laser energy into the cold shell, TELIOS was able to recover the gain by about 8, but it was not enough to create a significant amount of leeway in the percentage of laser energy in the

cold shell tolerable to the gain. For all five other conditions of preheat, TELIOS was unable to recover the gain by more than 5.
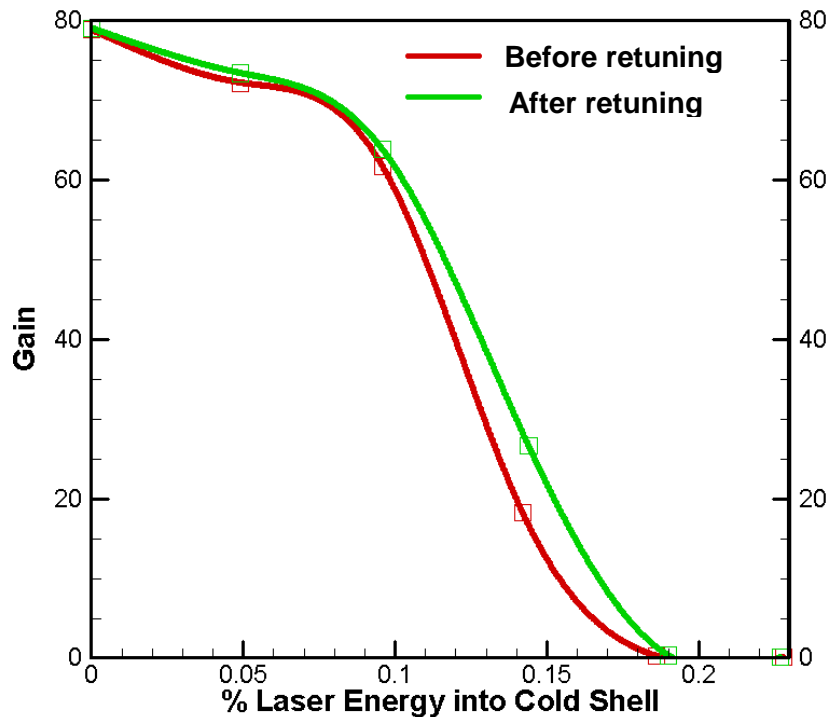
Figure 5: Effects on gain of retuning the picket timings. The curves are fitted to data points from the six different conditions of preheat that TELIOS retuned.

The initial retuning attempts were done with a straight-line model for fast electron transport. Under this model, the fast electrons are simulated as single particles that travel in straight lines and bounce off the outer edges of the target. The modeled electrons bounce inside the cold shell until they deposit all of their energy. Another model for electron transport in LILAC is the diffusion model, in which the electrons slowly diffuse throughout the cold shell, depositing energy as they move through it. It is unknown which model presents the more accurate picture of what actually occurs during fusion reactions, and the reality is most likely a combination of both. So, the diffusion model was also used in TELIOS retunings in order to see whether there was a difference in results between the two models. The results for the TELIOS

runs using the diffusion model saw more improvement than the runs with the straight line model [Fig. 6]. The fourth condition of preheat, where around 0.23% of the laser energy went into the cold shell, showed the most significant improvement. The retunings at 0.17% and 0.29% were also more successful than the retunings using the straight line electron transport model. But the retuning still gave less than 0.05% of leeway for the amount of laser energy into the cold shell permitted without severely damaging the gain. It was clear that retuning the three picket timings alone was not enough to significantly recover the gain from the effects of fast electron preheat.
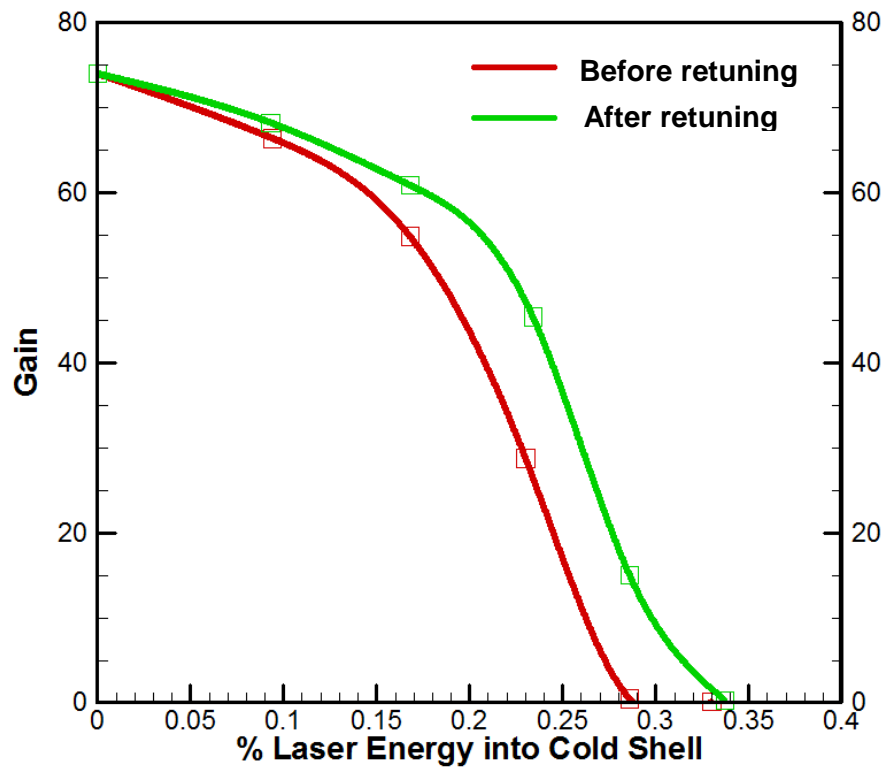
Figure 6: TELIOS retunings using the diffusion model of fast electron transport. These retunings showed much greater improvements, including an increase in gain of almost 20 when about 0.23% of the laser energy went into the cold shell.

4. Picket timing and power retunings

The next logical step was to retune the picket powers as well as the timings. TELIOS was therefore allowed to adjust the three picket timings as well as the three picket powers, for the same six conditions of preheat. This produced slightly better results [Fig. 7]. Figure 8 gives the change in the picket pulse parameters from the original setting to the one that produced the best improvement in gain. Several conditions of preheat saw larger recoveries in gain than when only the picket timings were retuned. The most dramatic improvement was seen in the fourth condition of preheat, with around 0.14% of the laser energy deposited into the cold shell. In this case, TELIOS was able to more than double the gain, giving about 0.03% more tolerance of laser energy into the cold shell. Although this was an improvement over the retuning using only the picket timings, it is not enough to significantly reduce the effects of fast electron preheat. Other factors will need to be explored to determine if it is possible to cancel out its effects on the gain.
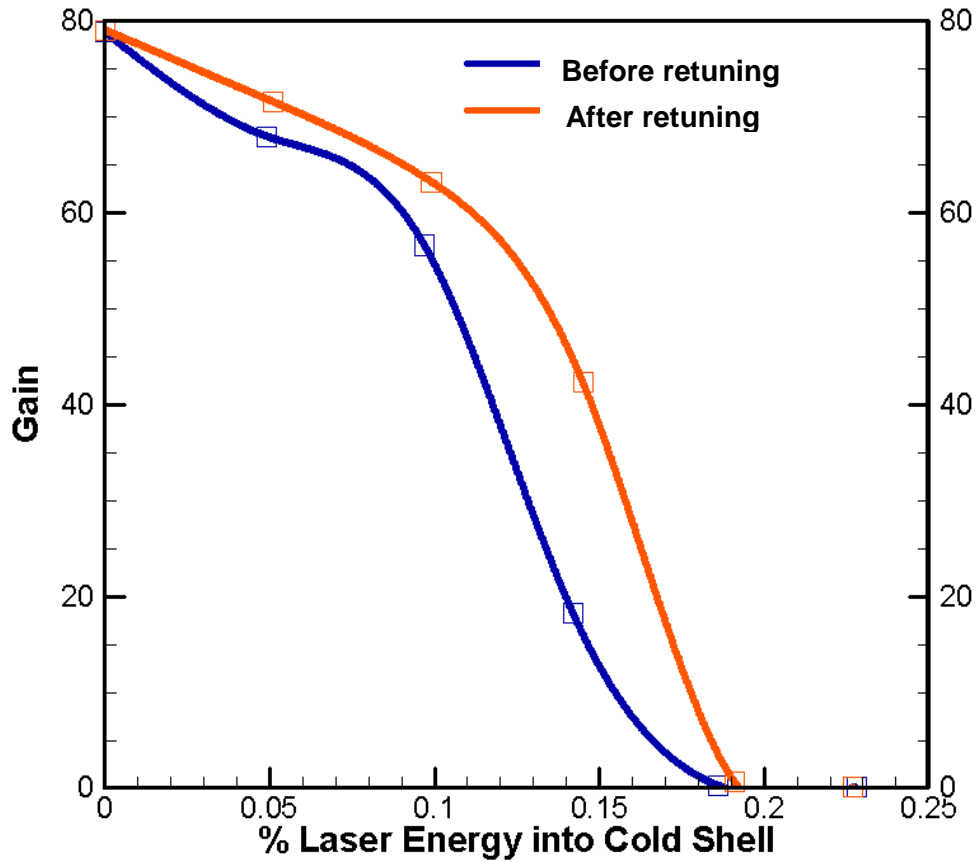
Figure 7: Results of TELIOS retuning of both picket timings and powers (straight line model).

	ΔT_1	ΔT_2	ΔT_3
Original	1.87	0.61	0.35
Optimized	2.17	0.65	0.32
	P_1 (Power in TW)	P_2 (Power in TW)	P_3 (Power in TW)
Original	42.02	50.40	47.00
Optimized	34.56	48.91	47.10

Figure 8: Parameters before and after TELIOS optimization for the fourth case of preheat. ΔT_1 is the time from the end of the first picket to the beginning of the second picket, ΔT_2 is the time from the end of the second picket to the beginning of the third picket, and ΔT_3 is the time from the end of the third picket to the beginning of the main pulse.

11

5. Conclusion

Fast electron preheat greatly reduces the gain of inertial confinement ignition designs by reducing the density and compressibility of the fuel. The optimizing code TELIOS was used to improve the gains of these designs by retuning the picket timings over a range of preheat conditions. It was unable to achieve significant improvements with either the straight-line model or the diffusion model of fast electron transport. Later tests where TELIOS was allowed to adjust both the picket timings and the picket powers yielded better results. However, these improvements were not significant enough to substantially counteract the effects of fast electron preheat. Other factors will therefore need to be optimized in order to reduce the problem of fast electrons.

6. Acknowledgements

7. References

1. J. Nuckolls, L. Wood, A. Thiessen, and G. Zimmerman, Nature (London) **239**, 139 (1972).

2. J. Delettrez *et al.*, Phys. Rev. A**36**, 3926 (1987)

3. T. J. B. Collins *et al*., Phys. Plas. <u>19</u>, 056308 (2012)

Statistical Investigation of Cryogenic Target Defects

Robin Zhang

Webster Schroeder High School

Advisor: Colin Kingsley

Laboratory for Laser Energetics

University of Rochester

Rochester, New York

March 2015

1. Abstract

After hollow cryogenic targets are filled with a frozen layer of DT, images of them are taken and analyzed for quality control. Often, imperfections with an appearance of either cracks (dendrites) or dark spots (darks) appear on the surface of the target. Many aspects of these defects, including origin, composition, and impact on target performance, are not well understood. In order to work towards elimination of these defects, more needs to be known about their nature. Images and information pertaining to a large sample of targets were drawn from a database and different properties were analyzed using various statistical techniques. The numerous tests performed resulted in many small pieces of information about the nature of the defects (e.g. location, size) that rule out some theories and support others. Additional analysis is necessary in order to more fully understand the defects.

2. Introduction

Fusion is the process by which separate nuclei are combined together to form a single heavier nucleus, generally releasing a large amount of energy in the process. In order to achieve fusion, atoms must collide with enough energy to overcome their electrostatic repulsion. In laser fusion, high-intensity lasers are uniformly focused onto a small spherical target (roughly 2 mm in diameter) containing the fuel to be fused.[1] The energy of the lasers causes the surface of the targets to explode, thereby imploding the inner contents at a high velocity. This results in very high temperature and pressure, making fusion reactions possible. At the Laboratory for Laser Energetics, the targets used contain a mixture of deuterium (D) and tritium (T), which fuse together to create helium and a neutron as well as a large amount of energy.

In order for a target to implode properly and initiate fusion, it must contain minimal imperfections. Even minor discrepancies in the target's shell thickness can become magnified greatly during the implosion process, resulting in much lower fusion yield.[2] Because of this required precision, the preparation of a serviceable target involves highly precise operations on the small and delicate target, a complex and laborious process. Targets begin as empty shells prepared in batches by General Atomics. These are then inspected, and only the select few that are pure enough make it to the next stage. At a filling station, the plastic shell is subject to 1,000 atm of pressure and is slowly permeation filled with DT vapor. Then, the temperature is gradually reduced to just below the DT triple point (19.8 K) while the difference in pressure across the shell boundary is maintained below 1 atm.[2] This allows for the formation a thin uniform layer of DT ice contouring the inside of the shell while the center contains some DT gas. When the layer has been formed, the target is held in a cryostat until it is ready to be imploded.
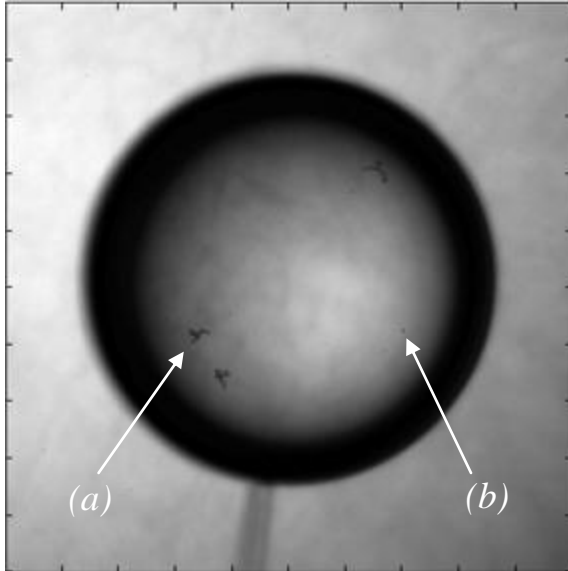
Figure 1: Example image of a typical filled target. Note the two distinct types of defects: (a) dendrite (b) dark

Having DT exist in the solid state is important as it allows for the packing of more fuel into the small shell, resulting in more fusion reactions.

Over the years, procedure optimizations have allowed for more-perfect targets with respect to uniformity of DT ice layers, but the targets still are not without flaws. While held in the cryostat before being imploded, each target is documented with a variety of different information, including images. Ever since images of the first DT targets have been documented, the images have consistently revealed small imperfections (i.e. defects) on the surfaces of the targets.[3] These defects have the appearance of either cracks (dendrites) or dark spots (darks) [Figure 1]. For both types of defects, details including the origin, composition, and impact on target performance are unknown.

After images are taken of each target from multiple points of view, they are processed in a MATLAB routine designed to categorize and characterize the defects. Although the current camera setup cannot capture every viewpoint, the portions that can be imaged are patched together and displayed as an area-preserving Mollweide projection [Figure 2]. The MATLAB code then identifies the defects and gathers various information for each one, including classification, area, and position.

4
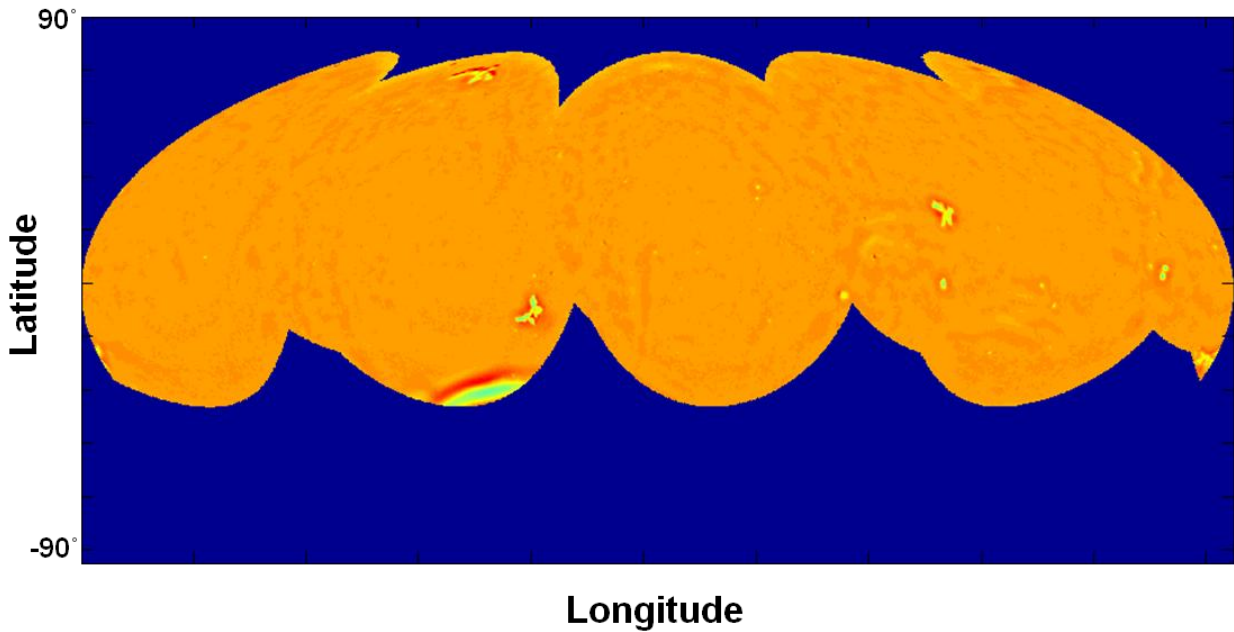
Figure 2: Mollweide projection image of a target. Due to the current camera setup, data is missing from the polar regions of the target, especially around the bottom.

3. Data Analysis

In an effort to understand these defects, a series of statistical tests was performed on data gathered from approximately 175 targets containing thousands of defects. Finding any correlations between defect count and variables such as position on target could provide some insight into the origin of the defects. The results found could support existing theories on why the defects form or reject them and prompt the formation of new theories.

3.1. Presence of Defects vs. Latitude

One existing idea about the defects was that the defects have something to do with particulate falling from machinery above the target while being filled. If this were true, then defects would likely be clustered in the northern hemisphere of the target.

5

In order to test whether the presence of defects was related to its latitude on the targets, the total surface area at each latitude value was compared to the number of defects found at those corresponding latitude values. If the relative frequency of defects at the latitude values matched that of the relative area, it could be concluded that there is no relationship between the presence of defects and the latitude. Because the images do not reflect the entirety of the target's actual surface area, the appropriate surface area at each latitude range could not be determined using mathematical equations applicable to spheres. Instead, because the image is an area-preserving projection, pixels were used as a unit of area, and the areas at each latitude value were found by counting up the pixels on the image.

After the number of pixels and defects were determined at each latitude value, a two-sample Kolmogorov-Smirnov test (KS test) was used to determine whether the difference between the two samples' cumulative distribution functions (CDFs) was statistically significant. In a KS test, the null hypothesis is that the two CDFs are drawn from the same fundamental distribution (meaning the likelihood of finding a defect would be uniform with respect to latitude), while the alternate hypothesis is the opposite. Inputting two CDFs into the KS test yields a value known as the KS statistic, which then can be used in a preexisting KS equation to determine the p-value based on the two sample sizes. If this p-value is less than the chosen significance level, α, then the null hypothesis is rejected. Otherwise, it is not rejected.

When the KS test was used to look for correlations between latitude and presence of dendrites using a typical significance level of $\alpha = 0.05$, the obtained p-value was 0.32, greater than the significance level. Therefore, the conclusion was that the likelihood of finding a dendrite is uniform with respect to latitude [Figure 3]. As a result, it can be reasonably concluded that dendrites are not related to falling particulate.

(a)

Dendrites and Pixels Distribution

(b)

KS-Test CDFs
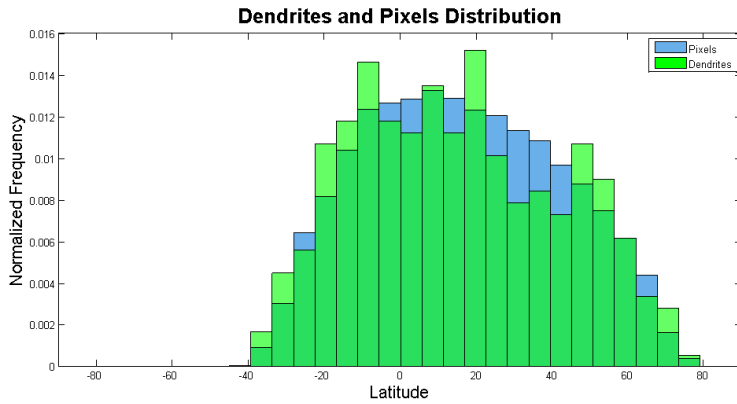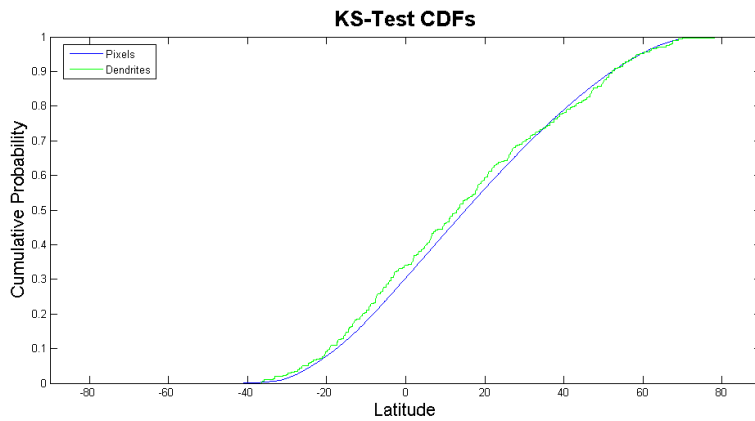
Figure 3: Statistical comparison between the position of dendrites and area vs. latitude. (a) The normalized histograms of number of pixels vs. latitude and number of dendrites vs. latitude superimposed on one another. Note the similar form. (b) A plot of the cumulative distribution functions of pixels and dendrites vs. latitude. The data corresponding to this graph reveals an insignificant difference between the two functions.

The same process was performed on the data for darks. However, the resulting *p*-value was 1.65×10^{-9}, much smaller than the significance level of 0.05. The conclusion, then, was that the likelihood of finding a dark is not uniform with respect to latitude [Figure 4]. Instead, the likelihood of finding a dark appears to be larger between latitude values 0 and 40 [Figure 4(a)].

7

(a)

Darks and Pixels Distribution

(b)

KS-Test CDFs
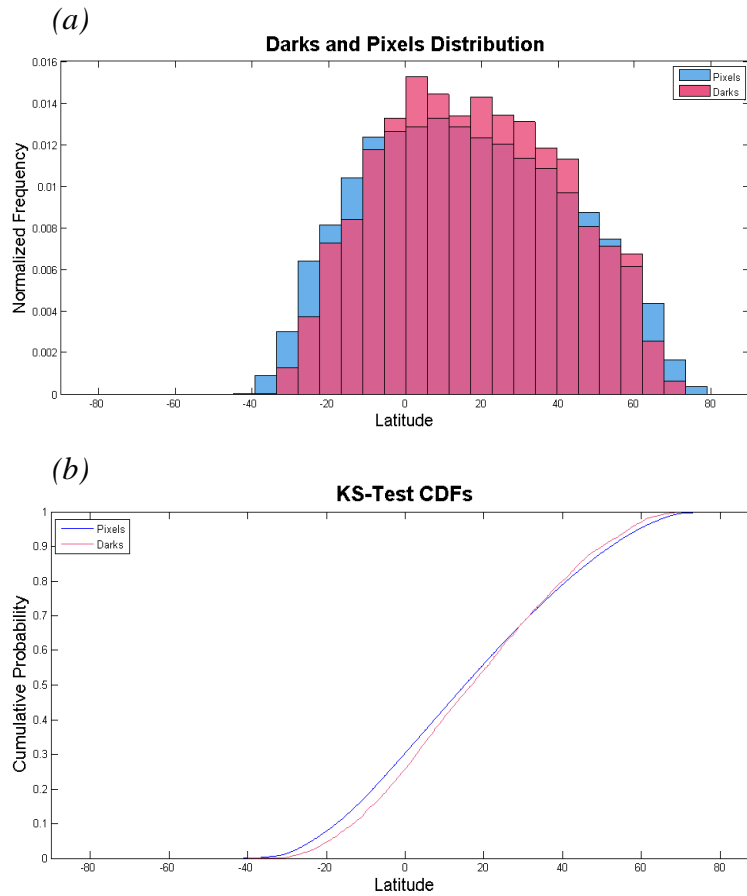
Figure 4: Statistical comparison between the position of dendrites and area vs. latitude. (a) Same as Figure 3(a), but with darks. The relative frequency of darks appears to be higher between latitudes 0 and 40. (b) Same as Figure 3(b), but with darks. The data corresponding to this graph reveals a statistically significant difference between the two functions.

3.2. Presence of Defects vs. Longitude

When targets are prepared for filling, they are positioned in batches of six, surrounding a pole [Figure 5]. Each of the six slots was labeled, and the slot number for the every target was recorded. Another theory regarding the formation of defects was that particulate floating within the filling chamber caused the defects to appear. If this were true, then defects should appear only at longitudes facing away from the pole, exposed to the open air.
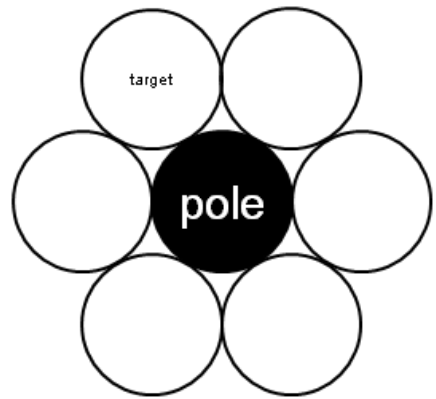
Figure 5: Top view of the target fill rack.

8

(a)

(b)

(c)
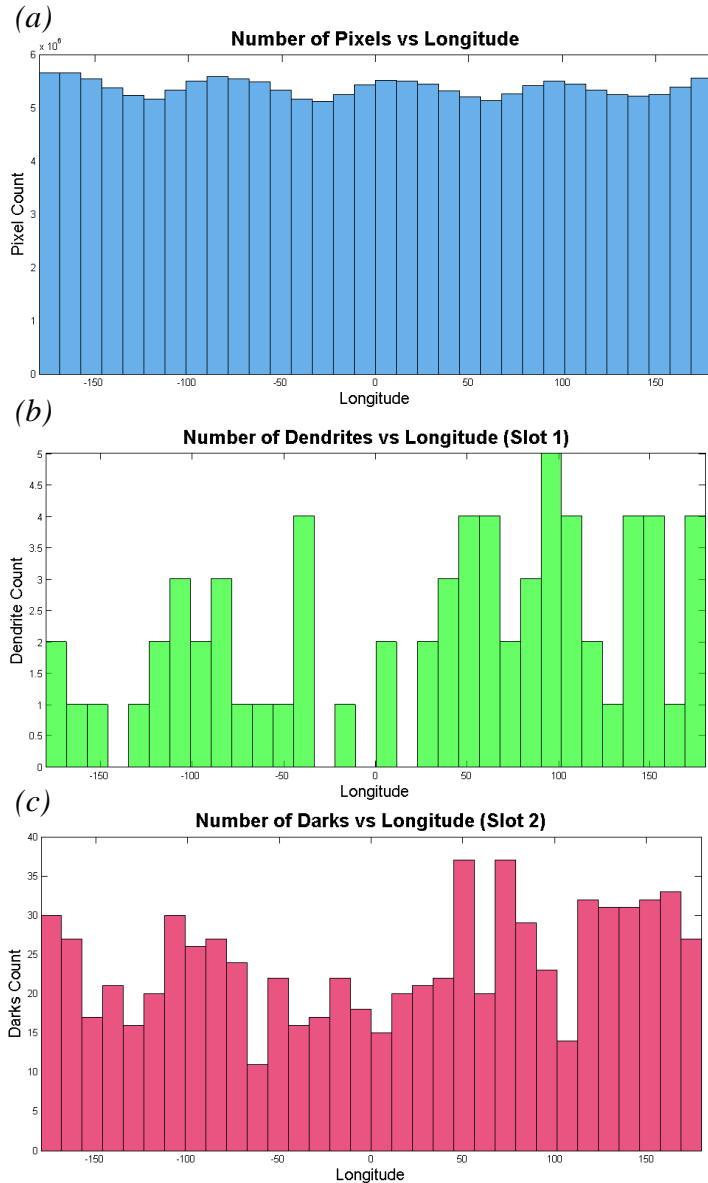
Figure 6: Statistical comparison between position of defects and area vs. longitude. (a) Histogram of number of pixels at each longitude interval. (b) Histogram of the number of dendrites at each longitude interval for targets in slot 1. The histograms of the other 5 slots have a similar appearance. (c) Histogram of the number of darks at each longitude interval for targets in slot 2. The histograms of the other 5 slots have a similar appearance.

The procedure for testing whether the appearance of defects is related to its longitudinal position was similar to that of *Section 3.1*. Before performing the test, however, the targets were separated by their slot number, and the KS test was performed on the targets grouped by slot. In total, twelve tests were done (6 for dendrites, 6 for darks).

For the dendrites, the resulting *p*-values for the 6 slots were mostly above the significance level (0.05), and the histograms did not reveal any noticeable clumping of dendrites. It was concluded that the likelihood of finding a dendrite is uniform with respect to longitude.

For the darks, the resulting *p*-values for the 6 slots were mostly below the significance level, meaning that the distribution of area across longitude does not match the distribution of

9

darks across longitude. However, the histograms do not appear to reveal any noticeable clumping in certain regions, so no other conclusion could be made [Figure 6(c)].

3.3. Defect Count vs. Time Elapsed from Filling to Firing

As mentioned in the introduction, after being filled, targets are held in a cryostat until they are ready to be shot. The amount of time can range from days to weeks, and because of the radioactive nature of tritium, it was proposed that the formation of defects was related to the amount of time a target spent idle.

The number of days elapsed from filling to shooting was determined for all the targets, and the targets were grouped together based on the number of days elapsed. Within each group, the mean number of defects was calculated, and these values of average defects per target were plotted against their respective number of days elapsed [Figure 7]. However, for both types of defects, no relationship was found between the two variables. Linear regression models created for the two plots resulted in coefficients of determination, r^2, of 0.0147 and 0.0562 for dendrites and darks, respectively.

(a)

(b)
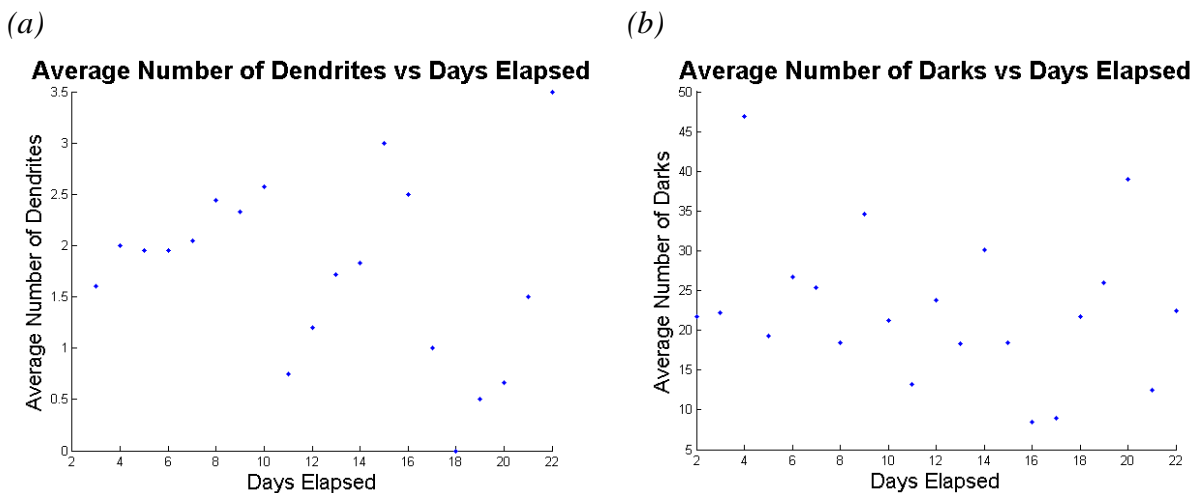
Figure 7: Plot of average number of defects on a target vs. the number of days elapsed between filling and shooting. In both cases, no trend can be seen. (a) dendrites. (b) darks.

10

4. History of Target Defects at LLE

In addition to attempting to discover more about the nature of the defects by comparing certain variables with others, a few plots were created in order to gauge the prevalence of defects and whether there have been any trends in the past few years of target fabrication at LLE.

4.1. Number of Defects per Target over Time

For both types of defects, a simple scatter plot was created of the defect count on targets vs. the date the target was imaged. In both cases, the plots did not reveal any striking trends [Figure 8]. The number of defects per target has remained consistently unpredictable over the past several years.

(a)
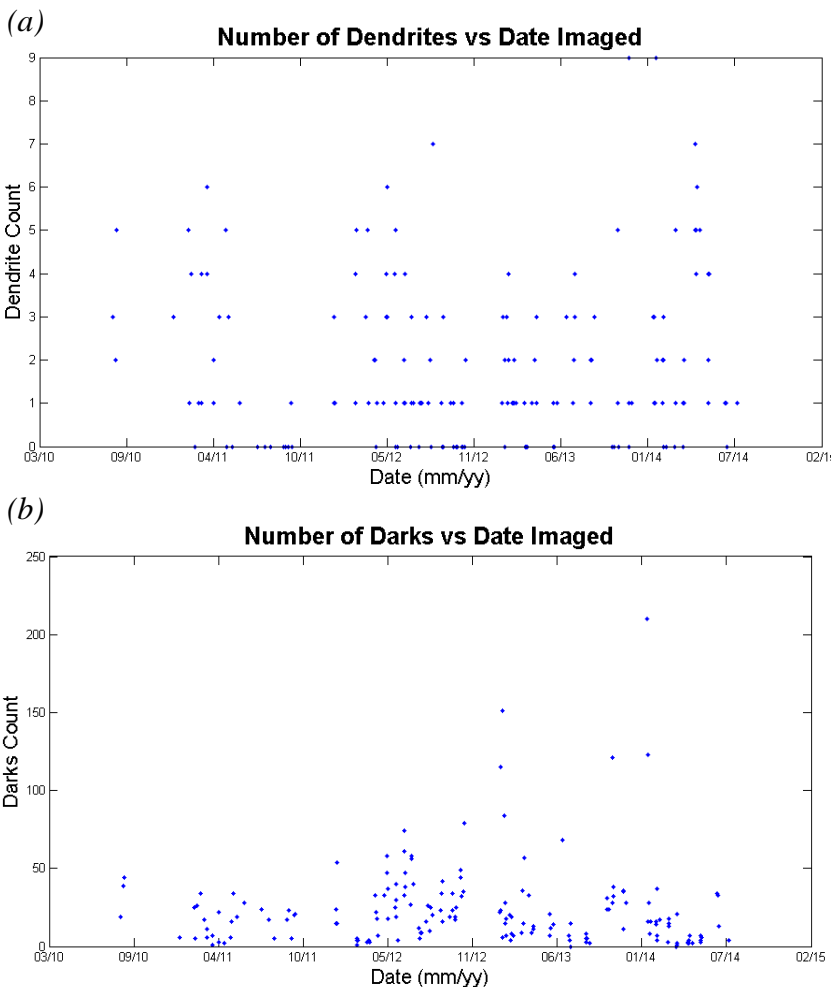
Figure 8: Plot of number of defects per target vs. date imaged for (a) dendrites and (b) darks. There does not appear to be any predictable trend.

(b)
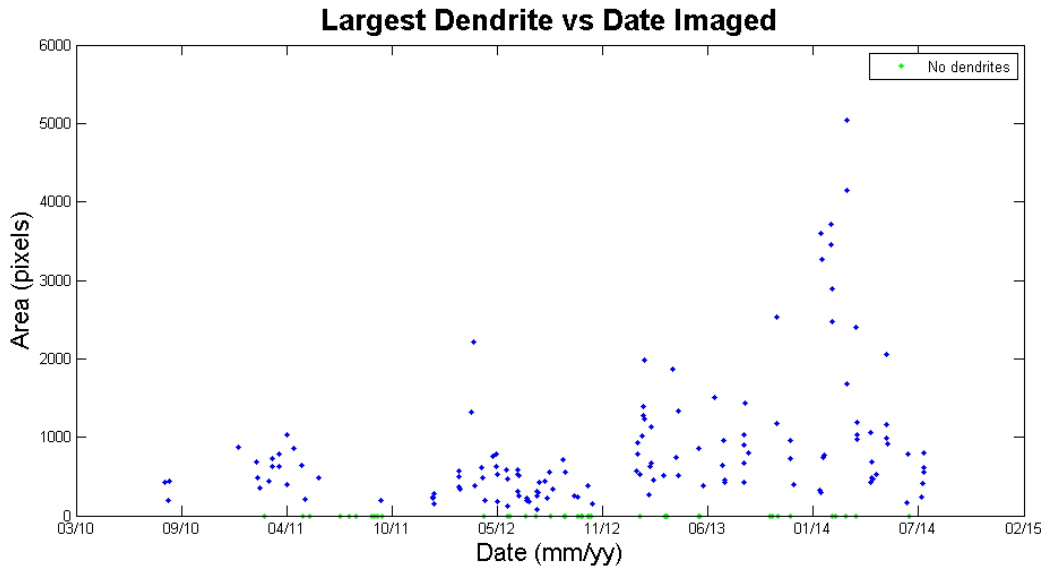
Figure 9: Plot of largest dendrite on a single target vs. date imaged. In the past several years, it appears that the largest dendrite has become larger.

4.2. Largest Dendrite on a Single Target over Time

While darks are small and generally look the same, dendrites have varying shapes and can be very large at times. Based on the assumption that larger dendrites would impact target performance more, there is particular interest in the size of the largest dendrite on targets. To determine whether there was any trend within the past years, the area of the largest dendrite on each target was determined and plotted based on the date it was imaged [Figure 9]. It was found that the largest dendrite has been increasing in size over the past several years.

5. Conclusion

Existing data on past targets and defects was analyzed for any possible correlations between the count of defects and variables such as position. It was concluded that the probability of finding a dendrite on a target is uniform with respect to latitude and longitude. However, for darks, it was concluded that the probability of finding one is not uniform with respect to latitude or longitude, though no obvious patterns were found in the data. For both dendrites and darks, no relationship was found between their frequency and the amount of time a target spent idle between filling and shooting. Additionally, no obvious trends were observed when comparing the number of these defects per target over the past few years. However, it was found that the largest dendrite on a single target seems to have grown in size over the past years. In the future, a continued search for relationships between variables about the defects could provide further insight into the defects' nature.

References

[1] J. Nuckolls et al., "Laser Compression of Matter to Super-High Densities: Thermonuclear (CTR) Applications," Nature 239, 139 (1972).

[2] "Cryogenic DT and D_2 Targets for Inertial Confinement Fusion," LLE Review **108**, 167 (2006)

[3] W. Shmayda et al. (2012, May). "Mitigating Defects on Cryogenic Targets," presentation at 20th Target Fabrication Meeting.

Polar-Driven X-ray Backlighter Targets for the National Ignition Facility

Roger Zhang

Webster Schroeder High School

Advisor: **Dr. R. S. Craxton**

Laboratory for Laser Energetics

University of Rochester

Rochester, NY

January 2015

1. Abstract

Imploding x-ray backlighter targets on the National Ignition Facility (NIF) can be used to gather information about primary targets; an initial proposal involves measuring the opacity of materials while they are heated by the NIF laser beams. The backlighter target radiates x rays that are absorbed as they pass through the primary target to a detector. An optimized beam configuration has been developed to maximize the implosion uniformity of the backlighting target (a SiO_2 shell with diameter 2.1 mm and thickness 10 μm) using only the four most polar rings of beams (rings at 23.5° and 30.0° from the poles). Optimization was performed by adjusting parameters such as beam aim points and defocus distances in SAGE, a hydrodynamics simulation code. The uniformity was measured using the rms variation in the center-of-mass radius of the shell, calculated when the target had imploded to approximately half of its original radius. The rms variation was reduced from 26.2% in the initial design to 5.4% in the optimized design. This was achieved primarily by directing 75% of the beams beyond the equator and decreasing their defocus distances to maximize energy deposition near the equator.

2. Introduction

Nuclear fusion has the potential to provide the world with clean, renewable energy. Inertial confinement fusion (ICF) is a method of achieving fusion that involves high power lasers. In ICF, lasers irradiate a plastic or glass shell containing a mixture of deuterium and tritium (DT), causing the shell to ablate outwards and the DT fuel inside to compress. The lasers provide the fuel with enough energy and pressure to fuse together, releasing energy in the process.
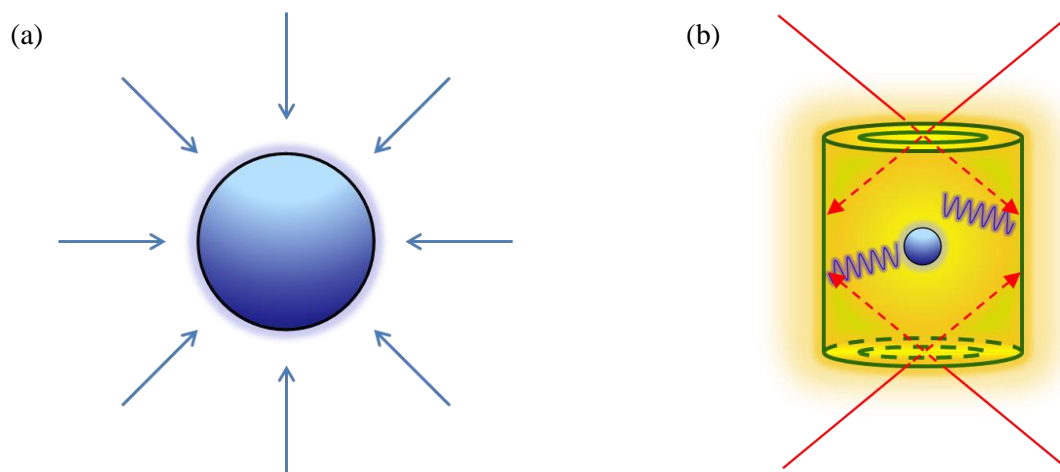
Figure 1: The two main approaches for conducting inertial confinement fusion. (a) In direct drive, beams (represented with arrows) are aimed directly at the target. (b) In indirect drive, beams strike the interior walls of the hohlraum, which emits x rays at the target, compressing it. (Adapted from Fig. 1 of Ref. 5)

There are two primary methods of imploding a target: direct drive[1] and indirect drive,[2] shown in Fig. 1. Direct drive [Fig. 1(a)] involves pointing laser beams directly at the target, thus allowing the laser energy to be used directly in compressing the target. In order to achieve uniform compression using direct drive, the beams must be placed evenly around the target and aimed directly at the center of the target. Indirect drive [Fig. 1(b)] involves placing the target inside a hohlraum, a hollow cylinder typically made of gold with small openings on each of the circular faces. Rather than being pointed directly at the target, the beams are aimed through the

holes at each pole of the hohlraum so that they strike the interior walls. As these walls are struck by the beams, they emit x rays uniformly within the interior of the hohlraum, causing the target inside to heat up and compress. Because indirect drive calls for the beams to enter only through the two holes, a target chamber configured for indirect drive has beam ports positioned around the poles of the target chamber and lacks beam ports surrounding the equator. A disadvantage of indirect drive is that much of the laser energy is absorbed by the hohlraum walls. Only about 20% of the laser energy is absorbed by the target. However, indirect drive does offer the advantage of a more uniform compression.

The National Ignition Facility (NIF) located at the Lawrence Livermore National Laboratory (LLNL) is currently configured for indirect drive; its target chamber has laser beam ports around the poles but not around the equator. The ports are arranged in a total of eight horizontal rings surrounding the target at angles $\theta = 23.5°$, $30.0°$, $44.5°$, and $50.0°$ from the north pole and corresponding angles in the lower hemisphere [Fig. 2]. Beams located on these rings are grouped together in fours (2x2 squares) known as quads. Rings 1, 2, 7, and 8 (the rings closest to the poles) each contain four quads and rings 3, 4, 5, and 6 (the rings closer to the equator) contain eight quads for a total of 48 quads (192 beams).
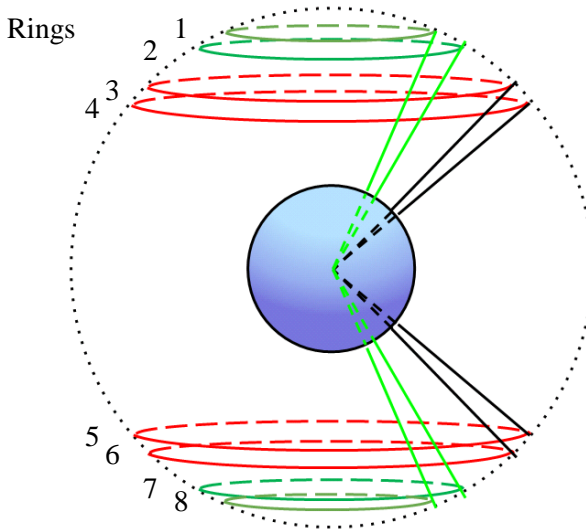
Figure 2: The NIF target chamber. Quads surround the target on rings at 23.5°, 30.0°, 44.5°, and 50.0° from both poles. Rings 1, 2, 7, and 8 each contain four quads and rings 3, 4, 5, and 6 each contain eight quads. Note the lack of beam ports around the equator.

Conducting direct drive experiments with an indirect-drive-configured laser system results in non-uniform implosions. Since beam ports are grouped around the poles, the target's poles are driven with much more energy, causing them to collide long before the equator collapses [Fig. 3(a)]. More uniform direct drive implosions can be achieved on indirect drive-configured lasers by using a technique known as polar drive[3]. In polar drive, beams that were originally aimed at the target's poles are repointed towards the equator, thus compensating for the lack of beam ports surrounding the equator [Fig. 3(b)]. Beam configuration designs optimized to produce more uniform implosions on the NIF based on the concept of polar drive have been developed successfully for DT gas-filled targets.[4]

23.5°
30.0°
44.5°
50.0°

(a)

(b)

Initial Target

Compressed Target
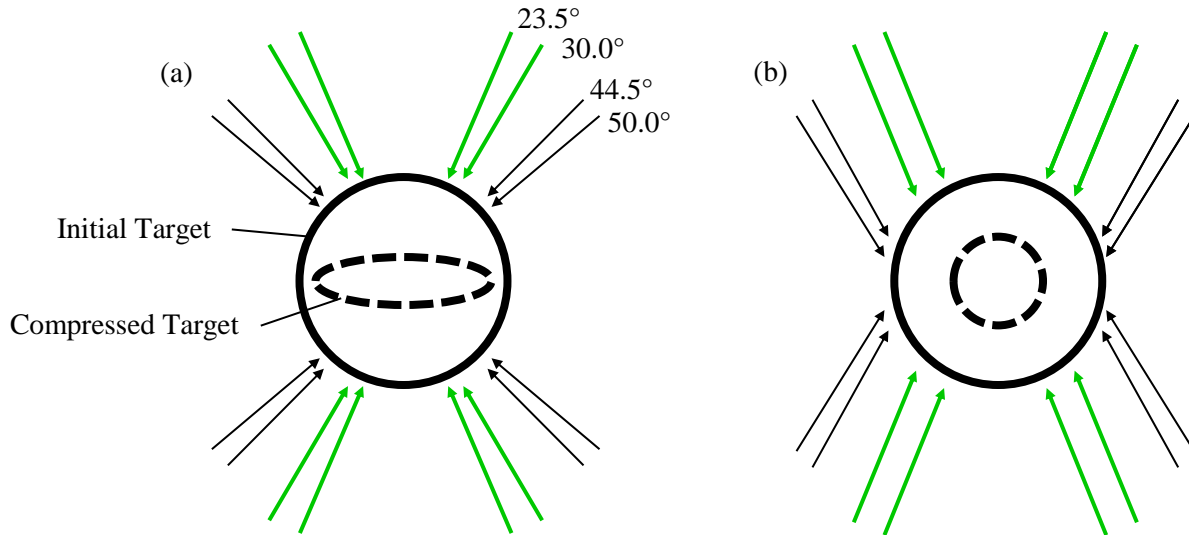
Figure 3: Direct drive on the NIF with and without repointing beams. (a) Keeping the beams pointed directly at the center of the target (as is traditional with direct drive experiments) results in a non-uniform implosion in which the poles of the target collide long before the equator. (b) Repointing the beams allows for more drive near the equator, resulting in a more uniform implosion. (Adapted from Fig. 2 of Ref. 5)

Polar drive can be used to implode other types of targets aside from the usual DT-filled shell. Configurations based on polar drive have been designed to implode D^3He-filled targets for use in proton backlighting.[5] Another useful application of polar drive is x-ray backlighting, when a backlighter target is placed in the target chamber together with a primary target. The backlighter target emits x rays that pass through the primary target and are absorbed by a detector. As the x rays pass through, they can be deflected, absorbed by, or transmitted through the primary target, resulting in an image on the detector. In some experiments the backlighter target needs to be imploded to release x rays, with a certain number of beam ports allocated to the backlighter target and the rest of the beams reserved for the primary target. Such implosion experiments can be useful for testing material properties.

In an initial proposal by Dr. Robert Heeter of LLNL, an x-ray backlighter will be used to measure the opacity of a material when the material is heated up. This primary target (the material) will be mounted onto a half-hohlraum. The beams on the four rings closest to the poles (rings 1, 2, 7, and 8) will be used to implode the x-ray backlighter and the beams on rings 5 and 6 will be aimed into the half-hohlraum to heat up the primary target [Fig. 4]. Since only the four rings of beams closest to the poles are available for the backlighter in this experiment, the beam configuration needed to be optimized to achieve a uniform implosion.

Figure 4: Schematic for the proposed x-ray backlighting experiment. Selected beams are allocated to strike the backlighter target while the others are aimed into the half-hohlraum. The backlighter target implodes, releasing x rays that pass through the primary target and into a detector, creating an image.

3. Simulation Results

The hydrodynamics code *SAGE* was used to simulate target compression with a variety of beam configurations. In these simulations, the backlighter target was a hollow glass shell with an outer diameter of 2100 μm and a thickness of 10 μm. Throughout the optimization process, simulations with different beam configurations were run with the goal of minimizing non-uniformity of the target's center-of-mass radius. The root mean square (rms) deviation percentage was used as the measurement of non-uniformity.

3.1 Initial Design

Figure 5: A two-dimensional projection of the target's center-of-mass radius when it has imploded to approximately half of its original radius using the initial design. Shades of red and blue indicate the percent deviation from the average center-of-mass radius of the target. The groups of four squares (2x2) represent the locations of the quads in the target chamber. Quads colored green are used to implode the backlighter while clear quads are used for the primary target (or turned off). Black points show the beam aim points. Examples of quads and their aim points on rings 1 and 2 are shown with arrows. The rms deviation was 26.2% for this initial design.

Figure 5 is a two-dimensional projection of the target's center-of-mass radius when it has imploded to approximately half of its original radius using the initial design. The contours and shading show the percent variation of the target's center-of-mass radius. In the initial design, beam aim points (shown by black points) were positioned at angles of 20°, 40°, 60°, and 80° from each pole, and were spread evenly across in the horizontal direction. This resulted in a very uneven compression. As shown by the dark blue shading around the equator and the dark red shading near the poles, the target's poles were compressed far more than the equator. The target's center-of-mass radius over the entire surface had an rms variation value of 26.2%. The first step in improving this design was to increase energy deposition around the equator.

The process of minimizing the rms variation of the target's surface was carried out through changing the beam aim points and defocus distances. The defocus distance is the distance between the laser beam's best focus and the target (if the defocus distance is zero, the beam will be at best focus on the target). Increasing the defocus distance results in an increased beam spot size on the target's surface; this spreads out the laser energy over a greater surface area. Decreasing it results in a smaller beam spot size.

3.2 Improved Design

Due to the nature of polar drive, beams shifted towards the equator don't strike the target at normal incidence. Since these beams are oblique, less energy is deposited, resulting in a need to direct more beam energy towards the equator. To counteract the reduced energy absorption near the equator, beam aim points for 75% of the beams were shifted beyond the equator (see Fig. 6). In addition, the defocus distances of these beams were decreased, resulting in smaller but more focused beam spots on the target. The beam aim points for the other 25% of beams (the upper beams on the 23.5° ring) were positioned on rings at only 25° from the poles. Since these beams strike the target at a much less slanted angle, there is greater energy deposition in the region near the poles. It was found that sufficient energy deposition could be achieved near the poles by using these beams and that uniformity could be improved by increasing the defocus distances of these beams.

As seen in Fig. 6, the equator no longer shows dark blue shading as it did in Fig. 5, indicating success in increasing the drive near the equator and resulting in a much more uniform implosion. The rms variation of the target's center-of-mass radius using the improved design was 5.7%, significantly less than the original 26.2%.

9
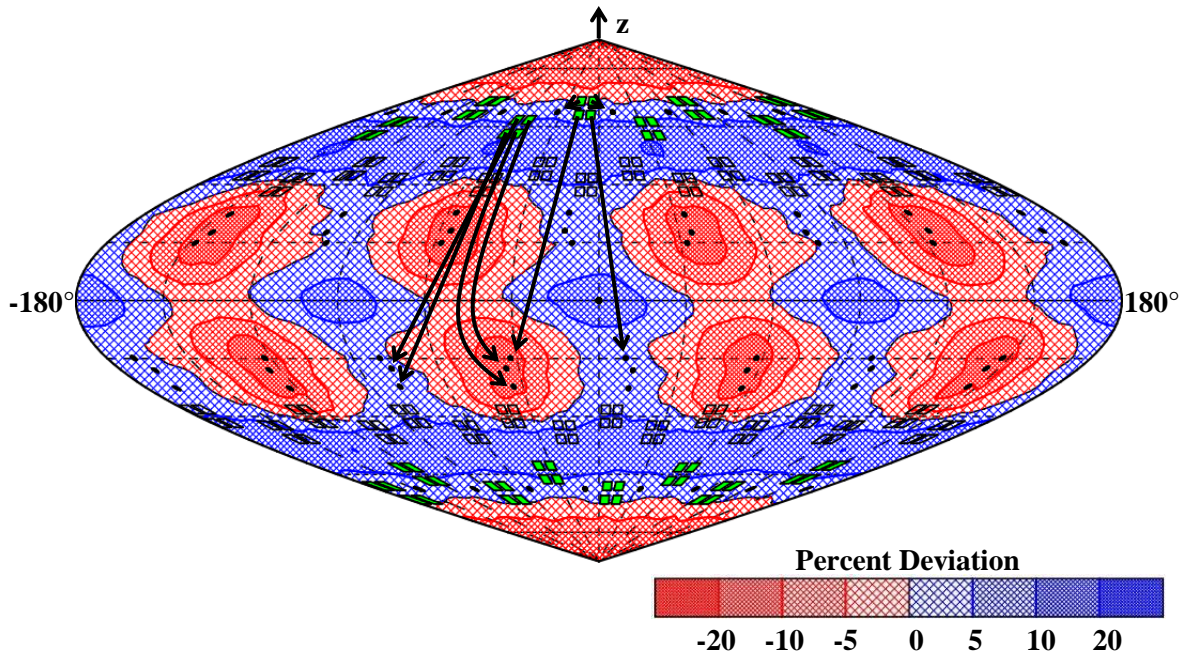
Figure 6: Same as Figure 5 except for the improved design. In this design, all but the very top (and very bottom) rows of beams are aimed beyond the equator in an effort to increase the drive at the equator. The rms deviation for this improved design was 5.7%.

Figure 7 shows the shifts of the beam aim points more clearly. In the improved design [Fig. 7(b)], beams that were originally aimed near the poles in the initial design [Fig. 7(a)] were repointed towards the equator. The slight decrease in defocus distance can also be seen; each of the two beams shown is slightly narrower in the improved design.
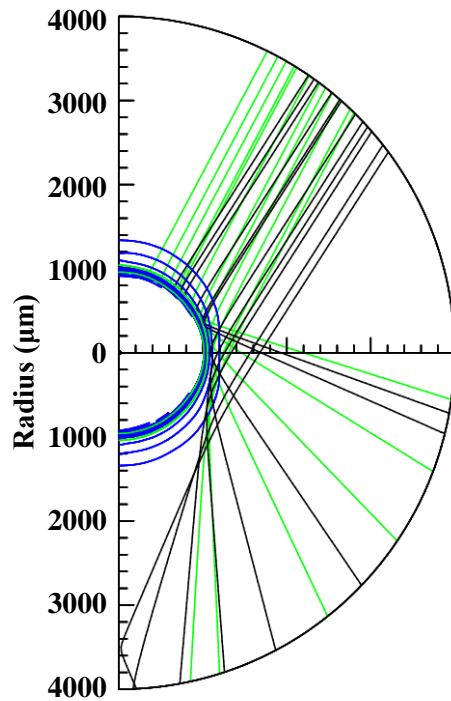
(a) Initial Design　　　　　　**(b) Improved Design**
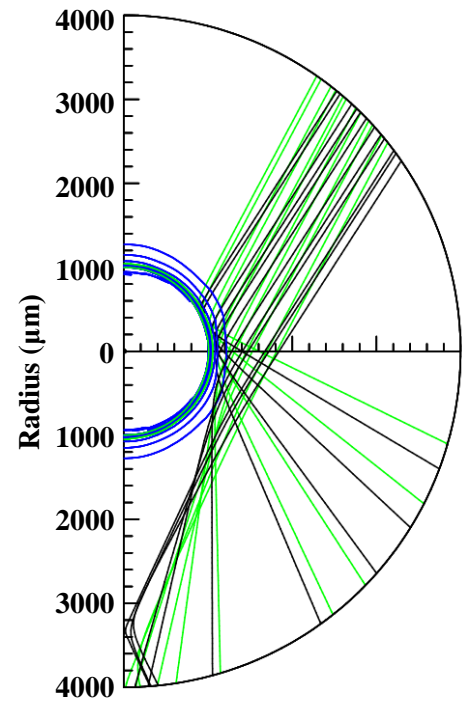
Figure 7: Raytrace plots of two beams (colored green and black) very early on in the simulation (1000 ps). The target's shell is shown in blue. (a) In the initial design, not enough beams are aimed towards the equator, resulting in low compression near the equator. (b) In the improved design, a greater number of beams are aimed near the equator to increase the drive there.

Even with the significant improvement with this design, however, there were still a few problems. As shown in Fig. 6, there existed horizontal regions just below the poles with too little energy. Furthermore, areas of above average compression near the equator (shown by the red circles) on the upper hemisphere lined up with those on the lower hemisphere.

3.3 Optimized Design
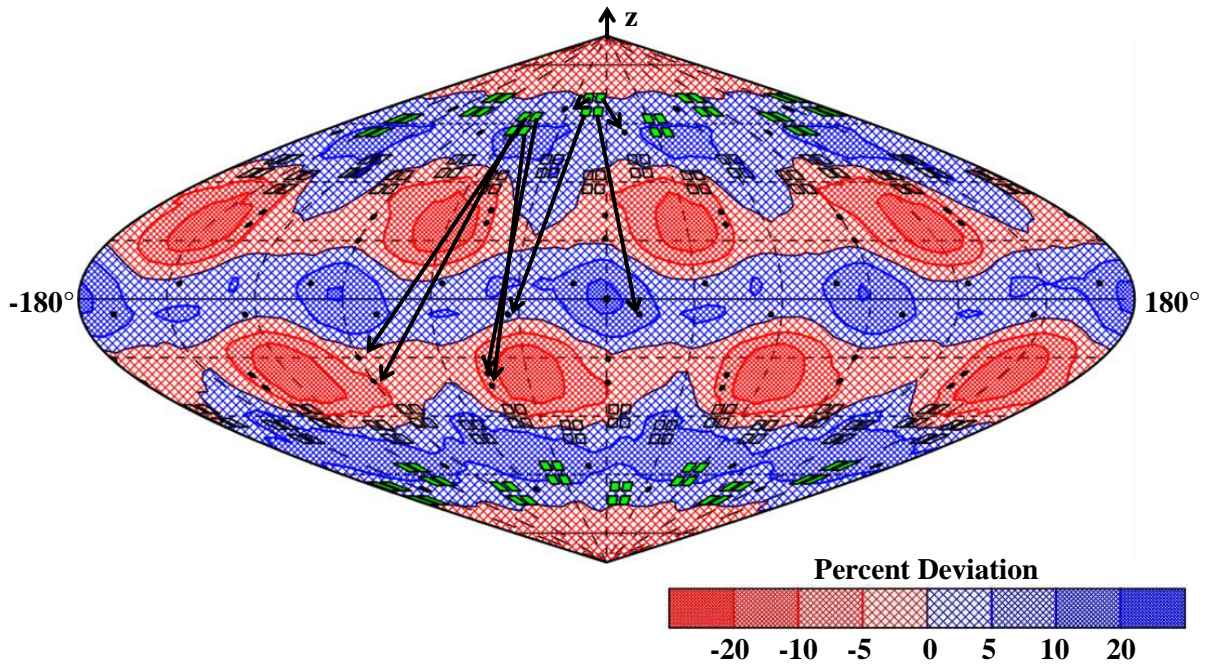
Figure 8: Same as Figure 6 except now using the optimized design. The rms deviation for this optimized design was 5.4%.

Figure 8 is a projection of the target's center-of-mass radius deviation using an optimized beam configuration. The optimized design resolves some of the issues with the previous design. The aim points for the beams aimed towards the poles have been altered slightly and the remaining beams have been shifted in the horizontal (ϕ) direction to reduce overlapping of the high energy spots. The rms non-uniformity for this optimized design was 5.4%, slightly below the previous design's 5.7% and much lower than the initial design's 26.2%.

The target's center-of-mass radius as a function of θ (averaged over ϕ), measured when the target has imploded to approximately half of its original radius, is shown in Fig. 9 (blue) for the initial design. The poles ($\theta = 0°$ and 180°) received too much energy, resulting in a quick compression of the poles while the equator ($\theta = 90°$) received little energy, resulting in a very slow compression near the equator. Using the optimized design, the target's center-of-mass

radius (green), while still exhibiting some degree of variation, is much more even during the implosion.

Table 1 shows the beam aim points and defocus distances used in the optimized design.

Ring	Port Position	θ (deg.)	Δϕ (deg.)	Defocus (cm)	Ring	Port Position	θ (deg.)	Δϕ (deg.)	Defocus (cm)
1 (23.5°)	T, L	25.00	-22.5	3.0	7 (156.5°)	T, L	60.00	-11.25	1.0
	T, R	33.00	22.5	3.0		T, R	61.67	33.75	1.0
	B, L	95.33	-22.5	1.0		B, L	64.30	-11.25	1.0
	B, R	95.33	22.5	1.0		B, R	69.71	33.75	1.0
2 (30.0°)	T, L	110.26	-33.75	1.0	8 (150.0°)	T, L	84.67	-22.5	1.0
	T, R	115.69	11.25	1.0		T, R	84.67	22.5	1.0
	B, L	118.30	-33.75	1.0		B, L	147.0	-22.5	3.0
	B, R	120.00	11.25	1.0		B, R	155.0	22.5	3.0

Table 1: Beam aim points and defocus distances used in the optimized design. All quads on the same ring are configured identically with the same θ and Δϕ (horizontal shift) values, and the same defocus distances. The ports within each quad are denoted by T (top) or B (bottom), and L (left) or R (right). For example, (T, L) would indicate the top left port of a quad.
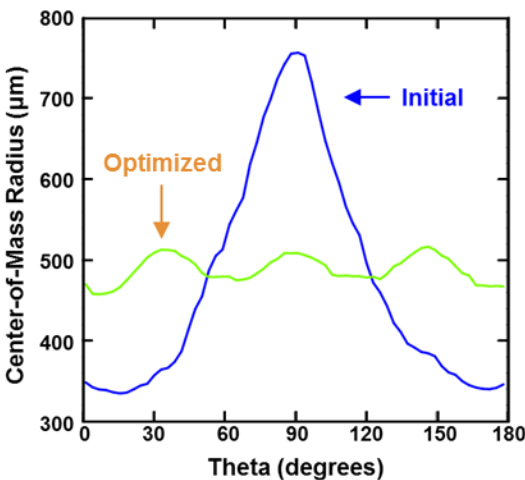
Figure 9: A comparison of the target's center-of-mass radius during implosion using the initial design (blue) and the optimized design (green). The poles lie at 0° and 180° and the equator at 90°.

The laser pulse profile was changed for the optimized design from that used for the initial and improved designs to reduce the maximum power and energy. The laser pulse for both the initial and improved designs (Fig. 10) called for a total power of 220 TW to be used for the backlighter. However, because only one third of the NIF's beams are being used for this backlighter (beams on rings 1, 2, 7, and 8), the equivalent total power output would be three times as much, 660 TW, in excess of the 400 TW limit that is usually imposed. A revised laser pulse shape was used for the

13

optimized design. Figure 10 shows how the peak power was reduced to 133 TW, decreasing the energy needed for the backlighter from 350 kJ to only 260 kJ. The equivalent total energy was decreased from 1050 kJ to 780 kJ. While the NIF is designed for a maximum energy of 1.8 MJ, it is preferred to operate below 800 kJ to minimize damage to the laser system.

Figure 10: A comparison of the pulse shape used for the initial and improved designs (dark blue) to the pulse shape used for the optimized design (light blue).

4. Future Applications

As discussed previously, there is an initial proposal to use this optimized design to backlight a heated material to measure its opacity. However, x-ray backlighting can be used to image several other types of targets such as a polar-driven target or a hohlraum.

5. Conclusion

A design has been developed to provide an implosion source for x-ray backlighting on the NIF using only the beams from the four rings closest to the poles. Optimization of the beam configuration to increase the uniformity of the implosion was performed using the hydrodynamics simulation code *SAGE*. The rms non-uniformity of the target's center-of-mass radius during implosion was reduced from 26.2% to 5.4%.

6. Acknowledgements

I would like to thank Dr. Stephen Craxton for providing me with this unique research opportunity and for his advice and support throughout the project. I would also like to thank the Laboratory for Laser Energetics for running the high school summer research program.

References

[1] J. Nuckolls, L. Wood, A. Thiessen, and G. Zimmerman, "Laser compression of matter to super-high densities: Thermonuclear (CTR) applications," Nature **239**, 139 (1972).

[2] J. D. Lindl, *Inertial Confinement Fusion: The Quest for Ignition and Energy Gain Using Indirect Drive* (Springer-Verlag, New York, 1998).

[3] S. Skupsky, J. A. Marozas, R. S. Craxton, R. Betti, T. J. B. Collins, J. A. Delettrez, V. N. Goncharov, P. W. McKenty, P. B. Radha, T. R. Boehly, J. P. Knauer, F. J. Marshall, D. R. Harding, J. D. Kilkenny, D. D. Meyerhofer, T. C. Sangster, and R. L. McCrory, "Polar direct drive on the National Ignition Facility," Phys. Plasmas **11**, 2763 (2004).

[4] A. M. Cok, R. S. Craxton, and P. W. McKenty, "Polar-drive designs for optimizing neutron yields on the National Ignition Facility," Phys. Plasmas **15**, 082705 (2008).

[5] Y. Kong, "Beam-Pointing Optimization for Proton Backlighting on the NIF," Laboratory for Laser Energetics High School Summer Research Program (2013).

Analyzing the Sensitivity of a Hard X-Ray Detector Using Monte Carlo Methods

Junhong Sam Zhou

Victor Senior High School

LLE Advisor: Christian Stoeckl

1. Abstract

An improved sensitivity function was created for the HERIE hard x-ray detector used in direct-drive inertial confinement fusion experiments done on the Omega and Omega-EP laser systems at the Laboratory for Laser Energetics (LLE). In order to infer the spectrum of x rays emitted from the target, data was gathered from the HERIE and HXRD hard x-ray detectors. A sensitivity function was used to infer the slope of the x-ray spectrum from the measured signals. Based on previously calculated sensitivity functions for these detectors, there was a discrepancy between the spectra inferred from the two diagnostics. To better understand this discrepancy, Monte Carlo simulations of the HERIE setup were performed using the GEANT4 framework. Tests were performed on the simulated image plate in order to validate the simulation against published experimental data. Once validated, the detector's sensitivity was calculated at various energy levels and compiled into an improved sensitivity function. Using data derived from the simulation of the detector has significantly reduced the difference between the inferred spectra from the HERIE and HXRD detectors. This will aid in the analysis of future experiments.

2. Introduction

During direct-drive fusion experiments on the Omega and Omega-EP laser systems, hard x rays are emitted from the target as a result of the interaction of the high-intensity laser beams with the target. On the Omega system, the 4-channel HXRD[1] and the 9-channel HERIE[2] detectors are used to measure the hard x rays. Because of their unique geometries, data from each detector needs to be interpreted with a sensitivity function in order to infer the spectrum of the x rays. The expected result is an identical spectrum inferred from both detectors. Currently, a significant discrepancy is observed between the two diagnostics. A Monte Carlo simulation was set up using GEANT4[3] in order to create a more accurate sensitivity function for the HERIE detector.

3. HERIE Physical Setup
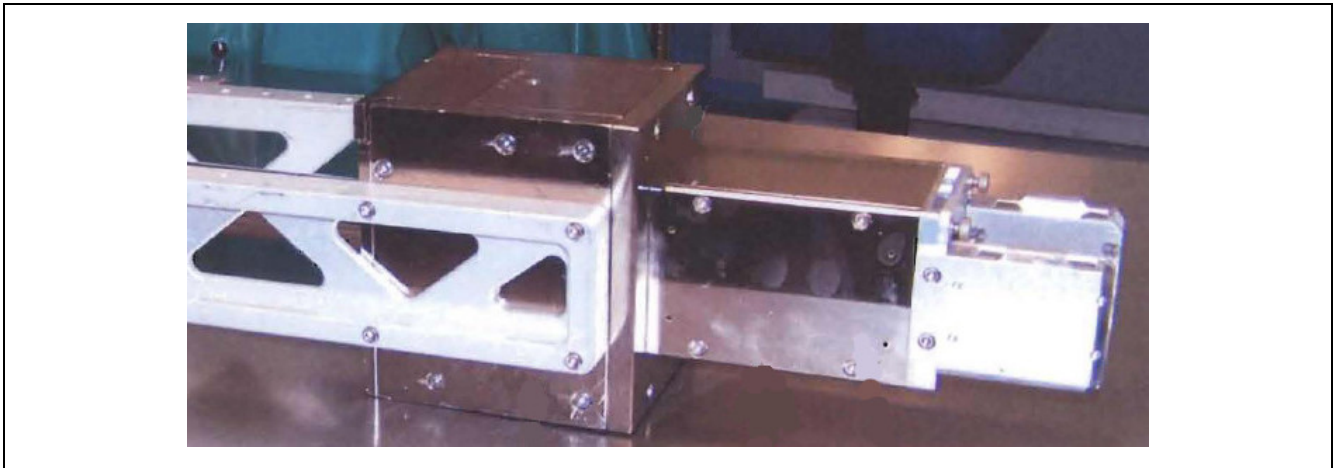
Figure 1. *Physical HERIE hard x ray detector*

The HERIE detector, shown in Figure 1, consists of a lead shell that houses an image plate. Inside this shell, there are three layers made of copper, aluminum, and plastic that help shield the image plate. The image plate itself consists of multiple layers of plastics and a single sensitive layer as listed

in Table 1. This sensitive layer absorbs the x ray photons and stores the absorbed energy to be read out later.

Table 1. *Composition of the image plate.[4]*

	Composition	Density (g/cm^3)	Thickness (μm)
Mylar Layer	$C_{10}H_8O_4$	1.64	9
Sensitive Layer	$BaFBr_{0.85}I_{0.15}$:Eu	3.18	124
Back Layer	$C_{10}H_8O_4$	1.4	12
Base Layer	$C_{10}H_8O_4$	1.4	190
Ferromagnetic Layer	MnO, ZnO, Fe_2O_3 + Plastic	3.0	80
Back Protective Layer	$C_{10}H_8O_4$	1.4	25

In front of the lead shell and image plate sits a filter stack that has nine channels. The stack consists of 30 plates of either tungsten, aluminum or copper. Each plate has a different configuration of nine holes, creating nine channels with different thicknesses. This in turn creates nine different regions of sensitivity on the image plate. When the image plate is scanned and the data is retrieved, nine values for deposited energy will be collected for each experiment.

4. Simulation Model

The simulations were carried out in the GEANT4 framework. This was chosen because GEANT4 has historically been used to model the HXRD x-ray detector. GEANT4 has the capability to model the passage of particles through matter and is often used in areas dealing with high energy, medical studies, and nuclear physics.[3] Previous simulations of the detector included only the filter stack and the image plate, but the current model, as seen in Figure 2, includes the full geometry of the detector.

Figure 2. *Visual representation of GEANT4 simulation. The full HERIE detector is seen with a filter stack (left). The cross section (right) has multiple x rays running through it.*
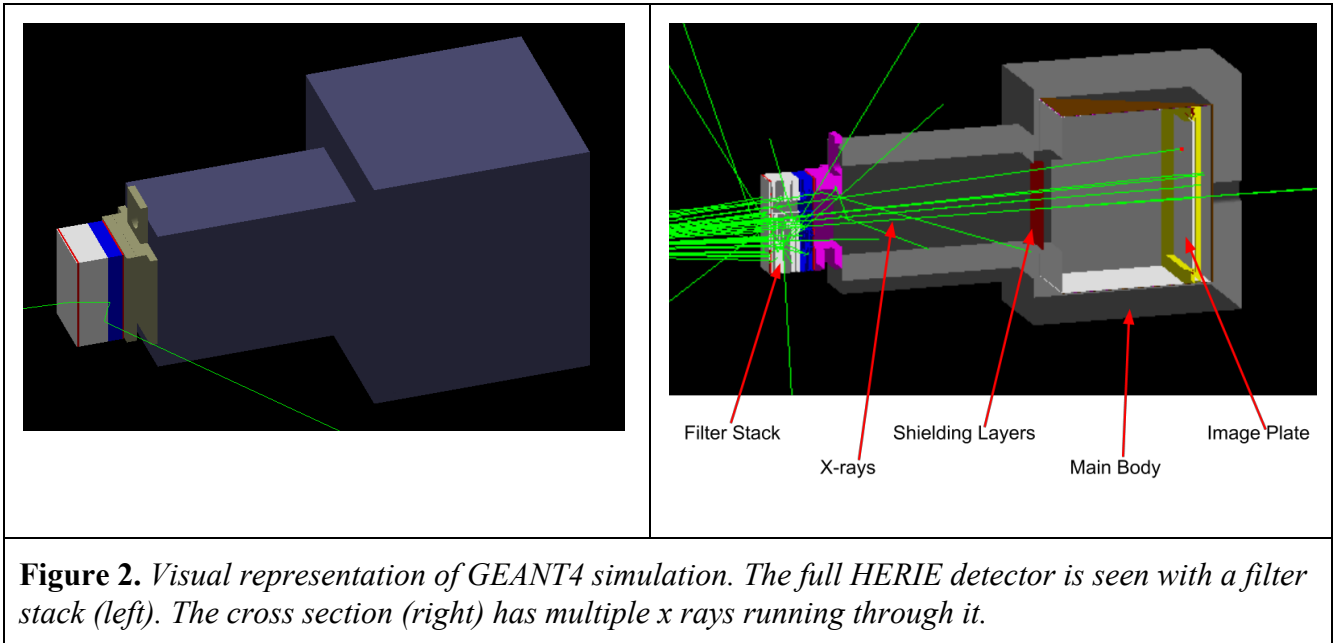
Figure 2 also shows visuals from a simulation with multiple beams running through the detector. Each beam of energy has the possibility of deflecting from, passing through, or being absorbed into each layer of matter it encounters. GEANT4 handles every interaction and ultimately determines how much energy was absorbed in the sensitive layer.

4.1 Validation Using the Image Plate

The simulation model was validated by being used to simulate the image plate before it was incorporated into the full geometry of the detector. This was done by comparing values taken from the simulation with experimental data published by *B. R. Maddox et al.*[4] The first test was of the image plate's absorption, i.e., how much energy is trapped in an isolated image plate. This was done by creating a large second sensitive layer behind the image plate in GEANT4. A known amount of energy would be sent towards the image plate and any energy that was not absorbed would be detected by the second sensitive layer.
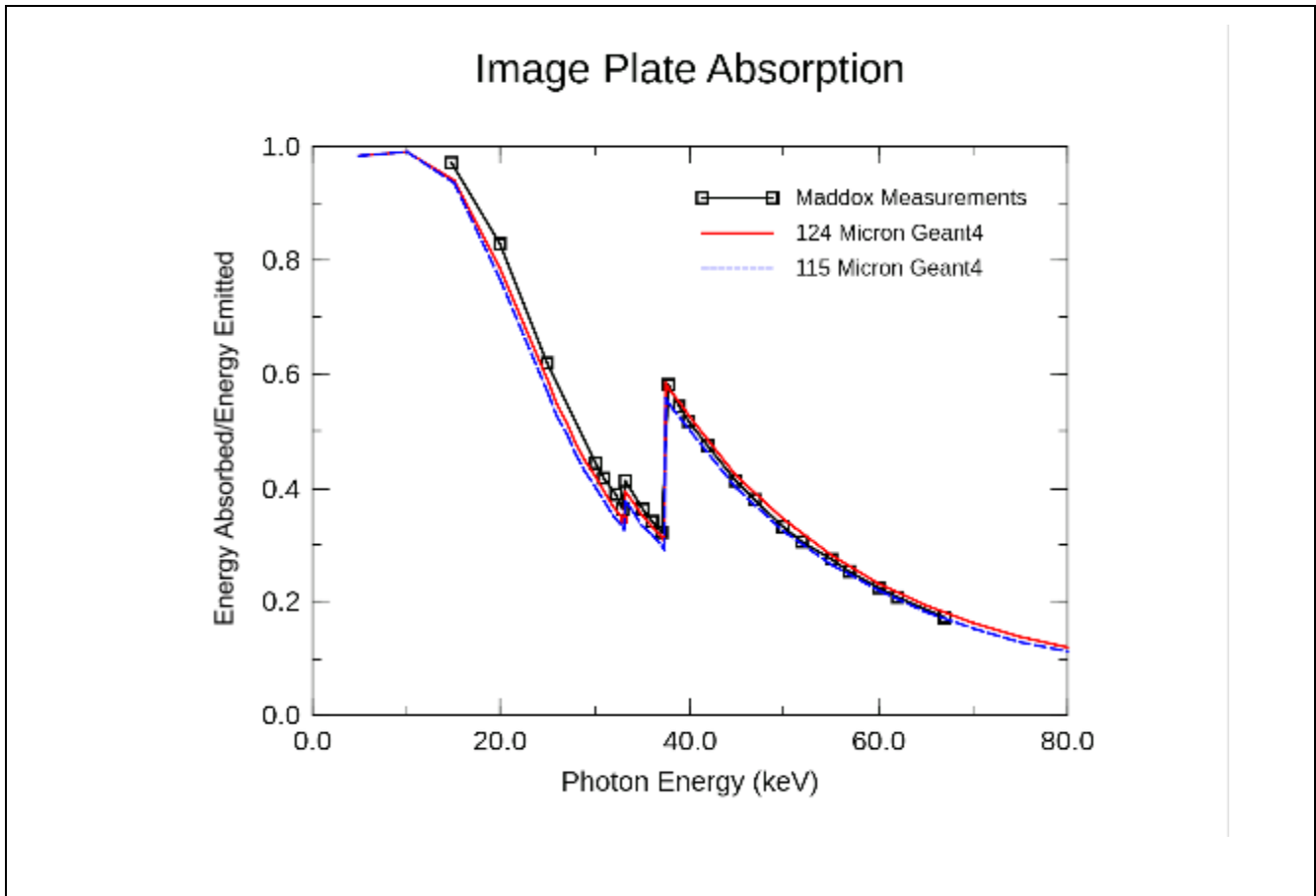
Figure 3. *Graph of absorption functions for the image plate calculated by GEANT4 for image plate thicknesses of 124 and 115 microns. Published data from B. R. Maddox et al[4] are included.*

Figure 3 shows the results of two simulations done in GEANT4 compared to the published data. Like the measurements, the simulated values show sharp increases, known as absorption edges, near energies of 32 keV and 38 keV, which is a characteristic created by the composition of the plate.[4] This implies a good match between the composition of the physical plate and the simulated plate. The two simulations differed only in the thickness of the image plate, since the published values for the thickness vary.

A second test was done to validate the image plate's sensitivity, i.e., the amount of energy absorbed by the image plate alone compared to the amount of energy directed towards it. The second sensitive layer was removed and the energy deposited in the sensitive layer of the image plate was

recorded. Published data from the experiment, as well as a model described in *B. R. Maddox et al.,* is compared to the GEANT4 data in Figure 4.The sharp increases in sensitivity correspond to the

Figure 4. *Graph of sensitivity values for the image plate calculated by GEANT4 for image plate thicknesses of 125 and 115 microns. Published data from B. R. Maddox et al[4] are included.*
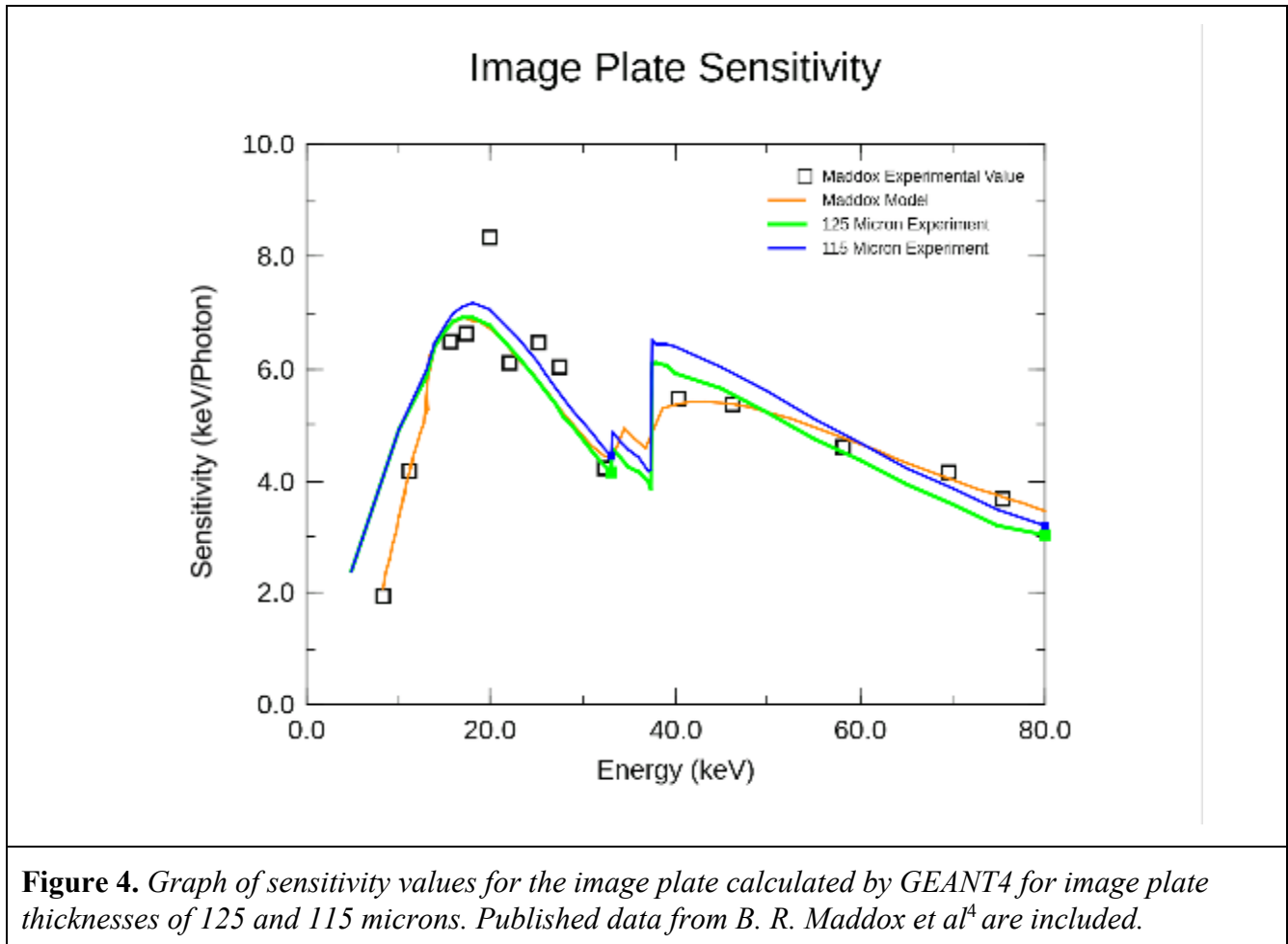
absorption edges found earlier. The difference between the two thicknesses appears larger in this test, but both are very close to the experimental data. The 125 micron thick plate was chosen for the rest of the simulations.

4.2 Validation Using the Full Geometry

Once the model of the image plate was confirmed to be accurate, the full geometry was added in and the model was tested against experimental data generated at LLE. This data was collected from

the emission of a predetermined spectrum of x rays corresponding to typical inferred spectra from experimental HERIE data. This hard x-ray spectrum was used in the GEANT4 model.

Figure 5. *Visual representation of energy deposited in image plate. GEANT4 simulation (left). LLE experiment (right). The scales are logarithmic to base 10.*
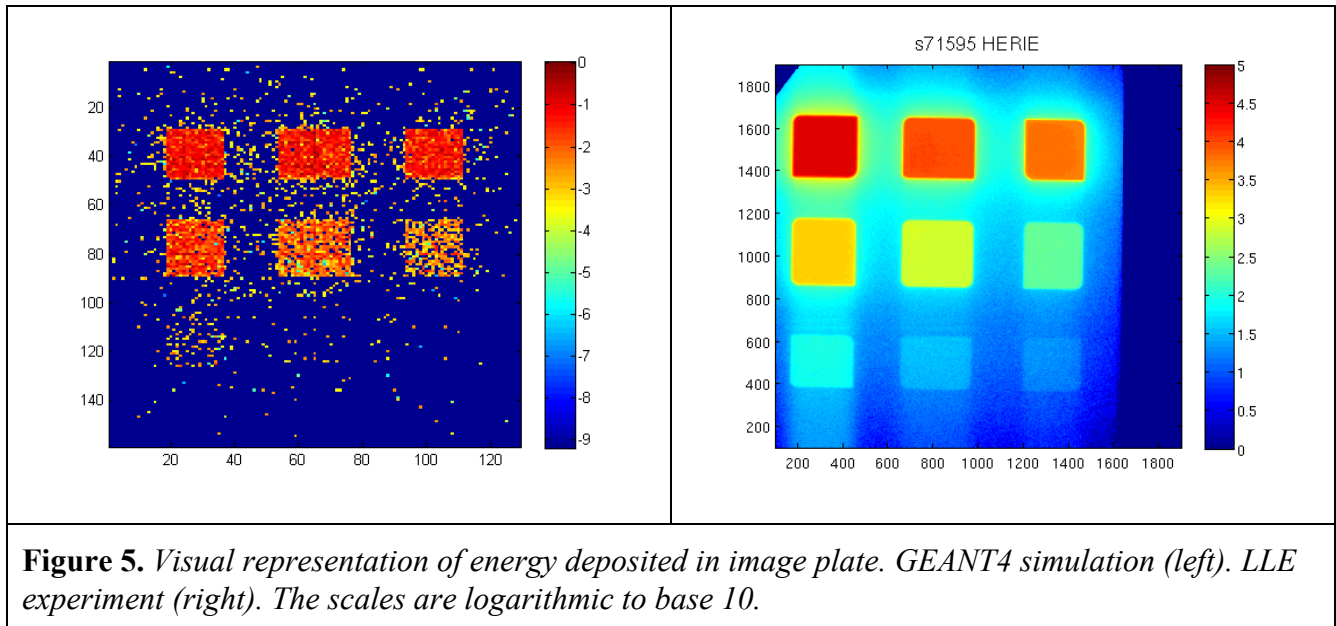
Shown in Figure 5, the simulation produced the same pattern of energy deposition in the image plate as the experiment did. The data collected from GEANT4 was plotted using a much lower spatial resolution compared to the experiment. However, the average values in each channel were compared to each other and the error was found to be small. This indicates that the full geometry properly accounts for the spread and deflection of beams within the detector and can be used to generate accurate sensitivity functions.

5. Creating the Sensitivity Functions

The full geometry was incorporated into the simulation with GEANT4 handling the probability of every interaction between energy and matter. In order to produce a realistic and accurate model of the sensitivity functions for each individual channel, the simulation stepped through small increments of x-ray energy and ran millions of x-ray photons during each step.

Figure 6. *Sensitivity functions generated by GEANT4 for all 9 channels.*
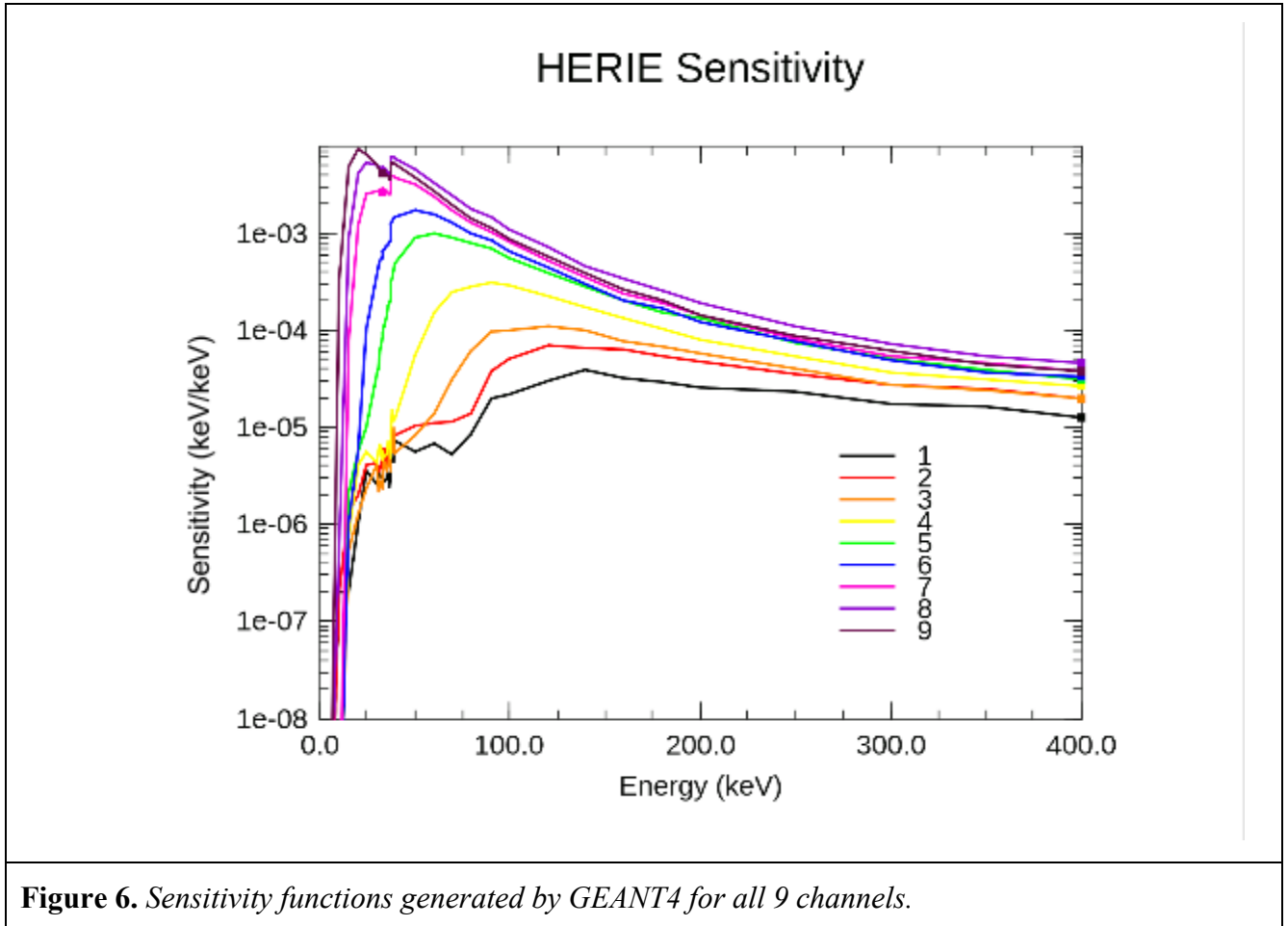
The combination of the functions shown in Figure 6 with the x-ray spectrum emitted by the target gives the total energy deposited in the image plate, which can compared to the data collected during an experiment. The x-ray spectrum emitted from the target can be approximated by an exponential function of energy

$$I \propto e^{\frac{-E}{kT}} \, , \tag{1}$$

where I is intensity, E is x-ray energy, and kT is a slope parameter. Summing up the squares of the differences between the measured signals on the different channels and the estimated signals as a function of slope parameter kT generates an error sum, which can drive an optimization procedure. The

slope parameter kT that produces the smallest error is determined to be the best representation of the actual x-ray spectrum (see Figure 7).
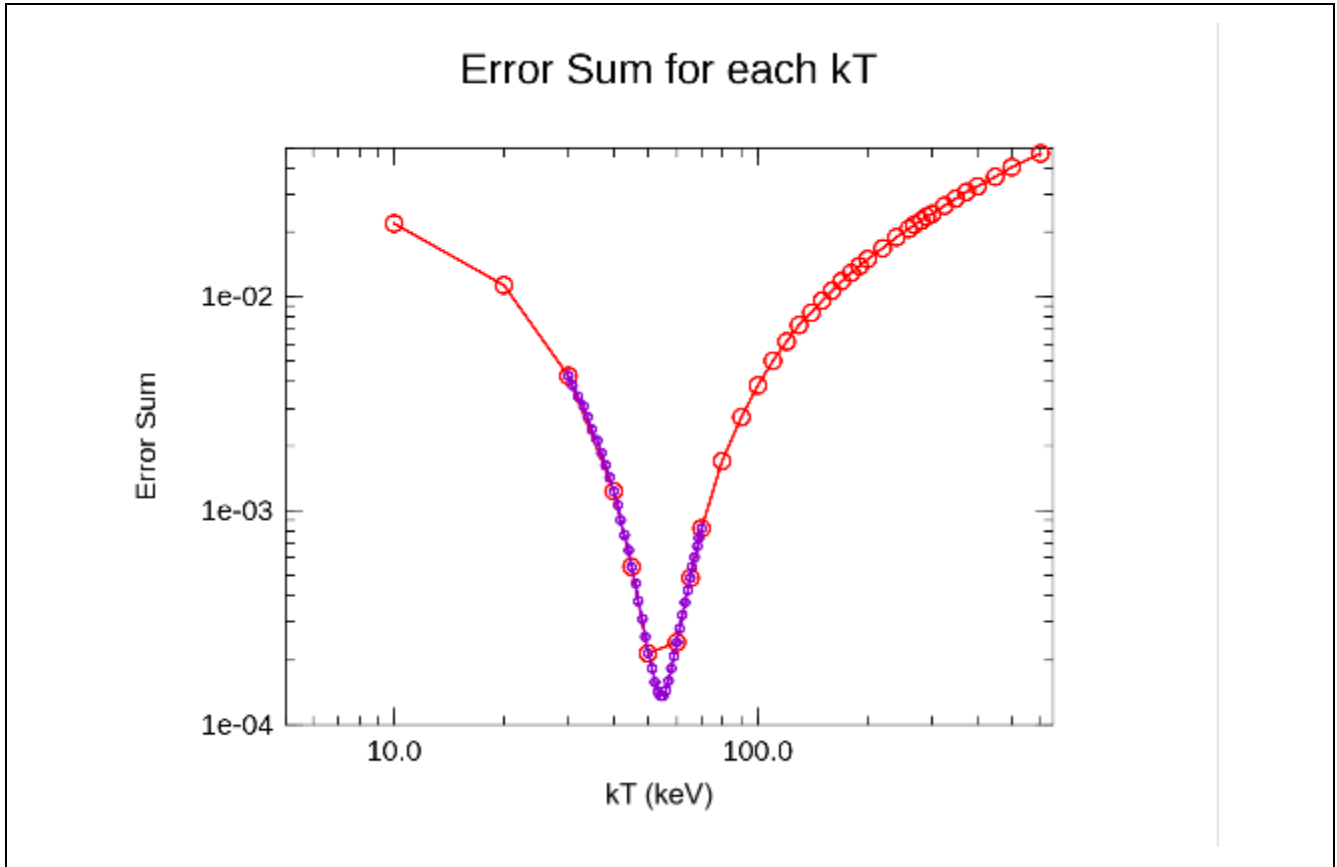
Figure 7. *Error sum for a sample spectrum. The red model uses larger increments as a function of slope parameter kT to guess what the slope parameter kT is while the purple model uses smaller increments around the prediction of the red model to determine kT more precisely.*

6. Results

After the new sensitivity functions were generated, slope parameters were calculated for multiple experiments and compared to slope parameters calculated for the same experiments using the old sensitivity functions (see Figure 8).
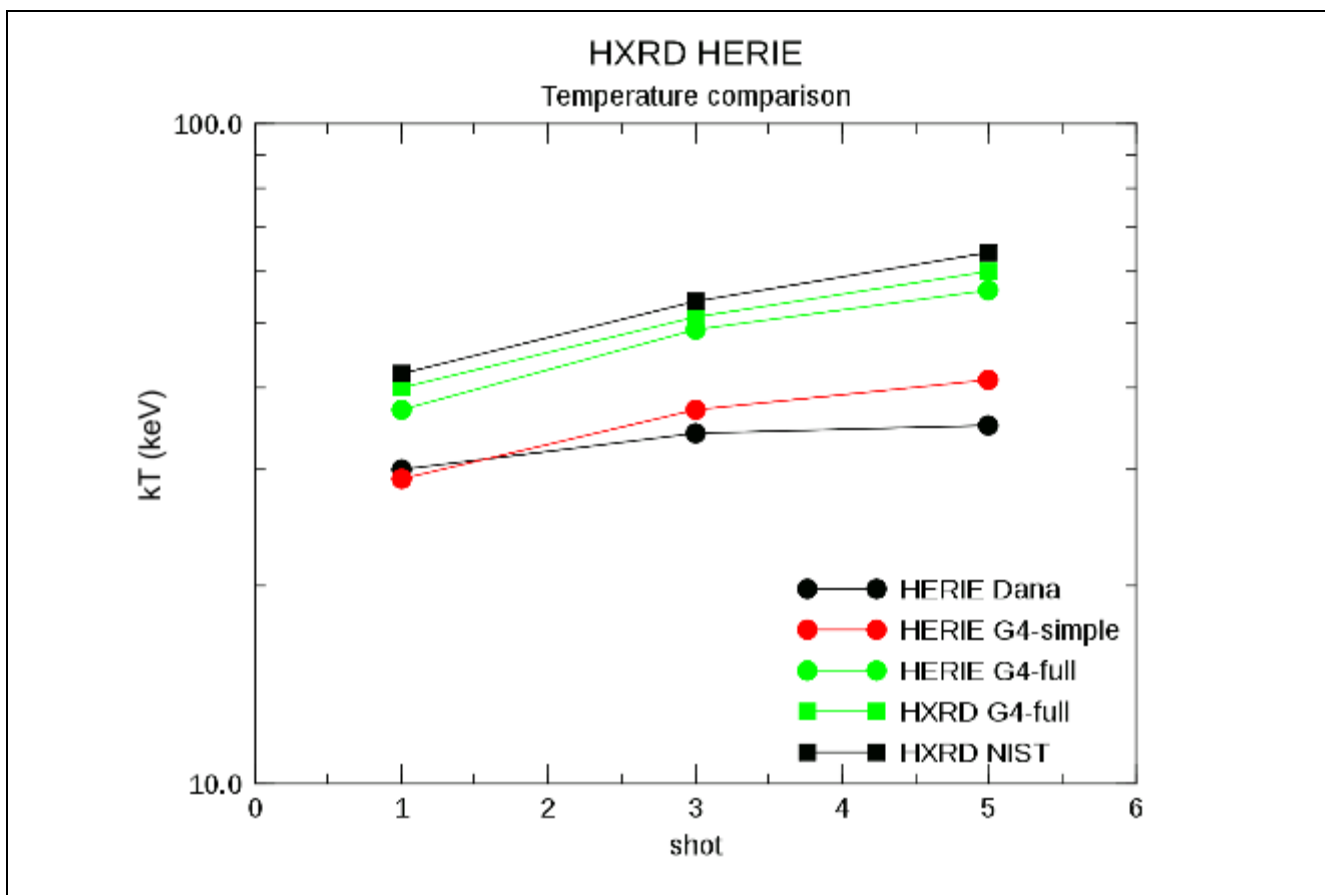
Figure 8. *Comparison of inferred slope parameter (kT) during multiple experiments using different sensitivity functions.*

The two black lines used the original sensitivity functions generated without the use of GEANT4 and demonstrate the discrepancy between the HERIE and HXRD detectors. The red line is produced by the function created by GEANT4 when only the filter stack and image plate are included. It only had a minor effect on the inferred spectra of the HERIE detector. The two green lines are the result of GEANT4 simulations that involve the full geometry. The HXRD simulations were created in parallel but separate from the simulations described by this paper. The adjustment on the HERIE detector appears greater because the HERIE geometry is more complicated and the difference between using the full geometry and the simplified geometry is greater than with the HXRD detector. Using the

newly corrected sensitivity functions involving the full geometry (green lines) demonstrates a very close agreement between the detectors.

7. Conclusion

The discrepancy between the HERIE and HXRD hard x ray detectors was significantly reduced by improved sensitivity functions generated through GEANT4 simulations. The Monte Carlo simulations created in the GEANT4 framework accurately modeled the image plate and the full geometry of the HERIE detector. This created a more accurate sensitivity function for each channel that can be used to accurately infer the spectrum of incident x rays. These new sensitivity functions will be used in future experiments on the Omega and Omega-EP system that involve the HERIE detector.

8. Acknowledgements

I owe a large thanks to my advisor Dr. Christian Stoeckl for his continual aid, his endless patience, and his complete understanding of unfortunate circumstances. I would also like to thank Dr. Stephen Craxton for running this program and allowing me to partake in an experience that has impacted my choices as I move towards college. Finally, I would like to thank every teacher and mentor I have had that has passed on their love for science and discovery to me.

9. References

[1] C. Stoeckl et al., "*Hard x ray detectors for OMEGA and NIF*", Review of Scientific Instruments **72**, 1197 (2001)

[2] Dana Edgell, private communication

[3] GEANT4 Applications and User Support, Page last modified 01/09/15, Website

http://geant4.cern.ch/

[4] B. R. Maddox et al., "*High-energy x ray Backlighter Spectrum Measurements Using Calibrated Image Plates*", Review of Scientific Instruments **82**, 023111 (2011).